Quantification and interpretation of glacier elevation changes

Christopher Nuth

Department of Geosciences

University of Oslo

A thesis submitted for the degree of

Philosophiae Doctor (PhD)

2011 January

Series of dissertations submitted to the
Faculty of Mathematics and Natural Sciences, University of Oslo
No. 1062

ISSN 1501-7710

Cover: Inger Sandved Anfinsen.
Printed in Norway: AIT Oslo AS.

Produced in co-operation with Unipub.
The thesis is produced by Unipub merely in connection with the
thesis defence. Kindly direct all inquiries regarding the thesis to the copyright
holder or the unit which grants the doctorate.

Abstract

Glaciers, ice caps and ice sheets constitute a large reservoir in the global hydrological cycle and provide a coupling between climate and sea-level. Observations of glacial change is important for constraining their contribution to sea-level fluctuations and to better understand the interactions between glaciers and climate. This thesis focuses on glacier observations through measurements of elevation change.

The research in this thesis is oriented towards the methodological detection of elevation changes using remote sensing techniques. The quality of glacier elevation change measurements is dependent on controlling the potential errors and biases within the data. Therefore, one aspect is focused on a universal co-registration method for elevation products and further identification and correction of biases that remain, specifically in satellite stereo products.

For glaciological studies, elevation changes require conversion into volume and mass changes. This is sometimes complicated when the data available is not spatially continuous and/or temporally consistent. Therefore, another aspect of this thesis explores methods for estimating regional glacier volume change. Specifically, Svalbard glacial contribution to sea-level has been estimated using regionalization techniques from scattered elevation measurements over roughly two time epochs. We observed that Svalbard glaciers over the past few decades have had a negative mass balance, contributing approximately 0.026 mm per year to the oceans. During the past few years, the sea-level contribution from Svalbard glaciers decreased slightly to 0.013 mm per year.

Interpretations of elevation changes are convoluted by their dependence on climatic and dynamic forces operating on glacier systems. The last aspect of this thesis experiments with surface mass balance modelling for quantifying the climatic component of an elevation change. Combining this with observed elevation changes using theory of mass continuity can yield estimates of the calving flux of icebergs into the ocean. We observed on one particular fast flowing glacier in Svalbard that the average calving flux in the 1966-1990 epoch increased in the 1990-2007 epoch.

Acknowledgements

A thesis comprises more than just the words on the following 141 pages. A thesis contains ideas shared and developed with colleagues. A thesis comprises many hours of field work providing shared adventures and experiences that create strong friendships. A thesis involves many hours of stress and struggle that work its way into our personal lives.

This thesis would not be possible without the support and guidance from my supervisors. Jack Kohler introduced me to glaciology and took me under his wing after a rather short meeting 5 years ago in Oslo Central Station (over a cup of coffee, of course!). He has been my mentor ever since and I owe much of my knowledge to him, and not to forget all the fun and frustrations of the yearly field work. Jon Ove Hagen has also mentored me from Day 1. With his years of experience in glaciology and nonchalant approach towards fieldwork, he has shaped many of the ideas contained in this thesis and led me on countless adventures. Thomas Vikhamar Schuler believed in one original idea of this thesis, and guided me throughout the process. Without his perseverance and patience, I would have never learned as much as I have. Andreas Kääb is the remote sensing mentor that opened my eyes to proper techniques and methods as well as guiding me towards better and more interesting science.

I must also acknowledge the numerous colleagues and friends at the Dept. of Geosciences (UiO) and the Norwegian Polar Institute who have provided great working conditions both in the office and the field. In particular, Geir Moholdt has taught me much through our time together sharing ideas and writing papers. Ola Brandt has been a great mentor in the field and the office. Bas Altena, Anne Chapuis and Mats Björkman have been great friends in the field and office. I am grateful to Kimberly Casey who took on the tedious job of proofing parts of this thesis. And not to forget the numerous others (Karsten, Thorben, Torborg, Tobi and Anna) for all the interesting discussions both scientific and non scientific that made lunch breaks interesting and coffee breaks plentiful.

I have to also thank my family for everything they have provided for me. Mom for pushing me into education when I least wanted to. Dad for supporting me whenever I needed an extra hand. Tara for holding high spirits and interest in this work which sometimes can feel meaningless. Last, I thank my beloved Ann-Live for her loving support and the final part of this thesis is, of course, dedicated to Trym.

Contents

1

Introduction

Glaciers, ice-caps and ice sheets together cover ≈14.5 million km^2 of the Earth's surface and have a potential to raise sea level[1] up to ≈64 m (Lemke et al., 2007). The relation between land-ice and other components of the present climate system is complex and large regional variability persists in the mass change of glaciers. It still remains unclear whether gain of mass in the accumulation areas is compensating for some of the loss at the peripherals (Walsh and others, 2005). The extensive volume of land-ice adjusts in response to climate, radiative forcing and ice dynamics and further represents a coupling between climatic change and sea-level fluctuation. As temperature and melt increase, the global area of ice declines reducing the albedo, the reflectivity of the Earth's surface. This allows more solar energy to be absorbed at the Earth's surface, further increasing temperature and melt (Barry, 2002). In addition, as the magnitude and area of surface melt increases on a glacier, the increased melt water potentially reaching the base of the glacier increases the sliding velocity (Iken and Bindschadler, 1986; Bartholomaus et al., 2008; Schoof, 2010) and thus the calving flux of ice into the ocean (Zwally et al., 2002a). Therefore, monitoring changes of glaciers, ice-caps and ice sheets is important in determining the past and present day contribution to sea level fluctuation and to better characterize the present day changes in relation to climatic fluctuations.

The principle parameter that characterizes glacier change is the mass balance, or the change in water equivalent volume of the glacier within some defined time interval.

[1] assuming an ocean area of 362 million km^2, an ice density of 917 kg m^{-3}, a seawater density of 1.028 kg m^{-3}

Generally, this mass balance may be divided into three components: the surface and basal mass balance and the mass loss due to calving icebergs. Proxies for the seasonal or annual mass balance include the equilibrium line altitude (ELA) which represents the elevation that divides the ablation and accumulation zones on the glacier or the accumulation area ratio (AAR), the percentage of area above the ELA. Proxies for the longer temporal state of glaciers can be reflected in fluctuations of the glacier front position, inherently a function of mass balance and proxy for temperature (e.g. Oerlemans, 2005).

Monitoring glacier changes directly from the ground include measurements of the surface mass balance, velocity and/or elevation and terminus changes. The surface mass balance is determined by stakes drilled into the ice surface. The height from the glacier surface to the top of the stake is measured on a seasonal and/or annual interval and the change in this height multiplied by the density of the snow/ice results in the mass change at the stake (Østrem and Brugman, 1991). The point measurements are then integrated (extrapolated) over the entire glacier surface, commonly using the area-altitude distribution (also called the hypsometry). Alternately, extrapolation of point measurements can be accomplished by empirically or analytically modelling components of the mass balance (Hock, 2003; Arnold et al., 2006; Schuler et al., 2007; Sicart et al., 2008; Schuler et al., 2008). Glacier velocity may also be measured by determination of the stake positions through time, commonly using the global navigation satellite system (GNSS) with code (less accurate) and differential (more accurate) based receivers. Estimating the glacier flux in terms of calving icebergs require ice thickness measurements (acquired using radar and seismic techniques or directly drilling through the ice) and an assumption (or measurement) of the velocity profile with depth. Last, GNSS techniques on the ground may be used to measure the terminus position and glacier surface elevation that can help determine the volume change of a glacier.

The techniques of measuring the Earth's surface through remote sensing has provided the ability to measure numerous glacier parameters that are related to both the instantaneous and temporally averaged mass balance of the glacier. Over longer time periods (greater than a few years), the volume change of a glacier can be measured by comparing measurements of surface elevation obtained by either photogrammetric principles applied to stereo-optical imagery (either aerial or satellite-borne) (e.g. Kääb,

2005), interferometric techniques of radar imagery (e.g. Farr et al., 2007) or altimetric acquisition methods (e.g. Echelmeyer et al., 1996). Indirect proxies of the longer time glacier mass balance can be derived by remote sensing through measurements of area and length changes from terrestrial, aerial and satellite imagery comparison (e.g. Hoelzle et al., 2007; Andreassen et al., 2008). On a shorter time scale, snow line altitude, a proxy for the ELA, and the AAR can be detected using either visible or radar images which are related to the seasonal or annual surface mass balance of a glacier (e.g. König et al., 2004; Mathieu et al., 2009; Barcaza et al., 2009). Recently, international collaborations efforts have been concentrated on deriving a global glacier database (The GLIMS project, www.GLIMS.org) based upon measurements from space that help record the increasing amount of proxy data such as area changes and snow-line locations (Raup et al., 2007). Glacier velocity can also be measured remotely using either interferometric (Kwok and Fahnestock, 1996) or image matching (Joughin, 2002; Kääb et al., 2005) techniques, both dependent on the magnitude of the movement between two acquisitions. Translation of velocities into fluxes require knowledge of the ice thickness (cross sectional area) which is reliant on ground-based remote sensing technologies. Similarly, an assumption or measurement of the velocity profile with depth is required to translate surface velocities into calving fluxes.

The goals of many of these measurements and applied techniques are to better define the contribution of glaciers, ice-caps and ice sheets to sea-level change and to better define the processes that relate glacier behavior to driving and determining forces such as meteorology and climate, geology and hydrology. This thesis combines both direct and remotely sensed measurements in order to quantify glacier changes, analyze methods and approaches from which to determine those glacier changes, and if possible, offer quantifiable interpretations of the changes. With increasing capability to monitor glaciers continuously from space, observed glacier changes will help constrain models to predict the future behavior of glaciers.

2

Motivation and Objectives

The first glacier inventory of Svalbard classified 2229 glaciers making up ≈36,000 km^2, about 60% of the land area (Hagen et al., 1993). The archipelago contains small valley glaciers, larger tidewater glaciers, smaller ice fields and ice caps, many of which are polythermal in nature, exhibit surge-like behavior and some relic fast flowing glacier units. Svalbard contains two of the longest continuous direct mass balance time series (1967-present) in the Arctic, Midtre Lóvenbreen and Austre brøggerbreen located in western Svalbard. About 13 other small glaciers, mainly located in the central or south part of the archipelago have direct mass balance measurements available (Hagen et al., 2003b). Since 2004 and 2007, continuous mass balance measurements have been carried out on the largest ice mass in Svalbard, Austfonna (Moholdt et al., 2010a), and its smaller sibling Vestfonna (Möller et al., subm.), respectively. Previous estimates of the archipelagos mass balance have mainly been restricted to extrapolations of these direct surface mass balance estimates.

The location of Svalbard at the transition boundary between the tail end of the warm Atlantic current that transports heat from the tropics to the poles and the colder arctic atmosphere creates regionally variable meteorological conditions. This makes extrapolations of direct mass balance measurements significantly difficult due to undersampling both in space and with elevation (Hagen et al., 2003b). Therefore, previous estimation of Svalbard's present-day sea-level equivalent (SLE) contribution has varied between 0.01 SLE yr^{-1} (Hagen et al., 2003b), 0.038 SLE yr^{-1} (Hagen et al., 2003a) and 0.056 SLE yr^{-1} (Dowdeswell et al., 1997). In other regions of the world, like Alaska, Canada, Greenland and Antarctica, efforts have turned towards measuring geometric

changes to provide estimates of glacier volume change and contribution to sea level (Arendt et al., 2002; Abdalati et al., 2004; Thomas et al., 2008; Zwally et al., 2005).

The mass balance of Svalbard glaciers vary regionally, partly due to the large meteorological gradients (Sand et al., 2003; Førland and Hanssen-Bauer, 2003) but also due to the varied hypsometries that topography and the precipitation gradients mainly dictate (Hagen et al., 1993). Many also exhibit surge-like behavior though surges have not been observed related to location (Hamilton and Dowdeswell, 1996; Jiskoot et al., 2000; Sund et al., 2009). Therefore, interpretation of elevation changes (both their magnitude and their spatial distribution) is complicated by the numerous individual glacier response times and phases within potential surge-quiescent cycles, and also to the great regional variability of the surface mass balance around Svalbard.

The objectives of the research composed within this thesis is the quantification and interpretation of glacier changes, particularly on Svalbard where difficult direct mass balance extrapolations sanction independent geodetic estimates for comparison. With increasing production, availability and accuracy of elevation data, geometric changes of glaciers are becoming more abundant (e.g. Abermann et al., 2009; Haug et al., 2009; Peduzzi et al., 2010; Moholdt et al., 2010a; Berthier et al., 2010), and interpretations of changes remain difficult, and sometimes misleading, because of errors in the data and to the influences of both surface mass balance and dynamics that comprise a glacier elevation change. Therefore, this thesis additionally establishes standard methods for controlling errors in elevation differencing that can lead to mis-interpretation and biased estimates. The interpretation of elevation changes is aided by some knowledge of the local mass balance of the specified glaciers. An experiment based upon comparing an empirically derived mass balance model and elevation changes is performed on two dynamically different glaciers that contain at least 7 years of continuous annual surface mass balance measurements.

3

Scientific Background

The techniques of quantifying elevation and volume changes of glaciers started developing in 1950s with the use of terrestrial and aerial photogrammetry (Finsterwalder, 1954). Satellite based elevation differences began with the earliest radar altimeters on GEOS-3 (1975), Seasat (1978) and Geosat (1985) (Zwally et al., 1989; Lingle et al., 1994; Herzfeld et al., 1997) though digital photogrammetric techniques of multi-temporal space imagery from the Corona reconnaissance operation (1962) has also been used for elevation differencing to newer data products (Bolch et al., 2008). Today, elevation differences are calculated using both aerial and satellite based acquisition methods such as radar and lidar altimetry, interferometry and stereoscopy of optical imagery. This is increasing the amount of elevation data available for comparison, and advancing the capability to monitor glacier elevation changes at higher temporal resolution. However, more significant results are obtained when glacier changes are large, and in many cases when the time between elevation measurements is long (Arendt et al., 2002; Schiefer et al., 2007; Berthier et al., 2010). Nevertheless, measurement errors transferred to the change estimates may accumulate, sometimes systematically, resulting in spurious interpretation of elevation changes (e.g. Muskett et al., 2009; Berthier, 2010).

The methods for integration of the elevation changes into volume changes is largely dependent upon the data available. Ideally, full glacier DEMs are available (Larsen et al., 2007; Schiefer et al., 2007; Berthier et al., 2010), but in many cases only centerline altimetric profiles are available (Echelmeyer et al., 1996; Abdalati et al., 2004; Bamber et al., 2005) which require some extrapolation function. The first part of this thesis explores larger regional elevation change integration in Svalbard, mainly using ICESat

altimetry (Article I and II). The second part of this thesis focuses on the methodological comparison between full glacier DEMs (Article III) and the direct comparison with the surface mass balances to examine the potential to infer glacier dynamics (Article IV).

The intentions of this section are to briefly introduce the concepts that form the basis of this thesis. Each of the submitted articles describes the approaches and elevation change interpretations in greater detail. Section 3.1 describes basic glacier theory of mass continuity that relates the elevation changes to climate through the surface mass balance. Section 3.2 outlines the data, errors, methods and assumptions of generating volume changes from elevation changes. Section 3.3 introduces observations of surface mass balance and modelling approaches for extrapolation.

3.1 Mass continuity

Mass continuity relates glacier mass balance, flow and geometry changes. A detailed derivation and discussion of glacier mass continuity can be found in Cuffey and Paterson (2010). Here, we simplify the discussion and list the assumptions. For any volume element of a given material having density, ρ, mass continuity is written:

$$\frac{\partial \rho}{\partial t} + \nabla (\rho \vec{u}) + \beta = 0 \tag{3.1}$$

where $\vec{u}$ is a velocity vector and β is a production term. Equation 3.1 states that any local change in density is balanced by the net flux of material into or out of the considered volume plus any source or sink of mass. Integration from the bed (h_b) to the surface (h_s) provides the continuity equation for a vertical column through a glacier:

$$\frac{\partial}{\partial t} \int_{h_b}^{h_s} \rho \, dz = b - \nabla \vec{q} \tag{3.2}$$

where

$$b = b_s + b_e + b_b \tag{3.3}$$

$$\nabla \vec{q} = \bar{\rho} \int_{h_b}^{h_s} \vec{u} \, dz \tag{3.4}$$

The term on the left side of eq. 3.2 represents the change in mass of the given volume and may be approximated through gravity variations (e.g. Wahr et al., 2004; Luthcke et al., 2008) or elevation changes. On the right, the mass balance (b) is the sum of surface (b_s), englacial (b_e) and basal (b_b) components (eq. 3.3). The horizontal flux

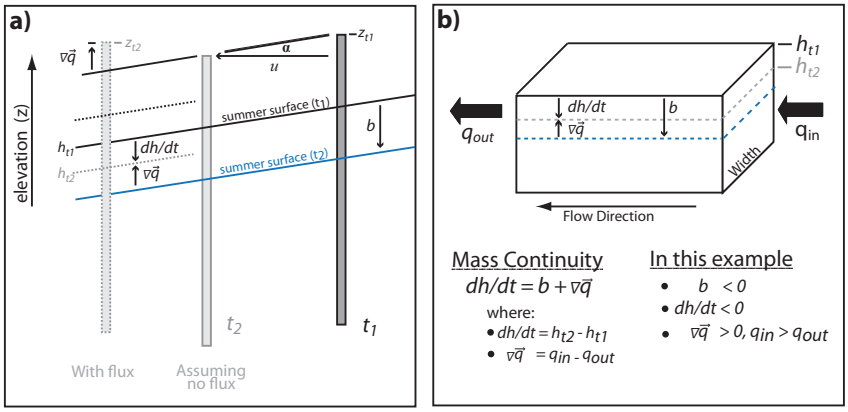

Figure 3.1: Schematic of mass continuity in the ablation area of a surface mass balance stake (a) and of a larger 3 dimensional cross sectional volume of a glacier (b). The surface elevation (h) and the top of the stake elevation (z) is shown for two discrete times (t_1 and t_2). b is the surface mass balance, u is the horizontal velocity, and α the surface slope of the surface between the stake position at t_1 and t_2. The flux divergence ($\nabla\vec{q}$) is the difference between flux in and out (q_{in} - q_{out}) of the column.

divergence ($\nabla\vec{q}$) is the column average velocity (eq. 3.4) multiplied by the density, ρ, which closely approximates the density of ice in cases where firn is a small proportion of the ice thickness (Cuffey and Paterson, 2010).

To relate the mass change (left side of eq. 3.2) to observed elevation changes ($\frac{\partial h}{\partial t}$), we introduce an effective density (ρ_{eff}) to express the vertical and temporal density changes of the column:

$$\frac{\partial}{\partial t}\int_{h_b}^{h_s} \rho \, dz \approx \frac{\partial h}{\partial t} \cdot \rho_{\text{eff}} \tag{3.5}$$

It is also convenient to continue in water equivalent units because this is the common measuring practice for the glacier mass balance (b). We now assume that englacial and basal mass balances are negligible ($b_e << b_s$ and $b_b << b_s$) and that the flux divergence ($\nabla\vec{q}$) represents mass change of incompressible ice. The continuity expression can then be reduced to:

$$\frac{\partial h}{\partial t} \cdot \kappa = (\, b_s + \cdot\nabla\vec{q}\,) \cdot \rho_w^{-1} \tag{3.6}$$

where ρ_w is the density of water and κ is a conversion factor from height differences to water equivalent changes:

$$\kappa = \frac{\rho_{\text{eff}}}{\rho_w} \tag{3.7}$$

If $\frac{\partial h}{\partial t}$ is observed over a significantly long time period, κ can be approximated by the density ratio of ice to water (0.9) below the ELA. This because small changes in the less dense snow have little impact on the column average density and thus all changes will be of incompressible glacier ice. In the firn area, changes in the proportion of firn to the ice column can alter κ due to the compressibility of firn. Often, it is assumed that firn thickness and density are constant through time ("Sorge's Law", Bader, 1954) in which case $\kappa = 0.9$.

Fig 3.1a shows an application of mass continuity using a stake in the ablation area as reference to measure the surface mass balance and $\nabla\vec{q}$. The surface slope (α) between the stake positions at t_1 and t_2 is required to adjust the change in stake elevation ($\frac{\partial z}{\partial t}$) due to downslope migration (see also Hagen et al., 2005):

$$\nabla\vec{q} = \frac{\partial z}{\partial t} + u \cdot tan(\alpha) \tag{3.8}$$

The vertical change in height of the top of the stake ($\frac{dz}{dt}$) and the horizontal velocity (u) can be measured by differential GNSS techniques. The slope of the surface (α)

must be estimated from a DEM or GNSS profile. Fig 3.1b demonstrates the same example as above over a cross sectional volume. The change in surface slope over the representative block is not considered here, however, slope changes may be significant on glaciers that have drastically changed their geometry, as in cases of glacier surges.

Solving mass continuity over the entire glacier system requires integration of eq. 3.6 over the glacier surface area (A):

$$\int\int_A \frac{\partial h}{\partial t} \cdot \kappa \cdot \; dxdy = \frac{\partial V}{\partial t} = B - \int\int_A \nabla \vec{\hat{q}} \; dxdy \tag{3.9}$$

All terms in water equivalent, this relates the volume change ($\frac{\partial V}{\partial t}$) to the flux divergence ($\nabla \vec{\hat{q}}$) and the glacier-wide mass balance (B). Applying the divergence theorem to the last term in eq. 3.9 results in the relationship between the glacier-wide integrated flux and the water equivalent flux through a boundary (R):

$$\int\int_A \nabla \vec{\hat{q}} \; dxdy = \oint_R \left(\vec{\hat{q}} \, \vec{n} \right) dr \tag{3.10}$$

and substitution into eq. 3.9 results in:

$$\frac{\partial V}{\partial t} = B - \oint_R \left(\vec{\hat{q}} \, \vec{n} \right) dr \tag{3.11}$$

where $\vec{n}$ is the normal vector to the closed boundary (R). The second term on the right may represent the influx of ice by avalanching or the loss through calving.

Using eq. 3.11, we consider two solutions: non-calving and calving glaciers. Often for non-calving glaciers, $\oint_R (\vec{q} \, \vec{n}) \, dr$ is assumed equal to zero resulting in:

$$\frac{\partial V}{\partial t} = B \tag{3.12}$$

This has formed the basis of many comparison studies aimed to control systematic errors in the cumulative direct surface mass balance integration by using geodetically measured volume changes (e.g. Krimmel, 1999; Elsberg et al., 2001; Cox and March, 2004; Thibert et al., 2008; Zemp et al., 2010, etc.). For a calving glacier, $\oint_R (\vec{q} \, \vec{n}) \, dr$ is equal to the flux (Q) through the boundary (R) of the glacier:

$$\frac{\partial V}{\partial t} = B + Q \tag{3.13}$$

Practically solving mass continuity of an entire glacier system requires definition of the boundary geometry. For simplicity or due to lack of updated maps, this geometry

may be held constant. For example, Elsberg et al. (2001) introduce the concepts of a *reference* and *conventional* surface for mass balance integration and suggest a transformation between them. The *reference* surface is a constant map year and considered to be more climatically related as it removes the effects of surface change on the mass balance. The *conventional* mass balance is the actual mass change of the glacier relevant for hydrological and sea-level change studies. Equation 3.13 can be modified to handle the volume of retreat/advance separately:

$$\frac{\partial V_{r/a}}{\partial t} = B_{r/a} + Q_{r/a} \tag{3.14}$$

where

$$Q_{r/a} = Q' - Q \tag{3.15}$$

Derived in this way, $\frac{\partial V}{\partial t}$ and B of eq. 3.12 and 3.13 can be solved using a *reference* surface defined as the smallest glacier area. Q is then the ice flux through the cross sectional area (flux gate) defined by the glacier front at the time of smallest glacier area (i.e. the most recent area in cases of retreat). $\frac{\partial V_{r/a}}{\partial t}$, and $B_{r/a}$ are the volume change and mass balance of the receding (r) or advancing (a) area. $\frac{\partial V_{r/a}}{\partial t}$ is unproblematic to quantify provided knowledge of the basal elevation or depth below sea level in the retreat or advance area. $B_{r/a}$ can be solved by assuming a linear retreat of the front. $Q_{r/a}$ is defined as the retreat/advance flux and is the difference between the net flux into or out of the glacier and the flux out of the gate defined by the front of the smallest area (Q). Hence, $Q_a > 0$ and $Q_r < 0$.

3.2 Glacier elevation changes

With the increasing employment of satellite surface elevation measuring techniques, glacier volume change (as in equation 3.12, 3.13 and 3.14) becomes easier to monitor globally at higher spatial and temporal resolutions while the accuracy of modern techniques is also improving. The ability to measure glacier volume changes accurately is co-dependent on the magnitude of the glacier changes and the accuracy of the surface elevation measurements. This section provides a methodological background for deriving elevation changes from remote sensing, an application that is present within all articles of this thesis.

3.2.1 Elevation Data

Elevation data can be acquired from the ground or from airborne and space-borne platforms. Ground and aerial techniques may provide the highest data accuracy and precision, however space-borne techniques provide a larger spatial coverage in less time at the potential cost of spatial resolution than the former acquisition platforms. In this thesis, surface elevations are acquired using phase-based differential GPS transported on the Earth's surface (i.e. snow-mobile), by using RADAR (RAdio Detection And Ranging) and LIDAR (LIght Detection And Ranging) sensors at a significant distance from the target being observed or by photogrammetry using images of the same target from two or more observation points. All techniques are based upon remote sensing either utilizing the time (or phase) difference between sent and received signals or through solving the stereo parallax by the projected intersection of image path rays on the earth's surface.

Stereo photogrammetry

Photogrammetric elevation data are typically in the form of a Digital Elevation Model[1] (DEM), defined here as any elevation surface represented by a continuous collection of adjacent pixels that describes the mean elevation within every pixel. Measuring surface heights through photogrammetry relies on the principle of parallax which is the apparent shift in the position of an object due to a shift in the position of the observer (Mikhail et al., 2001). A parallax measurement is the difference between the stereo rays of the same target from each image projected onto the Earths ellipsoid and can be converted to height if the two observer positions and the focal length of the camera are known (Lillesand et al., 2004). The Base-To-Height (B/H) ratio is an *a priori* estimate of parallax precision based upon the stereo geometry (Toutin, 2008). Image matching techniques (e.g. Debella-Gilo and Kääb, 2011) are used to automatically detect the same target in two or more images, a technique dependent upon the visible contrast of the targets and the pixel resolution of the images. Thus, the low visible contrast of the higher firn areas of glaciers remain a weakness of this elevation determination technique. Correlation masks from the image matching routines provides control on

[1] A difference exists between a digital elevation model (DEM), digital surface model (DSM) and digital terrain model (DTM). A DEM may be either a DSM or DTM, the former including vegetation and man made structures such as buildings and constructions. The latter containing the terrain alone.

determining the same target in both images. Further details about photogrammetric methods can be found in the plethora of books and manuals about photogrammetric techniques (e.g. Schenk, 1999; Mikhail et al., 2001; Lillesand et al., 2004; Kääb, 2005).

Stereoscopic DEMs derived from airborne vertical frame images are used in all article of this thesis. In Article I, contour data made from an analogue photogrammetric workstation is used as the earliest map for elevation change comparison. This type of data contains limited accuracy and precision partly due to the dependence upon the individual photogrammetrist to locate the same target in the image pair. Article I also uses a digital photogrammetric DEM in which image matching techniques decrease the dependence of precision upon the photogrammetrist. In that study, elevation differences with ICESat over assumed stable terrain resulted in a 3 m RMSE for the digitally made DEM as compared to 12-15 m for the analogue data (Figure 1, Article I). The data used in Article IV also provided an interesting opportunity to directly compare analogue and digital methods applied upon the same images. Although not shown directly in that article, the standard deviation of differences between contour vertexes and the bilinear interpolation of the DEM was ≈12 m for the glacier surface and ≈22 m for the non-glacier terrain. This difference is partly a slope induced affect as the stable terrain surface contains steeper slopes than the glacier such that small horizontal distortions exaggerate vertical differences.

Two types of satellite stereoscopic DEMs are used in this thesis, both automatically generated without the use of ground control points (Fujisada et al., 2005; Bouillon et al., 2006). The ASTER instrument, on-board the Terra platform, contains stereo capability with a nadir and back-looking sensor (B/H ratio = 0.6) recording in the near-infrared part of the electromagnetic spectrum (ERSDAC, 2005; Toutin, 2008). Article III uses ASTER DEMs generated automatically from the SilcAst software downloaded from USGS LPDAAC (Land Process Distributed Active Archive Center) which provides a 30m pixel resolution product. Articles II, III and IV additionally use automatically generated DEMs from the SPOT5-HRS stereo sensors (B/H ratio = 0.8) acquiring ≈5 m panchromatic images resulting in 40 m DEM products (Bouillon et al., 2006; Korona et al., 2009).

The errors within stereoscopic DEMs can be classified as blunders, stochastic and systematic errors. Figure 3.2 shows examples of the three error types in ASTER stereoscopic DEMs. Blunders are errors that derive from image matching failure and are

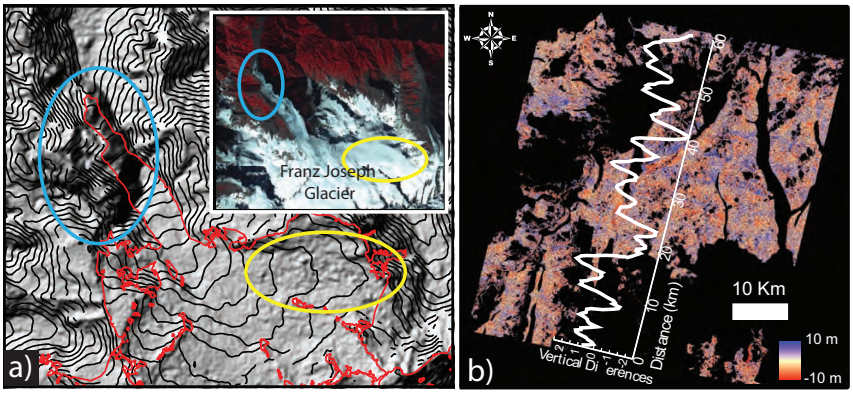

Figure 3.2: Examples of the stereoscopic error types. (a) is a hillshade from an ASTER SilcAst DEM (7 April 2001: L1A.003:2007486672) over Franz Joseph Glacier in New Zealand and the associated orthophoto (inset). The blue ellipse is an example of a blunder that appears as an artificial mountain/hill. The yellow ellipse shows the stochastic errors in the DEM when visible contrast is limited which appear as rough ("bumpy") surfaces in the hillshade. (b) shows the elevation differences between 2 ASTER SilcAst DEMs from 2002 and 2006 in the same region of New Zealand after co-registration and removal of a longer frequency elevation bias (see Article III for further details). The white lined plot shows the across-track elevation difference averages that exhibit a sinusoidal pattern along track that is related to satellite *jitter*, high frequency shaking of the instrument, that is not captured by the under-sampled satellite attitude measurements (Leprince et al., 2007).

strongly autocorrelated in space. They can typically occur in areas of similar looking contrast from either topography or clouds, on ice caps or lakes. Blunders will typically appear as large holes in the DEM, or as additional mountains. Stochastic errors are the random errors that mostly derive from the image matching process and will vary for different image resolutions, visible contrast conditions and pyramidal processing methodology. Systematic errors are generally in the form of translations, tilts, rotations and in the worst case, scale distortions. Systematic errors will also vary based upon the acquisition strategy, ie. whether frame imagery or pushbroom sensors are being used to collect the data. Article III provides a detailed description of how to detect, and suggestions for correcting, errors related to the geolocation of the original data, elevation dependent scale errors and along/across track biases, all of which are systematic errors that can commonly exist within pushbroom derived satellite stereoscopic DEMs.

LIght Detection And Ranging (LIDAR)

The principle behind LIDAR techniques is to measure the time it takes a transmitted pulse (signal) to be sent to an object, reflected, and returned to the receiver. This active remote sensing technique can be applied using sensors operated from the ground (terrestrial), carried by planes (aerial) and from space (satellite). The former two platforms for LIDAR acquisition are not used in this thesis, though the immensely improved accuracy and details contained within LIDAR DEMs has increased the applicability of these data sets to many fields within geoscience (Blair et al., 1999; Drake et al., 2002; Hopkinson and Demuth, 2006; James et al., 2006; Barrand et al., 2009; Abermann et al., 2010).

The LIDAR data used in this thesis is acquired from a satellite platform. The Ice, Cloud and land Elevation Satellite (ICESat) carrying the Geoscience Laser Altimeter System (GLAS) was launched in 2003. The acquisition strategy was reduced because of the abrupt failure of the first of three lasers. However, the mission surpassed the initial goal of a three year campaign by two years and it acquired nearly 2 billion elevation points before failure of the final laser in October 2009 (http://icesat.gsfc.nasa.gov). ICESat contained three lasers, each with two telescopes one infra-red (1024 nanometers) and one visible green (532 nanometers) for the land surface and atmosphere, respectively. The laser pulses at 40 Hz which translates into a seperation distance on

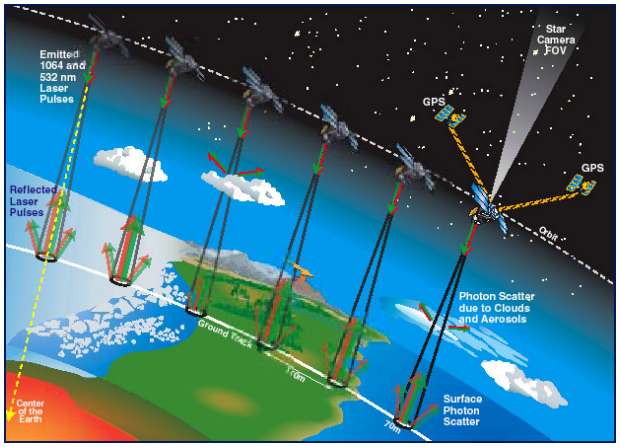

Figure 3.3: Schematic example of ICESat measurmenets of the earth's surface. ©NASA (Graphic created by Deborah McLean).

earth's surface of ≈170 m between each footprint (see schematic illustration, Fig. 3.3). ICESat averaged 2-3 acquisitions per year repeating similar reference tracks within a few hundred meters in the arctic. The amount of data is also much higher in the arctic as compared to the equator due to the polar orbiting strategy of the satellite. Full details of the ICESat mission can be found in Zwally et al. (2002b) and Schutz et al. (2005).

The GLAS instrument onboard ICESat is designed to measure the precise time it takes the laser pulse to travel from the satellite to the earth's surface and back again. The transmitted laser pulse is reflected from an elliptical footprint of the earth's surface that varied from 52X95m (lasers L1-L2c) to 47x61m (lasers L3a and L3b), an average of 64m (Abshire et al., 2005). For each transmitted laser pulse, the altimeter collects 4.5 million 1 nanosecond samples that is pre-processed onboard into 544 samples for transmission back to earth. To determine in which 544 sample time range the reflection from the earth's surface is contained, a generalized DEM is used to predict the time return (Brenner et al., 2003). Elevations are obtained by fitting Gaussian functions to the returned waveforms where the maximum amplitude of the return marks the two-way travel time which translates into distance from the satellite.

The transmitted waveform is 4 nanoseconds, equivalent to about 60 cm in surface el-

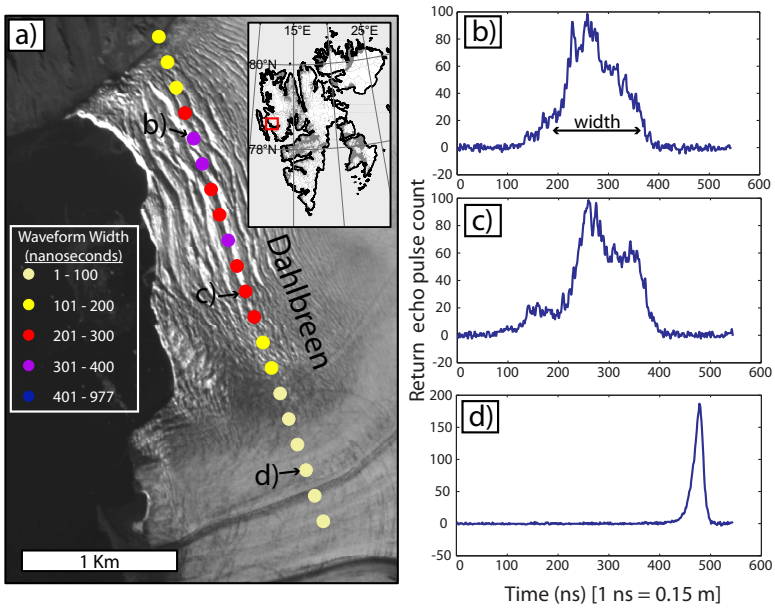

Figure 3.4: Examples of returned ICESat waveforms on varying glacier surfaces. (a) shows ICESat footprints from September 2003 that are color coded to a classification of return waveform widths. The background is a 2007 SPOT-HRS orthophoto. The exact crevasse pattern in the image may not correspond to the 2003 ICESat waveforms. The waveforms located in the crevasse zone (b and c) are wider than that located in a smoother glacier surface region (d). The width of the waveform represents the range of elevation from which the laser pulse is reflected, inferring crevasse depths of ≈30 meters.

evation (Brenner et al., 2003). The shape of the returned waveform is wider based upon the distribution of elevation within the reflected footprint. Therefore, slope broadens the waveform because of the larger range of elevation within a footprint and roughness increases the width because of the more uniform distribution of elevation within a footprint. Thus, only slope assuming no roughness or roughness assuming no slope may be extracted from the waveform (Brenner et al., 2003). Figure 3.4 shows an example of waveform widths on the tongue of a calving glacier in western Spitsbergen.

ICESat data is freely available, distributed by the National Snow and Ice Data Center (NSIDC; www.nsidc.org). In this thesis, two 2^{nd} level products are used, GLA06 (Zwally et al., 2010a) and GLA14 (Zwally et al., 2010b). The products differ by the number of potential Gaussian fits used to determine the mean elevation within the footprint. The GLA06 products are meant for glaciers and ice sheets because their relatively flat surfaces typically return waveforms that approximate a single gaussian and thus the average centroid of maximum two Gaussian fits are used to determine the mean elevation within the footprint. The GLA14 products are designed for land terrain surfaces as the steeper slopes, greater roughnesses and possible vegetation produce wider and multi-model echo waveforms. Therefore, GLA14 uses an average of maximum six Gaussian fits to determine the mean elevation within the reflected footprint (Zwally et al., 2002b). The difference between the two products is small, with average differences less than about 20 cm, standard deviations of ≈60 cm though maximum differences up to ±3 m in the alpine terrain of New Zealand and Svalbard (Figure 3.5).

The previous example shows that random errors (precision) associated with the Gaussian fitting method in the GLA06 and GLA14 products is ≈ 0.6 m in alpine terrain, which is equal in magnitude to the width of the transmitted laser pulse. Fricker et al. (2005) assessed the performance of the GLAS altimeters in optimal conditions (similar to an ice sheet) by comparison to an extremely precise DEM from dGPS kinematic profiles on the bright salt flats of salar de Uyuni, Bolivia (Borsa et al., 2008). They find an absolute accuracy (bias) of < 2 cm and precision (σ) < 3 cm though significant degradation was found on saturated returns which contained an increased bias (-1 m). In this thesis, ICESat releases newer than 28 have been used and thus saturation range corrections have been applied. In addition to saturated returns, Fricker et al. (2005) describes waveform returns in which atmospheric forward scattering of photons was present (e.g. within a thick cirrus cloud layer or from blowing snow) producing

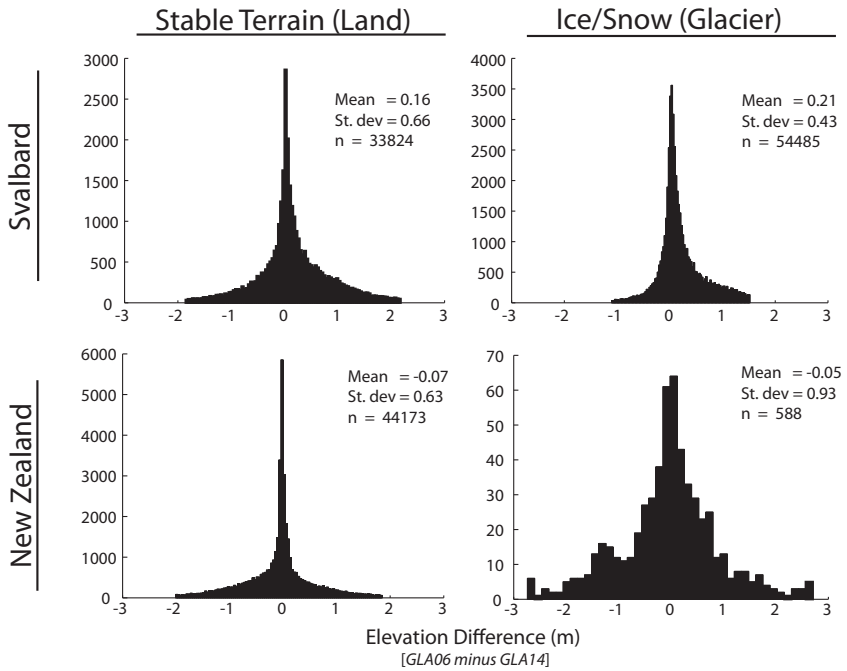

Figure 3.5: Histograms of the elevation differences between GLA06 and GLA14 ICESat products on stable terrain and over ice. The two datasets, Svalbard and New Zealand, are those used in Articles I, II, and III and are from the most recent release, 31. A larger dataset of glacier ice/snow comparisons are available in Svalbard, and many of those on stable terrain may be snow covered. The two distributions on Svalbard also seem slightly skewed towards more positive GLA06 elevations than GLA14 elevations. This is most likely the lack of saturation corrections in the GLA14 products since super-saturated signals generally result in a longer range, thus lower elevation of the GLA14 products (Fricker et al., 2005).

elongated tales on the waveforms (Duda et al., 2001) and increasing both the bias (-16 cm) and σ (8 cm). Accuracy can also be assessed by the cross over or intersection points of ascending and descending tracks over the ice sheets and ice caps. On surface slopes less than 1.15 degrees, the precision (σ) of ICESat crossovers were better than 0.5 meters (Brenner et al., 2007) and on slopes less then 5 degrees, σ was better than 0.7 m (Moholdt, 2010). In Antarctica, crossovers of laser 2a showed accuracies of ≈0.2-0.3 (2 m in worst case) and precisions of ≈0.25 m (Shuman et al., 2006). Combining this with the Fricker et al. (2005) precision estimates and those from the Gaussian fitting between GLA06 and GLA14 (Fig. 3.5) results in an average accuracy and precision of better than a meter. This estimate is however mainly based on the idealized case of low sloping glacier surfaces. The footprint of the laser increases in area over steep terrain and thus the wider waveform degrades elevation estimation. In addition, the laser does not penetrate thick clouds which can significantly reduce the amount of data.

RAdio Detection And Ranging (RADAR)

Measuring earth's surface using RADAR is accomplished by two techniques, radar pulse altimetry (similar to the LIDAR techniques described above) and radar interferometry. Only the nearly-global interferometric DEM from the Shuttle Radar Altimetry Mission (SRTM) is used in this thesis (Article III). SRTM launched an interferometric radar with two antennas attached to the space shuttle, Endeavor, in February 2000, and over the coarse of 11 days mapped ≈80% of the earth's surface (from 60^o N to 56^o S) (Farr et al., 2007). SAR interferometry uses the phase differences between two radar images acquired with a small base-to-height ratio (e.g. STRM has a baseline of 60m). These phase differences are the photogrammetric equivalent to a parallax measurement allowing retrieval of topography (Rosen et al., 2000). Typically reported vertical accuracies of the dataset are 10m which is lower than the mission standards of 16m (Rodriguez et al., 2006). However, vertical biases are present due to instability of the sensor and/or platform (Rabus et al., 2003), and biases have also been shown due to penetration of the C-band Radar waves into snow/ice (Rignot et al., 2001; Berthier et al., 2006).

3.2.2 Methods of comparison

From the two data types of point elevation measurements and semi-continuous DEMs, this thesis calculates elevation changes using three approaches:

[1] Extract the underlying DEM elevation to a point using a bilinear interpolation of the 4 nearest pixels. Other interpolation methods can be used, however, a nearest neighbor interpolation scheme induce horizontal shifts between the data products.

[2] Calculate repeat ICESat track elevation differences after correcting or solving for the across track slope between near-repeat tracks.

[3] Difference two continuous DEMs pixel by pixel. Re-sampling is often required and interpolation methods more advanced than a nearest neighbor should be used. Bilinear interpolation is used in all research presented here.

Method [1] is applied for any comparisons between ICESat and a DEM (Article I and III). Three methods for comparing ICESat tracks to contour lines were examined in Article I. The most precise method was the bilinear interpolation of the intersection point between an ICESat track and a contour line. However, intersections are limited on the flat glacier surfaces and the increased sampling by comparing the bilinear interpolation of ICESat into a contour interpolated DEM (Method [1]) generated a more statistically and spatially robust estimate. Mean glacier elevation changes did not show large variability between the three methods when estimated over larger spatial regions (Table 3 in Article I).

Method [2] is developed within the PhD thesis of G. Moholdt (2010) and applied in Article II to generate a 5 year elevation change estimate over the glaciers and glacier regions of Svalbard. The approach is developed for the rather small across-track spacing of the ICESat repeat tracks common in the polar regions (<200 m). It is based upon fitting planer surfaces to a set of at least 5 repeat tracks within 700 m windows using a multiple linear regression. The multiple linear regression solves for the surface slope and the linear average elevation change rate of all points that fall within that plane. The configuration of the repeat tracks in time and space is crucial for this method; for example, (1) if the two tracks furthest from the central track were in opposite seasons, the plane fitting compensates in the slope estimate leading to biased elevation change

estimates, and (2) inclusion of varying start and end season data in the population of planes over-samples either winter or summer which results in biased estimates of elevation changes. To verify the ICESat independent elevation change measurements, two additional approaches were applied; (1) cross-over (intersection) points and (2) along DEM-projected repeat tracks. Cross-over measurements are the most accurate, however, the amount and distribution of them were far too limited to estimate volume change. Using a DEM to re-project repeat tracks provides enough measurements but the precision of them was slightly less than the ICESat independent approach (method [2]) which does not require an external DEM.

Procedures for DEM differencing (Method [3]) are described in great length within Article III and applied in Article IV. The sub-pixel geolocation accuracies of the DEMs available depends strongly upon the acquisition of the data (aerial or satellite) and the formation of the photogrammetric model block. The geolocation of the satellite DEMs used in this thesis are strictly dependent on the on-board location and attitude measurements that are used to intersect the pixels onto earth's ellipsoid. Aerial photogrammetric DEMs are dependent upon the CGPs that form the stereoscopic model block. Therefore, comparison of the two (if both are not aerial DEMs constructed using the same GCPs) requires co-registration. In Article III, an analytic method based upon slope and aspect (Kääb, 2005) is programmed and applied universally to check and correct for horizontal and vertical shifts. After co-registration, elevation-dependent and along/cross track biases are checked and removed before performing the final differencing.

3.2.3 Determination of volume changes

Two methods for estimating the total volume change of a glacier or glacier region from elevation changes exist. Ideally, two DEMs are available such that pixel by pixel elevation changes can be summed over the glacier or glacier area of interest (n_A, equivalent to the number of glacier pixels) and multiplied by the pixel area (r^2) to estimate the volume change (Etzelmüller, 2000):

$$\frac{dV}{dt} = \sum_{1}^{n_A} \frac{dh}{dt} \cdot r^2 \tag{3.16}$$

This method will be referred to as the *grid* method. When continuous DEMs are not available, often a *hypsometric* approach is applied by deriving an elevation change by

elevation relationship, $\frac{dh}{dt}(z)$, and multiplying by the hypsometric distribution of the glacier, $A(z)$:

$$\frac{dV}{dt} = \sum_{1}^{z}[\frac{dh}{dt}(z) \cdot A(z)] \tag{3.17}$$

Equation 3.17 requires the assumption that the distribution of elevation changes within an elevation bin is normally distributed around the mean estimate derived along the centerline or averaged over an elevation bin (Berthier et al., 2004). The application of eq. 3.17 is most common in cases of centerline altimetric data (Arendt et al., 2002) but can also apply in cases where data is randomly distributed (Article I and II) or when missing data (i.e. holes in the DEM) render eq. 3.16 unsolvable over the entire glacier (Article IV).

3.2.4 Assumptions

The major assumption in studies of elevation and volume change is the conversion into mass or water equivalent changes[1]. The common approach is to assume Sorge's Law based upon Earnest Sorge's observation in the dry snow zone (no melting) at Eismitte, Greenland (1930-1931) that "the density of snow at a given depth below the surface does not change with time" given a constant accumulation rate (Bader, 1954). This also implies that the age of a particular snow layer at depth remains constant (Bader, 1954), and therefore the thickness of the firn layer constant. It is still unclear whether densification processes affect the interpretation of glacier elevation changes and what are the dominant factors affecting firn densification rates (Li et al., 2007; Reeh, 2008; Arthern et al., 2010). Nonetheless, Sorge's Law defines the assumption of a constant firn layer thickness and density, and therefore is the justification of assuming $\frac{\partial h}{\partial t}$ and $\frac{\partial V}{\partial t}$ are composed solely of ice.

Very few, if any, dry snow zones exist on Svalbard which brings into question the validity of Sorge's Law since it is based upon observations where there is no percolation. Even at some of the highest elevations in Svalbard, percolation persists practically every year (see e.g. Pohjola et al., 2002b) and thick ice layers and lenses are commonly found within the firn zone (Hawley et al., 2008; Langley et al., 2009). If the amount of

[1]Strong erosional forces of a glacier may also change the measured height of the surface, however this process (and the magnitude of) operates on a time-scale much longer than the measurements, and thus are assumed negligible.

percolation that occurs within each year is normally distributed through time (annually), then Sorge's Law most likely holds. On one of the highest glaciers in Svalbard, Holtedahlfonna, multiple ice cores with a time separation of 13 years (Uchida et al., 1993; Sjögren et al., 2007) showed a randomly varying density of the upper most firn layers, but the boundary transition to continuous glacier ice occurred at practically the same depth in both cores providing assurance that the firn thickness and density has not changed drastically within this time period (Fig. 7, Article I).

Another bias introduced by using the density of ice for conversion is if the ELA has migrated within the time epoch and firn is either gained or lost. For example, on Austfonna in the period 2003-2007, the spatial area of the firn zone increased (Dunse et al., 2009) warranting a lower density conversion factor (Moholdt et al., 2010a). Some studies have also determined the reduction in the density conversion factors using the estimated percent area of firn/ice change (Sapiano et al., 1998). Other approaches to account for this uncertainty are to apply the density of firn above the ELA and the density of ice below (Hagg et al., 2004) or an elevation dependent function of density (Article II). In summary, the uncertainty in mass conversion (density) reduces the accuracy of geodetic estimates and the effect of the bias has been estimated to be up to 5-6% of the volume change (Elsberg et al., 2001; Cuffey and Paterson, 2010), of course depending on the magnitude of the measured changes.

3.3 Glacier Surface Mass Balance

The surface mass balance of a glacier is defined as the sum of mass gain by accumulation and loss through melt water runoff. It represents the interaction between glacier and atmosphere and is the climatic driver of the glacier system. The mass balance is typically seasonal (except for low-latitude and tropical glaciers) in which accumulation falls in the winter and melting occurs in the summer. Both of these components contain gradients with elevation notably due to the general decrease of temperature with increasing elevation. Accumulation typically increases with elevation because the colder atmosphere holds less water thus more precipitation. Melt decreases with elevation due to the warmer temperatures lower. A given point lower on the glacier therefore experiences a longer ablation season with larger melt amplitudes than higher up that experience a longer accumulation season with larger snow depths. Glacier surface

mass balance can be observed directly by measuring the amount of water equivalent snowfall and melt in discrete temporal and spatial steps. Determining a continuous surface mass balance field remains nearly impossible, thus interpolation and extrapolation procedures are often required. Conveniently, the dominant parameter used for interpolation and extrapolation is elevation due to the good correlation to surface mass balance.

3.3.1 Direct mass balance observations

This section describes the surface mass balance as measured on Holtedahlfonna used for Article IV. Direct surface mass balance measurements are acquired using 6 m stakes drilled into the ice/firn, commonly aligned along the centerline of glaciers (e.g. Hagen et al., 1999) with enough stakes to capture the elevation variation of mass balance. As few as 5 stakes are required when the transverse mass balance variability is small (Fountain and Vecchia, 1999). Other glaciers contain immense stake networks that capture both elevation and lateral dependence of the surface mass balance (e.g. Krimmel, 1999; Jansson and Pettersson, 2007).

To measure the surface mass balance from a stake, the change in exposed stake length is measured on an annual or seasonal basis where the difference in height multiplied by the density of the material gained/lost returns the specific mass balance. In winter, snow density is measured traditionally using snow pits and/or ice cores. A collection of 196 snow pit bulk density measurements made between 2000 and 2009 on glaciers in northwest Svalbard (around Ny Ålesund) have a mean bulk density of 0.37 g cm^{-3} with a standard deviation of 0.04 g cm^{-3} (Figure 3.6, J. Kohler, unpublished). For winter measurements, the bulk density is used to convert the stake length changes into water equivalent. For summer measurements in the ablation area, the density of the snow pack is used to convert the exposed stake length change up to the winter snow pack thickness and the density of ice (0.9 g cm^{-3}) is used for conversion of all residual change in exposed stake length. If the exposed stake length is increasing in the firn area, the density of firn is required to convert to mass changes, assuming negligible internal accumulation. Common firn densities are quoted between 0.4 and 0.8 g cm^{-3} (Paterson, 1994) and firn density profiles with depth are available from the various ice cores around Svalbard (e.g, Uchida et al., 1993; Pinglot et al., 1999; Isaksson et al., 2001; Pohjola et al., 2002a; Sjögren et al., 2007). Figure 3.7 shows the 7 year series of

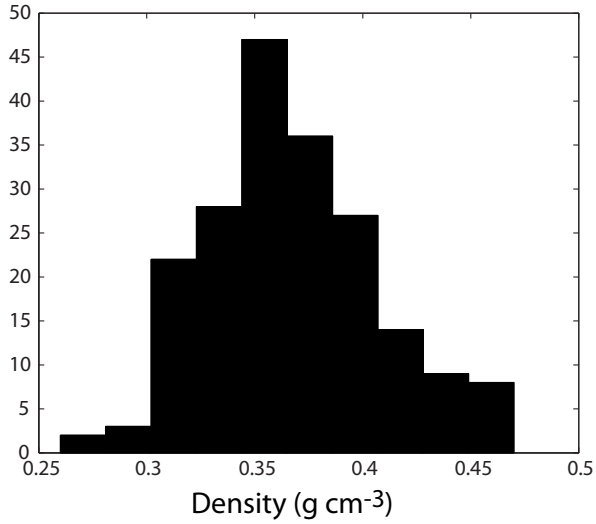

Figure 3.6: Histogram of 196 snow pack bulk densities over the period 2000 to 2009. The measurements are made on 3-4 glaciers in the Ny Ålesund area, and the number of pits varies for each year. The average bulk density of the winter snow pack is ≈0.37 g cm^{-3}. (Provided by J Kohler, Norwegian Polar Institute).

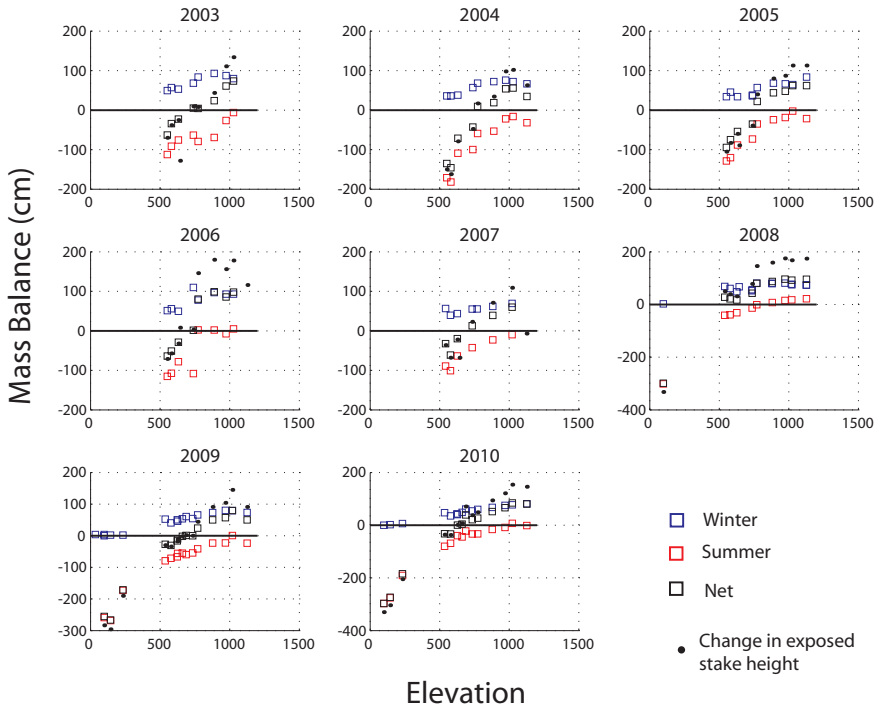

Figure 3.7: Change in exposed stake length and water equivalent conversions of the winter, summer and net surface mass balances plotted against elevation for the 2003-2010 time series on Holtedahlfonna and 2008-2010 time series on Kronebreen. The stake measurements are used to calibrate a surface mass balance model in Article IV.

stake measurements on Holtedahlfonna. The original change in exposed stake length is shown as dots. Squares are the surface mass balance estimates after conversion into water equivalent using densities of 0.37, 0.55 and 0.9 g cm^{-3} for snow, firn and ice, respectively.

To determine the glacier wide surface mass balance (B), the discrete specific mass balance measurements are extrapolated over the entire glacier surface utilizing the dependency with elevation (similar to equation 3.17):

$$B = \sum_{1}^{z} [b(z) \cdot A(z)] \tag{3.18}$$

where $b(z)$ is the winter, summer and/or net surface mass balance as a function of elevation or average within an elevation bin, and $A(z)$ is the hypsometry. The function of elevation may be solved as either a linear, piece-wise linear, or polynomial (Fountain and Vecchia, 1999). On glaciers with with a dense spatial distribution of specific point measurements, kriging has been applied (Hock and Jensen, 1999; Jansson and Pettersson, 2007). Typically the hypsometry for each individual mass balance year is not available. Therefore, if hypsometries at the start and end year of the mass balance time series are available, then a temporal interpolation can be applied assuming a linear transformation between the two map products (Cox and March, 2004; Thibert et al., 2008). If only one hypsometry is available, a *reference* surface mass balance can be estimated (Elsberg et al., 2001).

The errors associated with surface mass balance measurements include measurement errors, density conversion errors and sampling errors. Jansson (1999) finds that the surface mass balance of Storglaciären is not sensitive to density and sampling error and thus using only a sparse distribution of stakes results in a stochastic error of $\approx \pm 0.1$ m. Other studies have suggested errors of the specific measurements between 0.2 and 0.4 m (Lliboutry, 1974; Cogley and Adams, 1998; Cox and March, 2004) and even larger errors are derived by combining all stochastic and potential systematic errors (Thibert et al., 2008; Zemp et al., 2010). Systematic errors are difficult to detect and may derive from sinking stakes in the firn area (Østrem and Brugman, 1991), or from unaccounted superimposed ice and/or internal accumulation (Thibert et al., 2008; Zemp et al., 2010). Lastly, accumulation of errors can be common when summing annual mass balance measurements to derive a cumulative mass balance time series (Conway et al., 1999; Krimmel, 1999; Andreassen, 1999; Thibert et al., 2008).

3.3.2 Mass balance modelling

An alternative to using the raw specific mass balance measurements for extrapolation over the entire glacier is to use the measurements for calibrating a mass balance model that functions as a spatial and temporal interpolator/extrapolator. For the winter accumulation, if only a single season model is required, the snow depth at the end of winter can be used as initial input (Arnold et al., 2006; Schuler et al., 2007). For multi-annual applications, accumulation can be approximated by correlation to local measurement stations or by downscaling precipitation in regional climate models (e.g.

Barstad and Smith, 2005; Schuler et al., 2008; Rye et al., 2010). For ablation modelling, two approaches exist; the physically based energy balance approach and the empirical temperature-index model (Hock, 2005). Studies that have applied and compared both models on the same glacier suggest that the physical energy balance is more accurate and correct on models aiming to capture the daily variability of melt while empirical approaches perform equally well when experimenting with long time series (Gudmundsson et al., 2009; Pellicciotti et al., 2005)

The physically based melt modelling approach aims to solve the surface energy balance from measured (or simulated) radiation, temperature, humidity and wind to determine the turbulent fluxes and an estimate of the available energy for melt (Hock, 2005). However, the spatial distribution of the energy balance model is difficult as measurements of all the above parameters are not possible over the entire glacier, and thus estimates or simulations of the radiation fields and the evolution of albedo are required for proper distribution (e.g. Arnold et al., 1996; Brock et al., 2000; Dadic et al., 2008). Nevertheless, incorporation of satellite data sets such as MODIS may help constrain albedo in models operating within the lifetime of such satellites.

Empirical approaches can also be used to model the surface mass balance, provided proper calibration and constrain by melt measurements. The classical degree day approach relates melt solely to temperature while advanced degree day models include parameterizations for solar radiation (Hock, 1999; Pellicciotti et al., 2005). In Article IV, both empirical models were tested though a classical degree day approach was chosen due to equifinality of the calibrated parameter sets in the advanced model (lack of model constrain[1]). In the classical degree day approach, melt is assumed to vary linearly with temperature only if the temperature (T) is above some temperature-melt threshold (T_0):

$$Melt = DDF_{\left(\text{snow}/\text{ice}\right)} \cdot (T - T_0) \tag{3.19}$$

Degree Day Factors (DDF) are typically determined through statistical methods of minimizing the residuals between modelled and measured values (e.g. Hock, 1999). The degree day factors vary for snow and ice due to the varying albedo of the surfaces (Braithwaite, 1995). This implies that the DDF_{snow} should be lower than DDF_{ice}

[1]All stake measurements used to calibrate and constrain the models are located along the centerline which do not provide information on lateral variability due to differential shading.

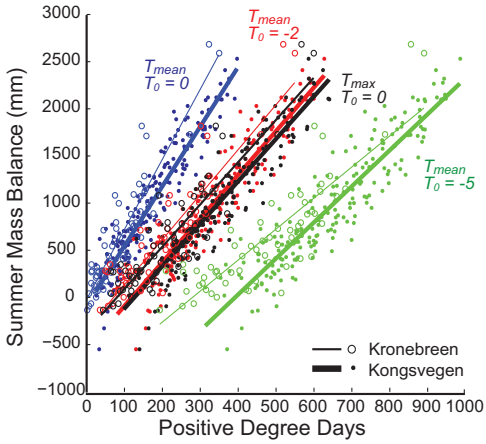

Figure 3.8: Positive Degree Days estimated for each annual stake measurement on Kongsvegen and Kronebreen, presented in Article IV. For each glacier, 4 parameter set combinations are shown; [1,2,3] T = daily average temperature (T_{mean}) and T_0 = 0,-2 and -5^{o}C and [4] T = daily maximum temperature (T_{max}) and T_0 = 0^{o}C.

because the albedo of snow is higher than that of ice. Determining the threshold temperature for melt (T_0) has important repercussions on the calibrated DDFs. Van den Broeke et al. (2010) showed that setting T_0 to 0^o C when driving the model with the daily average temperature (T) resulted in $DDF_{\text{snow}} > DDF_{\text{ice}}$, which is not reasonable. The cause is the temporal under-sampling as melting conditions may be experienced within the daily time step even if the daily average temperature is below T_0. The under-sampling misses many potential melt days in the spring and autumn, and DDF_{snow} must increase to generate the amount of melt within a smaller summer time window (Van den Broeke et al., 2010). Figure 3.8 shows that varying T_0 stretches the positive degree day scale (i.e.increases the range). Alternately, setting T equal to the daily maximum temperature and T_0 to 0^oC results in the same affect as setting T to the daily average temperature and T_0 =-2^oC.

4

Summary of Research

4.1 Article I: Svalbard glacier elevation changes and contribution to sea level rise

Previous estimates of the present day Svalbard glacier contribution to sea-level changes (expressed in sea level equivalents, SLE), were generated by extrapolations of the available direct mass balance measurements and varied from 0.01 mm yr^{-1} SLE (Hagen et al., 2003b) to 0.038 mm yr^{-1} SLE (Hagen et al., 2003a) and 0.056 mm yr^{-1} SLE (Dowdeswell et al., 1997). The aim of this research is to generate an independent estimate of Svalbard glacier sea-level contributions. We combine recent elevation data from ICESat (2003-2007) and earlier topographic maps (1966/1971) and DEMs (1990) to generate long term elevation changes and conversion into total SLE.

On Svalbard, the first topographic maps were made from 1936 oblique aerial photographs, followed by aerial photogrammetric campaigns acquiring vertical photographs between 1965 and 1971. These aerial campaigns comprised of the first published topographic map series covering Svalbard, at a scale of 1:100,000. More recently, the Norwegian Polar Institute (NPI) operated 2 more aerial campaigns in 1990 and 2008-2009 collecting vertical aerial imagery. The 1990 DEM contains a 20 m pixel resolution and does not fully cover the entire archipelago while the DEM from the most recent campaign is under construction. Previously, elevation changes have been calculated using the 1936 and 1990 data, though accuracy of contours generated from the oblique aerial photographs is limited, especially in the far-view of the photograph and in the upper parts of glaciers with low visible contrast (Nuth et al., 2007). Therefore, in this study we choose only data derived from vertical aerial photography. The generation of a single Svalbard volume change estimate from a single time epoch using this data is impossible. The study divides Svalbard into 5 major regions which is partially based upon the date of the original DEM (see Figure 5 in Article I). The ICESat campaign provided the next full coverage elevation product over Svalbard. Due to the high latitude location, the cross-track separation of repeat tracks and the separation between adjacent tracks is relatively small increasing the spatial density of ICESat coverage. Similar to the maps and DEMs, the ICESat data is also time-varying between 2003 and 2007 acquired in different seasons; for example winter snow may be present during the acquisition.

4. SUMMARY OF RESEARCH

Our geodetic estimation of a long term estimate of Svalbard glacier contribution to sea-level is dependent on the compilation of multi-temporal data and therefore a number of assumptions must be considered. For each region, a DEM or contour data from an initial year is compared to four years of the seasonally varying ICESat acquisitions. The temporally varying population of $\frac{\partial h}{\partial t}$ assumes that the varying mass balance conditions within the 2nd data acquisition is sampled randomly in space and time. Thus, we argue that a regionally compiled $\overline{\frac{\partial h}{\partial t}}$ is a temporally smoothed estimate that removes seasonal bias from the long-term estimate. Of course, repeat track analysis has also been shown to be able to extract seasonal signal from ICESat data alone (Moholdt et al., 2010a) and Article II. The second assumption in this study is the regional extrapolation/interpolation procedures. Here we use a *hypsometric* approach to integrate elevation changes into volume changes (equation 3.17). At the regional scale, the population of elevation change points are generally normally distributed around the mean estimate. Thus, we must assume that the spatial sampling scheme of ICESat within the 4 year period samples the glaciers within the region similarly to the proportionate distribution of land and marine terminating glaciers and surge/non-surge glaciers. Figure 3 in Article I show the $\frac{\partial h}{\partial t}(z)$ curves and the hypsometric distributions of each glacier region. The number of $\frac{\partial h}{\partial t}$ points per elevation bin approximates the hypsometric distribution of the glacier inferring an appropriate elevation sample of the entire region. The last crucial assumption to estimate glacier change SLE involves the conversion of height changes into water equivalent changes, which we assume to be of glacier ice.

The significance of this research is methodological and geographically related to Svalbard. Previously, ICESat has mainly been applied to ice sheet terrain in Antarctica and Greenland where surface slopes are small and spatial interpolation/extrapolation is simplified. Here, ICESat laser altimetry proved to be a highly valuable data set for estimating the regional-scale glacier volume changes for smaller glaciers and ice caps at high latitudes and with mountainous topography. Previous elevation and volume changes of Svalbard glaciers have been limited to centerline-profiles over selected glaciers (Bamber et al., 2004, 2005) or to the smaller valley glaciers (Kohler et al., 2007). This research provides a long term elevation change history over the entire archipelago[1]. Despite the

[1]except for Austfonna which lacked an early map accurate enough for change studies, though the recent elevation change history is discussed by Moholdt et al. (2010a)

decreased accuracy of smaller glacier basins in the analysis, it seems the most negative geodetic balances occur in the south and west while the northeast has the smallest change. This regional variability is further discussed in Article II.

In summary, the total volume change for Svalbard glaciers (excluding Austfonna and Kvitøya ice caps) over the past 15-40 years is -9.71 $\pm$ 0.53 km^3 yr^{-1} or -0.36$\pm$0.02 m yr^{-1} w. equivalent. This corresponds to a global sea level rise of about +0.026 mm yr^{-1} SLE, a value which lies between two previous estimates (+0.01 and +0.038 mm yr^{-1} SLE) of Svalbards contribution to sea level rise over the past 40 years (Hagen et al., 2003b,a). Globally, the volume contribution to sea-level from Svalbard is relatively small. However, when comparing the area averaged geodetic balance, Svalbard was the most negative in the arctic, twice as negative as the Canadian Arctic (Abdalati et al., 2004), four times as negative as the Russian Arctic (Glazovsky and Macheret, 2006; Meier et al., 2007) but less negative than lower latitude regions like Alaska (Arendt et al., 2002; Berthier et al., 2010), Iceland (Björnsson and Pälsson, 2008) and Patagonia (Rignot et al., 2003).

4.2 Article II: Recent elevation changes of Svalbard glaciers derived from ICESat laser altimetry

The ambitions of this research was to test methods introduced by Moholdt et al. (2010a) for estimating ICESat elevation changes from repeat tracks and intersections in regions where the geometry of the glaciers are varied (i.e. mountainous terrain) as opposed to the flat simple geometries of ice sheets and ice caps. Additionally, we aimed to examine whether the regionalization method (interpolation/extrapolation using equation 3.17 regionally over many glaciers) applied in Article I can be used for the ICESat measurements alone to generate a modern estimate of Svalbard glacier change over a consistent time epoch.

Three methods of generating elevation changes from ICESat were tested (Figure 4 in Article II):

[1] Intersections (also called cross-overs) between ascending and descending ICEsat tracks using a bilinear interpolation from the four nearest footprints.

[2] Repeat tracks in which one track is projected onto the second track by correcting for the across-track slope using independent DEM topography (slope and aspect)

[3] Repeat track comparison generated by fitting 700 x 200m planes linearly through all points using a multiple linear regression of the directional derivatives of elevation (slope and aspect) and average elevation change rate.

Method [1] is the most precise method to generate an elevation difference, though the spatial distribution of intersection points is limited to a population of ≈300 points. Both methods [2] and [3] provide an increased population and spatially distributed $\frac{\partial h}{\partial t}$ and resulted in similar $\frac{\partial V}{\partial t}$ estimates, though the RMS error of elevation change rate residuals between intersection (method [1]) and repeat-track methods (method [2] and [3]) showed that the plane fitting (method [3]) resulted in a smaller error (Figure 2 and Table 2 in Article II). This led to the conclusion that ICESat alone, without external information from DEMs, can be used to estimate the average 2003-2008 $\frac{dV}{\partial t}$.

Nevertheless, there are a number of conditions that must be fulfilled using regionalization approaches and errors may persist within the measurements. The relatively

short time interval (5 years) increases the contribution of seasonal mass balance fluctuations to the elevation change signal (decreases the signal to noise ratio). A seasonal filter was applied to the data because "the risk of a seasonal bias in $\frac{\partial h}{\partial t}$ is especially high for planes where the earliest and latest ICESat observations stem from different seasons" (Moholdt et al., 2010b). Also, the short time interval of estimates increases the sensitivity of the measurements to the density conversion factor. This is tested by applying three simple density conversion schemes, the first assuming Sorge's Law (density = 900 kg m^{-3}) and two other cases that use a lower density for conversion at higher elevations (Article II, pg 84). The three schemes resulted in overall water equivalent mass balances for Svalbard of -3.7 Gt yr^{-1}, -4.9 Gt yr^{-1} and -4.2 Gt yr^{-1}, respectively. This experiment shows that the effect of uncertainty in firn thickness changes in this case results in a more negative estimate of the volume change of Svalbard.

In conclusion, the overall 2003-2008 geodetic mass balance (excluding calving front retreat below sea-level or advance) is estimated to be -4.3±1.4 km^3 yr^{-1}, corresponding to an area-averaged thinning of 0.12±0.4 m w.e. yr^{-1}. This is less negative than the previous few decades as estimated from Article I and consistent with direct surface mass balance observations recently in western Svalbard (Article IV) and Austfonna (Dunse et al., 2009; Moholdt et al., 2010a). The difference between longer term estimates (Article I) and shorter time estimates (Article II) expresses the temporal volume change variability that Svalbard can experience. Reasons for this temporal decrease in sea-level contribution from Svalbard is not certain. Hypotheses include a generally lower mean summer temperature, increased accumulation, or simply to a larger number of summer snow fall events that significantly halt summer melting by increasing the albedo. Last, regional variability of elevation changes are consistent between the two studies; the most negative geodetic balances are experienced in the south and west.

4.3 Article III: What is in an elevation difference? Accuracy and corrections of satellite elevation data sets for quantification of glacier changes

Within the course of this thesis many different data types have been used, the most continuous product being that of a DEM which can be derived from different techniques (See Section 3.2.1). Initially, we would have liked to confirm the accuracy of the ICESat repeat track plane method (results of Article II) using a continuous coverage $\frac{\partial h}{\partial t}$ field from DEMs acquired at the start and end of the ICESat campaign. We had an ASTER SilcAst DEM from 2003 and a 2008 SPOT5-HRS DEM (from the IPY-SPOT-SPIRIT campaign, Korona et al., 2009). The comparison between these differences with those generated in Article II proved disappointing with low coherency between the specific $\frac{\partial h}{\partial t}$ estimates. It was difficult to determine the reasons at that time, besides the visible relationship between the elevation differences and terrain aspect (Figure 10 in Article III). The knowledge that recent publications of ASTER DEM elevation differences (Muskett et al., 2009) contained significant systematic biases (Berthier, 2010) and cylindrical distortions of the stereo model, similar to ASTER DEM examples we have seen in central Norway (pers. comm. Kääb, 2009), warranted deeper investigation into the accuracy of these products.

The previously mentioned insecurities in deriving elevation differences provided the motivation for this study where the initial goals were to exemplify an analytically based co-registration technique (Kääb, 2005) that can be applied universally independent of the data types. The authors felt that demonstrating and testing this approach alone was worthy of publication, though the co-registration only opened "Pandora's Box" into the various uncertainties and biases present within satellite derived elevation products. The analytic solution for a linear three-dimensional shift between two terrain surfaces is rudimentary as shown by the similarity of elevation differences between shifted DEMs and the hillshade of one of the DEMs (Figure 1 in Article III). The magnitude of the shift is strongly related to the slope of the terrain and the direction of the shift to the aspect of the terrain. Together, this can be approximated with a cosine relationship due to the circularity of aspect. Practically, the method requires up to three iterations because the terrain is not analytically defined. Compared to the alternate co-registration method of minimizing the residuals by iteratively shifting one of the DEMs (e.g. Rodriguez

et al., 2006; Berthier et al., 2007; Howat et al., 2008), our approach is faster as it requires considerably less iterations. This article shows examples where the horizontal co-registration accuracy using the analytical co-registration is as great as $^{1}/_{10}{}^{\text{th}}$ of a pixel, and that the approach can be applied in situations where stable terrain is limited ($< 10\%$ of the scene) and using spatially limited ICESat point differences (with as few as 600 points).

After co-registration of the elevation products, distortions and biases were found in ASTER satellite stereo DEMs. Obvious differences are apparent between the newly released ASTER GDEM (METI/NASA/USGS, 2009) and the SRTM (Figure 5 in Article III) including a number of artifacts related to the along track flight path of the ASTER orbit. A comparison between a series of 4 individual ASTER SilcAst DEMs and the SRTM revealed elevation dependent biases on the ASTER scenes that covered $> 30\%$ ocean (Figure 3, Article III) and low frequency along and cross track bias (Figure 6, Article III) in all of the ASTER SilcAst DEMs. Interestingly, after correction of these systematic biases, a higher frequency pattern unveiled (Figure 7, Article III). This higher frequency bias is related to satellite *jitter*, or shaking of the extraterrestrial telescopic instruments, previously found in nadir images of ASTER (Leprince et al., 2007) as well as in cross-track stereo DEMs from SPOT5 (Berthier et al., 2007). Specifically, it is related to the under-sampling of the satellite attitude data (Leprince et al., 2007), most dominant in the back-looking acquisition where errors in the pointing angle directly translate into vertical bias. Impressively, the lower frequency along track bias is clearly visible and quantifiable in comparisons where stable terrain differences are limited to $\approx 10\%$ of the scene (Figure 12, Article III). In this example, elevation differences after correcting the 2003 ASTER DEM for the along-track bias estimated by the differences with the 2008 SPOT5-HRS DEM was checked and verified by an independent ICESat 2003 - 2008 repeat-track difference profile.

As a main conclusion, a methodological approach (Figure 14, Article III) was suggested for whenever DEM (or elevation) comparison is to be performed for glacier research that involves first co-registration, and after checking and correcting for elevation scale and along/cross track biases, if they exist. ICESat is suggested to be the most consistent globally available elevation data product to date. It can be used to co-register DEMs, even when stable terrain elevation difference populations are as small as 600 points.

4.4 Article IV: Estimating the long term calving flux of Kronebreen, Svalbard, from geodetic elevation changes and a mass balance modelling

This research is focused at a rather local scale compared to the previous articles that were regionally focused. Specifically, geodetic elevation changes and a surface mass balance model calibrated by stake data are combined to solve the calving flux using an inverted form of the mass continuity equation. Previously, other studies have attempted to invert mass continuity to solve for the surface mass balance (Gudmundsson and Bauder, 1999; Kääb and Funk, 1999). Two glaciers in northwest Svalbard are used to test and exemplify the approach due to their dynamically opposite behavior and the availability of surface mass balance data for at least the past seven years.

Many studies have used the comparison between geodetic volume changes and direct surface mass balance time series to detect, analyze and possibly correct for errors mainly related to the direct measurements (e.g. Andreassen, 1999; Østrem and Haakensen, 1999; Krimmel, 1999; Elsberg et al., 2001; Cox and March, 2004; Thibert et al., 2008; Zemp et al., 2010). Some studies have also used geodetic volume changes to constrain mass balance models (Huss et al., 2009). Few studies have attempted the comparison on tidewater glaciers where the flux out of the glacier does not equal zero. This article suggests that over long time periods, the differences between geodetic volume changes and the surface mass balance may be large enough on tidewater glaciers to provide a statistically significant estimate of the calving flux. However, careful consideration of the assumptions, glacier geometry and extrapolation procedures used for the geodetic changes and the surface mass balance are required as systematic errors in either of the two will induce a systematic bias in the calving flux estimate.

In order to derive temporally compatible estimates of the surface mass balance over the geodetic balance time epoch, we employ an empirical model based upon the relation between the direct stake measurements, elevation and the meteorological parameters, precipitation and maximum temperature, measured in the vicinity of the glaciers (Ny Ålesund). We consider the model as a type of surface mass balance homogenization using the Ny Ålesund meteorological record. This particular case study allows the verification of the surface mass balance model as Kongsvegen is in the quiescent phase of a surge cycle resulting in elevation changes equal to the surface mass balance (Melvold

and Hagen, 1998; Hagen et al., 2005). Results showed that the modelled surface mass balance was slightly biased to the centerline estimates (since the model was tuned to centerline stake measurements) confirmed by the consistency to the geodetic elevation changes measured along the centerline (Figure 5, 6 and 7, Article IV). The reason for the bias is a mis-representation of the centerline as an average of the elevation bin caused by larger accumulation in the center of the glacier than at the edges. Overestimated accumulation changes the timing of the transition between DDFs for snow and ice, and thus underestimates melt along the sides, and in the cirques of the glacier. This is confirmed by the more negative geodetic balance estimated from the full spatial field of elevation changes as compared to that estimated using the centerline (Figure 6, Article IV). On the dynamically active Kronebreen, lateral variability does not seem to be a problem because centerline $\frac{\partial h}{\partial t}$ estimates approximate well the full elevation bin averages (Figure 5g, Article IV). Furthermore, the difference between geodetic balances and the surface mass balance is significantly larger than the magnitude of the modelled surface mass balance. This residual is our estimate of the decadal average calving flux when converted into volumetric units (Table 3, Article IV). This calving flux nearly doubled from the period 1969-1990 to 1990-2007. The increase in flux is the only clear, quantifiable explanation for the inverted pattern of elevation changes presented in Figure 5 (Article IV). The cause for the increased flux may only be speculated to be related to the more negative surface mass balance experienced in the second epoch.

Estimating the calving flux of a marine terminating glacier involves the combination of many types of data, deriving from the ground and remote sensing. The velocity of ice at the front is required, optimally measured continuously throughout a mass balance year. The thickness of the glacier at the terminus must be known to derive a cross-sectional area from which to multiply by a representative estimate of the velocity within that cross-section. This approach requires application of remote sensing image matching techniques or continuous GPS measurements on the glacier tongue as well as airborne radar to measure the thickness if crevasses are present. The method is logistically expensive and difficult, especially if estimates are desired over many glaciers. Alternately, the approach described in this Article has the potential to provide calving flux estimates without the requirement of glacier thickness or velocity data. Geodetic elevation changes are becoming more readily available over large areas. If surface mass balance models are successfully driven from regional climate models (e.g. De Woul and

Hock, 2005; Rasmussen and Kohler, 2007; Rye et al., 2010) such that their coverage is equal to the geodetic coverage available today, then calibration may be performed following Huss et al. (2009) using a collection of geodetic changes on land terminating glaciers in the vicinity of marine terminating glaciers. In this way, calving fluxes may be estimated on the marine terminating glaciers without the collection of glacier thickness data that is logistically intense.

5

Conclusions and Future Perspectives

The importance of quantifying glacier changes is to better constrain the glacier contribution in the global hydrological cycle and to increase knowledge about the behavior of glaciers in relation to the climatic forcing mechanisms. Observations of glaciers have become more prevalent in the past 50-75 years especially due to the advanced remote sensing techniques that are creating a higher spatially and temporally sampled data set from satellites. Nevertheless, the dynamic response of a glacier to a shift in climate is not immediate but is subjected to a lag that may be on the order of decades to centuries (Jóhannesson et al., 1989). Therefore, interpretations of glacier changes may be difficult due to lack of data spanning time longer than the response times. Consequently, modelling has become an important component in glacier research to both reproduce the past and present conditions of glaciers as well as predict the future response of glaciers to climate scenarios. Observed glacier changes are and will increasingly become important to constrain such models.

The objectives of the research in this thesis are based upon the quantification and interpretation of glacier geometrical changes, with special reference to Svalbard where direct mass balance extrapolations resulted in a wide variation in estimates of the recent past contribution of Svalbard to sea-level. In addition, the interpretation of glacier changes is difficult without prior knowledge of the surface mass balance conditions or the dynamical characteristics. As a secondary objective, this thesis aimed to determine the accuracy of various elevation products to quantifying glacier elevation and volume

changes, and assess the feasibility of combining elevation changes with an estimate or reproduction of the surface mass balance.

The contributions of this thesis are both methodological and geographically related to Svalbard and are oriented towards the fields of geomatics and glaciology. Articles I and II showed the feasibility of ICESat to derive volume changes of glacierized areas other than the ice sheets using regionalization techniques. The results of those two studies exemplified the temporal variation of Svalbard's mass loss in which the long-term trend (1965/1990-2005) of negative mass balance (-0.36 m yr^{-1}, Article I) was less negative in the 2003-2008 period (-0.12 m yr^{-1}, Article II). The data in both articles also detailed the strong spatial gradients of the geodetic balance from south/southwest to northeast in Svalbard. Article III presented universal methods to co-register elevation products and analyze and possibly correct systematic errors contained within them. These methods formed the basis for deriving elevation differences of two glaciers in northwest Svalbard presented in Article IV. The significance of Article IV lies in the combination of the geodetic changes with an empirically based surface mass balance model, that when constrained accurately enough, can help determine the decadal average calving flux through some defined flux gate.

The applicability of deriving elevation changes is increasing tremendously due to the increased availability of data (particularly from satellites) and also to the improved accuracy and precision of modern elevation data. Therefore, universal methods for accurately estimating glacier elevation changes may help constrain estimate variation due to the methodology invoked, improving the quality of estimates. The most recent elevation products from satellites such as ICESat and SPOT provide elevation data of sufficient accuracy that even seasonal variation may be analyzed. Older elevation data from e.g. ASTER provide DEMs from the early 2000s with a slightly reduced accuracy due to systematic biases from the acquisition system. However, provided an accurate reference DEM, many of these systematic biases can be removed and thus these data have the potential to provide an important reference dataset for future elevation changes. An important glaciological outcome of this thesis is the feasibility to indirectly estimate the calving flux given knowledge of the volume change and surface mass balance. With the ongoing evolution of surface mass balance models driven by regional climate models, the spatial availability of surface mass balance estimates are

increasing. Given the large spatial coverage of elevation change data today, the combination of these surface models with observed surface changes may provide the ability to estimate the calving fluxes without measuring velocity or glacier thickness.

6

References

Abdalati, W., Krabill, W., Frederick, E., Manizade, S., Martin, C., Sonntag, J., Swift, R., Thomas, R., Yungel, J., and Koerner, R.: 2004, Elevation changes of ice caps in the Canadian Arctic Archipelago, Journal of Geophysical Research-Earth Surface, 109, 11, URL http://dx.doi.org/10.1029/2003JF000045. 5, 6, 35

Abermann, J., Lambrecht, A., Fischer, A., and Kuhn, M.: 2009, Quantifying changes and trends in glacier area and volume in the Austrian Otztal Alps (1969-1997-2006), Cryosphere, 3, 205–215, URL http://dx.doi.org/10.5194/tcd-3-415-2009. 5

Abermann, J., Fischer, A., Lambrecht, A., and Geist, T.: 2010, On the potential of very high-resolution repeat DEMs in glacial and periglacial environments, The Cryosphere, 4, 53–65, doi: 10.5194/tc-4-53-2010, URL http://www.the-cryosphere.net/4/53/2010/. 15

Abshire, J. B., Sun, X. L., Riris, H., Sirota, J. M., McGarry, J. F., Palm, S., Yi, D. H., and Liiva, P.: 2005, Geoscience Laser Altimeter System (GLAS) on the ICESat mission: On-orbit measurement performance, Geophysical Research Letters, 32, 4, URL http://dx.doi.org/10.1029/2005GL024028. 16

Andreassen, L. M.: 1999, Comparing traditional mass balance measurements with long-term volume change extracted from topographical maps: A case study of Storbreen glacier in Jotunheimen, Norway, for the period 1940-1997, Geografiska Annaler Series A-Physical Geography, 81A, 467–476, URL http://dx.doi.org/10.1111/1468-0459.00076. 28, 40

Andreassen, L. M., Paul, F., Kääb, A., and Hausberg, J. E.: 2008, Landsat-derived glacier inventory for Jotunheimen, Norway, and deduced glacier changes since the 1930s, The Cryosphere, 2, 131–145, URL http://www.the-cryosphere.net/2/131/2008/. 3

Arendt, A. A., Echelmeyer, K. A., Harrison, W. D., Lingle, C. S., and Valentine, V. B.: 2002, Rapid wastage of Alaska glaciers and their contribution to rising sea level, Science, 297, 382–386, URL http://dx.doi.org/10.1126/science.1072497. 5, 6, 23, 35

Arnold, N. S., Willis, I. C., Sharp, M. J., Richards, K. S., and Lawson, W. J.: 1996, A distributed surface energy-balance model for a small valley glacier. I. Development and testing for Haut Glacier d'Arolla, Valais Switzerland, Journal of Glaciology, 42, 77–89. 29

Arnold, N. S., Rees, W. G., Hodson, A. J., and Kohler, J.: 2006, Topographic controls on the surface energy balance of a high Arctic valley glacier, Journal of Geophysical Research-Earth Surface, 111, 15, URL http://dx.doi.org/10.1029/2005JF000426. 2, 28

Arthern, R. J., Vaughan, D. G., Rankin, A. M., Mulvaney, R., and Thomas, E. R.: 2010, In situ measurements of Antarctic snow compaction compared with predictions of models, Journal of Geophysical Research-earth Surface, 115, F03 011, doi:10.1029/2009JF001306. 23

Bader, H.: 1954, Sorge's Law of densification of snow on high polar glaciers, Journal of Glaciology, 2, 319–323. 9, 23

Bamber, J., Krabill, W., Raper, V., and Dowdeswell, J.: 2004, Anomalous recent growth of part of a large Arctic ice cap: Austfonna, Svalbard, Geophysical Research Letters, 31, URL http://dx.doi.org/10.1029/2004GL019667. 34

Bamber, J. L., Krabill, W., Raper, V., Dowdeswell, J. A., and Oerlemans, J.: 2005, Elevation changes measured on Svalbard glaciers and ice caps from airborne laser data, Annals of Glaciology, 42, 202–208, URL http://dx.doi.org/10.3189/172756405781813131. 6, 34

Barcaza, G., Aniya, M., Matsumoto, T., and Aoki, T.: 2009, Satellite-Derived Equilibrium Lines in Northern Patagonia Icefield, Chile, and Their Implications to Glacier Variations, Arctic Antarctic and Alpine Research, 41, 174–182, URL http://dx.doi.org/10.1657/1938-4246-41.2.174. 3

Barrand, N. E., Murray, T., James, T. D., Barr, S. L., and Mills, J. P.: 2009, Optimizing photogrammetric DEMs for glacier volume change assessment using laser-scanning derived ground-control points, Journal of Glaciology, 55, 106–116, URL http://dx.doi.org/10.3189/002214309788609001. 15

Barry, R. G.: 2002, The Role of Snow and Ice in the Global Climate System: A Review, Polar Geography, 26, 235–246, URL http://dx.doi.org/10.1080/789610195. 1

Barstad, I. and Smith, R. B.: 2005, Evaluation of an orographic precipitation model, Journal of Hydrometeorology, 6, 85–99, URL http://dx.doi.org/10.1175/JHM-404.1. 29

Bartholomaus, T. C., Anderson, R. S., and Anderson, S. P.: 2008, Response of glacier basal motion to transient water storage, Nature Geoscience, 1, 33–37, doi:10.1038/ngeo.2007.52. 1

Berthier, E.: 2010, Volume loss from Bering Glacier, Alaska, 1972-2003: comment on Muskett and others (2009), Journal of Glaciology, 56, 558–559, URL http://dx.doi.org/10.3189/002214310792447716. 6, 38

Berthier, E., Arnaud, Y., Baratoux, D., Vincent, C., and Rémy, F.: 2004, Recent rapid thinning of the "Mer de Glace" glacier derived from satellite optical images, Geophysical Research Letters, 31, URL http://dx.doi.org/10.1029/2004GL020706. 23

Berthier, E., Arnaud, Y., Vincent, C., and Rémy, F.: 2006, Biases of SRTM in high-mountain areas: Implications for the monitoring of glacier volume changes, Geophysical Research Letters, 33, L08 502, URL http://dx.doi.org/10.1029/2006GL025862. 20

6. REFERENCES

Berthier, E., Arnaud, Y., Kumar, R., Ahmad, S., Wagnon, P., and Chevallier, P.: 2007, Remote sensing estimates of glacier mass balances in the Himachal Pradesh (Western Himalaya, India), Remote Sensing of Environment, 108, 327–338, URL http://dx.doi.org/10.1016/j.rse.2006.11.017. 39

Berthier, E., Schiefer, E., Clarke, G. K. C., Menounos, B., and Remy, F.: 2010, Contribution of Alaskan glaciers to sea-level rise derived from satellite imagery, Nature Geoscience, 3, 92–95, URL http://dx.doi.org/10.1038/ngeo737. 5, 6, 35

Björnsson, H. and Pälsson, F.: 2008, Icelandic Glaciers, Jøkull, 58. 35

Blair, J. B., Rabine, D. L., and Hofton, M. A.: 1999, The Laser Vegetation Imaging Sensor: a medium-altitude, digitisation-only, airborne laser altimeter for mapping vegetation and topography, Isprs Journal of Photogrammetry and Remote Sensing, 54, 115–122, URL http://dx.doi.org/10.1016/S0924-2716(99)00002-7. 15

Bolch, T., Buchroithner, M., Pieczonka, T., and Kunert, A.: 2008, Planimetric and volumetric glacier changes in the Khumbu Himal, Nepal, since 1962 using Corona, Landsat TM and ASTER data, Journal of Glaciology, 54, 592–600, URL http://dx.doi.org/10.3189/002214308786570782. 6

Borsa, A. A., Fricker, H. A., Bills, B. G., Minster, J.-B., Carabajal, C. C., and Quinn, K. J.: 2008, Topography of the salar de Uyuni, Bolivia from kinematic GPS, Geophysical Journal International, 172, 31–40, URL http://dx.doi.org/10.1111/j.1365-246X.2007.03604.x. 18

Bouillon, A., Bernard, M., Gigord, P., Orsoni, A., Rudowski, V., and Baudoin, A.: 2006, SPOT 5 HRS geometric performances: Using block adjustment as a key issue to improve quality of DEM generation, ISPRS Journal of Photogrammetry and Remote Sensing, 60, 134 – 146, URL http://dx.doi.org/10.1016/j.isprsjprs.2006.03.002. 13

Braithwaite, R.: 1995, Positive degree-day factors for ablation on the Greenland ice-sheet studied by energy-balance modeling, Journal of Glaciology, 41, 153–160. 29

Brenner, A., Zwally, H., Bentley, C., Csatho, B., Harding, D., Hofton, M., Minster, B., Roberts, L., Saba, J., and Thomas R.H., Yi, D.: 2003, Derivation of Range and Range Distributions From Laser Pulse Waveform Analysis for Surface Elevations, Roughness, Slope, and Vegetation Heights, Geoscience Laser Altimeter System (GLAS). Algorithm theoretical basis document 4.1, nASA Goddard Space Flight Center. 16, 18

Brenner, A. C., DiMarzio, J. R., and Zwally, H. J.: 2007, Precision and accuracy of satellite radar and laser altimeter data over the continental ice sheets, IEEE Transactions on Geoscience and Remote Sensing, 45, 321–331, URL http://dx.doi.org/10.1109/TGRS.2006.887172. 20

Brock, B. W., Willis, I. C., and Sharp, M. J.: 2000, Measurement and parameterization of albedo variations at Haut Glacier d'Arolla, Switzerland, Journal of Glaciology, 46, 675–688, URL http://dx.doi.org/10.3189/172756500781832675. 29

Cogley, J. G. and Adams, W. P.: 1998, Mass balance of glaciers other than the ice sheets, Journal of Glaciology, 44, 315–325. 28

Conway, H., Rasmussen, L., and Marshall, H.-P.: 1999, Annual Mass Balance of Blue Glacier, USA: 1955-1997, Geografiska Annaler: Series A, Physical Geography, 81, 509–520, URL http://dx.doi.org/10.1111/1468-0459.00080. 28

Cox, L. H. and March, R. S.: 2004, Comparison of geodetic and glaciological mass-balance techniques, Gulkana Glacier, Alaska, USA, Journal of Glaciology, 50, 363–370, URL http://dx.doi.org/10.3189/172756504781829855. 10, 28, 40

Cuffey, K. and Paterson, W.: 2010, The Physics of Glaciers, Elsevier, Inc., fourth edn. 7, 9, 24

Dadic, R., Corripio, J. G., and Burlando, P.: 2008, Mass-balance estimates for Haut Glacier d'Arolla, Switzerland, from 2000 to 2006 using DEMs and distributed mass-balance modeling, Annals of Glaciology, Vol 49, 2008, 49, 22–26, URL http://dx.doi.org/10.3189/172756408787814816. 29

De Woul, M. and Hock, R.: 2005, Static mass-balance sensitivity of Arctic glaciers and ice caps using a degree-day approach, Annals of Glaciology, Vol 42, 2005, 42, 217–224, URL http://dx.doi.org/10.3189/172756405781813096. 41

Debella-Gilo, M. and Kääb, A.: 2011, Sub-pixel precision image matching for measuring surface displacements on mass movements using normalized cross-correlation, Remote Sensing of Environment, 115, 130–142, URL http://www.sciencedirect.com/science/article/B6V6V-5132N95-3/2/4cb3d8bb4c17865c986c1de9e32b1be1. 12

Dowdeswell, J. A., Hagen, J. O., Bjornsson, H., Glazovsky, A. F., Harrison, W. D., Holmlund, P., Jania, J., Koerner, R. M., Lefauconnier, B., Ommanney, C. S. L., and Thomas, R. H.: 1997, The mass balance of circum-Arctic glaciers and recent climate change, Quaternary Research, 48, 1–14, URL http://dx.doi.org/10.1006/qres.1997.1900. 4, 33

Drake, J. B., Dubayah, R. O., Clark, D. B., Knox, R. G., Blair, J. B., Hofton, M. A., Chazdon, R. L., Weishampel, J. F., and Prince, S. D.: 2002, Estimation of tropical forest structural characteristics using large-footprint lidar, Remote Sensing of Environment, 79, 305–319, URL http://dx.doi.org/10.1016/S0034-4257(01)00281-4. 15

Duda, D. P., Spinhirne, J. D., and Eloranta, E. W.: 2001, Atmospheric multiple scattering effects on GLAS altimetry - Part I: Calculations of single pulse bias, IEEE Transactions On Geoscience and Remote Sensing, 39, 92–101, URL http://dx.doi.org/10.1109/36.898668. 20

Dunse, T., Schuler, T. V., Hagen, J. O., Eiken, T., Brandt, O., and Hgda, K. A.: 2009, Recent fluctuations in the extent of the firn area of Austfonna, Svalbard, inferred from GPR, Annals of Glaciology, 50, URL http://dx.doi.org/10.3189/172756409787769780. 24, 37

Echelmeyer, K. A., Harrison, W. D., Larsen, C. F., Sapiano, J., Mitchell, J. E., DeMallie, J., Rabus, B., Adalgeirsdottir, G., and Sombardier, L.: 1996, Airborne surface profiling of glaciers: A case-study in Alaska, Journal of Glaciology, 42, 538–547. 3, 6

Elsberg, D. H., Harrison, W. D., Echelmeyer, K. A., and Krimmel, R. M.: 2001, Quantifying the effects of climate and surface change on glacier mass balance, Journal of Glaciology, 47, 649–658, URL http://dx.doi.org/10.3189/172756501781831783. 10, 11, 24, 28, 40

6. REFERENCES

ERSDAC: 2005, ASTER Users Guide Part III. DEM Product (L4A01). (Ver.1.1), Tech. rep., Earth Remote Sensing Data Analysis Center (ERSDAC), URL http://www.science.aster.ersdac.or.jp/en/documnts/users_guide/index.html. 13

Etzelmüller, B.: 2000, On the Quantification of Surface Changes using Grid-based Digital Elevation Models (DEMs), Transactions in GIS, 4, 129–143, URL http://dx.doi.org/10.1111/1467-9671.00043. 22

Farr, T. G., Rosen, P. A., Caro, E., Crippen, R., Duren, R., Hensley, S., Kobrick, M., Paller, M., Rodriguez, E., Roth, L., Seal, D., Shaffer, S., Shimada, J., Umland, J., Werner, M., Oskin, M., Burbank, D., and Alsdorf, D.: 2007, The Shuttle Radar Topography Mission, Rev. Geophys., 45, RG2004, URL http://dx.doi.org/10.1029/2005RG000183. 3, 20

Finsterwalder, R.: 1954, Photogrammetry and glacier research with special reference to glacier retreat in the eastern Alps, Journal of Glaciology, 2, 306–314. 6

Førland, E. J. and Hanssen-Bauer, I.: 2003, Past and future climate variations in the Norwegian Arctic: overview and novel analyses, Polar Research, 22, 113–124, URL http://dx.doi.org/10.1111/j.1751-8369.2003.tb00102.x. 5

Fountain, A. G. and Vecchia, A.: 1999, How many stakes are required to measure the mass balance of a glacier?, Geografiska Annaler Series A-physical Geography, 81A, 563–573, URL http://onlinelibrary.wiley.com/doi/10.1111/1468-0459.00084/pdf. 25, 28

Fricker, H. A., Borsa, A., Minster, B., Carabajal, C., Quinn, K., and Bills, B.: 2005, Assessment of ICESat performance at the Salar de Uyuni, Bolivia, Geophysical Research Letters, 32, 5, URL http://dx.doi.org/10.1029/2005GL023423. 18, 19, 20

Fujisada, H., Bailey, G., Kelly, G., Hara, S., and Abrams, M.: 2005, ASTER DEM performance, Geoscience and Remote Sensing, IEEE Transactions, 43, 2707–2714, URL http://dx.doi.org/10.1109/TGRS.2005.847924. 13

Glazovsky, A. F. and Macheret, Y. Y.: 2006, Fluctuations of glaciers in the second half of 20th century caused by climate change, Russian Academy of Sciences, Moscow. 35

Gudmundsson, G. H. and Bauder, A.: 1999, Towards an indirect determination of the mass-balance distribution of glaciers using the kinematic boundary condition, Geografiska Annaler Series A-Physical Geography, 81A, 575–583, URL http://dx.doi.org/10.1111/1468-0459.00085. 40

Gudmundsson, S., Björnsson, H., Palsson, F., and Haraldsson, H. H.: 2009, Comparison of energy balance and degree-day models of summer ablation on the Langjøkull ice cap, SW-Iceland, Jøkull, 59, 1–18. 29

Hagen, J. O., Liestøl, O., Roland, E., and Jørgensen., T.: 1993, Glacier atlas of Svalbard and Jan Mayen, Oslo. 4, 5

Hagen, J. O., Melvold, K., Eiken, T., Isaksson, E., and Lefauconnier, B.: 1999, Mass balance methods on Kongsvegen, Svalbard, Geografiska Annaler Series A-Physical Geography, 81A, 593–601, URL http://dx.doi.org/10.1111/1468-0459.00087. 25

Hagen, J. O., Kohler, J., Melvold, K., and Winther, J. G.: 2003a, Glaciers in Svalbard: mass balance, runoff and freshwater flux, Polar Research, 22, 145–159, URL http://dx.doi.org/10.1111/j.1751-8369.2003.tb00104.x. 4, 33, 35

Hagen, J. O., Melvold, K., Pinglot, F., and Dowdeswell, J. A.: 2003b, On the net mass balance of the glaciers and ice caps in Svalbard, Norwegian Arctic, Arctic Antarctic and Alpine Research, 35, 264–270, URL http://dx.doi.org/10.1657/1523-0430(2003)035[0264:OTNMBO]2.0.CO;2. 4, 33, 35

Hagen, J. O., Eiken, T., Kohler, J., and Melvold, K.: 2005, Geometry changes on Svalbard glaciers: mass-balance or dynamic response?, Annals of Glaciology, 42, 255–261, URL http://dx.doi.org/10.3189/172756405781812763. 9, 41

Hagg, W. J., Braun, L. N., Uvarov, V. N., and Makarevich, K. G.: 2004, A comparison of three methods of mass-balance determination in the Tuyuksu glacier region, Tien Shan, Central Asia, Journal of Glaciology, 50, 505–510, URL http://dx.doi.org/10.3189/172756504781829783. 24

Hamilton, G. and Dowdeswell, J.: 1996, Controls on glacier surging in Svalbard, Journal of Glaciology, 42, 157–168. 5

Haug, T., Rolstad, C., Elvehoy, H., Jackson, M., and Maalen-Johansen, I.: 2009, Geodetic mass balance of the western Svartisen ice cap, Norway, in the periods 1968-1985 and 1985-2002, Annals of Glaciology, 50, 119–125, URL http://dx.doi.org/10.3189/172756409787769528. 5

Hawley, R. L., Brandt, O., Morris, E. M., Kohler, J., Shepherd, A. P., and Wingham, D. J.: 2008, Techniques for measuring high-resolution firn density profiles: case study from Kongsvegen, Svalbard, Journal of Glaciology, 54, 463–468, URL http://dx.doi.org/10.3189/002214308785837020. 23

Herzfeld, U. C., Lingle, C. S., Freeman, C., Higginson, C. A., Lambert, M. P., Lee, L. H., and Voronina, V. A.: 1997, Monitoring changes of ice streams using time series of satellite-altimetry-based digital terrain models, Mathematical Geology, 29, 859–890, URL http://dx.doi.org/10.1007/BF02768907. 6

Hock, R.: 1999, A distributed temperature-index ice- and snowmelt model including potential direct solar radiation, Journal of Glaciology, 45, 101–111. 29

Hock, R.: 2003, Temperature index melt modelling in mountain areas, Journal of Hydrology, 282, 104–115, URL http://dx.doi.org/10.1016/S0022-1694(03)00257-9. 2

Hock, R.: 2005, Glacier melt: a review of processes and their modelling, Progress in Physical Geography, 29, 362–391, URL http://dx.doi.org/10.1191/0309133305pp453ra. 29

Hock, R. and Jensen, H.: 1999, Application of Kriging Interpolation for Glacier Mass Balance Computations, Geografiska Annaler: Series A, Physical Geography, 81, 611–619, URL http://dx.doi.org/10.1111/1468-0459.00089. 28

Hoelzle, M., Chinn, T., Stumm, D., Paul, F., Zemp, M., and Haeberli, W.: 2007, The application of glacier inventory data for estimating past climate change effects on mountain glaciers: A comparison between the European Alps and the Southern Alps of New Zealand, Global and Planetary Change, 56, 69–82, URL http://dx.doi.org/10.1016/j.gloplacha.2006.07.001. 3

6. REFERENCES

Hopkinson, C. and Demuth, M. N.: 2006, Using airborne lidar to assess the influence of glacier downwasting on water resources in the Canadian Rocky Mountains, Canadian Journal of Remote Sensing, 32, 212–222. 15

Howat, I. M., Smith, B. E., Joughin, I., and Scambos, T. A.: 2008, Rates of southeast Greenland ice volume loss from combined ICESat and ASTER observations, Geophysical Research Letters, 35, URL http://dx.doi.org/10.1029/2008GL034496. 39

Huss, M., Bauder, A., and Funk, M.: 2009, Homogenization of long-term mass-balance time series, Annals of Glaciology, 50, 198–206, URL http://dx.doi.org/10.3189/172756409787769627. 40, 42

Iken, A. and Bindschadler, R. A.: 1986, Combined Measurements of Subglacial Water-pressure and Surface Velocity of Findelengletscher, Switzerland - Conclusions About Drainage System and Sliding Mechanism, Journal of Glaciology, 32, 101–119. 1

Isaksson, E., Pohjola, V., Jauhiainen, T., Moore, J., Pinglot, J. M., Vaikmae, R., van de Wal, R. S. W., Hagen, J. O., Ivask, J., Karlof, L., Martma, T., Meijer, H. A. J., Mulvaney, R., Thomassen, M., and van den Broeke, M.: 2001, A new ice-core record from Lomonosovfonna, Svalbard: viewing the 1920-97 data in relation to present climate and environmental conditions, Journal of Glaciology, 47, 335–345, URL http://dx.doi.org/10.3189/172756501781832313. 25

James, T. D., Murray, T., Barrand, N. E., and Barr, S. L.: 2006, Extracting photogrammetric ground control from lidar DEMs for change detection, Photogrammetric Record, 21, 312–328, URL http://dx.doi.org/10.1111/j.1477-9730.2006.00397.x. 15

Jansson, P.: 1999, Effect of Uncertainties in Measured Variables on the Calculated Mass Balance of Storglaciären, Geografiska Annaler: Series A, Physical Geography, 81, 633–642, URL http://dx.doi.org/10.1111/1468-0459.00091. 28

Jansson, P. and Pettersson, R.: 2007, Spatial and temporal characteristics of a long mass balance record, Storglaciären, Sweden, Arctic Antarctic and Alpine Research, 39, 432–437, URL http://dx.doi.org/10.1657/1523-0430(06-041). 25, 28

Jiskoot, H., Murray, T., and Boyle, P.: 2000, Controls on the distribution of surge-type glaciers in Svalbard, Journal of Glaciology, 46, 412–422, URL http://dx.doi.org/10.3189/172756500781833115. 5

Jóhannesson, T., Raymond, C., and Waddington, E.: 1989, Time-scale for adjustment of glaciers to changes in mass balance, Journal of Glaciology, 35, 355–369. 43

Joughin, I.: 2002, Ice-sheet velocity mapping: a combined interferometric and speckle-tracking approach, Annals of Glaciology, 34, 195–201, URL http://dx.doi.org/10.3189/172756402781817978. 3

Kääb, A.: 2005, Remote Sensing of Mountain Glaciers and Permafrost Creep, Geographisches Institut der Universitürich, Zürich. 2, 13, 22, 38

Kääb, A. and Funk, M.: 1999, Modelling mass balance using photogrammetric and geophysical data: a pilot study at Griesgletscher, Swiss Alps, Journal of Glaciology, 45, 575–583. 40

Kääb, A., Lefauconnier, B., and Melvold, K.: 2005, Flow field of Kronebreen, Svalbard, using repeated Landsat 7 and ASTER data, Annals of Glaciology, 42, 7–13, URL http://dx.doi.org/10.3189/172756405781812916. 3

Kohler, J., James, T. D., Murray, T., Nuth, C., Brandt, O., Barrand, N. E., Aas, H. F., and Luckman, A.: 2007, Acceleration in thinning rate on western Svalbard glaciers, Geophysical Research Letters, 34, 5, URL http://dx.doi.org/10.1029/2007GL030681. 34

König, M., Winther, J. G., Kohler, J., and Konig, F.: 2004, Two methods for firn-area and mass-balance monitoring of Svalbard glaciers with SAR satellite images, Journal of Glaciology, 50, 116–128, URL http://dx.doi.org/10.3189/172756504781830286. 3

Korona, J., Berthier, E., Bernard, M., Rémy, F., and Thouvenot, E.: 2009, SPIRIT. SPOT 5 stereoscopic survey of Polar Ice: Reference Images and Topographies during the fourth International Polar Year (2007-2009), ISPRS Journal of Photogrammetry and Remote Sensing, 64, 204–212, URL http://dx.doi.org/10.1016/j.isprsjprs.2008.10.005. 13, 38

Krimmel, R. M.: 1999, Analysis of difference between direct and geodetic mass balance measurements at South Cascade Glacier, Washington, Geografiska Annaler Series A-Physical Geography, 81A, 653–658, URL http://dx.doi.org/10.1111/1468-0459.00093. 10, 25, 28, 40

Kwok, R. and Fahnestock, M. A.: 1996, Ice sheet motion and topography from radar interferometry, Ieee Transactions on Geoscience and Remote Sensing, 34, 189–200, URL http://dx.doi.org/10.1109/36.481903. 3

Langley, K., Lacroix, P., Hamran, S. E., and Brandt, O.: 2009, Sources of backscatter at 5.3 GHz from a superimposed ice and firn area revealed by multi-frequency GPR and cores, Journal of Glaciology, 55, 373–383, URL http://dx.doi.org/10.3189/002214309788608660. 23

Larsen, C. F., Motyka, R. J., Arendt, A. A., Echelmeyer, K. A., and Geissler, P. E.: 2007, Glacier changes in southeast Alaska and northwest British Columbia and contribution to sea level rise, Journal of Geophysical Research-Earth Surface, 112, URL http://dx.doi.org/10.1029/2006JF000586. 6

Lemke, P., Ren, J., Alley, R., Allison, I., Carrasco, J., Flato, G., Fujii, Y., Kaser, G., Mote, P., Thomas, R., and Zhang, T.: 2007, Observations: Changes in Snow, Ice and Frozen Ground., Climate Change 2007: The Physical Science Basis. Contribution of Working Group I to the Fourth Assessment Report of the Intergovernmental Panel on Climate Change. 1

Leprince, S., Ayoub, F., Klingert, Y., and Avouac, J.-P.: 2007, Co-Registration of Optically Sensed Images and Correlation (COSI-Corr): an operational methodology for ground deformation measurements, in: Geoscience and Remote Sensing Symposium, 2007. IGARSS 2007. IEEE International, pp. 1943 –1946, URL http://dx.doi.org/10.1109/IGARSS.2007.4423207. 14, 39

Li, J., Zwally, H. J., and Comiso, J. C.: 2007, Ice-sheet elevation changes caused by variations of the firn compaction rate induced by satellite-observed temperature variations (1982-2003), Annals of Glaciology, 46, 8–13, URL http://dx.doi.org/10.3189/172756407782871486. 23

6. REFERENCES

Lillesand, T., Kiefer, R., and Chipman, J.: 2004, Remote Sensing and Image Interpretation, John Wiley & Sons, Inc., 5 edn. 12, 13

Lingle, C. S., Lee, L. H., Zwally, H. J., and Seiss, T. C.: 1994, Recent Elevation Increase On Lambert Glacier, Antarctica, From Orbit Cross-over Analysis of Satellite-radar Altimetry, Annals of Glaciology, 20, 26–32. 6

Lliboutry, L.: 1974, Multivariate statistical analyses of glacier annual balances, Journal of Glaciology, 13(69), 371–392. 28

Luthcke, S. B., Arendt, A. A., Rowlands, D. D., McCarthy, J. J., and Larsen, C. F.: 2008, Recent glacier mass changes in the Gulf of Alaska region from GRACE mascon solutions, Journal of Glaciology, 54, 767–777. 7

Mathieu, R., Chinn, T., and Fitzharris, B.: 2009, Detecting the equilibrium-line altitudes of New Zealand glaciers using ASTER satellite images, New Zealand Journal of Geology and Geophysics, 52, 209–222, URL http://dx.doi.org/10.1080/00288300909509887. 3

Meier, M. F., Dyurgerov, M. B., Rick, U. K., O'Neel, S., Pfeffer, W. T., Anderson, R. S., Anderson, S. P., and Glazovsky, A. F.: 2007, Glaciers Dominate Eustatic Sea-level Rise in the 21st century, Science, 317, 1064–1067, URL http://dx.doi.org/10.1126/science.1143906. 35

Melvold, K. and Hagen, J.: 1998, Evolution of a surge-type glacier in its quiescent phase: Kongsvegen, Spitsbergen, 1964-95, Journal of Glaciology, 44, 394–404. 40

METI/NASA/USGS: 2009, ASTER Global DEM Validation Summary Report, Tech. rep., METI/ERSDAC, NASA/LPDAAC, USGS/EROS. 39

Mikhail, E., Bethel, J., and J.C., M.: 2001, Introduction to Modern Photogrammetry, John Wiley & Sons, Inc. 12, 13

Moholdt, G.: 2010, Elevation change and mass balance of Svalbard glaciers from geodetic data, Ph.D. thesis, University of Oslo. 20, 21

Moholdt, G., Hagen, J. O., Eiken, T., and Schuler, T. V.: 2010a, Geometric changes and mass balance of the Austfonna ice cap, Svalbard, The Cryosphere, 4, 1–14, URL http://dx.doi.org/10.5194/tc-4-21-2010. 4, 5, 24, 34, 36, 37

Moholdt, G., Nuth, C., Hagen, J., and Kohler, J.: 2010b, Recent elevation changes of Svalbard glaciers derived from ICESat laser altimetry, Remote Sensing of Environment, 114, 2756–2767, URL http://dx.doi.org/10.1016/j.rse.2010.06.008. 37

Möller, M., Finkelnburg, R., Jonsell, U., Braun, M., Scherer, D., Pohjola, V., Hock, R., and Schneider, C.: subm., Surface mass balance of the ice cap Vestfonna, Svalbard - a spatially distributed assessment using ERA-Interim, weather station and MODIS data, Journal of Geophysical Research. 4

Muskett, R. R., Lingle, C. S., Sauber, J. M., Post, A. S., Tangborn, W. V., Rabus, B. T., and Echelmeyer, K. A.: 2009, Airborne and spaceborne DEM- and laser altimetry-derived surface elevation and volume changes of the Bering Glacier system, Alaska, USA, and Yukon, Canada, 1972-2006, Journal of Glaciology, 55, 316–326, URL http://dx.doi.org/10.3189/002214309788608750. 6, 38

Nuth, C., Kohler, J., Aas, H. F., Brandt, O., and Hagen, J. O.: 2007, Glacier geometry and elevation changes on Svalbard (1936-90): a baseline dataset, Annals of Glaciology, 46, 106–116, URL http://dx.doi.org/10.3189/172756407782871440. 33

Oerlemans, J.: 2005, Extracting a Climate Signal from 169 Glacier Records, Science, 308, 675–677, URL http://www.sciencemag.org/content/308/5722/675.abstract. 2

Østrem, G. and Brugman, M.: 1991, Glacier mass-balance measurements: a manual for field and office work, vol. NHRI Science Report 4, Environment Canada, National Hydrology Research Institute, Saskatoon. 2, 28

Østrem, G. and Haakensen, N.: 1999, Map comparison or traditional mass-balance measurements: which method is better?, Geografiska Annaler Series A-Physical Geography, 81A, 703–711, URL http://dx.doi.org/10.1111/1468-0459.00098. 40

Paterson, W.: 1994, The Physics of Glaciers, Elsevier Science Ltd, New York. 25

Peduzzi, P., Herold, C., and Silverio, W.: 2010, Assessing high altitude glacier thickness, volume and area changes using field, GIS and remote sensing techniques: the case of Nevado Coropuna (Peru), The Cryosphere, 4, 313–323, URL http://dx.doi.org/10.5194/tc-4-313-2010. 5

Pellicciotti, F., Brock, B., Strasser, U., Burlando, P., Funk, M., and Corripio, J.: 2005, An enhanced temperature-index glacier melt model including the shortwave radiation balance: development and testing for Haut Glacier d'Arolla, Switzerland, Journal of Glaciology, 51, 573–587, URL http://dx.doi.org/10.3189/172756505781829124. 29

Pinglot, J. F., Pourchet, M., Lefauconnier, B., Hagen, J. O., Isaksson, E., Vaikmae, R., and Kamiyama, K.: 1999, Accumulation in Svalbard glaciers deduced from ice cores with nuclear tests and Chernobyl reference layers, Polar Research, 18, 315–321, URL http://dx.doi.org/10.1111/j.1751-8369.1999.tb00309.x. 25

Pohjola, V. A., Martma, T. A., Meijer, H. A. J., Moore, J. C., Isaksson, E., Vaikmae, R., and Van de Wal, R. S. W.: 2002a, Reconstruction of three centuries of annual accumulation rates based on the record of stable isotopes of water from Lomonosovfonna, Svalbard, Annals of Glaciology, 35, 57–62, URL http://dx.doi.org/10.3189/172756402781816753. 25

Pohjola, V. A., Moore, J. C., Isaksson, E., Jauhiainen, T., van de Wal, R. S. W., Martma, T., Meijer, H. A. J., and Vaikmae, R.: 2002b, Effect of periodic melting on geochemical and isotopic signals in an ice core from Lomonosovfonna, Svalbard, Journal of Geophysical Research-Atmospheres, 107, 14, URL http://dx.doi.org/10.1029/2000JD000149. 23

Rasmussen, L. A. and Kohler, J.: 2007, Mass balance of three Svalbard glaciers reconstructed back to 1948, Polar Research, 26, 168–174, URL http://dx.doi.org/10.1111/j.1751-8369.2007.00023.x. 42

6. REFERENCES

Raup, B., Kääb, A., Kargel, J. S., Bishop, M. P., Hamilton, G., Lee, E., Paul, F., Rau, F., Soltesz, D., Khalsa, S. J. S., Beedle, M., and Helm, C.: 2007, Remote sensing and GIS technology in the global land ice measurements from space (GLIMS) project, Computers & Geosciences, 33, 104–125, URL http://dx.doi.org/10.1016/j.cageo.2006.05.015. 3

Reeh, N.: 2008, A nonsteady-state firn-densification model for the percolation zone of a glacier, Journal of Geophysical Research-Earth Surface, 113, F03 023, URL http://dx.doi.org/10.1029/2007JF000746. 23

Rignot, E., Echelmeyer, K., and Krabill, W.: 2001, Penetration depth of interferometric synthetic-aperture radar signals in snow and ice, Geophysical Research Letters, 28, 3501–3504, URL http://dx.doi.org/10.1029/2000GL012484. 20

Rignot, E., Rivera, A., and Casassa, G.: 2003, Contribution of the Patagonia Icefields of South America to sea level rise, Science, 302, 434–437, URL http://dx.doi.org/10.1126/science.1087393. 35

Rodriguez, E., Morris, C. S., and Belz, J. E.: 2006, A global assessment of the SRTM performance, Photogrammetric Engineering and Remote Sensing, 72, 249–260. 38

Rye, C. J., Arnold, N. S., Willis, I. C., and Kohler, J.: 2010, Modeling the surface mass balance of a high Arctic glacier using the ERA-40 reanalysis, Journal of Geophysical Research-Earth Surface, 115, URL http://dx.doi.org/10.1029/2009JF001364. 29, 42

Sand, K., Winther, J. G., Marechal, D., Bruland, O., and Melvold, K.: 2003, Regional variations of snow accumulation on Spitsbergen, Svalbard, 1997-99, Nordic Hydrology, 34, 17–32. 5

Sapiano, J., Harrison, W., and Echelmeyer, K.: 1998, Elevation, volume and terminus changes of nine glaciers in North America, Journal of Glaciology, 44, 119–135. 24

Schenk, T.: 1999, Digital Photogrammetry, vol. 1, TerraScience. 13

Schiefer, E., Menounos, B., and Wheate, R.: 2007, Recent volume loss of British Columbian glaciers, Canada, Geophysical Research Letters, 34, L16 503–, URL http://dx.doi.org/10.1029/2007GL030780. 6

Schoof, C.: 2010, Ice-sheet acceleration driven by melt supply variability, Nature, 468, 803–806, URL http://dx.doi.org/10.1038/nature09618. 1

Schuler, T. V., Loe, E., Taurisano, A., Eiken, T., Hagen, J. O., and Kohler, J.: 2007, Calibrating a surface mass-balance model for Austfonna ice cap, Svalbard, Annals of Glaciology, 46, 241–248, URL http://dx.doi.org/10.3189/172756407782871783. 2, 28

Schuler, T. V., Crochet, P., Hock, R., Jackson, M., Barstad, I., and Jóhannesson, T.: 2008, Distribution of snow accumulation on the Svartisen ice cap, Norway, assessed by a model of orographic precipitation, Hydrological Processes, 22, 3998–4008, URL http://dx.doi.org/10.1002/hyp.7073. 2, 29

Schutz, B. E., Zwally, H. J., Shuman, C. A., Hancock, D., and DiMarzio, J. P.: 2005, Overview of the ICESat Mission, Geophysical Research Letters, 32, 4, URL http://dx.doi.org/10.1029/2005GL024009. 16

Shuman, C. A., Zwally, H. J., Schutz, B. E., Brenner, A. C., DiMarzio, J. P., Suchdeo, V. P., and Fricker, H. A.: 2006, ICESat Antarctic elevation data: Preliminary precision and accuracy assessment, Geophysical Research Letters, 33, 4, URL http://dx.doi.org/10.1029/2005GL025227. 20

Sicart, J. E., Hock, R., and Six, D.: 2008, Glacier melt, air temperature, and energy balance in different climates: The Bolivian Tropics, the French Alps, and northern Sweden, Journal of Geophysical Research-Atmospheres, 113, URL http://dx.doi.org/10.1029/2008JD010406. 2

Sjögren, B., Brandt, O., Nuth, C., Isaksson, E., Pohjola, V., Kohler, J., and Van De Wal, R. S. W.: 2007, Determination of firn density in ice cores using image analysis, Journal of Glaciology, 53, 413–419, URL http://dx.doi.org/10.3189/002214307783258369. 24, 25

Sund, M., Eiken, T., Hagen, J. O., and Kääb, A.: 2009, Svalbard surge dynamics derived from geometric changes, Annals of Glaciology, 50, URL http://dx.doi.org/10.3189/172756409789624265. 5

Thibert, E., Blanc, R., Vincent, C., and Eckert, N.: 2008, Glaciological and volumetric mass-balance measurements: error analysis over 51 years for Glacier de Sarennes, French Alps, Journal of Glaciology, 54, 522–532, URL http://dx.doi.org/10.3189/002214308785837093. 10, 28, 40

Thomas, R., Davis, C., Frederick, E., Krabill, W., Li, Y. H., Manizade, S., and Martin, C.: 2008, A comparison of Greenland ice-sheet volume changes derived from altimetry measurements, Journal of Glaciology, 52, 203–212, URL http://dx.doi.org/10.3189/002214308784886225. 5

Toutin, T.: 2008, ASTER DEMs for geomatic and geoscientific applications: a review, International Journal of Remote Sensing, 29, 1855–1875, URL http://dx.doi.org/10.1080/01431160701408477. 12, 13

Uchida, T., Kamiyama, K., Fujii, Y., Takahashi, A., Suzuki, T., Yoshimura, Y., Igarashi, M., and Watanabe, O.: 1993, Ice core analyses and borehole temperature measurements at the drilling site on Asgardfonna, Svalbard, in 1993, Memoirs of National Institute of Polar Research. (Special issue), 51, 377 – 386. 24, 25

Van den Broeke, M., Bus, C., Ettema, J., and Smeets, P.: 2010, Temperature thresholds for degree-day modelling of Greenland ice sheet melt rates, Geophysical Research Letters, 37, L18 501–, URL http://dx.doi.org/10.1029/2010GL044123. 31

Wahr, J., Swenson, S., Zlotnicki, V., and Velicogna, I.: 2004, Time-variable gravity from GRACE: First results, Geophysical Research Letters, 31, L11 501–, URL http://dx.doi.org/10.1029/2004GL019779. 7

Walsh, J. E. et al.: 2005, Arctic Climate Impact Assessment. Chapter 6: Cryosphere and Hydrosphere. 1

Zemp, M., Jansson, P., Holmlund, P., Gärtner-Roer, I., Koblet, T., Thee, P., and Haeberli, W.: 2010, Reanalysis of multi-temporal aerial images of Storglaciären, Sweden (1959-1999); Part 2: Comparison of glaciological and volumetric mass balances, The Cryosphere, 4, 345–357, doi:10.5194/tc-4-345-2010, URL http://www.the-cryosphere.net/4/345/2010/. 10, 28, 40

6. REFERENCES

Zwally, H., Schutz, R., Bentley, C., Bufton, J., Herring, T., Minster, J., Spinhirne, J., and Thomas., R.: 2010a, GLAS/ICESat L2 Global ElevationData V031, Febuary 2003 to November 2009, Digital Media. 18

Zwally, H., Schutz, R., Bentley, C., Bufton, J., Herring, T., Minster, J., Spinhirne, J., and Thomas., R.: 2010b, GLAS/ICESat L2 Global Land Surface Altimetry Data V531, Febuary 2003 to November 2009, Digital Media. 18

Zwally, H. J., Brenner, A. C., Major, J. A., Bindschadler, R. A., and Marsh, J. G.: 1989, Growth of Greenland Ice-sheet - Measurement, Science, 246, 1587–1589, URL http://dx.doi.org/10.1126/science.246.4937.1587. 6

Zwally, H. J., Abdalati, W., Herring, T., Larson, K., Saba, J., and Steffen, K.: 2002a, Surface melt-induced acceleration of Greenland ice-sheet flow, Science, 297, 218–222. 1

Zwally, H. J., Schutz, B., Abdalati, W., Abshire, J., Bentley, C., Brenner, A., Bufton, J., Dezio, J., Hancock, D., Harding, D., Herring, T., Minster, B., Quinn, K., Palm, S., Spinhirne, J., and Thomas, R.: 2002b, ICESat's laser measurements of polar ice, atmosphere, ocean, and land, Journal of Geodynamics, 34, 405–445, URL http://dx.doi.org/10.1016/S0264-3707(02)00042-X. 16, 18

Zwally, H. J., Giovinetto, M. B., Li, J., Cornejo, H. G., Beckley, M. A., Brenner, A. C., Saba, J. L., and Yi, D. H.: 2005, Mass changes of the Greenland and Antarctic ice sheets and shelves and contributions to sea-level rise: 1992-2002, Journal of Glaciology, 51, 509–527, URL http://dx.doi.org/10.3189/172756505781829007. 5

7

Peer-Reviewed Articles

I

7.1 Article I:

Nuth C., Moholdt G., Kohler J., Hagen J.O., Kääb A (2010) Svalbard glacier elevation changes and contribution to sea level rise. ***Journal of Geophysical Reasearch- Earth Surface.*** **115, F01008.**

JOURNAL OF GEOPHYSICAL RESEARCH, VOL. 115, F01008, doi:10.1029/2008JF001223, 2010

Svalbard glacier elevation changes and contribution to sea level rise

Christopher Nuth,[1] Geir Moholdt,[1] Jack Kohler,[2] Jon Ove Hagen,[1] and Andreas Kääb[1]

Received 16 December 2008; revised 28 September 2009; accepted 16 October 2009; published 2 March 2010.

[1] We compare satellite altimetry from the Ice, Cloud, and Land Elevation Satellite (ICESat, 2003–2007) to older topographic maps and digital elevation models (1965–1990) to calculate long-term elevation changes of glaciers on the Svalbard Archipelago. Results indicate significant thinning at most glacier fronts with either slight thinning or thickening in the accumulation areas, except for glaciers that surged which show thickening in the ablation area and thinning in the accumulation areas. The most negative geodetic balances occur in the south and on glaciers that have surged, while the least negative balances occur in the northeast and on glaciers in the quiescent phase of a surge cycle. Geodetic balances are related to latitude and to the dynamical behavior of the glacier. The average volume change rate over the past 40 years for Svalbard, excluding Austfonna and Kvitøya is estimated to be -9.71 ± 0.55 km^3 yr^{-1} or -0.36 ± 0.02 m yr^{-1} w. equivalent, for an annual contribution to global sea level rise of 0.026 mm yr^{-1} sea level equivalent.

Citation: Nuth, C., G. Moholdt, J. Kohler, J. O. Hagen, and A. Kääb (2010), Svalbard glacier elevation changes and contribution to sea level rise, *J. Geophys. Res.*, *115*, F01008, doi:10.1029/2008JF001223.

1. Introduction

[2] The most recent IPCC assessment estimates that glaciers and ice caps outside Greenland and Antarctica contain between 15 and 37 cm of sea level equivalent (SLE) [*Lemke et al.*, 2007]. Even though this is small compared to the >60 m SLE of Antarctica and Greenland, it is the smaller glaciers and ice caps that are expected to be the greatest contributors to near-future sea level rise [*Meier et al.*, 2007]. Recent studies estimate that their contribution to sea level rise has been accelerating from about 0.35–0.40 mm yr^{-1} SLE for the period 1960–1990 to about 0.8–1.0 mm yr^{-1} SLE for 2001–2004 [*Kaser et al.*, 2006], about one third of the total observed global sea level rise. It is therefore important to quantify glacier volume changes for the various glaciated regions in the world, both to estimate glacial sea level contribution and to link such contributions to regional climatic changes. In this paper we estimate the contribution of Svalbard glaciers to sea level rise.

[3] Various methods exist to estimate regional volume changes of ice masses around the world. Traditional glacier mass balance measurements are typically extrapolated to estimate regional mass balances [*Dowdeswell et al.*, 1997; *Dyurgerov and Meier*, 1997; *Haeberli et al.*, 2007; *Hagen et al.*, 2003a, 2003b]. Using mass balance data, the contribution of Svalbard glaciers to sea level rise has been estimated previously to be 0.01 mm yr^{-1} SLE [*Hagen et al.*, 2003b], 0.038 mm yr^{-1} SLE [*Hagen et al.*, 2003a], and 0.056 mm yr^{-1} SLE [*Dowdeswell et al.*, 1997]. The differences in these estimates arise from the procedures used to extrapolate traditional mass balance measurements over unmeasured areas. *Hagen et al.* [2003a] derive a single relation between mass balance and elevation, which is then integrated over the entire archipelago, whereas *Hagen et al.* [2003b] integrate 13 regional mass balance curves over the archipelago. *Dowdeswell et al.* [1997] use an averaged net mass balance estimated from three glaciers to integrate over the glacier area. The large variation in previous SLE estimates of Svalbard exemplifies the uncertainty in extrapolations of traditional mass balance measurements in a region where climatic spatial variability is significant.

[4] Remote sensing provides an independent approach for mass balance estimation through measurements of elevation changes using for example photogrammetry [*Cox and March*, 2004; *Krimmel*, 1999] or altimetry [*Arendt et al.*, 2002; *Howat et al.*, 2008; *Zwally et al.*, 2005]. Airborne laser altimetry conducted over Svalbard in 1996 and 2002 along ~1000 km of profiles was too spatially limited to allow integration of the elevation changes into volume changes; however, the data suggest that eastern parts of Svalbard may be closer to mass balance equilibrium than the western and southern regions [*Bamber et al.*, 2004; *Bamber et al.*, 2005]. Long-term volume changes estimated from maps made by a variety of methods over smaller glaciers and ice fields indicate increases in the rate of loss within the last 15 years [*Kohler et al.*, 2007; *Kääb*, 2008; *Nuth*, 2007].

[5] Satellite measurements can provide accurate estimates of recent volume and mass changes. In this paper we use the NASA Geoscience Laser Altimetry System (GLAS) instruments aboard the Ice, Cloud, and Land Elevation Satellite (ICESat) [*Schutz et al.*, 2005]. The period of ICESat observations (2003–2007) is relatively short, and it is not always possible to distinguish snowfall and mass balance

[1]Department of Geosciences, University of Oslo, Oslo, Norway.
[2]Norwegian Polar Institute, Polarmiljøsenteret, Tromsø, Norway.

0148-0227/10/2008JF001223$09.00

Table 1. Data Sources, Time of Acquisition, Bias From Stable Terrain, and Estimated Errors for Each Region[a]

Region	DEM Year	ICESat Years	Bias (m)	RMSE (m)	DEM Error (m)	ICESat Error (m)	Ablation Error (m yr^{-1})	ELA Error (m yr^{-1})	Firn Error (m yr^{-1})
NW	1965	2003–2007	−0.4	16	9	1	0.23	0.45	0.68
NE	1966	2003–2007	1.8	12	9	1	0.23	0.46	0.70
EI	1971	2003–2007	0	10	9	1	0.27	0.53	0.80
SS	1990	2003–2007	1.8	3	2	1	0.15	0.30	0.45
VF	1990	2003–2007	2.7	10	9	1	0.60	1.21	1.81

[a]See equation (2) for error definitions. Individual point errors are defined for the ablation area, for the area around the ELA and the firn area.

variability from true climatic signals using the satellite data alone. Longer-term comparisons, important for determining present-day anomalies, must rely on comparing the modern satellite data to older topographic data.

[6] Problems encountered with the GLAS lasers forced a greatly curtailed measurement program, both spatially and temporally. There is nevertheless sufficient data over the entire Svalbard archipelago in a 4 year period (2003–2007) to allow comparison of ICESat elevations with older photogrammetric maps and digital elevation models (DEMs) from 1965 to 1990. This comparison is used to generate a long-term estimate of glacier volume change of various regions and subregions for the entire archipelago except Austfonna and Kvitøya.

2. Geographic Setting

[7] Svalbard is an Arctic archipelago (~78°N to ~15°E) situated north of Norway between Greenland and Novaya Zemlya. The islands lie between the Fram Strait and the Barents Sea, which are at the outer reaches of the North Atlantic warm water current [*Loeng*, 1991]. Therefore, Svalbard experiences a relatively warm and variable climate as compared to other regions at the same latitude. To the north lies the Arctic Ocean where winter sea ice cover limits moisture supply. To the south is a region where cyclones gain strength as storms move northward [*Tsukernik et al.*, 2007]. These geographical and meteorological conditions make the climate of Svalbard not only extremely variable (spatially and temporally), but also sensitive to deviations in both the heat transport from the south and to the sea ice conditions to the north [*Isaksson et al.*, 2005].

[8] The archipelago comprises four major islands. Some 60% of the landmasses, or about 36,000 km^2, are covered by glaciers [*Hagen et al.*, 1993]. The glaciers are generally polythermal [*Björnsson et al.*, 1996; *Hamran et al.*, 1996; *Jania et al.*, 2005; *Palli et al.*, 2003], and many of them are surge type [*Hamilton and Dowdeswell*, 1996; *Jiskoot et al.*, 2000; *Murray et al.*, 2003b; *Sund et al.*, 2009]. Typical Svalbard glaciers are characterized by low velocities (<10 m yr^{-1}) [*Hagen et al.*, 2003b] with glacier beds often frozen to the underlying permafrost [*Björnsson et al.*, 1996]. The largest island, Spitsbergen, has a landscape dominated by steep, rugged mountains containing ~22,000 km^2 of glaciers. Barentsøya and Edgeøya, two islands off the eastern coast of Spitsbergen, are dominated by plateau-type terrain [*Hisdal*, 1985] containing ~2800 km^2 of low-altitude ice caps. The island of Nordaustlandet, northeast of Spitsbergen, is mainly covered by the Vestfonna (~2450 km^2) and Austfonna (~8000 km^2) ice caps, the two largest single ice bodies within Svalbard. Climate conditions are spatially variable; the relatively continental central region [*Humlum*, 2002; *Winther et al.*, 1998] receives 40% less precipitation than the east and south while the north experiences about half the accumulation of the south [*Sand et al.*, 2003].

[9] In this study, we divide Svalbard into five major regions; South Spitsbergen (SS), Northeast Spitsbergen (NE), Northwest Spitsbergen (NW), the Eastern Islands (EI), and Vestfonna (VF). This division derives partly from natural climatic conditions and partly from the temporal distribution of the available DEMs. In addition, subregions are defined within each region which are based upon drainage basins and the availability of spatially representative ICESat profiles. Throughout this study, two-letter abbreviations are used within the text to identify the five large regions. Three-letter codes are abbreviations for the defined subregions in the maps and tables though full names are used in the text.

3. Data

[10] Digitized 1:100,000 scale topographic maps made from vertical aerial photographs taken between 1965 and 1990 at scales between 1:15,000 and 1:50,000 (the Norwegian Polar Institute (NPI) S100 Series Topographic maps of Svalbard) form the base data that are compared to ICESat. In NE, NW, EI, and VF contour maps were constructed by NPI on analog stereoplotters using 1965, 1966, 1971, and 1990 imagery, respectively. The DEM for SS was constructed by NPI using the digital photogrammetry software package SOCET SET®, from 1:50,000 scale vertical photographs taken in 1990. The grid spacing is 20 m. Table 1 lists the regions and time intervals from which elevation changes are calculated. Austfonna and Kvitøya ice caps are not included in this analysis because the available topographic maps are of too low accuracy due to limited ground control available and due to the large low-contrast zones in the firn and snow areas which render photogrammetric elevation-parallax measurement very inaccurate or impossible. The 2002–2008 volume change of Austfonna has been estimated in a separate study [*Moholdt et al.*, 2009].

[11] ICESat contains a laser altimeter system (GLAS) that has been acquiring data since 2003. GLAS retrieves average surface elevations within ~70 m diameter footprints every ~170 m along track. The single shot elevation accuracy is reported to be ~15 cm over flat terrain [*Zwally et al.*, 2002], although accuracies better than 5 cm have been achieved under optimal conditions [*Fricker et al.*, 2005]. However, some data are lost to cloud cover, and ICESat performance degrades over sloping terrain and under conditions of pronounced atmospheric forward scattering and detector saturation. When the GLAS laser is transmitting pulses with high

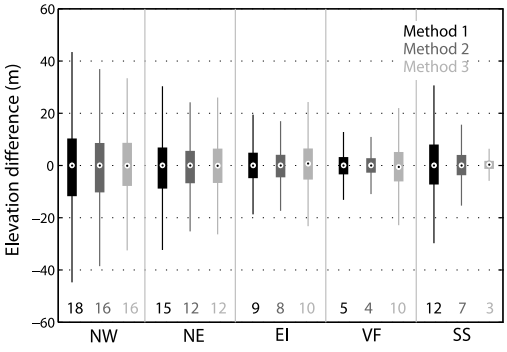

Figure 1. Box plots of the elevation differences between topographic DEMs and ICESat elevations on nonglacier terrain for the three methods outlined in section 4.1 for each region. The central point is the median, the box edges are the 25th and 75th quantile of the data, and the edges of the whiskers contain 99.3% of the data. The numbers at the bottoms of the box plots are the RMSE values of the elevation differences.

energies (i.e., during the early stages of an instrument's life) toward flat ice terrain, higher than normal echo-return energies cause detector saturation (i.e., pulse distortion) [*Abshire et al.*, 2005]. A saturation range correction [*Fricker et al.*, 2005] available since ICESat Release 28 has been added to the elevations to account for the delay of the pulse center in saturated returns. In this study, we use the GLA06 product between 2003 and 2007 from ICESat data release 428 available from the National Snow and Ice Data Center (NSIDC [*Zwally et al.*, 2008]).

4. Methods

4.1. Intersections Between ICESat Points and DEMs

[12] The satellite data, digital topographic maps, and photogrammetric DEMs are first established in the same horizontal and vertical datum and projection. The early NPI maps are referenced to the European Datum 1950 (ED50) while the 1990 DEMs are referenced to the World Geodetic System of 1984 (WGS84). A seven-parameter transformation between the UTM projections in both datums is used to convert the early maps from ED50 to WGS84. Elevation conversions are not required since the topographic maps, and photogrammetric DEMs are referenced to mean sea level using NPI mean sea level reference markers positioned around Svalbard. ICESat elevations, on the other hand, are first converted from TOPEX/Poseidon to WGS84 ellipsoid heights, and then converted to orthometric heights by subtracting the EGM96 model of geoid heights in the mean tide system. A horizontal transformation between WGS84 and TOPEX/Poseidon was not necessary since the displacements are only a few centimeters.

[13] There are various ways to produce elevation changes between ICESat profiles and contour maps. *Kääb* [2008], for example, averages eight different methods of comparison between contours, a stereo satellite-derived DEM and ICESat profiles to estimate volume changes on Edgeøya, eastern Svalbard. For region SS, a photogrammetric raster DEM is the original data product such that elevation changes are simply calculated as differences between the ICESat point elevations and the bilinear interpolation of the underlying DEM at the locations of the ICESat footprint center.

[14] For NW, NE, EI, and VF, 50 m contours were digitized by NPI from the original map foils. Three methods for calculating the vertical differences between the contours and the ICESat-derived elevations are implemented:

[15] 1. Use only ICESat points where the waveform footprint directly overlays a contour. The elevation difference is then, without any interpolation, directly calculated between the ICESat point elevation and the contour elevation included in the footprint. This method results in a small number of differences but avoids interpolation artifacts.

[16] 2. Interpolate the intersection between two successive ICESat points and a contour between them. This method results in a larger number of differences but assumes a linear slope between two successive ICESat points, i.e., over 170 m across the contours.

[17] 3. Interpolate a DEM (50 m grid spacing) from the contours using an iterative finite difference interpolation technique [*Hutchinson*, 1989], and subtract the DEM from the ICESat points as described above for the SS region. This method results in the largest number of differences but involves DEM-interpolation artifacts, in particular where contour lines are scarce due to low slopes.

[18] As a first measure to assess the characteristics and uncertainties of these three methods, elevation differences on nonglacier terrain, assumed to be stable, are analyzed for each region (Figure 1). The sample size of the three methods within each region is normalized to ensure proper inter-method comparison. The regional sizes are 4250 (NW), 2671 (NE), 1261 (EI), 954 (VF), and 5904 (SS) points. In all regions, method 1 results in a larger root-mean-square error (RMSE) than method 2 because elevation errors on steep slopes increase with distance between the ICESat center point and the contour. At 35 m distance, the radius of an ICESat footprint, the potential elevation error is 5 m for a 10° slope and up to 30 m for a 40° slope. The RMSE difference between methods 1 and 2 is greatest in NW, NE, and SS, where topography is dominated by jagged mountains with steep flanks rather than the plateau-type terrain characteristic as found for EI and VF. The RMSE for method 3 is significantly greater than for methods 1 and 2 in EI and VF. DEM interpolators are less accurate on terrain with large roughness (e.g., cliffs and plateau edges) and where distances between contours are large (relatively flat terrain, e.g., plateaus and strand flats). Both these topographic characteristics are predominant in EI and VF. The RMSE from method 3 is similar to that of method 2 in NW and NE since the DEM interpolation is as accurate as a linear interpolation between ICESat points in the more alpine mountainous terrain, with its dense contours and evenly steep slopes. The RMSE for method 3 in region SS is exceptionally small because the underlying raster DEM was directly measured using digital photogrammetry and did not have to be interpolated from contours.

[19] Method 2 is considered the most precise of the three methods for comparing ICESat to contours, especially over large flat surfaces. However, the distribution of ICESat-

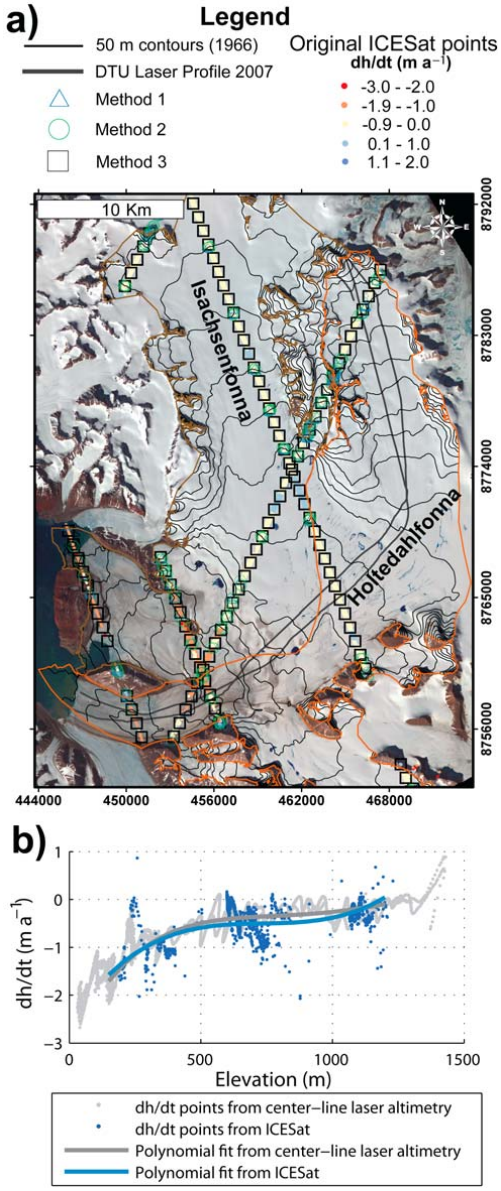

Figure 2. (a) Holtedahlfonna (orange basin outline) and Isachsenfonna (brown basin) in NW. Location of ICESat points are shown with *dh*/*dt* values indicated by color and method used by symbol. Black lines show the 2007 centerline airborne laser altimetry profile (The National Space Institute at the Technical University of Denmark). Background is an ASTER image from 12 July 2002. (b) Holtedahlfonna *dh*/*dt* points measured from ICESat and from the centerline laser altimetry along with their corresponding polynomial relationships with elevation.

contour intersections is limited in areas where profiles are transverse to the glacier centerline (for example, Figure 2a). Also, DEM interpolation of slope surfaces with limited topographic roughness, such as glaciers, introduces smaller errors than, for example, mountainous terrain outside these glaciers. Therefore, both methods 2 and 3 are implemented at the regional scale, whereas only method 3 is implemented at the subregional scale because the enhanced spatial distribution and number of elevation differences provide enough information to estimate volume change.

[20] Vertical uncertainty of the DEMs is estimated by the RMSE between ICESat elevations and the DEMs over stable terrain, assuming that the ICESat data have no error (method 3). The RMSE is largest in NW and smallest in SS (Figure 1). Accuracy of contours in the firn area may be poorer due to low optical contrast and fewer control points for the photogrammetric compilation. However, glaciers and ice caps have smoother slopes than nonglacier areas, reducing vertical errors caused by horizontal distortions and DEM interpolation.

4.2. Estimation of Elevation Change and Volume Change

[21] ICESat surface point elevations (h_1) are differenced to the underlying DEM pixels (h_0) using bilinear interpolation producing elevation changes: $dh = h_1 - h_0$. Because the ICESat points are acquired in multiple years (2003–2007), the elevation change points are divided by their respective time interval to produce point elevation change rates (dh/dt). Some outliers are present due to noisy ICESat points from atmospheric contamination, erroneous DEM elevations, or from extreme changes due to glacier surges. Outliers are removed regionally with an iterative 3σ filter within 50 m elevation bins until the improvement of the resulting standard deviation (σ) is less than 2% [*Brenner et al.*, 2007]. Because of variable cloud cover, some repeat track profiles are measured more often than others, biasing the spatial distribution of points toward those tracks that contain the most cloud-free profiles. Therefore, neighboring elevation differences within a 500 m radius are averaged to create one point for every kilometer along track. The original population of 92,811 elevation change points is reduced to 5631 points through this block smoothing.

[22] To regionalize thickness changes, relations describing the variation of dh/dt with elevation are created by fitting higher-order polynomial curves: $dh_z/dt = f(h_0)$. Higher-order polynomial fitting is less influenced by noise and outliers than averaging per elevation bin, while preserving the general trend of the elevation changes, especially at lower altitudes where thickness changes approach zero due to glacier retreat and debris-covered tongues [*Arendt et al.*, 2006; *Kääb*, 2008]. Moreover, continuous curves allow us to estimate average thickness changes also at elevation intervals where little or no data are available due to the spatial distribution of ICESat profiles. The order of the polynomials is generally increased until the RMSE converges but also requires some subjective judgment as lower-order fits can experience relatively low RMSE while still producing runaway tails at the edges of the data. At the regional scale, sixth-order polynomials were used while second- to sixth-order were used at the subregional scale. Glacier hypsometries (area-altitude distribution) for each

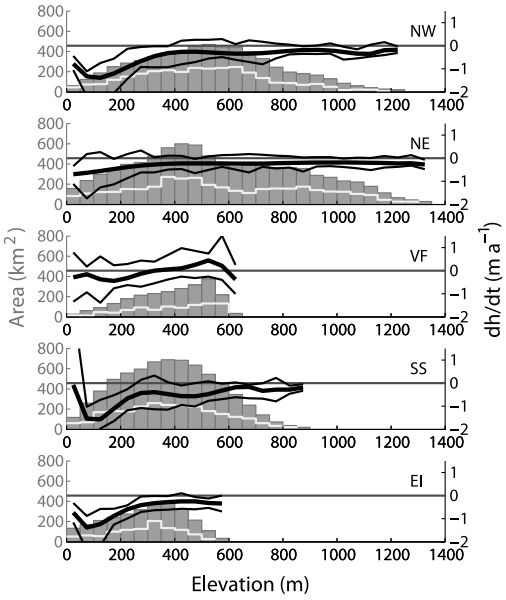

Figure 3. Area/altitude distributions of the five regions (gray, scale to the left) and the chosen polynomial fit to dh/dt by elevation (black bold line, scale to the right). The lighter black lines are one standard deviation of the original data points from the median to show the spread of the data. The lighter gray line is the number of smoothed ICESat points (see section 4.2, 5631 points for the entire study area) within each elevation bin multiplied by two for scaling purposes. The number of points thus corresponds to the y axis on the left divided by two.

region are created from the DEMs by summing the glaciated areas into 50 m elevation bins. The volume change rate (dV_{ice}/dt) is

$$\frac{dV}{dt} = \sum_{1}^{Z} \left(\frac{dh_Z}{dt} * A_Z \right), \quad (1)$$

where dh_z/dt is the elevation change curve and A is the area at each elevation bin, Z. The dh_z/dt curves and hypsometries for the five regions are shown in Figure 3.

[23] At the regional scale, a sufficient spatial distribution of dh/dt points allows robust estimates of dV_{ice}/dt. We combine these five regional estimates to calculate the total contribution of Svalbard glaciers to sea level rise. At the subregional scale, it can be more difficult to obtain a spatially representative dh/dt distribution. Approximately 33% of the glaciated area in this study did not have a suitable spatial distribution to estimate subregional volume changes. Some glaciers have only a few ICESat profiles resulting in large data gaps at some elevation bins. In cases where these data gaps are greater than 3–4 elevation bins, a straight line is used to interpolate dh/dt between higher and lower ICESat profiles. In cases where the data distribution was still too sparse, adjacent glaciers are combined to produce better dh/dt relationships. As an alternative to using polynomial elevation change curves to generate volume change rates, we could also have used the mean [*Nuth et al.*, 2007] or median [*Abdalati et al.*, 2004] dh/dt for each elevation bin. The differences in estimated volume changes between using mean, median, or polynomial fits are typically 4%–7%.

[24] We assume that all volume changes are of glacier ice [*Bader*, 1954] and multiply dV_{ice}/dt by 0.917 (the density of ice) to obtain water equivalent volume change rates (dV_{water}/dt). This assumption is valid in the ablation areas, but is more uncertain in the accumulation areas, where firn thickness or density may increase or decrease. Dividing dV_{water}/dt by the average of new and old glacier areas [*Arendt et al.*, 2002] provides geodetic mass balance rates ($\dot{b}$ in m yr^{-1}). Updated glacier areas are not yet available for the ICESat epoch, and thus we divide by the older glacier area (1966, 1971, or 1990 depending on the region) which slightly underestimates geodetic mass balances due to glacier retreat. Thickness changes (dh/dt) are given in meters of ice equivalent (m ice), while volume changes and geodetic mass balances are provided in meters of water equivalent (m w. equivalent).

4.3. Errors

[25] ICESat elevations are accurate to better than 1 m [*Brenner et al.*, 2007]. Our analysis of 237 crossover points within individual ICESat observation periods (<30 days) over Svalbard glaciers yielded a standard deviation of the elevation differences of 0.6 m, for slopes <15°. Therefore, the greatest sources of error within our estimates derive from the photogrammetrically derived topographic maps and DEMs. Errors in these products typically result from low radiometric contrast in the images, and lack of availability and quality of ground control points. To estimate single point accuracies of the DEMs relative to ICESat, we use the population of elevation differences over nonglaciated surfaces (see section 4.1) with slopes similar to those of glaciers (<15°). The population sizes for the stable terrain data sets range from 6500 points in NW to 11,826 points in SS, all distributed along the ICESat tracks. The regional ICESat-DEM differences approximate Gaussian distributions with mean differences ranging from −0.4 to 2.7 m (Table 1). We attribute these biases to ground uplift (0.10–0.24 m within our measurement periods [*Sato et al.*, 2006]), to snow cover in the ICESat observation periods (maximum 1 m), and to deviations between the EGM96 geoid model and the mean sea level references used in NPI maps (maximum 1 m). Individual vertical biases are removed from their respective regions.

[26] Individual point elevation change uncertainties (E_{PT}) are estimated by the root sum squares (RSS) of the uncertainties of each data set (Table 1). Image contrast in glacier firn areas is typically low, leading to a problem known as "floating contours" [*Arendt et al.*, 2002]. This effect has previously been accounted for by assigning accumulation area contours a vertical uncertainty of two to three times that of an ablation area contour [*Adalgeirsdottir et al.*, 1998; *Arendt et al.*, 2006; *Nolan et al.*, 2005]. We use a stepwise assignment of accuracies to the different surface types by assuming that the lowermost one-third of the elevation bins for each region and subregion corresponds to the ablation

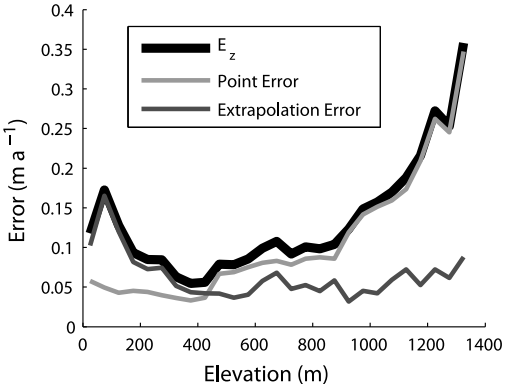

Figure 4. The estimated standard point (E_{PT}), extrapolation (E_{EXT}), and combined errors (E_Z) here exemplified for region NE. E_{PT} increases with elevation because higher elevations have poorer image contrast, and thus less accurate contour elevations from photogrammetry. E_{EXT} increases toward lower elevations because the spatial variability of *dh*/*dt* is larger because of differential ablation.

zone, the middle one-third to the zone around the equilibrium line altitude (ELA), and the upper one-third to the accumulation zone. Individual point elevation change uncertainties are then estimated by

$$E_{PT(z)} = c(z)\sqrt{\sigma^2_{DEM} + \sigma^2_{ICESat}}, \quad (2)$$

where z is the respective elevation bin, σ_{DEM} is the standard deviation of terrain differences on slopes less than 15° (Table 1), σ_{ICESat} is conservatively assigned to 1 m, and c is 1, 2, or 3 for the ablation, ELA, and accumulation zones, respectively. The middle one-third of elevations for each region (Figure 3) corresponds to a rough ELA map of Svalbard [*Hagen et al.*, 2003b]. The simplicity of this parameterization for c does not warrant a precise ELA location because anything above the lowest one-third elevation bins receives an uncertainty at least double the estimated elevation errors in the ablation area. Moreover, the resulting errors for each zone in Table 1 are provided as average annual rates to emphasize the reduction of error by having a longer time span between measurements.

[27] An additional error source arises from extrapolation (E_{EXT}) of a limited number of *dh*/*dt* points to the entire glaciated surface. E_{EXT} represents the uncertainty about the mean elevation change rate, estimated by the spatial variability of thickness changes rates [*Arendt et al.*, 2006; *Thomas et al.*, 2008]. We use the standard deviation of glacial *dh*/*dt* within each 50 m elevation bin as an approximation for the extrapolation error. At the subregional scale, elevation bins that have too few measurements (less than 5 *dh*/*dt* points) are set to twice the regional mean E_{EXT} within corresponding elevation bins.

[28] Errors in volume changes and geodetic mass balances are estimated as the combination of the two error components in each elevation bin; (1) the point elevation error (E_{PTz}), and (2) extrapolation error (E_{EXT}). Elevation changes are averaged by elevation, thus errors are reduced by the square root of the number of independent measurements within each elevation bin. Both E_{PTz} and E_{EXT} are random so that the combined errors are summed by RSS to produce the total elevation change error at each elevation bin (z):

$$E_z = \sqrt{\left(\frac{E_{PTz}}{\sqrt{N_z}}\right)^2 + \left(\frac{E_{EXTz}}{\sqrt{N_z}}\right)^2}. \quad (3)$$

When full spatial coverage is available, N may be represented by the number of pixels or measurements, assuming there is no spatial autocorrelation [*Etzelmüller*, 2000]. Conservatively, we account for spatial autocorrelation and the varying distribution of ICESat profiles over subregions and regions by defining N as the number of independent ICESat profiles within each elevation bin, rather than the number of actual data points. Thus, profiles containing more than one point within an elevation bin are, for error assessment purposes, reduced to one measurement. In our study, the total number of ICESat footprints on glaciers (92,811) is reduced by smoothing to 5631 points (see section 4.2) whereas N for the entire study area becomes 2482. Figure 4 shows an example of the elevation dependency of the error types. The standard point errors are largest at higher elevations where poor radiometric contrast makes photogrammetry difficult while the extrapolation errors are largest at the lowest elevations where spatial variability of elevation changes is greatest due to glacier retreat and differential ablation (clean ice versus dirty ice).

[29] Volume change errors (E_{VOL}) are then estimated by the RSS of the elevation errors (E_Z) multiplied by the area (A_Z) assuming that the errors are independent between the elevation bins (Z):

$$E_{VOL} = \sqrt{\sum_1^Z (E_Z * A_Z)^2}. \quad (4)$$

Uncertainties in the glacier outlines of the DEMs are an additional source of error. We expect this error to be small at the spatial scale of our volume change estimates, and therefore do not account for it. Updated glacier outlines are not available for the ICESat epoch, so while total volume change estimates are correct, geodetic mass balances are slightly underestimated due to the prevalent glacier retreat on Svalbard during the study period [*Hagen et al.*, 2003b]. Errors from seasonal differences between the end of summer DEMs and the multiseasonal ICESat acquisitions (in February/March, May/June, and September/October) are not more than 1 m or ~ 0.02–0.13 m yr^{-1} over the decadal measurement period. However, after accounting for the mean ICESat-DEM bias, the seasonal acquisition of ICESat introduces errors in both directions due to snow depths in acquisitions before July/August (photographic acquisitions for the topographic maps and DEMs) and additional melt that occurs after July/August thus becoming a part of our random point error. Last, the 4 year time span of ICESat

smoothes out mass balance anomalies during the 2003–2007 period.

5. Results

5.1. Thickness Changes

[30] Average annual elevation change rates (*dh*/*dt*) over Svalbard are shown in Figure 5. The mean observed *dh*/*dt* for Svalbard (excluding Austfonna and Kvitøya) is -0.40 m yr^{-1} with 95% of the data ranging between -1.65 and $+0.85$ m yr^{-1}. Frontal thinning is observed nearly everywhere except for those glaciers that have surged in the observation period. Regionally, the most negative average annual frontal thinning rates occur on SS, NW, and EI, respectively, while NE and VF have the lowest average annual frontal thinning rates (Figure 3). At higher elevations, glaciers experience only slight vertical changes, with both thinning and thickening found. Regionally, only VF experiences an average annual thickening at higher elevations while NW, NE, EI, and SS experience thinning varying between -0.15 and -0.30 m yr^{-1}. Extreme *dh*/*dt* occurs where the calving fronts of marine terminating glaciers changed their position or on glaciers that have surged. For example, the minimum and maximum change rates for the entire study area (-4.92 and $+8.21$ m yr^{-1}) are found on two glaciers that have surged recently: Perseibreen which surged in 2000 [*Dowdeswell and Benham*, 2003] and Fridtjovbreen, which surged in the mid-1990s [*Murray et al.*, 2003a].

[31] Northwest Spitsbergen (NW) glaciers experience widespread frontal thinning of -1 to -2 m yr^{-1}. The largest frontal thinning occurs on Borebreen and in Trollheimen Land. Some glaciers in NW are thinning throughout their accumulation areas (e.g., Isachsenfonna and Holtedahlfonna) while others experience significant increases at higher elevations (e.g., Kongsvegen, Borebreen, Holmströmbreen, Morabreen, and Orsabreen). On Kongsvegen, the thickening of $\sim$0.5 m yr^{-1} at upper elevations and thinning of -1 m yr^{-1} at lower elevations correspond well to previous measurements between 1991 and 2001 [*Hagen et al.*, 2005] but is less than that measured between 1966 and 1996 [*Melvold and Hagen*, 1998], +1 and -2.5 m yr^{-1} at upper and lower elevations, respectively. The surge on Abrahamsenbreen in 1978 [*Hagen et al.*, 1993] resulted in +80 m vertical increases at the tongue and -40 to -80 m decrease in the reservoir, while the surge of Osbornebreen in 1987 [*Rolstad et al.*, 1997] is seen as +50 m frontal increases and -20 m decreases at higher elevations. The larger elevation changes measured using 1966 and 1990 maps [*Rolstad et al.*, 1997] result because the latter map was made more or less at the termination of the surge, and the glacier has been rebuilding since 1990.

[32] Frontal thinning rates in NE are more moderate than in NW, ranging between -1.5 and 0 m yr^{-1}, with the most negative rates occurring at the calving fronts draining Lomonosovfonna, Kongsfonna, and Negribreen. Large thinning rates (-1.5 to -0.5 m yr^{-1}) also occur in the upper elevations of Tunabreen and Hinlopenbreen due to recent surges. Thickening of +0.5 to +1 m yr^{-1} is observed at the higher elevations of Negribreen from 1966 to $\sim$2005, slightly larger than the *dh*/*dt* measurements of +0.2 to +0.5 m yr^{-1} between 1996 and 2002 from airborne laser scanning [*Bamber et al.*, 2005]. The upper elevations of Kongsfonna and Balderfonna ice caps have thinned by -0.2 to -0.3 m yr^{-1}. Åsgardfonna ice cap is generally thinning (-0.1 to -0.3 m yr^{-1}) at higher elevations although slight thickening is observed toward the northeast. Similar patterns and magnitudes of elevation change rates were observed at high elevations ($\pm$0.10 m yr^{-1}) between 1996 and 2002 [*Bamber et al.*, 2005]. Ursafonna has thinned across the top of the ice cap (-0.1 to -0.3 m yr^{-1}) although +60 to +80 m frontal increases occur at the confluence between Chydeniusbreen and Polarisbreen. No surges have previously been recorded for these glaciers. On Oslobreen, the southern outlet glacier of Ursafonna, mid-elevation thickening of +0.3 to +0.5 m yr^{-1} is apparent both between 1966 and 2005 (this study) and from 1996 to 2002 [*Bamber et al.*, 2005].

[33] Frontal thinning of glaciers on the EI is most similar to that of NW, ranging between -0.3 and -2.0 m yr^{-1}. The largest frontal thinning occurs on Edgeøyjøkulen and Digerfonna. Elevation changes of Digerfonna are similar to those reported by *Kääb* [2008] who use the same data as in this study as well as a DEM from ASTER satellite stereo imagery. Slight thickening is observed at the higher elevations of Barentsøyjøkulen and Edgeøyjøkulen (+0.2 m yr^{-1}), where many of the outlets are suggested to be surge type [*Dowdeswell and Bamber*, 1995]. Storskavelen, a small ice cap northwest of Edgeøyjøkulen, experiences moderate thinning (0–1 m yr^{-1}) across the entire surface.

[34] Vestfonna (VF) contains the largest *dh*/*dt* variation out of all the regions, and is the only region in which significant thickening is observed. On the south side, Aldousbreen, Frazerbreen, and Idunbreen experience frontal thinning (up to -1 m yr^{-1}) and upper elevation thickening (up to +1 m yr^{-1}). Gimlebreen in the southwest has thinned over the entire surface. Bodleybreen surged in the late 1970s [*Dowdeswell and Collin*, 1990]. Since 1990, the upper glacier has thinned dramatically (-1 to -2 m yr^{-1}) implying another surge may have occurred or is occurring. Franklinbreen has thickened, greatest at lower elevations, consistent with a post-1990 advance reported by *Sneed* [2007]. To the north, both Maudbreen and Sabinebreen experience slight frontal thinning and high-elevation thickening. Rijpbreen has advanced since 1990, with mid-elevation thinning and high-elevation thickening. In general, the greatest thickening of the Vestfonna ice cap occurs along the northern ridge. Note however that point elevation errors on VF are estimated to be as much as $\pm$0.6 m yr^{-1} at lower elevations (see section 4.3), such that most of the *dh*/*dt* values are not statistically significant.

[35] In SS, frontal thinning ranges from -0.3 to -3.0 m yr^{-1}. High-elevation *dh*/*dt* values range from -1.0 to +0.5 m yr^{-1}; however, most of SS is thinning at rates of -0.1 to -0.3 m yr^{-1}. On Sørkapp, all *dh*/*dt* are negative, with frontal thinning rates up to -2.5 m yr^{-1}. In Wedel Jarlsberg Land, all glaciers have thinned. Thinning rates on the middle elevations of Rechecherbreen (1990–2005) from -0.5 to -1.0 m yr^{-1} are similar to those measured between 1996 and 2002 [*Bamber et al.*, 2005]. Zawadskibreen, Polakkbreen, and Vestre Torrellbreen experienced high-elevation thinning and mid-elevation thickening due to surges in an early stage [*Sund et al.*, 2009]. In Heerland, many glaciers have thinned, with the exception of glaciers

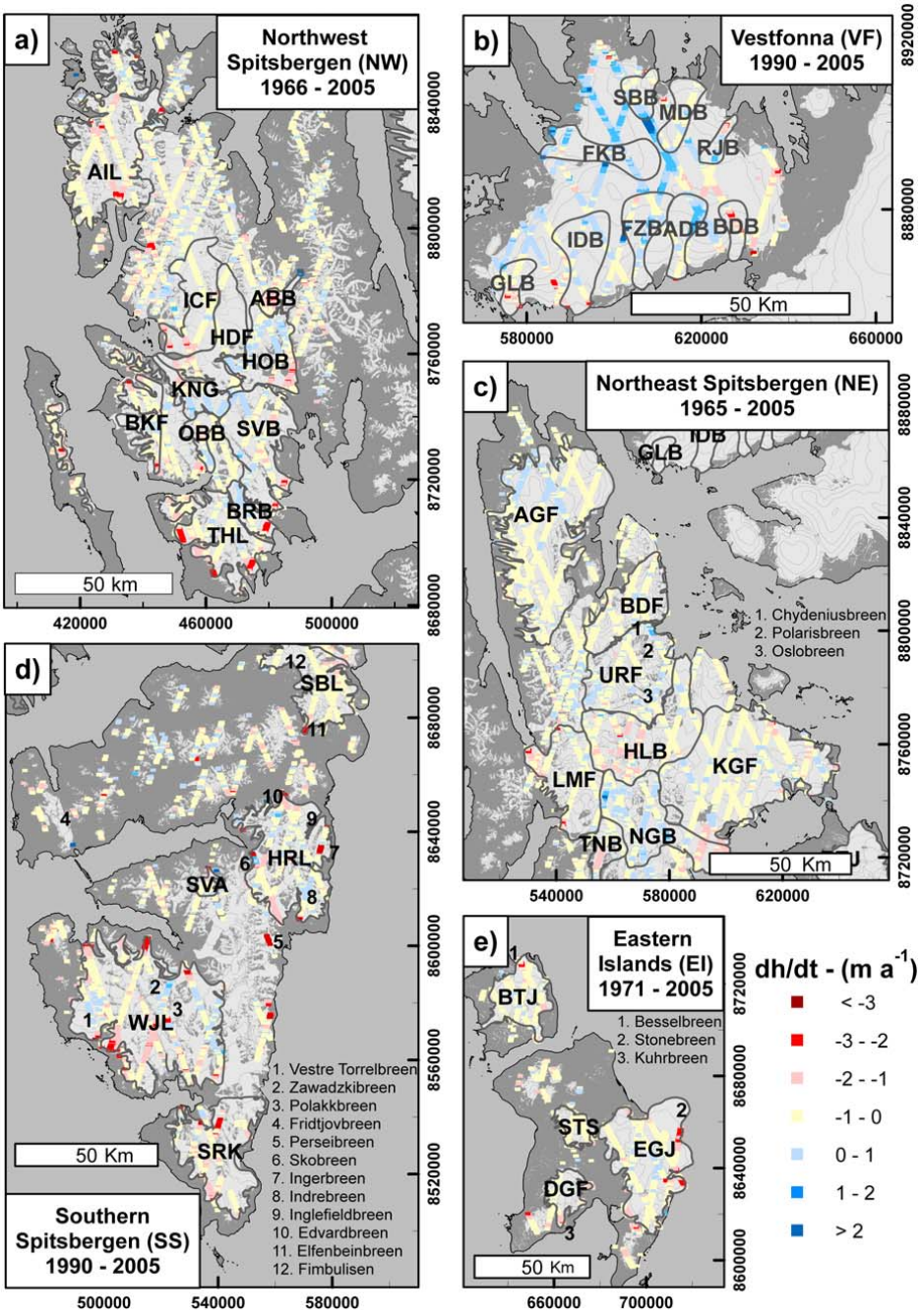
a)
Northwest Spitsbergen (NW) 1966 - 2005
AIL
ICF
ABB
HDF
HOB
KNG
BKF
OBB
SVB
BRB
THL
50 km
420000
460000
500000
8840000
8800000
8760000
8720000
8680000
b)
Vestfonna (VF) 1990 - 2005
SBB
MDB
FKB
RJB
IDB
FZB
ADB
BDB
GLB
50 Km
580000
620000
660000
8920000
8880000
c)
Northeast Spitsbergen (NE) 1965 - 2005
IDB
GLB
AGF
BDF
1
2
URF
3
1. Chydeniusbreen
2. Polarisbreen
3. Oslobreen
HLB
KGF
LMF
TNB
NGB
50 Km
540000
580000
620000
8880000
8840000
8800000
8760000
8720000
d)
12
SBL
11
10
9
4
6
HRL
7
SVA
8
5
2
1
3
WJL
1. Vestre Torrelbreen
2. Zawadzkibreen
3. Polakkbreen
4. Fridtjovbreen
5. Perseibreen
6. Skobreen
7. Ingerbreen
8. Indrebreen
9. Inglefieldbreen
10. Edvardbreen
11. Elfenbeinbreen
12. Fimbulisen
SRK
50 Km
Southern Spitsbergen (SS) 1990 - 2005
500000
540000
580000
8680000
8640000
8600000
8560000
8520000
e)
Eastern Islands (EI) 1971 - 2005
1
BTJ
1. Besselbreen
2. Stonebreen
3. Kuhrbreen
2
STS
EGJ
DGF
3
50 Km
660000
700000
8720000
8680000
8640000
8600000
dh/dt - (m a-1)
< -3
-3 - -2
-2 - -1
-1 - 0
0 - 1
1 - 2
> 2

Figure 5

that surged recently (e.g., Skobreen, Perseibreen, and Ingerbreen), and glaciers that are potentially in a quiescent phase of a surge cycle (e.g., Indrebreen, Inglefieldbreen, and Edvardbreen), which experience mid- and high-elevation increases. Glaciers in South Sabine Land have thinned at all elevations, with values ranging from -2.7 m yr^{-1} at the front of Elfenbeinbreen to -0.1 m yr^{-1} at high elevations of Fimbulisen.

5.2. Volume Changes and Geodetic Mass Balances

[36] The average volume change rate for 27,000 km^2 glaciers on Svalbard is -9.71 ± 0.53 km^3 yr^{-1} w equivalent, the equivalent to a geodetic balance of -0.36 ± 0.02 m yr^{-1} (Table 2). The most negative regional geodetic mass balance occurs in SS. However, SS is estimated over a shorter and more recent time interval (1990–2005), compared to the other regions. We note that the mass balance for the latter period is almost twice as negative as its 1936–1990 geodetic balance estimate [*Nuth et al.*, 2007], consistent with *Kohler et al.*'s. [2007] conclusion. Northeast Spitsbergen has the least negative balance of -0.25 ± 0.02 m yr^{-1} while VF is the only region with a positive geodetic balance ($+0.05 \pm 0.17$ m yr^{-1}) though not significantly different from zero. Austfonna, not included in this study, has experienced interior thickening [*Bamber et al.*, 2004] concurrent with extensive marginal thinning and retreating. *Dowdeswell et al.* [2008] suggest a volume change rate between -2.5 and -4.5 km^3 yr^{-1}, although recent altimetric measurements for the period 2002–2008 indicate total losses on the order of -1.3 km^3 yr^{-1} [*Moholdt et al.*, 2009].

[37] Table 2 provides a list of the regions and subregions with their associated volume changes, geodetic mass balances, and error estimates. The spatial variability of the subregional geodetic balances can be seen in Figure 6. As with the regional estimates, the most negative geodetic balances occur in the south and along the western and eastern coasts. Moderately negative geodetic balances occur toward NE while the subregions of Vestfonna show the most positive balances though the largest errors. Our estimate for Digerfonna in EI of -0.49 m yr^{-1} is similar to *Kääb* [2008], who estimated -0.5 m yr^{-1} by comparing the same NPI map data to a 2002 DEM generated from ASTER stereo imagery. In NW, the most negative balances occur on the surged glaciers of Abrahamsenbreen and Osbornebreen, and in subregions such as Trollheimen Land and Albert I Land that are thinning at most elevation bins. The least negative balances occur on those glaciers suspected to be in a quiescent phase of a surge cycle that experience thickening such as Kongsvegen, Borebreen, and Holmströmbreen. Similarly in NE, the most negative balances occur on the surged glaciers Hinlopenbreen and Tunabreen, and on Lomonosovfonna which is drained by two large tidewater glaciers. The least negative geodetic mass balance occurs on Negribreen which shows significant high-elevation thickening. In SS and EI, the most negative balances occur in the south while VF is the only region that shows a mix of positive and negative balances.

[38] *Hagen et al.* [2003a, 2003b] provide an overview of the in situ mass balance measurements available around Svalbard. The time periods for such measurements vary; however, they are the only available measurements from which to compare. In NW, Midre Lovénbreen and Austre Brøggerbreen are among the longest arctic mass balance measurement series [*Hagen and Liestøl*, 1990]. Their mean annual net balances of -0.38 and -0.48 m yr^{-1} are similar to our subregional estimate for Brøgger-halvøya and Prins Karls Forland of -0.43 m yr^{-1}. There is a discrepancy on Kongsvegen, however, where our estimate of -0.23 m yr^{-1} is significantly more negative than the published in situ mass balance estimate of 0.00 to $+0.04$ m yr^{-1} [*Hagen et al.*, 2003a, 2003b], or including the most recent years, -0.06 m yr^{-1}. Kongsvegen mass balance measurements start from 1987, representing about 20 years of data; this is only about half of our measurement period, roughly 40 years. In SS, mean net balances on Hansbreen (-0.52 m yr^{-1}) and Finsterwalderbreen (-0.51 m yr^{-1}) are less negative than our subregional estimate for Wedel Jarlsberg Land (-0.65 m yr^{-1}), which probably relates to spatial and temporal differences between the measurements. However, they correspond well to the regional SS estimate of -0.55 m yr^{-1}, which also includes glaciers such as Longyearbreen, Vøringbreen, Austre, and Vestre Grønnfjordbreane. In situ measurements on the latter glaciers show balances of -0.55, -0.64 -0.46, and -0.63 m yr^{-1}, respectively [*Jania and Hagen*, 1996].

6. Discussion

6.1. Elevation Change Estimation Methods

[39] Section 3.1 outlined three methods to derive elevation changes between ICESat and contour lines. On nonglacier terrain, method 2 proved to be the most accurate, especially in plateau-type terrain of EI and VF. Method 2, however, requires that the ICESat profiles cross contour lines. The distribution of such intersections on glacier tongues is limited in Spitsbergen, where glaciers tend to flow through steep valleys (see Figure 2a for an example). The opposite is true for the rest of Svalbard because the perimeter of lower-elevation contours on ice caps is largest. Method 3 introduces errors between contour lines, in places where the distance between contours is large. On the other hand, method 3 increases the number and spatial distribution of elevation change points. In using a "hypsometric" approach to estimate volume changes, we assume that the sampling distribution is representative for each elevation bin. The undersampling of method 2 at the lowest elevations has a larger impact on the volume loss of retreating glaciers than the uncertainty of the interpolation at higher elevations. Geodetic balances calculated by method 2 are 10% less

Figure 5. Annual elevation change rates (dh/dt) in (a) NW, (b) VF, (c) NE, (d) SS, and (e) EI obtained by comparing ICESat profiles from 2003 to 2007 to older DEMs from 1965 to 1990. The maps are projected in WGS84-UTM33X. Two-letter abbreviations represent the five larger regions, three-letter codes are the smaller subregions (Table 2). Numbers refer to glaciers mentioned in the text without individual estimates of volume changes and geodetic mass balances. Note that elevation changes in the subregion Brøgger-halvøya/Prins Karls Forland (BKF) within NW is from 1990 to 2005.

Table 2. Regional and Subregional Areas, Volume Changes, and Geodetic Mass Balances in Water Equivalent Along With Error Estimates[a]

Regions and Subregions[b]	Abbreviation	Area (km^2)	Volume Change ($km^3\ yr^{-1}$)	Net Mass Balance ($m\ yr^{-1}$)
Northwest Spitsbergen	NW	6027	−2.46 ± 0.15	−0.41 ± 0.02
Abrahamsenbreen[c]	ABB	76	−0.05 ± 0.01	−0.67 ± 0.14
Albert I Land[d]	AIL	931	−0.53 ± 0.06	−0.57 ± 0.07
Borebreen[e]	BRB	117	−0.03 ± 0.02	−0.22 ± 0.15
Holtedahlfonna/Kronebreen[d]	HDF	370	−0.18 ± 0.05	−0.49 ± 0.13
Holmström-/Mora-/Orsa-breenene[e]	HOB	331	−0.08 ± 0.03	−0.24 ± 0.10
Isachsenfonna/Kongsbreen[d]	ICF	408	−0.18 ± 0.05	−0.43 ± 0.13
Kongsvegen/Sidevegen[c]	KNG	180	−0.04 ± 0.03	−0.23 ± 0.14
Osbornebreen[c]	OBB	101	−0.05 ± 0.02	−0.47 ± 0.17
Svea-/Wahleen-/Sefstrom breenene[e]	SVB	523	−0.19 ± 0.05	−0.36 ± 0.10
Trollheimen[d]	THL	474	−0.29 ± 0.04	−0.60 ± 0.09
Northeast Spitsbergen	NE	8636	−2.19 ± 0.18	−0.25 ± 0.02
Asgardfonna/Vallhallfonna[d]	AGF	1613	−0.31 ± 0.09	−0.19 ± 0.06
Balderfonna[e]	BDF	491	−0.11 ± 0.04	−0.23 ± 0.08
Hinlopenbreen[c]	HLB	860	−0.50 ± 0.06	−0.58 ± 0.07
Kongsfonna/Hachstetterbreen[d]	KGF	1650	−0.51 ± 0.10	−0.31 ± 0.06
The Lomonosovfonna basin[d]	LMF	602	−0.21 ± 0.06	−0.35 ± 0.09
Negribreen[e]	NGB	711	−0.03 ± 0.05	−0.05 ± 0.07
Tunabreen[c]	TNB	174	−0.06 ± 0.02	−0.35 ± 0.14
Ursafonna/Chydeniusbreen/Oslobreen[f]	URF	703	−0.08 ± 0.05	−0.11 ± 0.07
Southern Spitsbergen	SS	6934	−3.79 ± 0.18	−0.55 ± 0.03
Brøgger-halvøya and Prins Karls Forland[d]	BKF	375	−0.16 ± 0.03	−0.43 ± 0.09
Heerland[f]	HRL	838	−0.36 ± 0.07	−0.43 ± 0.09
Sabine Land[d]	SBL	473	−0.26 ± 0.05	−0.55 ± 0.11
Sørkapp[d]	SRK	750	−0.61 ± 0.08	−0.82 ± 0.10
Svalbreen[d]	SVA	53	−0.02 ± 0.01	−0.38 ± 0.14
Wedel Jarlsberg Land[f]	WJL	1743	−1.14 ± 0.14	−0.65 ± 0.08
The Eastern Islands	EI	2799	−1.39 ± 0.14	−0.50 ± 0.05
Barentsjøkulen[d]	BTJ	566	−0.24 ± 0.06	−0.42 ± 0.11
Digerfonna[d]	DGF	264	−0.13 ± 0.06	−0.49 ± 0.21
Edgeøyjøkulen[d]	EGJ	1373	−0.79 ± 0.15	−0.58 ± 0.11
Storskavlen[d]	STS	184	−0.08 ± 0.04	−0.42 ± 0.21
Vestfonna	VF	2408	0.12 ± 0.35	0.05 ± 0.15
Aldousbreen[d]	ADB	107	0.04 ± 0.06	0.33 ± 0.52
Bodleybreen[c]	BDB	59	−0.04 ± 0.04	−0.76 ± 0.63
Franklinbreen[e]	FKB	167	0.06 ± 0.12	0.37 ± 0.72
Frazerbreen[d]	FZB	134	0.03 ± 0.07	0.24 ± 0.56
Gimlebreen[d]	GLB	61	−0.04 ± 0.03	−0.70 ± 0.45
Idunbreen[d]	IDB	188	−0.05 ± 0.09	−0.29 ± 0.46
Maudbreen[d]	MDB	92	−0.01 ± 0.05	−0.07 ± 0.52
Rijpbreen[e]	RJB	39	0.00 ± 0.03	0.07 ± 0.89
Sabinebreen[d]	SBB	64	0.01 ± 0.04	0.11 ± 0.57
Region total		26,804	−9.71 ± 0.48	−0.36 ± 0.02

[a]Abbreviations correspond with those in Figures 5 and 6. Glacier names correspond to those published by *Hagen et al.* [1993]. Subregions with multiple names indicate either that the glacier has two names, one for the upper area and one for the tongue, or that glaciers were combined to form one subregion. Footnotes c–f represent a classification of surge/quiescent/normal glaciers. Note, however, that the classification is not strict, and some glaciers may be surge-type though not inferred here to be so (the same for glaciers in a quiescent phase). Also, some subregions classified as normal glaciers may contain surge-type glaciers (i.e., Barentsøyjøkulen) and other subregions may contain a mix of surge/nonsurge glaciers (i.e., Wedel Jarlsberg Land) and are identified as such.
[b]For each group, the region is listed first, followed by the subregions.
[c]Surge glaciers.
[d]Normal glaciers.
[e]Quiescent phase glaciers.
[f]Subregions containing a surge glacier.

negative than method 3 in NW and SS (Table 3) because glacier tongues in these regions experience the greatest thinning rates and are situated in glacier valleys with few intersections between ICESat profiles and contours. The methods differ only slightly in NE because of the smaller frontal thinning rates (Figure 3). On EI, the geodetic balances calculated from the two methods are similar, while the difference on Vestfonna is hardly significant.

[40] At the subregional scale, the distribution of elevation change points has a much larger impact on the estimates.

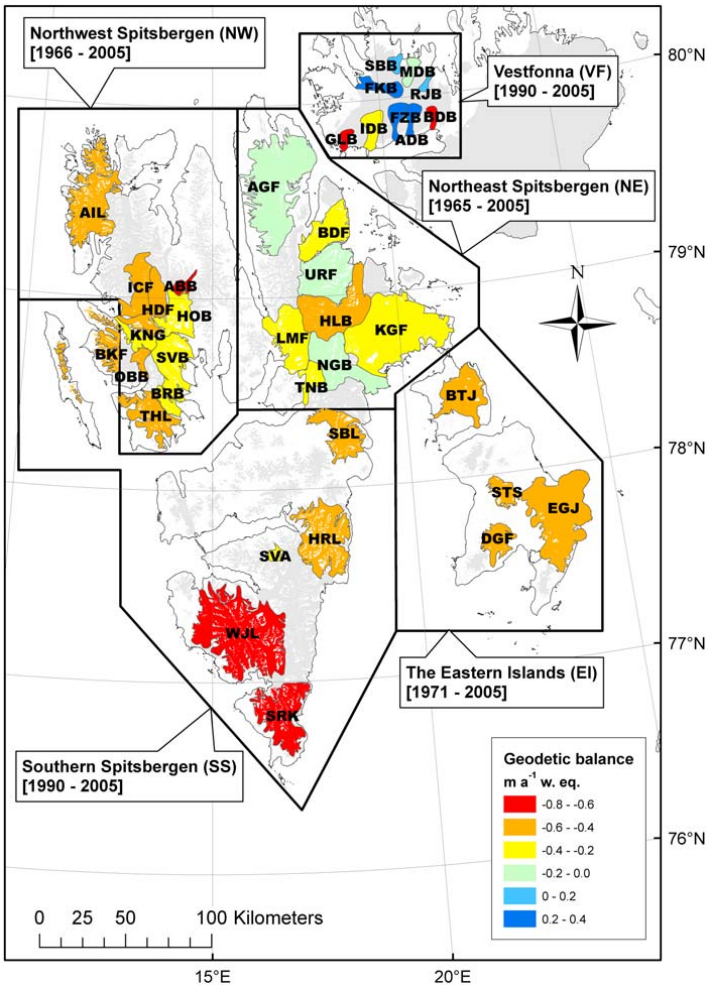

Figure 6. Estimated geodetic mass balances (w. equivalent) from subregional basins that contained a sufficient distribution of ICESat profiles. The gray areas in the background are glaciers that are not estimated individually (~33% of the total glaciated area), but are included in the total estimate for Svalbard. The exception is Austfonna which lies to the east of Vestfonna, and is not included within this study.

Table 3. Regional Geodetic Mass Balance Estimates in Water Equivalent as Estimated From Using the Three Methods Described in Section 4.1[a]

	Method 1		Method 2		Method 3	
Region	*n*	Geodetic Balance	*n*	Geodetic Balance	*n*	Geodetic Balance
NW	6706	−0.37	13509	−0.36	49536	−0.41
NE	5416	−0.26	10303	−0.26	55519	−0.25
EI	1851	−0.49	4024	−0.49	33752	−0.50
VF	1372	−0.03	2659	0.00	28706	0.05
SS	8198	−0.60	10287	−0.49	45315	−0.55

[a]Also shown is the number of original ICESat elevation change points (*n*) resulting from each of the three methods. The variation between the methods provides a reliability assessment based on different geodetic methods to compare the ICESat points to contours.

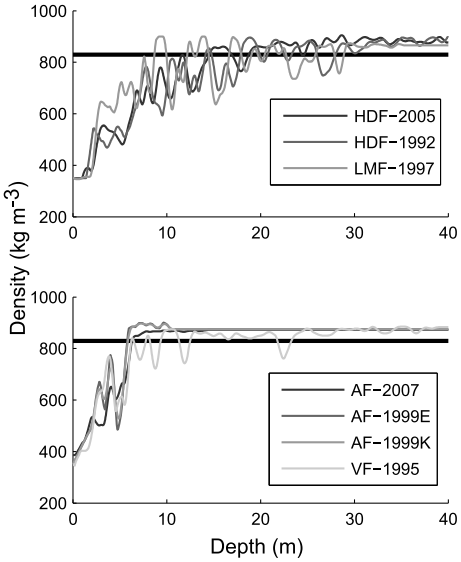

Figure 7. Firn densities profiles from the highest elevations on various glaciers in NE, NW, VF, and AF. (top) Profiles from Lomonosovfonna (LMF), 1997 [*Pohjola et al.*, 2002b]; Holtedahlfonna (HDF), 1992 [*Uchida et al.*, 1993], and 2005 [*Sjögren et al.*, 2007]. Firn-ice transition is between 15 and 19 m. (bottom) Profiles from Vestfonna (VF), 1995 [*Watanabe et al.*, 2001]; Austfonna, 1999 [*Pinglot et al.*, 2001], and 2007 [*Brandt et al.*, 2008; *Dunse et al.*, 2009]. Firn-ice transition in Nordaustlandet ranges between 7 and 10 m. Density curves on Holtedahlfonna and Austfonna are similar despite 15 and 7 year time difference, respectively, suggesting no significant changes in the firn thickness.

Errors in volume changes and geodetic mass balances are therefore considerably larger for the subregions than for the regions (Table 2). The sensitivity of the polynomial fitting to these limited data sets is tested on Holtedahlfonna, where airborne laser altimetry on the centerline was acquired in 2007 by the National Space Institute at the Technical University of Denmark (Figure 2). No formal error estimate has been made on the latter data, but airborne laser altimetry typically achieves accuracies on the order of no more than a few tens of centimeters. The centerline profiles are compared to the DEM via method 3 and a polynomial is fit following the same procedures as in section 4.3. Despite only five transverse ICESat tracks across the glacier, the *dh*/*dt* curve from ICESat is similar to that produced by the centerline profile (Figure 2b). The geodetic balance calculated from the centerline laser altimetry is -0.40 m yr^{-1}, $\sim$20% less than our estimate of -0.49 ± 0.13 m yr^{-1} but within the error estimate.

[41] Overall, the regionalization of multitemporal thickness change rates from ICESat to map comparisons provides relatively robust estimates of volume changes and geodetic mass balances as measurements from extreme mass balance years will be smoothed out in the overall change rates due to the many different time spans involved. In addition, the multiseasonal acquisition of ICESat (February/March, May/June, and September/October) introduces a quasi-random error (see section 4.3) that limits the need for seasonal elevation adjustments, typically important in areas of high melt [*Andreassen et al.*, 2002; *Cox and March*, 2004]. The ICESat point profiles are distributed in many orientations over many glaciers rather than being concentrated along the centerlines of selected glaciers, as in other altimetric studies [*Abdalati et al.*, 2004; *Arendt et al.*, 2006, 2002; *Bamber et al.*, 2005; *Echelmeyer et al.*, 1996]. Unfavorable track configurations make it more difficult to estimate geodetic mass balances from ICESat on individual glaciers, but on a regional scale the estimate benefits from containing a greater spatial distribution of points. In addition, the location of ICESat tracks relative to the glaciers is random in regional estimates, reducing the risk of systematic errors from measurement positions.

6.2. Geodetic Balance Uncertainties

[42] The geodetic mass balance on a glacier is estimated by dividing the total volume change by the average of the old and new areas [*Arendt et al.*, 2002], and should be equivalent to the mass balance measured in situ [*Elsberg et al.*, 2001; *Krimmel*, 1999]. Since updated glacier masks for the ICESat epoch are not available, we underestimate geodetic balances because most of the glaciers are retreating. Glacier areas in SS retreated by $\sim$0.3% per year between 1936 and 1990 [*Nuth et al.*, 2007]. This rate is used to coarsely predict the glacier area during the ICESat epoch. Re-calculation of geodetic balances using the new predicted area results in an average difference of $\sim$5% which we take to represent the expected underestimation of our estimates. However, the final geodetic balance estimates in Table 2 do not consider area changes.

[43] The calculation of a water equivalent geodetic mass balance and sea level contribution assumes that elevation changes are the result of changes in ice thickness rather than variations in firn thickness. It is difficult to test this assumption because firn thickness varies in time and space. Long-term records (i.e., ice cores) exist only at single points at specific times. On Holtedahlfonna in NW and Lomonosovfonna in NE, the firn thickness was measured to be $\sim$20–30 m [*Kameda et al.*, 1993; *Pohjola et al.*, 2002b; *Sjögren et al.*, 2007]. On Åsgardfonna, Vestfonna, and Austfonna, the firn thickness was measured to be only 6–10 m [*Brandt et al.*, 2008; *Dunse et al.*, 2009; *Pinglot et al.*, 2001; *Uchida et al.*, 1993; *Watanabe et al.*, 2001]. Deep firn density curves are lacking in SS and EI. The available density curves (Figure 7) show that the depths to the firn-ice transition on Holtedahlfonna and Austfonna have not changed significantly within the 15 and 8 year time intervals, respectively.

[44] Alternatively, one can apply an exponential density function (for example, $\rho(z) = 0.9 - k(z)^a$) where k and a are tuning parameters, and z is the elevation bin. The function is forced such that the lowest elevations receive a water equivalent conversion of 0.917 where higher elevations gradually receive a lower conversion factor approaching 0.55. Re-calculation of volume changes results in a 3%–7% difference in estimates. It is likely that thinning glaciers will lose some firn as the ELAs rise. This would cause an

overestimation in the geodetic mass balances since the density of firn is lower (~550 kg m^{-3}) than that of ice (917 kg m^{-3}). Setting the water equivalent conversion to that of firn in the middle one-third of elevation bins results in a maximum volume change overestimation of 15%–20%. However, in reality the loss of firn around the ELA will only be a small fraction of this. These tests exemplify that the exact water equivalent conversion will have an effect on the final water equivalent volume change but only to a small degree because at least 50%–60% of the volume changes occur in the lowest one-third of the elevation bins, that is, on ice rather than firn.

[45] In Svalbard, all marine terminating glaciers are grounded [*Hagen et al.*, 2003b] while our elevation change measurements provide thickness change rates for ice above sea level. Therefore, thinning rates of marine terminating glaciers are underestimated within the retreat areas due to ice loss below sea level. This unaccounted mass loss is important to consider when interpreting volume changes and geodetic mass balances of tidewater glaciers at a subregion scale. *Dowdeswell et al.* [2008] found that the ice loss from ice-marginal retreat at Austfonna is as much as 1.4 km^3 yr^{-1} based on ice thickness data and retreat rates from optical imagery. *Hagen et al.* [2003b] assumed an average retreat rate of 10 m yr^{-1} and an average ice thickness of 100 m along the ~1000 km long calving front of Svalbard glaciers to estimate a marine retreat loss of 1 km^3 yr^{-1} for the entire archipelago. The underestimation in our volume change estimates should be well below this value since we exclude Austfonna and account for marine ice losses above sea level. Applying the same assumptions to the ~30 km calving fronts of Vestfonna results in a marine retreat loss on the order of 0.03 km^3 yr^{-1}, which is within our error estimates.

[46] When we convert the total Svalbard volume change into SLEs, the marine retreat of grounded glaciers has only a minimal effect since the ice masses below sea level are already displacing seawater. In fact, since the density of ice is less than water, ice mass loss below sea level slightly decreases Svalbard's contribution to sea level. Nonetheless, we choose not to account for this effect due to the lack of information about ice thicknesses and retreat rates of tidewater glaciers.

6.3. Interpretation of Elevation Changes

[47] In general, three geometric patterns of elevation changes are observed on Svalbard. The most predominant pattern is recognized by large frontal thinning with slight thinning at higher elevations (above the ELA). The second pattern is characterized by large frontal thinning and high-elevation thickening. The third pattern is seen on glaciers that surged, a frontal thickening and high-elevation thinning. Variations to these patterns may occur when surges are still in progress at the time of the second elevation data acquisition (for example, see *Sund et al.* [2009]). At the lowest elevations, thickness changes are the result of ice melting and changes in ice flux. At higher elevations, Svalbard glaciers are generally thinning at rates from −0.1 to −1 m yr^{-1}. In Svalbard, the end of the Little Ice Age (LIA) occurred around the 1920s [*Nordli and Kohler*, 2004] corresponding with the onset of glacier retreat and negative mass balances [*Hagen et al.*, 1993]. Thinning above the ELA may then be explained by a decrease in the thickness of the firn column which is not the case for Holtedahlfonna (Figure 7). An alternate hypothesis may be that ice submergence velocities are larger than accumulation inputs implying a delayed or prolonged response of the dynamic system to past mass balance conditions.

[48] Some glaciers experience significant elevation increases at higher elevations. Since accumulation is dependent on atmospheric circulation and orographic effects, one would expect thickening from precipitation increases to occur regionally. Also, if accumulation is increasing, elevation increases may result from a time lag between increased mass input and the densification processes (i.e., compaction) that convert firn to ice. However, this time lag is probably shorter than the time between measurements. It is plausible that some elevation increases may be due to local precipitation increases (i.e., Asgårdfonna and Vestfonna), though previous ice core research in other parts of Svalbard does not show any significant increases in accumulation rates since 1950 [*Pinglot et al.*, 1999, *Pohjola et al.*, 2002a]. Assuming that firn density profiles remain unchanged, elevation increases above the ELA probably result from a reduced downward flux of ice that is not in balance with the present climate, most likely attributed to surge-type glaciers in quiescent phase.

[49] It remains difficult to interpret geometric changes of glaciers because a change in elevation is the result of both the mass balance and the dynamical flux [*Paterson*, 1994]. *Melvold and Hagen* [1998] and *Hagen et al.* [2005] show that geometric changes on Kongsvegen, a surge-type glacier in quiescent phase, are equivalent to the mass balance because dynamics are stagnant after the surge in 1948. *Pinglot et al.* [1999] measured the mean accumulation rates from numerous ice cores around Svalbard through radioactivity measurements and dating by nuclear tests in 1963 and the Chernobyl accident in 1986. Their analysis of two ice cores on Kongsvegen results in mean net accumulation rates of +0.53 to +0.62 m yr^{-1} from ~1963 to 1991 which compares well to our dh/dt measurements of ~+0.5 m yr^{-1}. On Holtedahlfonna, two ice cores resulted in accumulation rate estimates between +0.47 and +0.57 m yr^{-1} [*Pinglot et al.*, 1999] where our dh/dt at the highest elevations show decreases of −0.25 m yr^{-1}. This implies a submergence ice flux of ~−0.75 m yr^{-1}, which although quite large is not unlikely considering that Kronebreen, one of the fastest glaciers in Svalbard, drains Holtedahlfonna. Both Holtedahlfonna and Kongsvegen are situated within the same region, yet dh/dt measurements show completely different signals. Caution should be used when interpreting elevation changes, especially in a climatic context, as dynamic effects can be a major factor.

[50] A geodetic mass balance is a volume change rate normalized by the hypsometry and is thus a combination of the longer-term mass balance conditions as well as the dynamical conditions which lead to ice emergence or submergence and possibly calving. In the case of Kongsvegen above, the volume change and geodetic mass balance are solely related to the surface mass balance of the glacier since the dynamical component is essentially zero. Geodetic mass balances on surging glaciers require some care in interpreting since the changes reflect the presurge mass balance history, the ice volume lost into the sea through

surging, and a postsurge mass balance history. Within this data set, the geodetic balances of surged glaciers tend to be more negative than glaciers that have not surged. A good example is that of Hinlopenbreen and Negribreen in the NE region. They are adjacent basins that have surged and are building up to a new surge, respectively. The last surge of Negribreen in 1935/1936 is reported to be one of the largest known surges in Svalbard [*Hagen et al.*, 1993]. The geodetic balance of Hinlopenbreen is the most negative in the NE region, partly reflecting the removal of $\sim$2 km^3 of ice by the 1973 surge [*Liestøl*, 1973] although this is not enough to completely explain the enhanced long-term volume loss. Negribreen has the least negative geodetic balance within NE due to an extensive thickening in the accumulation area that almost balances the large thinning rates on the tongue. Down-glacier transport of ice through surging should certainly lead to an immediate change in the mass balance regime by increasing the effective ablation zone, and conversely, decreasing the accumulation zone. Furthermore, crevassing increases the surface area of the ablation zone significantly, potentially also increasing melt [*Muskett et al.*, 2003].

[51] Previous work has suggested that latitude, after accounting for elevation, can explain up to 59% of elevation change variation on Svalbard [*Bamber et al.*, 2005]. In our data sets, elevation can significantly explain $\sim$30%–70% of the variation of individual dh/dt points within each region and subregion. We further test whether the volume change after normalizing by area (i.e., geodetic balance) has any spatial trends. A multiple linear regression applied to the subregional geodetic balances (population size = 37) against latitude and longitude determined that only latitude was significant in explaining 32% of the variation (α = 0.01). Removing surging (n = 5) and quiescent phase glaciers (n = 7) from the data set (population size = 25) increases the explained variance to 46% (α = 0.01). Analysis of variance (ANOVA) tests show that surged glaciers (as classified in Table 2) are more negative than quiescent-phase glaciers (α = 0.02). Variations in geodetic balances can partly be explained by latitude with southern glaciers more negative than northern glaciers and partly by the dynamical situation with surged glaciers more negative than those in a quiescent phase.

7. Conclusions

[52] Until now, ICESat has mainly been applied to ice sheet terrain in Antarctica and Greenland. Here, ICESat laser altimetry proved to be a highly valuable data set for estimating the regional-scale glacier volume changes for smaller glaciers and ice caps at high latitudes and with mountainous topography. The precision of ICESat elevations provides good ground control on DEM generation from satellite imagery [*Berthier and Toutin*, 2008; *Korona et al.*, 2009] but also for determining the uncertainty of older topographic maps. ICESat's applicability for smaller glaciers in mountainous regions is limited because the spatial distribution of tracks does not necessarily lie along the glacier centerlines, as would be the case with airborne laser altimetric profiles. However, the spatial distribution of ICESat tracks in Svalbard is sufficient over larger regions to estimate dh/dt variation with elevation, assuming dh/dt contains normal distributions within elevation bins. The annual average volume change estimates are relatively robust due to the long time span (15–39 years) and to the large number of measurements that 4 years of ICESat tracks provide. Errors associated with such estimates are smaller at the regional scale than at the subregional scale, mainly because of the sampling distribution. Overall, ICESat has proved to be a valuable tool to measure glacier elevation and volume changes in the Svalbard archipelago.

[53] Surface elevation changes on Svalbard glaciers vary largest with elevation, before latitude. In general, glaciers are thinning at lower elevations except on glaciers which have recently surged, where thickening is observed. At higher elevations, three change patterns are present. On some glaciers slight thinning (<-0.5 m yr^{-1}) occurs in the uppermost areas which may reflect a delayed dynamic adjustment to past mass balance conditions. On other glaciers, upper altitudes are thickening, which we generally attribute to build up in the quiescent phase, as the thickening tends to occur on glaciers that have surged in the past (i.e., Negribreen and Kongsvegen), and at a subregional scale rather than at a regional scale (i.e., Borebreen and Indrebreen). Last, some glaciers experience large thinning (>-1 m yr^{-1}) at the upper altitudes (i.e., Hinlopenbreen, Ingerbreen, and Polakkbreen) implying surge activity between the measurements.

[54] Geodetic balances are a measure of the long-term total glacier change, and thus reflect general climatic influences as well as local dynamic effects, mainly in surge-type glaciers. Surged glaciers have a more negative geodetic balance than neighboring glaciers that have not surged. Glaciers that seem to be in a quiescent phase of a surge-cycle have less negative geodetic balances than other glaciers. Ignoring surge-type glaciers, 46% of the geodetic mass balance variation can be explained by latitude. Spatially, the most negative geodetic balances occur in SS followed by the coastal regions of NW, Edgeøya, and Barentsøya. The glaciers in NE show moderate losses while Vestfonna is observed to be close to zero mass balance due to a moderate interior thickening that balances frontal thinning.

[55] In summary, the total volume change for Svalbard glaciers (excluding Austfonna and Kvitøya ice caps) over the past 15–40 years is -9.71 ± 0.53 km^3 yr^{-1} or -0.36 ± 0.02 m yr^{-1} w. equivalent. This corresponds to a global sea level rise of about +0.026 mm yr^{-1} SLE, a value which lies between two previous estimates (+0.01 and +0.038 mm yr^{-1} SLE) of Svalbard's contribution to sea level rise over the past 40 years [*Hagen et al.*, 2003a, 2003b]. Our estimate is about half of the SLE contribution as estimated by *Dowdeswell et al.* [1997], and about 85% of the SLE contribution from the estimated volume changes published by *Dyurgerov and Meier* [2005]. Gravity observations from the Gravity Recovery and Climate Experiment (GRACE) satellite mission between 2003 and 2007 indicate mass losses of 8.8 Gtons yr^{-1} [*Wouters et al.*, 2008] which is similar to our 9.71 Gton yr^{-1} estimate despite the different time periods of the studies. Globally, the Svalbard contribution to sea level rise is about 4% of the total contribution from smaller glaciers and ice caps, which roughly corresponds to the area ratio between Svalbard glaciers and the sum of global glaciers and ice caps [*Kaser et al.*, 2006]. The

average annual volume loss from Svalbard is about twice the 1952–2001 loss rates in the Russian Arctic [*Glazovsky and Macheret*, 2006; *Meier et al.*, 2007] and about 40% of the 1995–2000 loss rates in the Canadian Arctic [*Abdalati et al.*, 2004]. When glacier area is considered, the Svalbard geodetic mass balance is the most negative in the Arctic, twice as negative as the Canadian Arctic, and almost four times as negative as the Russian Arctic. Lower latitude glacier regions such as Alaska [*Arendt et al.*, 2006], Iceland [*Björnsson and Pálsson*, 2008], and Patagonia [*Rignot et al.*, 2003] are losing ice at a faster rate than Svalbard.

[56] **Acknowledgments.** We would like to thank the Associate Editor, Gordon Hamilton, whose comments and suggestions considerably improved the content and presentation of this article. We would also like to thank Hester Jiskoot and two anonymous reviewers for their thorough and constructive comments. This research was supported by the IPY-GLACIODYN project (176076) funded by the Norwegian Research Council (NFR). We would like to acknowledge the Norwegian Polar Institute Mapping Department for providing the maps and DEMs, and NASA and NSIDC for providing the ICESat data, which is a remarkably accurate data set. The National Space Institute at the Technical University of Denmark provided the 2007 airborne laser altimetry profile over Holtedahlfonna. We wish to thank Elisabeth Isaksson and Veijo Pohjola for providing firn density curves. We would also like to thank Thomas Vikhamar Schuler for improving this manuscript and providing valuable insight and discussion on the validity of "Sorge's law."

References

Abdalati, W., et al. (2004), Elevation changes of ice caps in the Canadian Arctic Archipelago, *J. Geophys. Res.*, *109*, F04007, doi:10.1029/2003JF000045.

Abshire, J. B., X. Sun, H. Riris, J. M. Sirota, J. F. McGarry, S. Palm, D. Yi, and P. Liiva (2005), Geoscience Laser Altimeter System (GLAS) on the ICESat mission: On-orbit measurement performance, *Geophys. Res. Lett.*, *32*, L21S02, doi:10.1029/2005GL024028.

Adalgeirsdottir, G., K. A. Echelmeyer, and W. D. Harrison (1998), Elevation and volume changes on the Harding Icefield, Alaska, *J. Glaciol.*, *44*(148), 570–582.

Andreassen, L. M., H. Elvehoy, and B. Kjollmoen (2002), Using aerial photography to study glacier changes in Norway, *Ann. Glaciol.*, *34*, 343–348, doi:10.3189/172756402781817626.

Arendt, A. A., K. A. Echelmeyer, W. D. Harrison, C. S. Lingle, and V. B. Valentine (2002), Rapid wastage of Alaska glaciers and their contribution to rising sea level, *Science*, *297*(5580), 382–386, doi:10.1126/science.1072497.

Arendt, A., et al. (2006), Updated estimates of glacier volume changes in the western Chugach Mountains, Alaska, and a comparison of regional extrapolation methods, *J. Geophys. Res.*, *111*, F03019, doi:10.1029/2005JF000436.

Bader, H. (1954), Sorge's Law of densification of snow on high polar glaciers, *J. Glaciol.*, *2*(15), 319–323.

Bamber, J., W. Krabill, V. Raper, and J. Dowdeswell (2004), Anomalous recent growth of part of a large Arctic ice cap: Austfonna, Svalbard, *Geophys. Res. Lett.*, *31*, L12402, doi:10.1029/2004GL019667.

Bamber, J. L., W. Krabill, V. Raper, J. A. Dowdeswell, and J. Oerlemans (2005), Elevation changes measured on Svalbard glaciers and ice caps from airborne laser data, *Ann. Glaciol.*, *42*, 202–208, doi:10.3189/172756405781813131.

Berthier, E., and T. Toutin (2008), SPOT5-HRS digital elevation models and the monitoring of glacier elevation changes in North-West Canada and South-East Alaska, *Remote Sens. Environ.*, *112*(5), 2443–2454, doi:10.1016/j.rse.2007.11.004.

Björnsson, H., and F. Pálsson (2008), Icelandic glaciers, *Joekull*, *58*, 365–386.

Björnsson, H., Y. Gjessing, S. E. Hamran, J. O. Hagen, O. Liestøl, F. Palsson, and B. Erlingsson (1996), The thermal regime of sub-polar glaciers mapped by multi-frequency radio-echo sounding, *J. Glaciol.*, *42*(140), 23–32.

Brandt, O., et al. (2008), Comparison of airborne radar altimeter and ground-based Ku-band radar measurements on the ice cap Austfonna, Svalbard, *Cryosphere Discuss.*, *2*(5), 777–810.

Brenner, A. C., J. R. DiMarzio, and H. J. Zwally (2007), Precision and accuracy of satellite radar and laser altimeter data over the continental ice sheets, *IEEE Trans. Geosci. Remote Sens.*, *45*(2), 321–331, doi:10.1109/TGRS.2006.887172.

Cox, L. H., and R. S. March (2004), Comparison of geodetic and glaciological mass-balance techniques, Gulkana Glacier, Alaska, USA, *J. Glaciol.*, *50*(170), 363–370, doi:10.3189/172756504781829855.

Dowdeswell, J., and J. Bamber (1995), On the glaciology of Edgeøya and Barentsøya, Svalbard, *Polar Res.*, *14*(2), 105–122, doi:10.1111/j.1751-8369.1995.tb00684.x.

Dowdeswell, J. A., and T. J. Benham (2003), A surge of Perseibreen, Svalbard, examined using aerial photography and ASTER high resolution satellite imagery, *Polar Res.*, *22*(2), 373–383, doi:10.1111/j.1751-8369.2003.tb00118.x.

Dowdeswell, J. A., and R. L. Collin (1990), Fast-flowing outlet glaciers on Svalbard ice caps, *Geology*, *18*(8), 778–781, doi:10.1130/0091-7613(1990)018<0778:FFOGOS>2.3.CO;2.

Dowdeswell, J. A., et al. (1997), The mass balance of circum-Arctic glaciers and recent climate change, *Quat. Res.*, *48*(1), 1–14, doi:10.1006/qres.1997.1900.

Dowdeswell, J. A., T. J. Benham, T. Strozzi, and J. O. Hagen (2008), Iceberg calving flux and mass balance of the Austfonna ice cap on Nordaustlandet, Svalbard, *J. Geophys. Res.*, *113*, F03022, doi:10.1029/2007JF000905.

Dunse, T., T. V. Schuler, J. O. Hagen, T. Eiken, O. Brandt, and K. A. Høgda (2009), Recent fluctuations in the extent of the firn area of Austfonna, Svalbard, inferred from GPR, *Ann. Glaciol.*, *50*, 155–162.

Dyurgerov, M. B., and M. F. Meier (1997), Mass balance of mountain and subpolar glaciers: A new global assessment for 1961–1990, *Arct. Antarct. Alp. Res.*, *29*(4), 379–391, doi:10.2307/1551986.

Dyurgerov, M. B., and M. F. Meier (2005), *Glaciers and the Changing Earth System: A 2004 Snapshot*, 117 pp., Inst. of Arct. and Alp. Res., Univ. of Colo. at Boulder, Boulder.

Echelmeyer, K. A., et al. (1996), Airborne surface profiling of glaciers: A case-study in Alaska, *J. Glaciol.*, *42*(142), 538–547.

Elsberg, D. H., W. D. Harrison, K. A. Echelmeyer, and R. M. Krimmel (2001), Quantifying the effects of climate and surface change on glacier mass balance, *J. Glaciol.*, *47*(159), 649–658, doi:10.3189/172756501781831783.

Etzelmüller, B. (2000), On the quantification of surface changes using grid-based digital elevation models (DEMs), *Trans. GIS*, *4*(2), 129–143, doi:10.1111/1467-9671.00043.

Fricker, H. A., A. Borsa, B. Minster, C. Carabajal, K. Quinn, and B. Bills (2005), Assessment of ICESat performance at the Salar de Uyuni, Bolivia, *Geophys. Res. Lett.*, *32*, L21S06, doi:10.1029/2005GL023423.

Glazovsky, A. F., and Y. Y. Macheret (2006), Fluctuations of glaciers in the second half of 20th century caused by climate change, in *Glaciation in North and Central Eurasia at Present Time*, edited by V. M. Kotlyakov, pp. 397–402, Russ. Acad. of Sci., Moscow.

Haeberli, W., M. Zemp, and M. Hoelzle (Eds.) (2007), Glacier mass balance, *Bull. 9*, World Glacier Monit. Serv., Zurich, Switzerland.

Hagen, J. O., and O. Liestøl (1990), Long-term glacier mass-balance investigations in Svalbard, 1950–1988, *Ann. Glaciol.*, *14*, 102–106.

Hagen, J. O., O. Liestøl, E. Roland, and T. Jørgensen (1993), Glacier atlas of Svalbard and Jan Mayen, *Meddelelse 129*, Norw. Polar Inst., Oslo.

Hagen, J. O., J. Kohler, K. Melvold, and J. G. Winther (2003a), Glaciers in Svalbard: Mass balance, runoff and freshwater flux, *Polar Res.*, *22*(2), 145–159, doi:10.1111/j.1751-8369.2003.tb00104.x.

Hagen, J. O., K. Melvold, F. Pinglot, and J. A. Dowdeswell (2003b), On the net mass balance of the glaciers and ice caps in Svalbard, Norwegian Arctic, *Arct. Antarct. Alp. Res.*, *35*(2), 264–270, doi:10.1657/1523-0430(2003)035[0264:OTNMBO]2.0.CO;2.

Hagen, J. O., T. Eiken, J. Kohler, and K. Melvold (2005), Geometry changes on Svalbard glaciers: Mass-balance or dynamic response?, *Ann. Glaciol.*, *42*, 255–261, doi:10.3189/172756405781812763.

Hamilton, G., and J. Dowdeswell (1996), Controls on glacier surging in Svalbard, *J. Glaciol.*, *42*(140), 157–168.

Hamran, S. E., E. Aarholt, J. O. Hagen, and P. Mo (1996), Estimation of relative water content in a sub-polar glacier using surface-penetration radar, *J. Glaciol.*, *42*(142), 533–537.

Hisdal, V. (1985), *Geography of Svalbard*, Norw. Polar Inst., Oslo.

Howat, I. M., B. E. Smith, I. Joughin, and T. A. Scambos (2008), Rates of southeast Greenland ice volume loss from combined ICESat and ASTER observations, *Geophys. Res. Lett.*, *35*, L17505, doi:10.1029/2008GL034496.

Humlum, O. (2002), Modelling late 20th-century precipitation in Nordenskiøld Land, Svalbard, by geomorphic means, *Norw. J. Geogr.*, *56*(2), 96–103, doi:10.1080/00291950260056413.

Hutchinson, M. F. (1989), A new procedure for gridding elevation and stream line data with automatic removal of spurious pits, *J. Hydrol.*, *106*(3–4), 211–232, doi:10.1016/0022-1694(89)90073-5.

Isaksson, E., et al. (2005), Two ice-core delta O-18 records from Svalbard illustrating climate and sea-ice variability over the last 400 years, *Holocene*, *15*(4), 501–509, doi:10.1191/0959683605hl820rp.

Jania, J., and J. O. Hagen (Eds.) (1996), Mass balance of arctic glaciers, *Rep. 5*, 62 pp., Int. Arct. Sci. Comm., Potsdam, Germany.

Jania, J., et al. (2005), Temporal changes in the radiophysical properties of a polythermal glacier in Spitsbergen, *Ann. Glaciol.*, *42*, 125–134, doi:10.3189/172756405781812754.

Jiskoot, H., T. Murray, and P. Boyle (2000), Controls on the distribution of surge-type glaciers in Svalbard, *J. Glaciol.*, *46*(154), 412–422, doi:10.3189/172756500781833115.

Kääb, A. (2008), Glacier volume changes using ASTER satellite stereo and ICESat GLAS laser altimetry. A test study on Edgeøya, eastern Svalbard, *IEEE Int. Geosci. Remote Sens.*, *46*(10), 2823–2830, doi:10.1109/TGRS.2008.2000627.

Kameda, T., S. Takahashi, K. Goto-Azuma, S. Kohshima, O. Watanabe, and J. O. Hagen (1993), First report of ice core analyses and borehole temperatures on the highest icefield on western Spitsbergen in 1992, *Bull. Glacier Res.*, *11*, 51–61.

Kaser, G., J. G. Cogley, M. B. Dyurgerov, M. F. Meier, and A. Ohmura (2006), Mass balance of glaciers and ice caps: Consensus estimates for 1961–2004, *Geophys. Res. Lett.*, *33*, L19501, doi:10.1029/2006GL027511.

Kohler, J., et al. (2007), Acceleration in thinning rate on western Svalbard glaciers, *Geophys. Res. Lett.*, *34*, L18502, doi:10.1029/2007GL030681.

Korona, J., E. Berthier, M. Bernard, F. Rémy, and E. Thouvenot (2009), SPIRIT. SPOT 5 stereoscopic survey of Polar Ice: Reference images and topographies during the fourth international polar year (2007–2009), *ISPRS J. Photogramm. Remote Sens.*, *64*(2), 204–212, doi:10.1016/j.isprsjprs.2008.10.005.

Krimmel, R. M. (1999), Analysis of difference between direct and geodetic mass balance measurements at South Cascade Glacier, Washington, *Geogr. Ann., Ser. A Phys. Geogr.*, *81*(4), 653–658.

Lemke, P., et al. (2007), Observations: Changes in snow, ice and frozen ground, in *Climate Change 2007: The Physical Science Basis—Contribution of Working Group I to the Fourth Assessment Report of the Intergovernmental Panel on Climate Change*, edited by S. Solomon et al., pp. 356–360, Cambridge Univ. Press, Cambridge, U. K.

Liestøl, O. (1973), Glaciological work in 1971, in *Norsk Polarinstitutt Årbok*, pp. 31–35, Norw. Polar Inst., Oslo.

Loeng, H. (1991), Features of the physical oceanographic conditions of the Barents Sea, *Polar Res.*, *10*(1), 5–18, doi:10.1111/j.1751-8369.1991.tb00630.x.

Meier, M. F., et al. (2007), Glaciers dominate Eustatic sea-level rise in the 21st century, *Science*, *317*(5841), 1064–1067, doi:10.1126/science.1143906.

Melvold, K., and J. O. Hagen (1998), Evolution of a surge-type glacier in its quiescent phase: Kongsvegen, Spitsbergen, 1964–95, *J. Glaciol.*, *44*(147), 394–404.

Moholdt, G., J. O. Hagen, T. Eiken, and T. V. Schuler (2009), Geometric changes and mass balance of the Austfonna ice cap, Svalbard, *Cryosphere*, *4*, 21–34.

Murray, T., A. Luckman, T. Strozzi, and A. M. Nuttall (2003a), The initiation of glacier surging at Fridtjovbreen, Svalbard, *Ann. Glaciol.*, *36*, 110–116, doi:10.3189/172756403781816275.

Murray, T., T. Strozzi, A. Luckman, H. Jiskoot, and P. Christakos (2003b), Is there a single surge mechanism? Contrasts in dynamics between glacier surges in Svalbard and other regions, *J. Geophys. Res.*, *108*(B5), 2237, doi:10.1029/2002JB001906.

Muskett, R. R., C. S. Lingle, W. V. Tangborn, and B. T. Rabus (2003), Multi-decadal elevation changes on Bagley Ice Valley and Malaspina Glacier, Alaska, *Geophys. Res. Lett.*, *30*(16), 1857, doi:10.1029/2003GL017707.

Nolan, M., A. Arendt, B. Rabus, and L. Hinzman (2005), Volume change of McCall Glacier, Arctic Alaska, USA, 1956–2003, *Ann. Glaciol.*, *42*, 409–416, doi:10.3189/172756405781812943.

Nordli, Ø., and J. Kohler (2004), *The Early 20th Century Warming—Daily Observations at Grønfjorden and Longyearbyen on Spitsbergen*, Norw. Meteorol. Inst., Oslo.

Nuth, C. (2007), Geodetic mass balance of Svalbard glaciers: 1936–2004, M.S. thesis, 94 pp., Univ. of Oslo, Oslo.

Nuth, C., J. Kohler, H. F. Aas, O. Brandt, and J. O. Hagen (2007), Glacier geometry and elevation changes on Svalbard (1936–90), A baseline dataset, *Ann. Glaciol.*, *46*, 106–116, doi:10.3189/172756407782871440.

Palli, A., J. C. Moore, and C. Rolstad (2003), Firn-ice transition-zone features of four polythermal glaciers in Svalbard seen by ground-penetrating radar, *Ann. Glaciol.*, *37*, 298–304, doi:10.3189/172756403781816059.

Paterson, W. S. B. (1994), *The Physics of Glaciers*, Elsevier, New York.

Pinglot, J. F., J. O. Hagen, K. Melvold, T. Eiken, and C. Vincent (2001), A mean net accumulation pattern derived from radioactive layers and radar soundings on Austfonna, Nordaustlandet, Svalbard, *J. Glaciol.*, *47*(159), 555–566, doi:10.3189/172756501781831800.

Pinglot, J. F., M. Pourchet, B. Lefauconnier, J. O. Hagen, E. Isaksson, R. Vaikmae, and K. Kamiyama (1999), Accumulation in Svalbard glaciers deduced from ice cores with nuclear tests and Chernobyl reference layers, *Polar Res.*, *18*(2), 315–321, doi:10.1111/j.1751-8369.1999.tb00309.x.

Pohjola, V. A., T. A. Martma, H. A. J. Meijer, J. C. Moore, E. Isaksson, R. Vaikmae, and R. S. W. Van de Wal (2002a), Reconstruction of three centuries of annual accumulation rates based on the record of stable isotopes of water from Lomonosovfonna, Svalbard, *Ann. Glaciol.*, *35*, 57–62, doi:10.3189/172756402781816753.

Pohjola, V. A., et al. (2002b), Effect of periodic melting on geochemical and isotopic signals in an ice core from Lomonosovfonna, Svalbard, *J. Geophys. Res.*, *107*(D4), 4036, doi:10.1029/2000JD000149.

Rignot, E., A. Rivera, and G. Casassa (2003), Contribution of the Patagonia Icefields of South America to sea level rise, *Science*, *302*(5644), 434–437, doi:10.1126/science.1087393.

Rolstad, C. A. J., J. O. Hagen, and B. Lunden (1997), Visible and near-infrared digital images for determination of ice velocities and surface elevation during a surge on Osbornebreen, a tidewater glacier in Svalbard, *Ann. Glaciol.*, *24*, 255–261.

Sand, K., J. G. Winther, D. Marechal, O. Bruland, and K. Melvold (2003), Regional variations of snow accumulation on Spitsbergen, Svalbard, 1997–99, *Nord. Hydrol.*, *34*(1–2), 17–32.

Sato, T., et al. (2006), A geophysical interpretation of the secular displacement and gravity rates observed at Ny-Alesund, Svalbard in the Arctic: effects of post-glacial rebound and present-day ice melting, *Geophys. J. Int.*, *165*(3), 729–743, doi:10.1111/j.1365-246X.2006.02992.x.

Schutz, B. E., H. J. Zwally, C. A. Shuman, D. Hancock, and J. P. DiMarzio (2005), Overview of the ICESat Mission, *Geophys. Res. Lett.*, *32*, L21S01, doi:10.1029/2005GL024009.

Sjögren, B., O. Brandt, C. Nuth, E. Isaksson, V. Pohjola, J. Kohler, and R. S. W. Van De Wal (2007), Instruments and methods: Determination of firn density in ice cores using image analysis, *J. Glaciol.*, *53*(182), 413–419, doi:10.3189/002214307783258369.

Sneed, W. (2007), Satellite remote sensing of Arctic Glacier: Climate interactions, M.S. thesis, 83 pp., Univ. of Maine, Orono.

Sund, M., T. Eiken, J. O. Hagen, and A. Kääb (2009), Svalbard surge dynamics derived from geometric changes, *Ann. Glaciol.*, *50*, 50–60, doi:10.3189/172756409789624265.

Thomas, R., C. Davis, E. Frederick, W. Krabill, Y. H. Li, S. Manizade, and C. Martin (2008), A comparison of Greenland ice-sheet volume changes derived from altimetry measurements, *J. Glaciol.*, *52*(185), 203–212, doi:10.3189/002214308784886225.

Tsukernik, M., D. N. Kindig, and M. C. Serreze (2007), Characteristics of winter cyclone activity in the northern North Atlantic: Insights from observations and regional modeling, *J. Geophys. Res.*, *112*, D03101, doi:10.1029/2006JD007184.

Uchida, T., et al. (1993), Ice core analyses and borehole temperature measurements at the drilling site on Asgardfonna, Svalbard, in 1993, *Mem. Natl. Inst. Polar Res.*, *51*, 377–386.

Watanabe, O., et al. (2001), Studies on climatic and environmental changes during the last few hundred years using ice cores from various sites in Nordaustlandet, Svalbard, *Mem. Natl. Inst. Polar Res.*, *54*, 227–242.

Winther, J. G., O. Bruland, K. Sand, A. Killingtveit, and D. Marechal (1998), Snow accumulation distribution on Spitsbergen, Svalbard, in 1997, *Polar Res.*, *17*(2), 155–164, doi:10.1111/j.1751-8369.1998.tb00269.x.

Wouters, B., D. Chambers, and E. J. O. Schrama (2008), GRACE observes small-scale mass loss in Greenland, *Geophys. Res. Lett.*, *35*, L20501, doi:10.1029/2008GL034816.

Zwally, H. J., et al. (2002), ICESat's laser measurements of polar ice, atmosphere, ocean, and land, *J. Geodyn.*, *34*(3–4), 405–445, doi:10.1016/S0264-3707(02)00042-X.

Zwally, H. J., et al. (2005), Mass changes of the Greenland and Antarctic ice sheets and shelves and contributions to sea-level rise: 1992–2002, *J. Glaciol.*, *51*(175), 509–527, doi:10.3189/172756505781829007.

Zwally, H. J., et al. (2008), GLAS/ICESat L1B global elevation data V028, February 2003 to November 2007, http://nsidc.org/data/icesat/index.html, Natl. Snow and Ice Data Cent., Boulder, Colo.

J. O. Hagen, A. Kääb, G. Moholdt, and C. Nuth, Department of Geosciences, University of Oslo, PO Box 1047, Blindern, N-0316 Oslo, Norway. (christopher.nuth@geo.uio.no)

J. Kohler, Norwegian Polar Institute, Polarmiljøsenteret, N-9296 Tromsø, Norway.

II

7.2 Article II:

Moholdt G., Nuth C., Hagen J.O., Kohler J. (2010) Recent elevation changes of Svalbard glaciers derived from ICESat laser altimetry. *Remote Sensing of Environment.* 114.

III

7.3 Article III:

Nuth, C. and Kääb, A. (2010) What is in an elevation difference? Accuracy and corrections of satellite elevation data sets for quantification of glacier changes. *The Cryosphere Discussions*. In Review.

Reviews of this discussion article can be viewed on the web:
http://www.the-cryosphere-discuss.net/4/2013/2010/tcd-4-2013-2010-discussion.html

The Cryosphere Discuss., 4, 2013–2077, 2010
www.the-cryosphere-discuss.net/4/2013/2010/
doi:10.5194/tcd-4-2013-2010

The Cryosphere Discussions

What's in an elevation difference? Accuracy and corrections of satellite elevation data sets for quantification of glacier changes

C. Nuth and A. Kääb

Dept. of Geosciences, University of Oslo, 0316 Oslo, Norway

Received: 28 September 2010 – Accepted: 8 October 2010 – Published: 13 October 2010

Correspondence to: C. Nuth (christopher.nuth@geo.uio.no)

Published by Copernicus Publications on behalf of the European Geosciences Union.

Abstract

There is an increasing number of DEMs available worldwide for deriving elevation differences over time, including vertical changes on glaciers. Most of these DEMs are heavily post-processed or merged, so that physical error modelling becomes impossible and statistical error modelling is required instead. We propose a three-step methodological framework for assessing and correcting DEMs to quantify glacier elevation changes: remove DEM shifts, check for elevation-dependent biases, and check for higher-order, sensor-specific biases. An analytic, simple and robust method to co-register elevation data is presented in regions where stable terrain is either plentiful (case study New Zealand) or limited (case study Svalbard). The method is exemplified using the three global elevation data sets available, SRTM, ICESat and the ASTER GDEM, and with automatically generated DEMs from satellite stereo instruments of ASTER and SPOT5-HRS. After three-dimensional co-registration, significant biases related to elevation were found in some of the stereoscopic DEMs. Biases related to the satellite acquisition geometry (along/cross track) were detected at two frequencies in the automatically generated ASTER DEMs. The higher frequency bias seems to be related to satellite *jitter*, most effective in the back-looking pass of the satellite. The origins of the more significant lower frequency bias is uncertain. ICESat-derived elevations are found to be the most consistent globally available elevation data set available so far. Before performing regional-scale glacier elevation change studies or mosaicking DEMs from multiple individual tiles (e.g. ASTER GDEM), we recommend to co-register all elevation data to ICESat as a global vertical reference system. The proposed methodological framework is exemplified for elevation changes on the Fox, Franz Joseph, Tasman and Murchison glaciers of New Zealand and the glaciers of central Spitsbergen, Svalbard.

1 Introduction

Applications of regional and global scale elevation products have increased substantially in geoscience. Surface elevation data are collected by many sensors using various techniques, and differencing between the multi-temporal elevation products is becoming a common method for monitoring surface changes, particularly of glaciers. The data are typically available as a continuous profile or swath of points, a network of points or a regular grid, the latter we will refer to as a Digital Elevation Model (DEM). There are three (nearly) global elevation products available to the public today. The Shuttle Radar Topography Mission (SRTM) in February 2000 provided the first product using interferometric SAR (InSAR) techniques (Farr et al., 2007). The ICESat mission from 2003 to 2009 provided the second using space-borne Light Detection and Ranging (Lidar) (Zwally et al., 2002). The third is the newly released ASTER GDEM based upon a composition of automatically generated DEMs from Advanced Spaceborne Emission and Reflection radiometer (ASTER) stereo scenes acquired from 2000–present (METI/NASA/USGS, 2009). Many of these products contain errors and biases resulting from sensor instabilities, limitations of the techniques, bad surveying conditions on the ground and various types of post-processing artifacts. The errors occur at a range of scales that directly affect measurement precision and increases the significance level an elevation change requires for adequate detection through elevation differencing.

The motivation behind this study is to address the accuracy of comparisons between the globally available elevation data sets with particular attention towards detecting glacier elevation changes. This involves classifying and understanding the errors and especially biases associated with each of the data products and to suggest corrections that may improve the accuracy and precision of the differences. Many of the data sets available to researchers today and those tested in this study are the result of second-level processing. This means that the conversion procedures between the original data acquisition (i.e. laser return waveforms, radar interferrograms or stereo-imagery) to

final elevation data is lost and thus errors can not be anymore physically determined or modeled based upon the original transformation equations and acquisition parameters. Therefore, we use statistical approaches to analyze errors and to determine potential bias corrections. Even if physical modelling of errors might be preferable, an advantage of the statistical error modelling approach is that universal methods can be developed that may be widely applicable to different types of elevation data and irrespective of the sensor systems and processing procedures applied.

Detection of glacier elevation changes through DEM or elevation differencing is not a new procedure. Repeat photogrammetry was being used as early as in the 1950s to quantify the retreat of glaciers (Finsterwalder, 1954). Today, comparisons of elevation data acquired from space are becoming more popular in research because of the high temporal and spatial availability in remote areas where glaciers are present. Some studies use the data sets as they are, without searching or correcting for biases between them (e.g. Rignot et al., 2003; Sund et al., 2009; Muskett et al., 2009) which may lead to biased estimates of glacier volume changes or false-detection of surging (Berthier, 2010). The consequences of un-corrected biases in the previously named and other studies is not known to us. However, many studies search for biases between the data pairs and apply corrections using various methods (e.g. Berthier et al., 2007, 2010; Racoviteanu et al., 2007; Peduzzi et al., 2010).

The most important correction is to co-register the two elevation data products such that the pixels of each DEM represent the same spots on the Earth surface. Some studies co-register by minimizing the Root Mean Square Error (RMSE) of stable terrain elevation differences using a 2-dimensional linear regression, or in other words shifting one DEM to the other, for example within ±5 pixels (Rodriguez et al., 2006; Berthier et al., 2007; Howat et al., 2008). Other studies have corrected DEMs using single or multiple linear regression corrections between elevation and the location and terrain parameters (Gorokhovich and Voustianiouk, 2006; Bolch et al., 2008; Peduzzi et al., 2010). In particular in terrestrial and airborne laser scanning, 3-dimensional least squares matching (LSM) is used to minimize the Euclidean distances between

the points of point clouds, often allowing not only for shifts but also for rotations and scales between the two or more datasets (Gruen and Akca, 2005).

Another commonly applied correction to DEMs is an elevation dependent bias (Berthier et al., 2004, 2007, 2010; Kääb, 2008) which may arise due to an uneven distribution of ground control points (GCPs) or to inaccurate satellite parameters. This correction may have significant implications for glacier elevation changes because glaciers spread a range of altitudes which define their ablation and accumulation areas. At this point it should be noted that such elevation biases might result solely from differences in the resolution of the DEMs compared (Paul, 2008). Last, biases associated with the satellite acquisition geometry have been found in some products related to satellite attitude parameters which was shown to be significant enough to warrant a correction (Berthier et al., 2007). This type of correction will only apply to those data products where it is significant; e.g. satellite stereoscopic DEMs.

2 Objectives and case study locations

The objectives of this study is to present a simple and effective *universal* method to co-register elevation products. We aim at a method that can easily be applied without specialized software necessary and with a high degree of automation. We argue that this method should be used as a first step in elevation comparison due to the varying location accuracies of the different sensors. In a second step, after centering the two data products to each other, analysis of remaining anomalies is compiled to detect both linear and non-linear biases and to determine which errors require correction and how they affect glacier elevation changes. In contrast to the first step, the universal 3-dimensional co-registration, the procedures applied in the second and third steps are highly dependent on the sensor type and post-processing used for the elevation data. We will therefore only show examples for this secondary adjustments, using ASTER satellite stereo as a scenario.

Two sites are chosen for this study. The first is the mid-latitude high alpine region of the southern Alps in New Zealand. The region is chosen because of its alpine glacier characteristics, high elevation range, and availability of stable terrain from which to exemplify the biases and derive corrections. In this case-study, SRTM, ICESat, ASTER GDEM, and automatically generated ASTER DEMs from the US Geological Survey Land Processes Distributed Active Archive Center (LPDAAC) are compared. The second site is the high Arctic alpine region of Svalbard where ground control is limited to nunataks and along the strandflats. Automatically generated DEMs from ASTER and SPOT5-HRS are used in combination with ICESat and an aero-photogrammetrically derived DEM.

3 Data

3.1 Stereoscopic DEMs

Stereoscopic DEMs are generated using photogrammetric techniques from either ground-, air- or space- borne platforms. Measuring surface heights through photogrammetry relies on the principle of *parallax* which is "the apparent shift in the position of an object due to a shift in the position of the observer" (Mikhail et al., 2001). A parallax measurement gives the difference between the projected stereo rays of the same object onto the Earths ellipsoid and can be converted to height if the two observer positions and the focal length of the camera are known (Lillesand et al., 2004). The Base-To-Height (B/H) ratio is an apriori estimate of parallax precision based upon the stereo geometry (Toutin, 2008).

Air-borne stereo geometry is typically defined by overlapping vertical frame photography acquired under airplanes. Space-borne stereo geometry is constructed using either cross-track or along-track stereo constellations. The latter constellations consist of nadir and backward looking sensors (e.g. ASTER), forward and backward looking sensors (e.g. SPOT-5 HRS), forward, nadir and backward looking sensors (e.g. ALOS

PRISM), or sensors that can be freely rotated to any stereo geometry (e.g. Ikonos, WoldView, Pleiades). Satellite stereoscopy is slightly more complicated than traditional photogrammetry as it uses pushbroom instead of frame sensors and must solve for additional unknown parameters related to the Earth's rotation and curvature (Toutin, 2004; Kääb, 2005). Exterior image orientation can be computed from ground control points (GCP) and a satellite orbital model (Toutin, 2004) that is implemented in commonly available software like PCI Geomatica®. Automated approaches are becoming more common for deriving the relative and/or absolute orientation of stereo images using direct measurements of the satellite's attitude and position (i.e. pointing information, auxiliary and ancillary data) (for more details, see Schenk, 1999). The latter is the approach for both satellite stereo DEMs used in the this study: the ASTER DEMs produced by LPDAAC using the SilcAst software (product AST14) (Fujisada et al., 2005) and the SPOT5-HRS DEMs (Bouillon et al., 2006; Korona et al., 2009), as for instance available through the IPY SPOT SPIRIT program.

The stereoscopic ASTER instrument, in orbit since 1999 aboard the Terra platform, contains a nadir and backward VNIR sensor (0.76–0.86 µm) separated by ≈ 30° corresponding to a B/H ratio of 0.6 (ERSDAC, 2005; Toutin, 2008). The ground swath is 60 km while the image and DEM ground resolution is 15 and 30 m, respectively. The HRS instrument, aboard the SPOT5 satellite since 2002, contains forward and backward panchromatic sensors (0.48–0.7 µm), both 20° from nadir providing a B/H ratio of 0.8 (Berthier and Toutin, 2008). The 120 km ground swath is twice as large as ASTER, with a ground pixel resolution of 10 m across track and 5 m along track, and a final DEM resolution of 40 m (Korona et al., 2009).

Errors associated with stereoscopic DEMs are related to the errors in the orientations of the stereo-scenes, either from GCP-based solutions or direct on-board determination, and to the ability of the matching algorithms to locate the corresponding points on two or more images. Errors in the parallax determination are both due to imperfect matching procedures and due to the imperfect image quality such as from lack of optical contrast, cloud cover, shadows, topographic distortions, etc. Errors related to the

parallax matching often result in blunders rather than bias, whereas errors related to the image orientation will typically induce bias. ASTER DEM accuracy is reported to be typically within 15–60 m RMSE in the vertical depending upon terrain type (Toutin, 2002, 2008; Kääb et al., 2002; Hirano et al., 2003; Kääb, 2005; Fujisada et al., 2005) and between 15 and 50 m horizontally (Fujisada et al., 2005; Iwasaki and Fujisada, 2005). SPOT5 accuracy is reported to be between 10–25 m vertically (Berthier and Toutin, 2008; Korona et al., 2009) and greater than 15 m in the horizontal (Bouillon et al., 2006; Berthier and Toutin, 2008). In relationship to pushbroom sensors (e.g. ASTER and SPOT5 HRS), it has been shown that variation in the satellites attitude induces biases within the raw images acquired as well as final DEMs produced (Leprince et al., 2007; Berthier et al., 2007).

3.2 Interferometric DEMs

The Shuttle Radar Topography Mission (SRTM), launched in February 2002, mapped the Earth from 60° N to 56° S using single-pass synthetic aperture radar (SAR) interferometry (Farr et al., 2007). SAR interferometry uses the phase differences between two radar images acquired using a small base-to-height ratio. These phase differences are the photogrammetric equivalent to a "parallax" measurement allowing retrieval of topography (Rosen et al., 2000). We use the SRTM3, V2 without void filling (NASA et al., 2002). Many glacier elevation change studies have used this as a base dataset to compare to both newer and older data products (Rignot et al., 2003; Berthier et al., 2004; Larsen et al., 2007; Schiefer et al., 2007; Paul and Haeberli, 2008). Typically reported vertical accuracies of the dataset are ≈ ±10 m which is lower than the mission standards of ±16 m (Rodriguez et al., 2006). However, vertical biases are present due to instability of the sensor and/or platform (Rabus et al., 2003), and elevation-dependent biases have also been shown due to penetration of the C-band Radar waves into snow/ice (Rignot et al., 2001; Berthier et al., 2004, 2006).

3.3 Lidar profiles

In 2003, the NASA Ice, Cloud, and land Elevation Satellite (ICESat) was launched with the Geoscience Laser Altimeter System (GLAS) acquiring elevation measurements in a 40–70 m elliptical footprint every 170 m (Zwally et al., 2002). The rapid failure of the first laser invoked a curtailed orbital acquisition program. Nonetheless, the GLAS lasers operated for the following 5 years before the last laser failed in November 2009. The altimeter has proven to be accurate to within ±15 cm over flat deserts (Fricker et al., 2005), and intersection accuracies over low sloped glaciers on the order of ±1 m (Brenner et al., 2007; Moholdt et al., 2010a), although variations between the GLA06 and GLA14 products may vary up to ±3 m. ICESat products are freely available from NSIDC (www.nsidc.org), and are the third global elevation product publicly available and tested in this study. ICESat has been extremely successful for glacier applications in terms of elevation changes (Howat et al., 2008; Pritchard et al., 2009; Moholdt et al., 2010b) but also for determining the accuracy of newer satellite products (Korona et al., 2009) and older topographic maps (Nuth et al., 2010). ICESat release 531 is used for this study; the GLA14 products (Zwally et al., 2010b) are used for analysis of stable terrain whereas analysis of ice is using the GLA06 product (Zwally et al., 2010a). Mean elevation differences between these products have been previously found to be less than 15 cm (Kääb, 2008).

3.4 Post-processing

All global elevation data sets used here are the result of the combination and post-processing of individual original data tiles, in particular SRTM (Rabus et al., 2003) and ASTER GDEM (METI/NASA/USGS, 2009). Among others, these procedures include vertical merging of overlapping elevations and horizontal mosaicking. These steps make the original sensor geometry inaccessible and thus prevent the physical modelling of errors and error propagation. Similar problems arise also for other elevation data sets such as from airborne laser scanning or aerophotogrammetry, but usually

at much lower levels if proper strip overlaps/adjustments and aerotriangulation procedures are applied.

4 Methods

To minimize the significance level an elevation change requires for detection, we seek to analyze elevation differences on terrain assumed to be stable (e.g. not on a glacier) for 3 potential biases

1. the geo-location of the data (x, y, and z matrices),
2. an elevation dependent bias, and
3. biases related to the acquisition geometry of the data.

Some previous studies have searched for elevation biases and derived adjustments based upon multiple linear regressions between elevation differences with the terrain parameters (Gorokhovich and Voustianiouk, 2006; Racoviteanu et al., 2007; Peduzzi et al., 2010). Other studies have co-registered the DEM pairs, or derived products such as orthoimages, using image matching techniques, or 2-dimensional least squares regression (Berthier et al., 2007; Howat et al., 2008; Berthier and Toutin, 2008), or by providing a full co-registration solution of the translation, rotation and scale matrices (Gruen and Akca, 2005; Miller et al., 2009). Here, we choose to analyze each bias individually and present solutions for each of these iteratively, rather than combining all into one full regression or co-registration adjustment. The reason for that is to be able to follow and understand individual error terms, and to decide individually on their correction. Furthermore, it will become clear why a multiple regression based upon some combination of these terrain parameters will be significant, though such a correction may not be geometrically appropriate (e.g., see Peduzzi et al., 2010).

Elevation differences are here calculated by re-sampling the spatial resolution of one of the DEMs to the other, or in cases involving ICESat, interpolating the DEM at the

estimated centroid of the ICESat footprint. Bi-linear interpolation is used in both cases. Determining which DEM should be re-sampled to the other is subjective and will vary for each study. However, this decision should be well considered as differences in the corrections may occur depending upon whether one samples to the larger pixel size or vice versa (Paul, 2008). It could be worthwhile to check corrections by re-sampling in each direction to determine such influences. In the case studies presented here, the oldest DEM is generally re-sampled to the newest DEM unless otherwise stated. We use the population of assumed stable terrain elevation differences to analyze the quality of the comparison. Glacier and water pixels/points are removed using land and glacier polygon masks. In New Zealand, the glacier masks are derived from ASTER imagery (Gjermundsen, 2007) while the ocean and lake boundaries were downloaded freely from GADM database of Global Administrative Areas (http://www.gadm.org) (GADM, 2010). In Svalbard, the glacier masks are a part of the new digital Svalbard glacier atlas which is soon to be released by the Norwegian Polar Institute. The ocean is masked using data from the Norwegian Polar Institute mapping department.

4.1 A *universal* co-registration correction

Two DEMs of the same terrain surface that are not perfectly aligned experience a characteristic relationship between elevation differences and the direction of the terrain (aspect) that is precisely related to the x-y-shift vector between them. The relationship between elevation error and aspect has been described previously (Schiefer et al., 2007; Gorokhovich and Voustianiouk, 2006; Peduzzi et al., 2010), although corrections applied in the latter two studies were not analytical but based upon multiple regression adjustments to elevation. Gorokhovich and Voustianiouk (2006) showed the significance of the relationship between elevation differences and aspects on large slopes but overlooked the underlying cause as described in Kääb (2005).

The simplicity of this relationship and detection of unaligned DEMs lies in the similarity of elevation differences with the hillshade of the terrain (Fig. 1), a function that is based upon terrain slope and aspect. The correction of the mis-alignment requires

a more detailed derivation. Figure 2 shows a schematic drawing and a real example where one DEM is shifted to the second DEM. Resulting elevation differences are larger on steeper slopes due to the relationship of the magnitude of the shift vector ($\boldsymbol{a}$) and the elevation errors to the tangent of the slope of the terrain (α):

$$\tan(\alpha) = \frac{dh}{\boldsymbol{a}} \quad (1)$$

Additionally, elevation differences are positive on eastern slopes and negative on western slopes, exemplifying the relationship of the differences to aspect (Ψ). Because terrain aspect is usually defined circular from the north (azimuth), the direction of the shift can be modeled using a cosine of the difference between terrain aspect and the horizontal directional component of the shift vector. Combining this with the relation described by Eq. (1) derives the full analytical solution by relating the elevation differences to the elevation derivatives slope and aspect (Kääb, 2005):

$$dh = \boldsymbol{a} \cdot \cos(b - \Psi) \cdot \tan(\alpha) + \overline{dh} \quad (2)$$

where dh is the individual elevation difference, b is the direction of the shift vector, α is the terrain slope, Ψ is the terrain aspect and $\overline{dh}$ is the overall elevation bias between the two elevation data sets. Slope and aspect can be calculated by any standard GIS or mathematical software, and different approaches exist depending upon application. In this case, the finite difference method is more appropriate then the D8 method (Wilson and Gallant, 2000). To remove the error dependency on slope due to an x-y shift, we normalize the vertical deviations by dividing by the tangent of slope at that pixel. This produces a very clean sinusoidal relationship between elevation difference and aspect (Fig. 2). The transformation of Eq. (2) after slope normalization is:

$$\frac{dh}{\tan(\alpha)} = a \cdot \cos(b - \Psi) + c \quad (3)$$

where

$$c = \frac{\overline{dh}}{\tan(\overline{\alpha})} \quad (4)$$

Three cosine parameters (a, b and c) are solved using least squares minimization where the amplitude of the cosine (a) is directly the magnitude of the shift vector, b is the direction of the shift vector and c is the mean bias between the DEMs divided by the mean slope tangent of the terrain (see Fig. 2). Because the solution to this actually analytical relationship is solved using the terrain which is not an analytical surface, the first solution may not be the final solution and iteration of the process is required to arrive at an ultimate solution. We choose to stop the iteration after the improvement of the standard deviation is less than 2% or if the magnitude of the solved shift vector is less than 0.5 m.

4.2 Elevation dependent correction

An elevation dependent bias can be commonly found within stereoscopic DEMs derived from optical satellite sensors (Berthier et al., 2004; Kääb, 2008). An elevation dependent bias can for instance result from an uneven spatial distribution of the GCPs in the x-y-z-planes which leads to a poorly resolved stereo orientation that could cause a distortion of the z-scale in the measurement of parallaxes. In these cases, either a linear or polynomial relationship between the elevation differences and elevation have been used to adjust the DEMs; e.g.:

$$dh = \sum_{1}^{n} (\kappa_n Z^n) + \tau \quad (5)$$

where Z is elevation, κ and τ are the regression parameters and n is the order of the polynomial (e.g. 1 for linear). The range of previously applied linear corrections varies from 1 to 40 m per 1000 m (Berthier et al., 2007; Kääb, 2008; Berthier et al., 2010). Figure 3 shows an example between a 2003 and 2002 ASTER DEM (as described in Sect. 5) where a significant elevation dependent bias is apparent, which leads to a correction of $\approx$ 10 m per 1000 m (Table 2).

An elevation dependent bias is also suggested to exist within the SRTM over non-glaciated terrain (Berthier et al., 2006, 2007) and has been corrected for in some

studies (Surazakov and Aizen, 2006; Schiefer et al., 2007), though this bias may also be the result of varying resolutions (see Paul, 2008). The SRTM is also expected to contain some bias due to penetration of the C and X Band radar waves into snow and ice which, has been suggested to be up to 10 m (Rignot et al., 2001). It is difficult to apply corrections for this type of bias since the snow/ice characteristics at the time of SRTM acquisition must be known.

Either way, an elevation dependent bias is extremely significant for estimating glacier volume changes because a glacier and its mass balance varies predominantly with elevation, and thus a bias with elevation either from failure of the z-scale or from radar wave penetration into snow/ice will directly affect the measurement and interpretation of either glacier thinning or thickening. Linear bias with elevation causes either over- or under- estimated elevation changes of a shrinking glacier depending upon whether the bias stems from the newest or oldest topography, respectively (Berthier et al., 2006).

4.3 Along/cross track corrections

While the above co-registration and elevation-dependent bias are in principle universal to all types of elevation data, additional individual error characteristics apply according to the sensor type and method used for DEM generation. Along/Cross track biases are the errors associated with the satellite geometry, and may only be relevant for satellite stereoscopic DEMs. Few studies demonstrate that such along/cross track error exists. Leprince et al. (2007) showed that an along track pattern with a frequency of 11–12 cycles per scene existed within the geo-location of pixels of an ASTER scene, corresponding to the 11–12 tie points where the Terra satellite acquires specific attitude information (ERSDAC, 2007). They relate this bias specifically to the under-sampling of the pitch information. Berthier et al. (2007) find elevation biases of a SPOT5 cross-track stereo DEM of up to 12 m which they can reproduce using the highly sampled attitude measurements, specifically the roll in this example. To analyze these errors, we rotate the coordinate system from X- and Y- to cross (X_{track}) and along (A_{track}) track directions, respectively, using a preliminary along track angle (θ) estimated from the

two corners of available data in the scene:

$$A_{\text{track}} = X\sin(\theta) + Y\cos(\theta) \quad (6)$$

$$X_{\text{track}} = X\cos(\theta) - Y\sin(\theta) \quad (7)$$

Bias adjustments, if required, are fitted to these parameters using higher order polynomials, as described in the following sections. Section 5.3 provides an example of this bias and a correction using polynomials.

Errors related to the acquisition geometry is not restricted to stereo elevation data, but may also be present in interferometric DEMs. Height errors in InSAR generated DEMs generally derive from phase noise, atmospheric distortions and the imaging geometry (Knöpfle et al., 1998). In terms of geometry, the baseline length, along track position and platform height will all induce elevation errors within InSAR generated DEMs (Farr et al., 2007).

4.4 Error propagation

Errors within elevation data, whether a DEM or individual points, are commonly estimated by comparing to independently acquired GCPs, generally of a much higher accuracy than that of the elevation source being tested. The quantification of this error, assuming the GCPs are absolutely correct, typically uses 2 measures of statistical spread of the residuals, the Root Mean Square Error (RMSE) or the standard deviation (σ), assuming Gaussian distribution of the residuals (or perfect randomness). However, if the mean difference of the residuals does not equal zero, then the RMSE is not a proper estimate of the statistical error distribution, and the mean and standard deviation should be reported (Li, 1988; Fisher, 1998). In this study, we do not use GCPs for accuracy determination, but rather create a residual population of the difference between two independent data sources over stable terrain. These residuals represents the *relative* errors between elevation data sets, rather than *absolute*.

Standard principles of error propagation are used for estimating errors between two DEMs (Burrough et al., 1998). For example, if one DEM has a random error, σ_1, and the second DEM, σ_2, then the resulting error of a statistically independent elevation difference point or pixel is defined as:

$$\varepsilon = \sqrt{\sigma_1^2 + \sigma_2^2} \quad (8)$$

However, elevation data, especially DEMs contain a degree of spatial autocorrelation that should be accounted for. The adapted error equation is then:

$$\varepsilon = \sqrt{\sigma_1^2 + \sigma_2^2 + 2\cdot\sigma_1\cdot\sigma_2\cdot r} \quad (9)$$

where r is the correlation between σ_1 and σ_2 (Burrough et al., 1998; Etzelmüller, 2000). Determination of r requires semi-variogram analysis and advanced statistical procedures (Bretherton et al., 1999; Rolstad et al., 2009). When analyzing and quantifying glacier elevation changes, not just the spread of elevation changes is desired but rather the mean of the elevation changes over a particular area, e.g. a glacier or glacier zone. The standard error equation about the mean is defined (Davis, 2002),

$$S_\varepsilon = \frac{\varepsilon}{\sqrt{n}} \quad (10)$$

where n is the number of measurements. Two approaches to apply this equation to autocorrelated datasets are to use ε as defined in Eq. (9) or to use ε as defined in Eq. (8) and define n as the amount of un-correlated measurements. In the latter approach, some studies have assumed an autocorrelation distance of 500 m (Berthier et al., 2010) or 1 km^2 (Nuth et al., 2007; Kääb, 2008).

4.5 Estimating the geodetic balance and its errors

There are two approaches for integrating glacier elevation changes into a volume change. The first is to apply the *grid* method by summation of all the differential DEM

pixels over the glacier multiplied by the pixel resolution (e.g. Etzelmüller, 2000; Kohler et al., 2007; Paul and Haeberli, 2008; Berthier et al., 2010):

$$dV = \sum_{1}^{n} (dh) \times r^2 \tag{11}$$

where dV is the volume change, r the resolution and n is the number of pixels. The second method is to use a *hypsometric* approach where an elevation change by elevation relationship is multiplied by the hypsometric area (A_z) of the glacier basin (e.g. Arendt et al., 2002; Berthier et al., 2004; Kääb, 2008; Nuth et al., 2010):

$$dV = \sum_{1}^{z} \left(\overline{dh_z} \cdot A_z \right) \tag{12}$$

where $\overline{dh}$ can either be the mean or median in elevation bins, or a polynomial model of the elevation changes as a function of elevation. Equation (12) assumes normality of the changes over an elevation bin. Situations in which the glacier has multiple upper basins behaving differently may lead to failure of the assumption. In this study we will define the geodetic balance as the annual average volume change per area. For the *grid* method, this is the average of the glacier elevation change pixels. For the *hypsometric* method, the volume change is divided by the total area. In both approaches, the geometry remains fixed (reference mass balance) which will be slightly more negative than the hydrologic mass balance of a retreating glacier (Elsberg et al., 2001).

We will calculate annual geodetic balances using both approaches and therefore derive error equations for each approach by making adaptations to Eqs. (8) and (10). The error equation for the *grid* method is:

$$\varepsilon_1 = \sqrt{\frac{\sigma_1^2 + \sigma_2^2 + \sigma_g^2}{N_\mathrm{m}}} \tag{13}$$

And that for the *hypsometric* method is:

$$\varepsilon_2 = \sqrt{\sum_{1}^{z} \left[\sqrt{\frac{\sigma_1^2 + \sigma_2^2 + \sigma_\mathrm{g}(z)^2}{N_\mathrm{m}(z)}} \times \frac{A(z)}{A_\mathrm{total}} \right]^2} \tag{14}$$

where σ_g is the standard deviation of glacier elevation changes, A is the area, z are the elevation bins, and N_m is the number of un-correlated measurements. Equation (13) varies from Eq. (10) in that an additional term, σ_g, is added to account for the representativeness of the mean ice elevation change. Equation (14) is different from Eq. (13) in that it includes weights based upon the hypsometric distribution of the glacier. Equation (14) also assumes that the estimation of each elevation bin of a glacier is independent, which may not be the case, especially when local systematic errors are present. Therefore, this error derivation assumes that all systematic biases have been removed from the dataset. In this study, we will assume an auto-correlation length of 1 km. All error estimates in this study are divided by the time between DEMs to convert them into annual estimates.

The conversion between volume and density is ignored in this study because the main focus is on errors within the DEMs. Common practice is to apply Sorge's Law (Bader, 1954) and multiply by the density ratio of ice to water (0.9). Other studies have adapted either a lower density related to the density of firn and the accumulation area ratio (Sapiano et al., 1998; Hagg et al., 2004), or a zonal or elevation dependent conversion (Moholdt et al., 2010b).

5 Case Study 1: New Zealand

5.1 Global data sets

Three publicly available nearly global elevation datasets, the SRTM DEM, ICESat and the ASTER GDEM are compared against each other. All three datasets are

well oriented to each other at the regional scale. The universal correction of ASTER GDEM to ICESat and the SRTM both resulted in a 10 m shift to the Northwest direction. The shift between SRTM and ICEsat was less than a meter. A triangulation of these three shift vectors resulted in error residuals less than 0.3 m in the x and y directions, and ≈ 1.5 m in the z-direction (triangulating residuals is described in more detail in Sects. 5.3 and 6.1). However in this case, the solution for the shifts are completely dependent upon the size of the area chosen for analysis. Both the ASTER GDEM and the SRTM products are compiled of many images and overlaying acquisitions and therefore may contain shifts in varying directions within different areas. Figure 4 shows normalized histograms of the elevation differences between the three data products after co-registration. The standard deviation between the SRTM and ICESat is ≈ 5 m whereas the standard deviation between the ASTER GDEM with SRTM and ICESat is twice that, ≈ 10 m.

5.2 The ASTER GDEM

The statistics presented above about the ASTER GDEM are similar to those from the validation summary (METI/NASA/USGS, 2009) with biases of up to 10 m and RMSE of 5–50 m. However the report states, "that the ASTER GDEM does contain residual anomalies and artifacts that most certainly degrade its overall accuracy, represent barriers to effective utilization of the GDEM for certain applications, and give the product a distinctly blemished appearance in certain renditions" (METI/NASA/USGS, 2009). The sources for the artifacts are residual cloud blemishes and the algorithm used to compile and generate the final DEM, the latter which is of most significance. Nonetheless, METI/NASA released this product publicly as an *experimental/research* grade product in hopes to derive a better Global DEM in the future.

Analysis of the spatial distribution of the elevation differences between SRTM and the GDEM reveal large-scale linear features (Fig. 5) which are highly related to the number of images used in the GDEM for a specific location (METI/NASA/USGS, 2009). Consistent bias persists over distances of 10–20 km with multiple slightly sinusoidal patterns

of amplitudes of up to 10–20 m. The implications of these large-scale linear features present within the GDEM infer that bias of individual ASTER scenes is incorporated into the GDEM. This bias can be quite significant and we hypothesize that it has roots within the original DEM generation and merging of the ASTER scenes. Simple inspection of the false hillshade (as shown in Fig. 1) of the elevation differences between the GDEM and SRTM reveal the multiple directional shifts within the product.

In terms of glaciological research, the GDEM may be an appropriate data source for deriving area-altitude distributions of glaciers which can be useful for volume change estimation using ICESat (Moholdt et al., 2010b) or for providing elevation input data required for spatial mass balance modelling. However, the GDEM is not appropriate for change detection because of the numerous artifacts present within the data and the lack of a time stamp for individual pixels. Thus, the next section provides an analysis of ASTER DEMs from individual scenes in order to determine the appropriateness of these data to detect glacier changes.

5.3 Individual ASTER DEMs

This section refers to individual ASTER DEMs as computed by LPDAAC using the SilcAst software and onboard-derived orientation parameters only (no GCPs; ASTER product AST14). Before calculating glacier elevation changes, we compare each possible combination of the data in Table 1 producing 10 differential DEMs. The population is first filtered using a 3σ filter which removes the largest outliers. For each DEM pair, three potential adjustments are applied iteratively using the population of stable terrain difference pixels:

1. Co-register the DEMs using Eq. (3). Practically, we solve for the parameters (*a* & *b*) iteratively until the improvement of the standard deviation is less than 2%. We convert each iteration of the magnitude (*a*) and angle (*b*) of the shift vector into its x- and y- components using trigonometry and sum up the iterations to determing the final adjustment that is applied either on the corner coordinates or the x and y

vectors of one of the DEMs.

2. Search and adjust for any elevation dependent bias. We use a robust regression of the elevation differences with elevation to solve Eq. (5) which is then used to correct one of the DEMs.

3. Search for any bias related to the acquisition geometry of the ASTER satellite. Here we search for biases that occur in the along and cross track directions of the satellite overpass. Higher order polynomials (6th to 8th order) are then fit to the elevation differences with along/cross track directions which is used to adjust one of the DEMs.

Table 2 shows the results for each DEM pair before any adjustments are applied and after each correction is applied iteratively. In total, the three corrections improve the standard deviation of stable terrain from 8–69%. The most significant improvement is obtained through co-registration of the DEM pair. Each individual ASTER DEM has a unique linear x-, y- and z-bias to the SRTM, independent of any other scenes. The direction of the shift is not uniform for all scenes which has important repercussions on the quality of the algorithms used to create the ASTER GDEM.

The most significant elevation dependent bias corrections occur in the 2001 and 2003 scenes where the corrections are as much as 10 m per 1000 m. In these scenes, the ocean covers ≈ 30% making the potential distribution of automatically generated tie points not uniformly distributed in space. Whether this refinement is performed within the DEM generation is not completely known to us, though it may provide an explanation to why these scenes contain large elevation scale distortions. Alternatively, the 2002 and 2006 scenes do not contain any ocean or significant distortions. However, an elevation dependent bias may be confounded with biases related to the sampling resolution (Paul, 2008). We test this on the 2001 and 2003 scenes by taking the inverse differences, i.e. resampling the ASTER to the 90 m SRTM DEM. We find that the slope of the elevation dependent bias does not change significantly though slightly smaller.

In 9 out of 10 cases, the along/cross track corrections improved the standard deviation of elevation difference residuals. It may be questionable whether this bias is significantly determined or not. For example, the 2001 and 2003 scenes in this study contain ≈ 30% ocean, and thus the spatial distribution of terrain differences are not uniformly distributed in the along and cross track directions. In these scenes, the cross track direction is undersampled where the along track correction is completely sampled, and vice versa, which leads to overcompensation in either end of the along/across track corrections. However, in the following paragraphs we discuss two examples that show that this bias can have important reprecussions on the elevation differences further warrenting a correction.

Figure 6 shows the processing sequence for differencing the 2006 ASTER DEM to the SRTM which we take to be the reference surface. About 20% of the ASTER scene is covered by semi-transparent clouds that result in erroneously high elevations in the DEM. These extremes are effectively removed by 3σ filters on the elevation differences. Figure 6a and b shows the original elevation differences and their relationship with aspect which results in a shift vector of 30 m to the northeast. The elevation-dependent bias is not significant enough to warrent a correction (see Table 2). After shifting (Fig. 6c), a visible pattern remains related to the along/cross track directions (Fig. 6d and e). We fit 8th and 6th order polynomials to the differences in the along/cross track direction, respectively, and adjust first along track before re-calculating the cross track correction. The two adjustments applied to the ASTER DEM (1st – Shifting, 2nd – Along/Cross track) resulted in a 35% and 6% improvement in the standard deviation, respectively, which can be seen in the elevation difference histograms of Fig. 6g. The final RMSE between the ASTER DEM and SRTM is 10.6 m, down from an original RMSE of 18 m.

Another interesting example is the difference between the 2006 and 2002 ASTER SilcAst DEMs. A shift of ≈ 45 m in a NE-SW direction is observed and corrected (Fig. 7a). An elevation dependent bias showed not more than ≈ 1 m per 1000 m which we do not correct for. Slight along/cross track biases are present up to ±5 m that are corrected

using a 6th order polynomial (Fig. 7b and c). The post-correction pattern of elevation difference (Fig. 7d) reveal linear cross track striations that run along track of the flight path of the ASTER scene. These features are similar to the linear features discovered by Leprince et al. (2007) which they relate to *jitter* of the instrument and under-sampling of the sensor attitude information in the along-track direction (specifically, the pitch). In particular, the geometric correction of the ASTER images relies on a lattice of 12 by 11 points along/cross track, respectively, where precise satellite attitude measurements are acquired. A linear interpolation is used for geolocating all pixels in between these lattice points (ERSDAC, 2007). The number of cycles apparent in the mean vertical differences along track (Fig. 6d) is ≈ 10–12 cycles. The vertical amplitude of these variations is ±2 m giving a full range of 4 m. We choose not to correct for this bias as it is below the significant level of our dataset. However, if an extremely *precise* DEM is available (e.g. laser scanning), these higher frequency bias corrections will probably be above the significance level.

This example both shows that along/cross track biases exist within the DEMs, and that corrections can be applied with relatively good confidence. We find that along/cross track bias seems to occur at 2 levels of frequency. A lower frequency pattern with generally 2–3 cycles within an ASTER scene is the most significant with an amplitude of up to 5 m. The higher frequency variability occurs with ≈ 10–12 cycles per scene. The visibility of this higher frequency error confirms the appropriateness of our lower frequency correction. The unrecorded pitch variations which are the hypothesized cause of the higher frequency bias occur independently for each scene acquisition. They are integrated into the DEM creation, most likely during the back-looking pass of the satellite because small variations (*jitter*) in the back-looking pitch cause slight variations in the looking angle directly affecting the vertical component of the parallax estimates. In this case, the unrecorded pitch variations of both stereo-pairs seem to have been in opposite directions and overlayed each other constructively (i.e. added to each other) as otherwise the vertical variations would vanish (i.e. destructive superposition).

For detecting glacier elevation changes, the most important correction is shifting the two DEMs to each other (co-registration). The universal co-registration correction can be solved for each DEM pair and the combination of three correction vectors (from 3 DEMs) can derive residuals, for example;

$$Z_{13} = Z_{12} + Z_{23} \quad (15)$$

where Z_{12} is the correction vector from DEM 1 to 2 etc., but can also be the elevation difference matrices themselves. The residuals reflect the internal accuracy or coherence between the three data sets or correction vectors. All 5 datasets (SRTM + 4 ASTER DEMs) are compared providing 10 residuals (Table 3). The standard deviations for the length of the 3 component residual vectors is ≈ 4 m. The shift solution has an internal horizontal accuracy of at least $^1/_3$ of an ASTER DEM pixel (30 m), though often $^1/_{10}$ of a pixel. The nominal vertical accuracy lies around 1–2 m, though 4–5 m in worst case scenario. Therefore in this example, a glacier must have more than 4 m of change to detect an elevation change and greater than at least 8 m to detect an elevation change that may not be 50% biased. The glacial implications is that the longer the time difference between the two DEMs, the smaller impact the bias has on annual averaged elevation change rates. The approach of residual triangulation of the shift vectors is also an effective way to detect erroneous or less significant shifts. It may also be used with elevation change matrices to determine if a time series is internally consistent after shifting and/or if any less significant along/cross track corrections applied have introduced vertical biases. The mean and standard deviations of the population of triangulated elevation change residuals reflects slightly the residuals of the vertical component and the total length of the shift vectors (ε_Z and ε_{rss}), respectively (Table 3).

An artifact in differential DEMs that involve the SRTM DEM and that we do not correct for is the penetration of radar waves into snow and firn (König et al., 2001). The SRTM DEM used here is derived from C-band radar (center frequency at 5.3 GHz). Rignot et al. (2001) determined that the phase center of the C-band signal return was 1 to 10 m into the surface depending upon the snow conditions (i.e. dry vs. wet) in Greenland and

Alaska. In Svalbard, the volumetric phase center of the C-band varied from ≈ 1 to 5 m along a profile from ablation to firn zones, respectively (Müller et al., 2010). Corrections for depth penetration are hardly used for the SRTM data, and is extremely difficult to correct for as knowledge of the snow conditions at the time of acquisition is required yet hardly available. Nonetheless, one should be aware of this bias, especially when using the SRTM to produce elevation changes over short time scales (as shown later).

5.4 Glacier elevation changes

We analyze four glaciers in the NZ Southern Alps, all located around Mt. Cook: Franz Joseph, Fox, Tasman and Murchison glaciers. They are the four largest glaciers in New Zealand, but vary in their mass balance characteristics, and thus their dynamical response times. The glaciers on the west (Franz Joseph and Fox) have large amounts of accumulation and ablation (Anderson et al., 2006) as compared to the glaciers on the east of the divide due to a large east-west precipitation gradient (Fitzharris et al., 1999) and are generally quite steep, with rather short response times (Oerlemans et al., 2005). The glaciers on the east side of the divide (Tasman and Murchison) have debris covered tongues with less accumulation and ablation (Kirkbride, 1995). This glacier variation between the east/west glaciers allow for an interesting comparison related to the significance an elevation change requires for adequate detection.

The detection of glacier elevation changes is dependent upon both glacier characteristics and data precision. Assuming an accuracy of ±15 m for each ASTER SilcAst DEM (i.e. the standard deviation of terrain differences presented in Sect. 5.3), the error associated with an individual difference pixel is ±21 m (using Eq. 8) for a single year DEM difference and $\pm 3.5\,\mathrm{m\,yr^{-1}}$ for a 6 year difference. Therefore, mainly glacier changes on the tongue are significantly different than zero.

For both east coast glaciers, the here-estimated rate of frontal thinning is ≈ 3–$4\,\mathrm{m\,yr^{-1}}$ between 2000 and 2002 and ≈ 1–$2\,\mathrm{m\,yr^{-1}}$ between 2002 and 2006. The most significant elevation changes measured are within the longest time period, 2000–2006, which show frontal thinning between 1 and $4\,\mathrm{m\,yr^{-1}}$. These rates compare well with

the longer term averages of $\approx -1\,\mathrm{m\,yr^{-1}}$ between 1890–1964/1971 (Skinner, 1964; Hochstein et al., 1995) as well as with a shorter term average frontal thinning between 1987 and 2007 of $\approx 4.5\,\mathrm{m\,yr^{-1}}$ (Quincey and Glasser, 2009). It is apparent in the 2000 to 2006 changes of Fig. 8 that Murchison glacier experiences more negative frontal thinning than the Tasman glacier. However, over these short time periods local bias may produce significant artifacts. We also attempted to calculate single year elevation changes between the ASTER SilcAst DEMs. However, the changes showed no coherent relationship with elevation, but rather looked like random noise. In summary, the small changes of these glaciers east of the divide would thus require a longer time period between DEMs than shown here to derive significant changes above the noise threshold induced by both random and systematic errors.

Figure 9 shows elevation change rates of the glaciers on the west side of the divide. The changes on these glaciers are large enough that detection of elevation changes within a single year is possible. The tongue of Fox glacier showed up to 20 m thickness losses from 2000 to 2001 (Fig. 9), similar to the annual melt measured at the front of Franz Joseph Glacier (Anderson et al., 2006; Purdie et al., 2008). From 2001 to 2002, the tongue experienced vertical increases of 7–10 m, which implies a glacier advance while at the same time the upper glacier basins decreased slightly (≈ 1–5 m). Interestingly, if we did not use the 2001 data, and simply compared 2000 to 2002, we would have measured a comparably stable glacier with thickness losses of up to $5\,\mathrm{m\,yr^{-1}}$. After 2002, the glacier seems to have continued to advance. Front position observations reported in the WGMS Fluctuations of Glaciers (WGMS, 2008) document a retreat from 2000–2001, a stable front from 2001-2002, retreat from 2002–2004 and an advance from 2004–2005. These observations neither agree or disagree with our findings, as thickness increases may or may not reach the front position, at least in cases of partial surges (Sund et al., 2009). It is difficult to conclude without any first-hand confirmation of thickening whether the increases between 2001 and 2002 is due to local biases within the ASTER scenes. Nonetheless, the longer period comparisons (2002–2006 and 2000–2006) show frontal thickening of ≈ 5–$10\,\mathrm{m\,yr^{-1}}$, and are less

susceptible to noise and error as can be seen by the smoother elevation change fields in Fig. 9.

Annual elevation changes measured on Franz Joseph glacier are however plagued by noise and bias. In particular, an artificial mountain at the front of the glacier is apparent in most of the SilcAst DEMs as a result of matching failure. This artifact is removed by 3σ filtering and explains why the front of the glacier is missing on most of the images in Fig. 9. The multi-annual measurements are smoother and less plagued by bias than the annual measurements. From 2000 to 2002, Franz Joseph seems to have thinned by ≈ 5–$10\,\mathrm{m\,yr^{-1}}$, though since 2002, the tongue thickened by about $5\,\mathrm{m\,yr^{-1}}$. These results are consistent with the neighboring Fox glacier which experiences similar elevation changes, even though the WGMS reports frontal retreats of 20 to $90\,\mathrm{m\,yr^{-1}}$ (WGMS, 2008). In conclusion, single year elevation changes were large enough on Fox glacier to permit significant detection of thickness changes, though the single year changes are the most susceptible to local biases that exist within the DEMs. Over multiple years, however, the signal-to-noise ratio between real elevation changes and the transported bias from DEM differencing is increased when computing annually averaged elevation change rates.

To complete this case study, total volume changes and associated geodetic balances are derived by applying both methods for estimating the geodetic balance (Eqs. 11 and 12) and the associated errors (Eqs. 13 and 14) for the four glaciers. Only estimates from 2000–2006 are presented because of the decreased sensitivity to bias, and despite the known penetration bias of the 2000 SRTM data. The DEM pair is co-registered and adjusted for along/cross track biases; elevation dependent bias was not considered significant. All estimates are in ice equivalent. Both Tasman and Murchison glaciers have negative geodetic balances. On Tasman glacier, Eqs. (11) and (12) result in an annually averaged estimate of -0.56 ± 0.16 and $-0.42 \pm 0.22\,\mathrm{m\,yr^{-1}}$, respectively. On Murchison, the geodetic balance estimates are -1.42 ± 0.30 and $-1.10 \pm 0.35\,\mathrm{m\,yr^{-1}}$, respectively. Fox glacier has a slightly less negative balance of -0.35 ± 0.26 and $-0.35 \pm 0.33\,\mathrm{m\,yr^{-1}}$ for Eqs. (11) and (12), respectively. Franz Joseph glacier was

not estimated because of the missing data at the glacier front. The variation between the two methods for volume change and geodetic balance estimates may be the result of outliers and non-normality of the elevation changes on a glacier. The error derivation using Eq. (14) is larger in all cases than that derived from Eq. (13). We believe that the hypsometric error method (Eq. 14) is probably a more reasonable error estimate, disregarding the inclusion of systematic bias.

The sensitivity of total volume change measurements to the bias adjustments is complex because of it's dependence on both whether the bias occurs in the newer or older dataset as well as the direction (positive or negative) and magnitude of the bias in relation to the glacier hypsometry (Berthier et al., 2006). The results are further difficult to analyze because the biases are generally scene (or study) dependent. The alpine glaciers in this study, and in most of the world, contain bottle-neck geometries which means the majority of the glacier area is at higher elevations where elevation changes are typically below or at the significance level depending upon the time period the changes are being calculated. Because we assume that there should be less change at higher elevations, a volume change estimate from DEM differencing of a bottleneck glacier may be highly sensitive to these bias adjustments. Therefore, it is stressed that the error estimates defined here are for situations containing only random errors, and we are not completely sure that all systematic biases have been completely removed. Therefore, such short term geodetic estimates should be considered with precaution. However, the longer the time between DEMs, the less the sensitivity of these types of measurements to scene bias because of the greater signal-to-noise ratio.

6 Case study 2: Svalbard

The archipelago of Svalbard contains $\approx 34\,000\,\mathrm{km^2}$ of glaciers, about 60% of the land area. The availability of stable terrain is limited to nunatak areas between the glaciers and the strandflats around the coastline (Hisdal, 1985). A 2003 ASTER SilcAst DEM is tested against a 2008 SPOT5-HRS DEM from the IPY-SPIRIT Project (Korona et al.,

2009), a 1990 aerophotogrammetric DEM from the Norwegian Polar Institute (description and accuracy of the dataset can be found in Nuth et al., 2007, 2010) and 2003–2008 ICESat data (Table 4). The 1990 dataset is partially incomplete with a missing strip over the center of the ASTER scene. This has little reprecussions besides the along/cross track adjustments described in Sect. 6.2. The landform characteristics within the ASTER scene is ≈ 65% glacier, 10% stable terrain and 25% ocean. The objective of this case-study is to demonstrate the ability of the universal co-registration correction and other bias adjustments in regions where stabile terrain is severly limited, typical of the higher latitude glaciated regions.

6.1 Universal co-registration correction

We begin our 2nd case study by showing an example of the vertical differences before and after adjusting the ASTER SilcAst DEM to the SPOT5-HRS DEM (Fig. 10). Before adjustment, a distinct sinusoidal relationship between the vertical deviations and aspect is rather strong (Fig. 10) resulting in a shift of 75 m to the west-north-west (≈ 2.5 ASTER pixels). The final fit solution was obtained after 3 iterations as opposed to 2 iterations common for all the ASTER DEMs tested in New Zealand. We additionally tested the two DEMs generated from the ASTER scenes acquired directly before and after the acquisition of the scene in Fig. 10. The shift vectors for these were all in the same direction and magnitude (not shown here).

The four datasets (Table 4) allow the derivation of 6 shift vectors (Table 5). The aerophotogrammetric DEM and ICESat (**DI**) resulted in the smallest shift vector (≈ 3 m) and an RMSE (3.6 m) of stable terrain after two iterations. We expect the aerophotogrammetric DEM to be of the highest quality and accuracy, thus the impressive coherence with ICESat further confirms previously published ICESat horizontal and vertical accuracies (Fricker et al., 2005; Luthcke et al., 2005; Magruder et al., 2005; Brenner et al., 2007). For the other 5 comparisons, the SPOT5-HRS DEM compared better than the ASTER, with a shift vector solution, **SD** and **SI**, of ≈ 20 m ($\frac{1}{2}$ pixel) and an RMSE of 8 and 5 m, respectively. All 3 shifts for the ASTER SilcAst (**AD**, **AS**, **AI**)

resulted in vector magnitudes of 80–100 m, or ≈ 2–3 times the pixel size. The vertical RMSE for the ASTER DEMs is within the reported range, about 15–20 m for the three comparisons.

The shift vector magnitudes for ASTER (2–3 pixels) is much larger than that of SPOT ($\frac{1}{2}$ pixel) in reference to ICESat and the aerophotogrammetric DEM, which reflects the more accurate satellite positioning and sensor pointing information of the SPOT5-HRS sensor as compared to ASTER. The elevation difference RMSE of the ASTER SilcAst products are double (≈ 20 m) those from the SPOT comparison to the aerophotogrammetric DEM or ICESat. This mainly reflects the different spatial image resolution, but presumably also the different stereo configuration (forward-backward) of the SPOT5-HRS sensor with a base-to-height ratio of 0.8 that provides a more precise parallax measurement than the nadir-backward configuration of ASTER (base-to-height ratio of 0.6). The results in Table 5 suggest also that the cross-track positioning is less accurate than the along-track positioning.

Despite the spatial limitation of ICESat to ascending and descending tracks, it may still be used as a reference for any relative DEM, given a large enough distribution of points over stable nunataks. Schenk et al. (2005) showed the feasibility of using ICESat as ground control for historical vertical imagery and complimentary aerophotogrammetric DEMs by selecting visible nunatak areas and minimizing the vertical deviations of these areas though a 2-dimensional regression. Figure 11 shows the first iteration for the comparison of ASTER to the aerophotogrammetric DEM (**AD**) and to ICESat (**AI**). The sinusoidal relationship in both graphs are similar, though the variation in the relationship between **AI** is much larger due to the smaller sample size (less than 600 pts) of available stable terrain ICESat footprints (Table 5).

The internal consistency of the universal co-registration correction is tested by triangulating the shift vectors presented in Table 5. From the 4 elevation products and 6 shift vectors available between them, four error vectors can be calculated (Table 6). The lowest errors occur between the combinations SDI and ASD with horizontal positioning errors of less than 5 m whereas larger errors of ≈ 10 m occurs in the combinations

ADI and AIS (Table 6). This difference is mainly caused by one poorly defined shift vector, **AI**. Figure 11 shows that the ASTER to ICESat comparison is noisier due to a smaller sample size (≈ 600) and spatial distribution of stable terrain elevation points. The solution to Eq. (3) is weaker than other solutions involving ICESat; for example, **SI** contain more than 6000 stable terrain elevation differences and the distribution of these differences with aspect are a lot more uniform than that of **AI** (Fig. 11b). Nonetheless, despite the limited number of points, the correction to ICESat was still as precise as $^1/_3$ an ASTER pixel (Table 6).

6.2 Glacier elevation changes

Svalbard glaciers, as opposed to New Zealand glaciers have much lower rates of ablation and accumulation. The elevation change rates of the previous decades are typically between −3 and +1 m yr^{-1} (Nuth et al., 2010; Moholdt et al., 2010b). Thus along track and cross track biases of up to 10 m as found in New Zealand will have a significant impact on any differences derived from less than 10 years. Other patterns of bias seem apparent within Fig. 10. To analyze these, we use ICESat acquisitions from the same year as the DEM acquisitions. One repeat track from 10 October 2003 and 3 March 2008 was available that is similar to the along track direction of the ASTER satellite overpass and contain a minimal cross-track separation (less than 15 m). The comparisons between the ASTER and SPOT5-HRS DEMs with the ICESat profiles is shown in Fig. 12. Despite the extreme limitation of stable terrain throughout the ASTER scene, we detect an along track bias of up to ±10 m between the ASTER and SPOT5 DEMs shown in Fig. 12a. The differences between the ASTER and the 2003 ICESat track (Fig. 12d) is similar to the along track bias. No along track biases are seen between the ICESat track and the SPOT5 DEM. The slightly negative mean difference is probably a summer melt signal, especially significant in the first 5 km of the profile which ascend the front of Storbreen glacier with an apparent 5 month loss of ≈ 2–2.5 m (Fig. 12d). After correction, the 2008–2003 differences between the DEMs is similar to the ICESat to ICESat repeat track differences. This example proves the significance

and feasibility of such corrections to the ASTER DEMs, even for situations when only a limited dataset of stable terrain (less than 10% of the scene) distributed unevenly over the scene is available.

Corrections of the along/cross track biases seem to remove most of the spatially visible trends between the ASTER and SPOT (Fig. 13). We use the same along/cross track corrections to difference the 2003 ASTER DEM with the 1990 aerophotogrammetric DEM because the missing strip in the 1990 data may weaken the significance of along/cross track biases. The mean bias between the adjusted 2003 ASTER DEM and the 1990 DEM (−0.7 m) is therefore corrected. We denote a number of significant anomalies and glacier trends within Fig. 13. First, large bias anomalies are present towards the edges of the scene [**A** and **B**] as well as blunders from low cloud anomalies [**C**] that infect the entire southwestern coast of the image. Given the lack of a correlation and/or cloud mask for the automatically generated ASTER DEMs, these blunders remain difficult to remove, and must be masked manually.

In terms of glacier changes, it is clearly visible that the 1990–2003 changes are smoother and less plagued by random noise and bias as in the 2003–2008 differences (Fig. 13). This is purely the effect of time difference between the DEMs. Other glacier anomalies apparently include the surges of Zawadskibreen [**Z**], Dobrowlskibreen [**Db**] and Perseibreen [**P**]. Zawadskibreen shows large losses of ≈ 30 m in the southeastern cirque with slight increases of +10 m along the central flow-line at 400 m a.s.l. The initiation of this surge could have been anytime between 1990 and 2003, though first visible signs appeared in the 2003 ASTER (Sund et al., 2009). After 2003, the progression of the surge is clearly visible where about 10–20 m losses are seen above 400 m a.s.l. and about 50–60 m increases towards the surge bulge at 200 m a.s.l. The surge of Dobrowlskibreen is clearest in the 1990–2003 differences with increases at the confluence with Nathorstbreen [**N**]. The 2003–2008 differences however show continued losses at the higher elevations, with little to no thinning at the lower elevations. The bulk of the surge of Perseibreen occurred during 2000–2001 with 3 month summer average speed of ≈ 3 m d^{-1} (Dowdeswell and Benham, 2003). The large geometric

change of the glacier is clearly seen between 1990–2003, despite the missing 1990 data in the upper cirque regions. Since 2003, the glacier continued to thin at higher altitudes with losses of up to 50 m in the western cirque. Slight increases occurred in the middle of the glacier while the front experienced slight thinning. These results imply that this surge was long-lived, possibly with multiple events, over the course of 5–10 years following the initial event in 2001. Both Doktorbreen [**Dk**] and Liestølbreen [**L**] show similar thinning between 1990 and 2003 though between 2003 to 2008 thinning increased on Doktorbreen and decreased on Listølbreen. Additionally, a region of increases around 350 m a.s.l. on Doktorbreen resemble a dynamic mass movement event. This may or may not be a precursor to a full-blown surge (Sund et al., 2009)

Full glacier volume and mass changes for both periods are not computed here for a variety of reasons. First, the time between DEMs is relatively short for the expected rates of change on the archipelago, such that volume change estimates may be quite susceptible to the various biases within the satellite DEMs. Additionally, there is a lack of data in the 1990 images (missing strip) and in the majority of the upper glacier zones within both the ASTER and SPOT5 DEMs. Recent volume and mass change numbers for this region are given in Nuth et al. (2010); Moholdt et al. (2010b).

7 Conclusions and perspectives

The aims of this study were to detect, analyze and statistically correct the various errors and biases that exist within publicly available elevation products. We present a simple and robust co-registration method for DEM pairs using the elevation difference residuals and the elevation derivatives of slope and aspect. This method is advantageous because it only requires 2–3 iterations as opposed to the method of RMSE minimization by iteratively shifting that requires often more than 20 iterations. The method represents the complete analytical solution of a 3-dimensional shift vector between two DEMs. The solution to Eq. (3) returns statistically significant results for situations when full continuous surface residuals are available but also when stable terrain is limited

to less than 10% of the scene and in comparisons between a DEM and the spatially limited ICESat elevation tracks. By triangulating the co-registration residuals between three elevation data sets, we estimate an internal precision of at least $^1/_3$ but up to $^1/_{10}$ of an ASTER or SPOT5 pixel in the horizontal and between 1–4 m vertically. The co-registration accuracy decreases with availability of stable terrain. In this study, ≈ 600 difference points between ICESat and ASTER effectively co-registered the data products to at least $^1/_3$ of a pixel. The improvement of the standard deviation of elevation residuals through co-registration amounted 5–70% depending upon the magnitude of the shift vector. We suggest that co-registration be tested and, if necessary, performed whenever elevation differencing is used for estimation of glacier changes. The magnitude of the bias induced by not co-registering is directly related to the direction and magnitude of the shift with the direction and slope of the glacier surface. That implies that for very flat glaciers a correction effect might be small, but also that the correction effect for steeper glaciers might by far exceed the signal intended to detect. Unless there is a perfectly random distribution of (glacier) slopes and aspects within a study area, omitting to correct a significant shift will not only result in an increased RMSE of the elevation differences, but induce a systematic vertical bias.

In this study, large elevation dependent biases occurred within the ASTER DEMs that covered less than 70% of the land surface. This may imply that the spatial and elevational distribution of automatically generated tie points affects the tuning of the stereo model within the automated process. It is difficult to determine whether the SRTM has a significant elevation dependent bias; all tests were not as convincing as Fig. 3. An elevation dependent bias caused by penetration of the SRTM C band radar is however much more dangerous. Determination of this type of bias is out of the scope of this paper. More research should certainly be focused on for example, comparing glacier DEMs created at roughly the same time as the SRTM to analyze the magnitude of this bias.

Significant along/cross track biases are specifically found within the ASTER DEMs. These biases are as large as ±10 m which we adjust using 6–8th-order polynomials. A

higher frequency bias has been detected in the automatically generated ASTER DEMs with ≈ 10–12 cycles per scene which may be related to the under-sampled pitch of the backward looking sensor, similar to those found with the nadir looking camera (Leprince et al., 2007). The amplitude of this bias in 2–4 m, which we regard as under the significant limitation of our statistical adjustments. It is important to note, that, since every ASTER SilcAst DEM individually is infected by these high-frequency variations, a differential DEM might contain in the best case a destructive superposition of these variations (i.e. error elimination), or in the worst case a constructive superposition (i.e. error maximization). A prime example is the ASTER GDEM (Fig. 5) where constructive superposition of this variation is apparent in the lower center of the scene (in flat terrain). The longer frequency distortion however is common in all the individual ASTER DEMs we analyze both in New Zealand and in Svalbard. The cause behind this bias is uncertain to us. However, Leprince et al. (2007) who also found *jitter* did not observe the lower frequency bias. In contrast to our data (i.e. LPDAAC), they use their own sensor model involving GCPs.

The detection of glacier elevation changes using the readily available global elevation products tested in this study is dependent upon the time between measurements and the magnitude of glacier changes. In New Zealand, a single year elevation difference from satellite elevation products was clearly detected on Fox glacier. However, the 6 year changes contain the highest significance, are smoother due to reduction of the random noise (increase in the signal to noise ratio), and are less susceptible to the 1–4 m elevation bias uncertainty. This is clearly evident on the Tasman and Murchison glaciers where changes not larger than ≈ 4 m per year are observed. In Svalbard, changes are even smaller than New Zealand except for occasional surges. Single year detection of a surging glacier should be possible using satellite products as long as the bias can be detected and adjusted.

Estimating volume changes and associated geodetic mass balances are also affected significantly by both vertical bias as well as an elevation dependent bias. The effect of these bias on estimations of volume change is dependent upon the magnitude

and sign of the bias in relation to the glacier hypsometry. We suggest that error may be more appropriately estimated using a hypsometric approach that includes systematic bias if known to exist. Increasing the time between DEMs improves annual average geodetic balance estimates significantly by reducing the impact of persistent bias.

As a main conclusion from our study, we suggest a methodological approach (Fig. 14) for whenever DEM (or elevation) comparison is to be performed for glacier research. The first and most important step is to test and, possibly, correct for shifts between DEMs. Our method for that can easily be implemented in free or standard geoinformation systems, table processing softwares, or standard programming environments such as MATLAB or IDL. The only functionalities necessary are: computation of DEM differences, DEM slope and aspect; simple DEM attribute algebra (here $^{dh}/_{\tan(\alpha)}$); curve-fitting including fitting of sines or cosines; and DEM shifting. If no curve fitting functionality is available, the necessary shift parameters can straight-forward be estimated from a scatter plot as shown in Fig. 2. The method can be fully automated. The correction of any further, secondary, biases is dependent on the individual sensor systems and DEM post-processing procedures. However, it should be noted that these biases can easily mimic real glaciological processes such as surges or mass-balance variations with altitude.

We found the ICESat-derived elevations to be the most consistent globally available elevation data set available so far. It could be used as reference to register DEMs to in any regional-scale study. This would lead to a consistent global reference frame for glacier elevation change studies. As a consequence, we recommend for instance, to consider within a new compilation of the ASTER GDEM to reference any individual ASTER DEM to ICESat elevations before merging these individual DEMs to the global data set. A similar procedure, at least for testing, might be appropriate for other ongoing or future global DEM projects such as TanDEM-X or SPOT5-HRS.

Acknowledgements. The authors would like to thank Geir Moholdt for proofing and critically analyzing an earlier version of the manuscript. Jack Kohler, Jon Ove Hagen, and Thomas Vikhamar Schuler for always providing positive feedback and guidance. This study

is the result of the IPY-Glaciodyn project (176076) funded by the Norwegian Research Council (NFR) and is a contribution to the ESA DUE GlobGlacier project and the ESA Climate Change Initiative (Essential Climate Variable CCI ECV "glaciers and ice caps"), which partially funded the work. The ASTER individual DEMs were provided within the framework of the Global Land Ice Measurements from Space project (GLIMS) through the USGS LPDAAC and is courtesy of NASA/GSFC/METI/ERSDAC/JAROS and the US/Japan ASTER science team. ASTER GDEM is a product of METI and NASA downloaded freely from the LPDAAC. The ICESat GLAS data were obtained from the NSIDC, Boulder. The SPOT5-HRS DEM (ID: SPI08-025-Svalbard) was obtained through the IPY-SPIRIT program (Korona et al., 2009) ©CNES 2008 and SPOT Image 2008 all rights reserved. The SRTM DEM was provided by EROS data center at the US Geological Survey. The NPI DEM and masks were provided in collaboration with the Norwegian Polar Institute.

Author Contributions. C.N. developed all algorithms, did all analyses and data interpretations, created the figures, and wrote the paper. A.K. contributed to the concepts, wrote and edited the paper and assisted in interpretations.

References

Anderson, B., Lawson, W., Owens, I., and Goodsell, B.: Past and future mass balance of 'Ka Roimata o Hine Hukatere' Franz Josef Glacier, New Zealand, J. Glaciol., 52, 597–607, http://dx.doi.org/10.3189/172756506781828449, 2006. 2037, 2038

Arendt, A. A., Echelmeyer, K. A., Harrison, W. D., Lingle, C. S., and Valentine, V. B.: Rapid wastage of Alaska glaciers and their contribution to rising sea level, Science, 297, 382–386, http://dx.doi.org/10.1126/science.1072497, 2002. 2029

Bader, H.: Sorge's Law of densification of snow on high polar glaciers, J. Glaciol., 2, 319–323, 1954. 2030

Berthier, E.: Volume loss from Bering Glacier, Alaska, 1972–2003: comment on Muskett and others (2009), J. Glaciol., 56, 558–559, http://dx.doi.org/10.3189/002214310792447716, 2010. 2016

Berthier, E. and Toutin, T.: SPOT5-HRS digital elevation models and the monitoring of glacier elevation changes in North-West Canada and South-East Alaska, Rem. Sens. Environ., 112, 2443–2454, http://dx.doi.org/10.1016/j.rse.2007.11.004, 2008. 2019, 2020, 2022

Berthier, E., Arnaud, Y., Baratoux, D., Vincent, C., and Rémy, F.: Recent rapid thinning of the "Mer de Glace" glacier derived from satellite optical images, Geophys. Res. Lett., 31, L17401, doi:10.1029/2004GL020706, http://dx.doi.org/10.1029/2004GL020706, 2004. 2017, 2020, 2025, 2029

Berthier, E., Arnaud, Y., Vincent, C., and Rémy, F.: Biases of SRTM in high-mountain areas: Implications for the monitoring of glacier volume changes, Geophys. Res. Lett., 33, L08502, http://dx.doi.org/10.1029/2006GL025862, 2006. 2020, 2025, 2026, 2040

Berthier, E., Arnaud, Y., Kumar, R., Ahmad, S., Wagnon, P., and Chevallier, P.: Remote sensing estimates of glacier mass balances in the Himachal Pradesh (Western Himalaya, India), Rem. Sens. Environ., 108, 327–338, http://dx.doi.org/10.1016/j.rse.2006.11.017, 2007. 2016, 2017, 2020, 2022, 2025, 2026

Berthier, E., Schiefer, E., Clarke, G. K. C., Menounos, B., and Remy, F.: Contribution of Alaskan glaciers to sea-level rise derived from satellite imagery, Nature Geosci., 3, 92–95, http://dx.doi.org/10.1038/ngeo737, 2010. 2016, 2017, 2025, 2028, 2029

Bolch, T., Buchroithner, M., Pieczonka, T., and Kunert, A.: Planimetric and volumetric glacier changes in the Khumbu Himal, Nepal, since 1962 using Corona, Landsat TM and ASTER data, J. Glaciol., 54, 592–600, http://dx.doi.org/10.3189/002214308786570782, 2008. 2016

Bouillon, A., Bernard, M., Gigord, P., Orsoni, A., Rudowski, V., and Baudoin, A.: SPOT 5 HRS geometric performances: Using block adjustment as a key issue to improve quality of DEM generation, ISPRS Journal of Photogrammetry and Remote Sensing, 60, 134–146, http://dx.doi.org/10.1016/j.isprsjprs.2006.03.002, 2006. 2019, 2020

Brenner, A. C., DiMarzio, J. R., and Zwally, H. J.: Precision and accuracy of satellite radar and laser altimeter data over the continental ice sheets, Ieee Transactions on Geoscience and Remote Sensing, 45, 321–331, http://dx.doi.org/10.1109/TGRS.2006.887172, 2007. 2021, 2041

Bretherton, C. S., Widmann, M., Dymnikov, V. P., Wallace, J. M., and Blad, I.: The Effective Number of Spatial Degrees of Freedom of a Time-Varying Field, J. Climate, 12, 1990–2009, http://dx.doi.org/10.1175/1520-0442(1999)012⟨1990:TENOSD⟩2.0.CO;2, 1999. 2028

Burrough, P., McDonnell, R., and Burrough, P.: Principles of geographical information systems, Oxford University Press, Oxford, 1998. 2028

Davis, J. C.: Statistics and data analysis in geology, J. Wiley, New York, 2002. 2028

Dowdeswell, J. A. and Benham, T. J.: A surge of Perseibreen, Svalbard, examined using aerial photography and ASTER high resolution satellite imagery, Polar Research, 22, 373–383,

http://dx.doi.org/10.1111/j.1751-8369.2003.tb00118.x, 2003. 2044
Elsberg, D. H., Harrison, W. D., Echelmeyer, K. A., and Krimmel, R. M.: Quantifying the effects of climate and surface change on glacier mass balance, J. Glaciol., 47, 649–658, http://dx.doi.org/10.3189/172756501781831783, 2001. 2029
ERSDAC: ASTER Users Guide Part III. DEM Product (L4A01). (Ver.1.1), Tech. rep., Earth Remote Sensing Data Analysis Center (ERSDAC), http://www.science.aster.ersdac.or.jp/en/documnts/users_guide/index.html, 2005. 2019
ERSDAC: ASTER Users Guide Part II Level 1 Data Products (Ver.5.1), Tech. rep., Earth Remote Sensing Data Analysis Center (ERSDAC), http://www.science.aster.ersdac.or.jp/en/documnts/users_guide/index.html, 2007. 2026, 2035
Etzelmüller, B.: On the Quantification of Surface Changes using Grid-based Digital Elevation Models (DEMs), Transactions in GIS, 4, 129–143, http://dx.doi.org/10.1111/1467-9671.00043, 2000. 2028, 2029
Farr, T. G., Rosen, P. A., Caro, E., Crippen, R., Duren, R., Hensley, S., Kobrick, M., Paller, M., Rodriguez, E., Roth, L., Seal, D., Shaffer, S., Shimada, J., Umland, J., Werner, M., Oskin, M., Burbank, D., and Alsdorf, D.: The Shuttle Radar Topography Mission, Rev. Geophys., 45, RG2004, http://dx.doi.org/10.1029/2005RG000183, 2007. 2015, 2020, 2027
Finsterwalder, R.: Photogrammetry and glacier research with special reference to glacier retreat in the eastern Alps, J. Glaciol., 2, 306–314, 1954. 2016
Fisher, P.: Improved Modeling of Elevation Error with Geostatistics, GeoInformatica, 2, 215–233, http://dx.doi.org/10.1023/A:1009717704255, 1998. 2027
Fitzharris, B., Lawson, W., and Owens, I.: Research on glaciers and snow in New Zealand, Progress In Physical Geography, 23, 469–500, http://dx.doi.org/10.1177/030913339902300402, 1999. 2037
Fricker, H. A., Borsa, A., Minster, B., Carabajal, C., Quinn, K., and Bills, B.: Assessment of ICESat performance at the Salar de Uyuni, Bolivia, Geophys. Res. Lett., 32, 5, http://dx.doi.org/10.1029/2005GL023423, 2005. 2021, 2041
Fujisada, H., Bailey, G., Kelly, G., Hara, S., and Abrams, M.: ASTER DEM performance, Geosci. Rem. Sens., IEEE Transactions, 43, 2707–2714, http://dx.doi.org/10.1109/TGRS.2005.847924, 2005. 2019, 2020
GADM: GADM database of Global Administrative Areas, http://www.gadm.org [Online-Accessed 21.Sept.2010], 2010. 2023
Gjermundsen, E. F.: Recent changes in glacier area in the Central Southern Alps of New

Zealand, Master's thesis, University of Oslo, 2007. 2023
Gorokhovich, Y. and Voustianiouk, A.: Accuracy assessment of the processed SRTM-based elevation data by CGIAR using field data from USA and Thailand and its relation to the terrain characteristics, Remote Sensing of Environment, 104, 409–415, http://dx.doi.org/10.1016/j.rse.2006.05.012, 2006. 2016, 2022, 2023
Gruen, A. and Akca, D.: Least squares 3D surface and curve matching, Isprs Journal of Photogrammetry and Remote Sensing, 59, 151–174, http://dx.doi.org/10.1016/j.isprsjprs.2005.02.006, 2005. 2017, 2022
Hagg, W. J., Braun, L. N., Uvarov, V. N., and Makarevich, K. G.: A comparison of three methods of mass-balance determination in the Tuyuksu glacier region, Tien Shan, Central Asia, J. Glaciol., 50, 505–510, http://dx.doi.org/10.3189/172756504781829783, 2004. 2030
Hirano, A., Welch, R., and Lang, H.: Mapping from ASTER stereo image data: DEM validation and accuracy assessment, Isprs Journal of Photogrammetry and Remote Sensing, 57, 356–370, http://dx.doi.org/10.1016/S0924-2716(02)00164-8, 2003. 2020
Hisdal, V.: Geography of Svalbard, vol. 2, Norwegian Polar Institue, Oslo, 1985. 2040
Hochstein, M. P., Claridge, D., Henrys, S. A., Pyne, A., Nobes, D. C., and Leary, S. F.: Downwasting of the Tasman Glacier, South Island, New-zealand – Changes In the Terminus Region Between 1971 and 1993, New Zealand Journal of Geology and Geophysics, 38, 1–16, http://dx.doi.org/10.1080/00288306.1995.9514635, 1995. 2038
Howat, I. M., Smith, B. E., Joughin, I., and Scambos, T. A.: Rates of southeast Greenland ice volume loss from combined ICESat and ASTER observations, Geophys. Res. Let., 35, L17505, doi:10.1029/2008GL034496, http://dx.doi.org/10.1029/2008GL034496, 2008. 2016, 2021, 2022
Iwasaki, A. and Fujisada, H.: ASTER geometric performance, Geoscience and Remote Sensing, IEEE Transactions on DOI – 10.1109/TGRS.2005.849055, 43, 2700–2706, 10.1109/TGRS.2005.849055, 2005. 2020
Kääb, A.: Remote Sensing of Mountain Glaciers and Permafrost Creep, Geographisches Institut der Universitürich, Zürich, 2005. 2019, 2020, 2023, 2024
Kääb, A.: Glacier Volume Changes Using ASTER Satellite Stereo and ICESat GLAS Laser Altimetry. A Test Study on Edgeya, Eastern Svalbard, IEEE International Geoscience and Remote Sensing, 46, 2823–2830, http://dx.doi.org/10.1109/TGRS.2008.2000627, 2008. 2017, 2021, 2025, 2028, 2029
Kääb, A., Huggel, C., Paul, F., Wessels, R., Raup, B., Kieffer, H., and Kargel, J.: Glacier

monitoring from ASTER imagery: Accuracy and Applications, in: Proceedings of EARSeL-LISSIG-Workshop Observing our Cryosphere from Space, 2002. 2020
Kirkbride, M. P.: Relationships Between Temperature and Ablation On the Tasman Glacier, Mount Cook National-park, New-zealand, New Zealand Journal of Geology and Geophysics, 38, 17–27, http://dx.doi.org/10.1080/00288306.1995.9514636, 1995. 2037
Knöpfle, W., Strunz, G., and Roth, A.: Mosaicking of Digital Elevation Models derived by SAR interferometry, ISPRS Commission IV Symposium on GIS – Between Visions and Applications, 32, 1998. 2027
Kohler, J., James, T. D., Murray, T., Nuth, C., Brandt, O., Barrand, N. E., Aas, H. F., and Luckman, A.: Acceleration in thinning rate on western Svalbard glaciers, Geophysical Research Letters, 34, 5, http://dx.doi.org/10.1029/2007GL030681, 2007. 2029
König, M., Winther, J. G., and Isaksson, E.: Measuring snow and glacier ice properties from satellite, Rev. Geophys., 39, 1–27, http://dx.doi.org/10.1029/1999RG000076, 2001. 2036
Korona, J., Berthier, E., Bernard, M., Rémy, F., and Thouvenot, E.: SPIRIT. SPOT 5 stereoscopic survey of Polar Ice: Reference Images and Topographies during the fourth International Polar Year (2007-2009), Isprs Journal of Photogrammetry and Remote Sensing, 64, 204–212, http://dx.doi.org/10.1016/j.isprsjprs.2008.10.005, 2009. 2019, 2020, 2021, 2040, 2049
Larsen, C. F., Motyka, R. J., Arendt, A. A., Echelmeyer, K. A., and Geissler, P. E.: Glacier changes in southeast Alaska and northwest British Columbia and contribution to sea level rise, J. Geophys. Res.-Earth Surface, 112, F01007, doi:10.1029/2006JF000586, http://dx.doi.org/10.1029/2006JF000586, 2007. 2020
Leprince, S., Ayoub, F., Klingert, Y., and Avouac, J.-P.: Co-Registration of Optically Sensed Images and Correlation (COSI-Corr): an operational methodology for ground deformation measurements, in: Geoscience and Remote Sensing Symposium, 2007, IGARSS 2007, IEEE International, pp. 1943–1946, doi:10.1109/IGARSS.2007.4423207, 2007. 2020, 2026, 2035, 2047
Li, Z. L.: On the Measure of Digital Terrain Model Accuracy, Photogrammetric Record, 12, 873–877, http://dx.doi.org/10.1111/j.1477-9730.1988.tb00636.x, 1988. 2027
Lillesand, T., Kiefer, R., and Chipman, J.: Remote Sensing and Image Interpretation, John Wiley & Sons, Inc., 5 edn., 2004. 2018
Luthcke, S. B., Rowlands, D. D., Williams, T. A., and Sirota, M.: Reduction of ICESat systematic geolocation errors and the impact on ice sheet elevation change detection, Geophys. Res.

Lett., 32(4), L21S05, doi:10.1029/2005GL023689, http://dx.doi.org/10.1029/2005GL023689, 2005. 2041
Magruder, L., Silverberg, E., Webb, C., and Schutz, B.: In situ timing and pointing verification of the ICESat altimeter using a ground-based system, Geophys. Res. Lett., 32(5), L21S04, doi:10.1029/2005GL023504, http://dx.doi.org/10.1029/2005GL023504, 2005. 2041
METI/NASA/USGS: ASTER Global DEM Validation Summary Report, Tech. rep., METI/ERSDAC, NASA/LPDAAC, USGS/EROS, 2009. 2015, 2021, 2031
Mikhail, E., Bethel, J., and McGlone, J. C.: Introduction to Modern Photogrammetry, John Wiley & Sons, Inc., 2001. 2018
Miller, P. E., Kunz, M., Mills, J. P., King, M. A., Murray, T., James, T. D., and Marsh, S. H.: Assessment of Glacier Volume Change Using ASTER-Based Surface Matching of Historical Photography, Ieee Transactions On Geoscience and Remote Sensing, 47, 1971–1979, http://dx.doi.org/10.1109/TGRS.2009.2012702, 2009. 2022
Moholdt, G., Hagen, J. O., Eiken, T., and Schuler, T. V.: Geometric changes and mass balance of the Austfonna ice cap, Svalbard, The Cryosphere, 4, 21–34, doi:10.5194/tc-4-21-2010, 2010a. 2021
Moholdt, G., Nuth, C., Hagen, J. O., and Kohler, J.: Recent elevation changes of Svalbard glaciers derived from ICESat laser altimetry, Rem. Sens. Environ., 114, 2756–2767, http://dx.doi.org/10.1016/j.rse.2010.06.008, 2010b. 2021, 2030, 2032, 2043, 2045
Müller, K., Hamran, S.-E., Sinisalo, A., and Hagen, J.-O.: Microwave backscatter from Arctic firn and its relation to the phase center, Ieee Transactions On Geoscience and Remote Sensing, submitted, 2010. 2037
Muskett, R. R., Lingle, C. S., Sauber, J. M., Post, A. S., Tangborn, W. V., Rabus, B. T., and Echelmeyer, K. A.: Airborne and spaceborne DEM- and laser altimetry-derived surface elevation and volume changes of the Bering Glacier system, Alaska, USA, and Yukon, Canada, 1972–2006, J. Glaciol., 55, 316–326, http://dx.doi.org/10.3189/002214309788608750, 2009. 2016
NASA, NGA, DLR, and ASI: Shuttle Radar Topography Mission (SRTM) Elevation Data Set, http://seamless.usgs.gov, 2002. 2020
Nuth, C., Kohler, J., Aas, H. F., Brandt, O., and Hagen, J. O.: Glacier geometry and elevation changes on Svalbard (1936–90): a baseline dataset, Ann. Glaciol., 46, 106–116, http://dx.doi.org/10.3189/172756407782871440, 2007. 2028, 2041
Nuth, C., Moholdt, G., Kohler, J., Hagen, J. O., and Kääb, A.: Svalbard glacier eleva-

tion changes and contribution to sea level rise, J. Geophys. Res., 115, F01008, http://dx.doi.org/10.1029/2008JF001223, 2010. 2021, 2029, 2041, 2043, 2045

Oerlemans, J., Bassford, R. P., Chapman, W., Dowdeswell, J. A., Glazovsky, A. F., Hagen, J. O., Melvold, K., de Wildt, M. D., and van de Wal, R. S. W.: Estimating the contribution of Arctic glaciers to sea-level change in the next 100 years, Ann. Glaciol., 42, 230–236, http://dx.doi.org/10.3189/172756405781812745, 2005. 2037

Paul, F.: Calculation of glacier elevation changes with SRTM: is there an elevation-dependent bias?, J. Glaciol., 54, 945–946, http://dx.doi.org/10.3189/002214308787779960, 2008. 2017, 2023, 2026, 2033

Paul, F. and Haeberli, W.: Spatial variability of glacier elevation changes in the Swiss Alps obtained from two digital elevation models, Geophys. Res. Lett., 35, L21502, doi:10.1029/2008GL034718, http://dx.doi.org/10.1029/2008GL034718, 2008. 2020, 2029

Peduzzi, P., Herold, C., and Silverio, W.: Assessing high altitude glacier thickness, volume and area changes using field, GIS and remote sensing techniques: the case of Nevado Coropuna (Peru), The Cryosphere, 4, 313–323, doi:10.5194/tc-4-313-2010, 2010. 2016, 2022, 2023

Pritchard, H. D., Arthern, R. J., Vaughan, D. G., and Edwards, L. A.: Extensive dynamic thinning on the margins of the Greenland and Antarctic ice sheets, Nature, 461, 971–975, http://dx.doi.org/10.1038/nature08471, 2009. 2021

Purdie, H. L., Brook, M. S., and Fuller, I. C.: Seasonal variation in ablation and surface velocity on a temperate maritime Glacier: Fox Glacier, New Zealand, Arctic Antarctic and Alpine Research, 40, 140–147, http://dx.doi.org/10.1657/1523-0430(06-032)[PURDIE]2.0.CO;2, 2008. 2038

Quincey, D. J. and Glasser, N. F.: Morphological and ice-dynamical changes on the Tasman Glacier, New Zealand, 1990-2007, Global and Planetary Change, 68, 185–197, http://dx.doi.org/10.1016/j.gloplacha.2009.05.003, 2009. 2038

Rabus, B., Eineder, M., Roth, A., and Bamler, R.: The shuttle radar topography mission – a new class of digital elevation models acquired by spaceborne radar, ISPRS Journal of Photogrammetry and Remote Sensing, 57, 241–262, http://dx.doi.org/10.1016/S0924-2716(02)00124-7, 2003. 2020, 2021

Racoviteanu, A. E., Manley, W. F., Arnaud, Y., and Williams, M. W.: Evaluating digital elevation models for glaciologic applications: An example from Nevado Coropuna, Peruvian Andes, Global and Planetary Change, 59, 110–125, http://dx.doi.org/10.1016/j.gloplacha.2006.11.036, 2007. 2016, 2022

Rignot, E., Echelmeyer, K., and Krabill, W.: Penetration depth of interferometric synthetic-aperture radar signals in snow and ice, Geophys. Res. Lett., 28, 3501–3504, http://dx.doi.org/10.1029/2000GL012484, 2001. 2020, 2026, 2036

Rignot, E., Rivera, A., and Casassa, G.: Contribution of the Patagonia Icefields of South America to sea level rise, Science, 302, 434–437, http://dx.doi.org/10.1126/science.1087393, 2003. 2016, 2020

Rodriguez, E., Morris, C. S., and Belz, J. E.: A global assessment of the SRTM performance, Photogrammetric Engineering and Remote Sensing, 72, 249–260, 2006. 2016, 2020

Rolstad, C., Haug, T., and Denby, B.: Spatially integrated geodetic glacier mass balance and its uncertainty based on geostatistical analysis: application to the western Svartisen ice cap, Norway, J. Glaciol., 55, 666–680, http://dx.doi.org/10.3189/002214309789470950, 2009. 2028

Rosen, P. A., Hensley, S., Joughin, I. R., Li, F. K., Madsen, S. N., Rodriguez, E., and Goldstein, R. M.: Synthetic aperture radar interferometry, Invited paper, Proceedings of the Ieee, 88, 333–382, http://dx.doi.org/10.1109/5.838084, 2000. 2020

Sapiano, J., Harrison, W., and Echelmeyer, K.: Elevation, volume and terminus changes of nine glaciers in North America, J. Glaciol., 44, 119–135, 1998. 2030

Schenk, T.: Digital Photogrammetry, vol. 1, TerraScience, 1999. 2019

Schenk, T., Csatho, B., van der Veen, C. J., Brecher, H., Ahn, Y., and Yoon, T.: Registering imagery to ICESat data for measuring elevation changes on Byrd Glacier, Antarctica, Geophys. Res. Lett., 32(4), L23S05, doi:10.1029/2005GL024328, http://dx.doi.org/10.1029/2005GL024328, 2005. 2042

Schiefer, E., Menounos, B., and Wheate, R.: Recent volume loss of British Columbian glaciers, Canada, Geophys. Res. Lett., 34, L16503, doi:10.1029/2007GL030780, http://dx.doi.org/10.1029/2007GL030780, 2007. 2020, 2023, 2026

Skinner, B.: Measurement of twentieth century ice loss on the Tasman Glacier, New Zealand, New Zealand Journal of Geology and Geophysics, 7, 796–803, 1964. 2038

Sund, M., Eiken, T., Hagen, J. O., and Kääb, A.: Svalbard surge dynamics derived from geometric changes, Ann. Glaciol., 50, doi:10.3189/172756409789624265, http://dx.doi.org/10.3189/172756409789624265, 2009. 2016, 2038, 2044, 2045

Surazakov, A. B. and Aizen, V. B.: Estimating volume change of mountain glaciers using SRTM and map-based topographic data, Ieee Transactions on Geoscience and Remote Sensing, 44, 2991–2995, http://dx.doi.org/10.1109/TGRS.2006.875357, 2006. 2026

Toutin, T.: Three-dimensional topographic mapping with ASTER stereo data in rugged topography, IEEE Transactions on Geoscience and Remote Sensing, 40, 2241–2247, http://dx.doi.org/10.1109/TGRS.2002.802878, 2002. 2020

Toutin, T.: Review article: Geometric processing of remote sensing images: models, algorithms and methods, Int. J. Rem. Sens., 25, 1893–1924, http://dx.doi.org/10.1080/0143116031000101611, 2004. 2019

Toutin, T.: ASTER DEMs for geomatic and geoscientific applications: a review, Int. J. Rem. Sens., 29, 1855–1875, http://dx.doi.org/10.1080/01431160701408477, 2008. 2018, 2019, 2020

WGMS: Fluctuations of Glaciers 20002005, vol. IX, ICSU(FAGS)/IUGG(IACS)/UNEP/UNESCO/WMO, World Glacier Monitoring Service, Zurich, Switzerland., 2008. 2038, 2039

Wilson, J. and Gallant, J.: Terrain Analysis. Principles and Applications, John Wiley & Sons, Inc., 2000. 2024

Zwally, H., Schutz, R., Bentley, C., Bufton, J., Herring, T., Minster, J., Spinhirne, J., and Thomas., R.: GLAS/ICESat L2 Global ElevationData V031, Febuary 2003 to November 2009, 2010a. 2021

Zwally, H., Schutz, R., Bentley, C., Bufton, J., Herring, T., Minster, J., Spinhirne, J., and Thomas., R.: GLAS/ICESat L2 Global Land Surface Altimetry Data V531, Febuary 2003 to November 2009, 2010b. 2021

Zwally, H. J., Schutz, B., Abdalati, W., Abshire, J., Bentley, C., Brenner, A., Bufton, J., Dezio, J., Hancock, D., Harding, D., Herring, T., Minster, B., Quinn, K., Palm, S., Spinhirne, J., and Thomas, R.: ICESat's laser measurements of polar ice, atmosphere, ocean, and land, J. Geodynamics, 34, 405–445, http://dx.doi.org/10.1016/S0264-3707(02)00042-X, 2002. 2015, 2021

Table 1. New Zealand elevation data type, date acquisition, resolution, and scene id.

Data type	Date	Res. (m)	Scene ID
SRTM	11–22 Feb 2000	90	–
ASTER	7 Apr 2001	30	L1A.003:2007486672
ASTER	14 Feb 2002	30	L1A.003:2013763401
ASTER	24 Feb 2003	30	L1A.003:2011883607
ASTER	9 Feb 2006	30	L1A.003:2033045873

Table 2. New Zealand southern Alps. ASTER DEM and SRTM difference statistics on stable terrain (σ) for the original population of elevation differences after adjusting for the mean and for each correction applied, in sequence. The parameter solutions for the corrections are given for both the shifting correction and the elevation bias correction. The improvement of the standard deviation is the total improvement of all three corrections. The units for all parameters are meters except for κ which has the units meters per 1000 m.

Difference	Original	Corr. 1 – Shifting				Corr. 2 – Elevation bias			Corr. 3 – Along/cross track		Improvement
	σ	a	b	$\overline{dh}$	σ	κ	τ	σ	Type	σ	in σ (%)
2000–2001	17.0	12	58	−23	16.3	6.6	−1.3	15.2	Along	13.8	19
2000–2002	12.5	14	215	−3	11.1	0.9	−1.4	11.0	Along/cross	10.3	18
2000–2003	14.5	7	341	2	13.9	10.1	−6.8	12.1	Along	11.3	22
2000–2006	17.8	31	38	4	11.4	3.3	−4.7	11.3	Along/cross	10.6	40
2001–2002	23.9	29	205	24	17.9	−4.3	5.5	17.6	Along/cross	16.4	31
2001–2003	17.3	12	270	26	16.4	5.1	−5.8	16.4	Along	15.9	8
2001–2006	18.5	14	62	30	16.6	−3.1	3.1	16.3	Along	14.7	21
2002–2003	20.4	27	5	1	14.1	10.3	−11.7	12.0	Along/cross	12.0	41
2002–2006	24.9	46	34	7	8.0	1.2	−1.8	8.0	Along	7.7	69
2003–2006	19.4	26	70	5	13.9	−9.0	9.0	12.0	Along/cross	11.1	43

Table 3. The universal shift correction vector residuals and the RSS (Root Sum of Squares) of the total vector mean and standard deviations of the elevation change residuals as solved through triangulation of three DEMs. $\overline{dz}$ and σ_{dz} are the mean and standard deviation of the triple vertical difference in the DEMs. These estimates represent an internal coherency between the three datasets that reflect the residual shift that result from uncertainties in the solution of the universal co-registration correction.

Residual	ε_x	ε_y	ε_z	ε_{rss}	$\overline{dz}$	σ_{dz}
2001-2002-2003	0.3	2.3	−0.4	2.4	−0.3	2.7
2000-2002-2006	2.4	−1.3	−0.4	2.7	−0.4	2.7
2000-2001-2003	−0.1	0.6	0.7	0.9	0.7	2.0
2001-2003-2006	2.0	−0.8	0.7	2.3	0.6	2.6
2002-2003-2006	−2.7	0.3	−1.6	3.1	−1.6	2.8
2001-2002-2006	5.0	1.1	1.9	5.5	1.8	3.9
2000-2001-2006	−10.9	4.0	2.6	11.9	3.1	6.2
2000-2003-2006	−8.7	2.5	2.6	9.5	2.9	5.2
2000-2002-2003	8.5	−3.5	−4.6	10.3	−4.9	4.9
2000-2001-2002	−8.3	6.4	4.9	11.5	5.4	5.5

Table 4. Data sources used in Svalbard for Case Study 2 (Sect. 6), their acquisition date(s) and resolution.

Data Type	Abbr	Date	Res. (m)
Aerophotogrammetric DEM	*D*	≈Jul 1990	20
ICESat Lidar	*I*	2003–2008	70
SPOT-HRS DEM	*S*	1 Sep 2008	40
ASTER SilcAst DEM	*A*	24 Jul 2003	30

Table 5. Shift vectors between the 4 data types in Svalbard as tested in Case Study 2 (Sect. 6.1). ΔX, ΔY and ΔZ are the 3 components of the full co-registration adjustment vector between the datasets in meters and the RMSE is calculated after correction.

Source	Vector	Iterations	Sample size	ΔX	ΔY	ΔZ	RMSE
DEM – ICESat	**DI**	2	4399	1.9	1.3	-1.0	3.6
SPOT – DEM	**SD**	3	1 173 537	−19.0	3.1	2.7	8.5
SPOT – ICESat	**SI**	3	6662	−16.8	6.3	2.5	5.1
ASTER – DEM	**AD**	3	271 784	−93.6	8.8	27.1	16.5
ASTER – SPOT	**AS**	3	289 830	−77.0	5.8	22.9	16.1
ASTER – ICESat	**AI**	2	588	−103.2	14.5	27.0	20.0

Table 6. Error vectors revealed through triangulation. All units are meters.

Abbr	Error Vector equation	ε_x	ε_y	ε_z	ε_{rss}
SDI	**[SD + DI] – SI**	−0.3	−1.9	−0.8	2.1
ASD	**[AD – AS] – SD**	2.4	−0.2	1.4	2.8
ADI	**[AD + DI] – AI**	11.5	−4.4	−1.0	12.4
AIS	**[AI – SI] – AS**	9.8	2.4	1.6	9.85

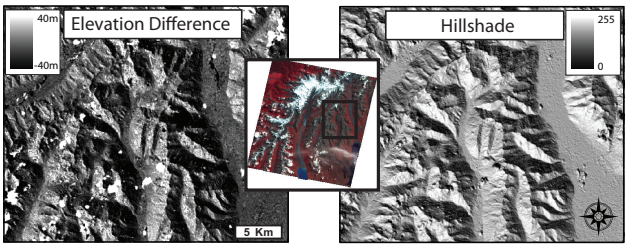

Fig. 1. The elevation differences before shifting (left) between ASTER DEMs in 2006 and 2002 from New Zealand (described in Sect. 5.3 and shown in Fig. 7) are remarkably similar to the hillshade of the DEMs (right). The location of the subsetted region is depicted in the 2006 ASTER image (center).

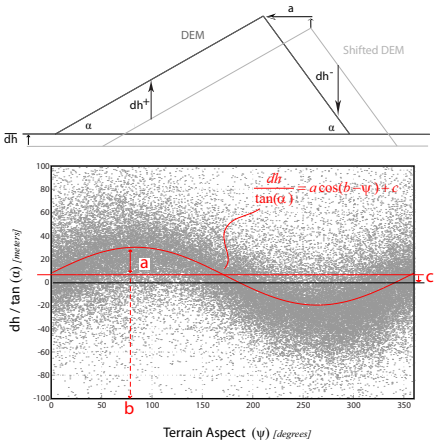

Fig. 2. Top: 2-dimensional scheme of elevation differences induced by a DEM shift. Bottom: The scatter of elevation differences between 2 DEMs showing the relationship between the vertical deviations normalized by the slope tangent (y-axis) and terrain aspect (x-axis). The example is the DEM differences between the 2002 and 2003 DEM used in Case Study 1 (Sect. 5). The equation for the solved sinusoidal curve fit is shown along with the three unknown solution parameters, *a*, *b* and *c*.

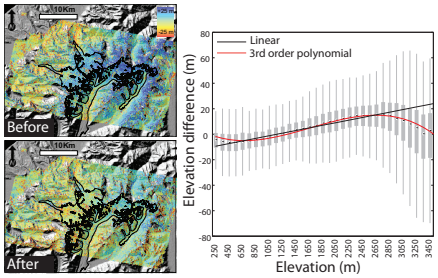

Fig. 3. Example of elevation differences between 2003 and 2002 ASTER DEMs from Case-Study 1 (Sect. 5.3) before and after applying an elevation dependent bias correction using a 3rd order polynomial. The two DEMs were first co-registered before checking for an elevation dependent bias. Glacier masks are indicated by black outlines.

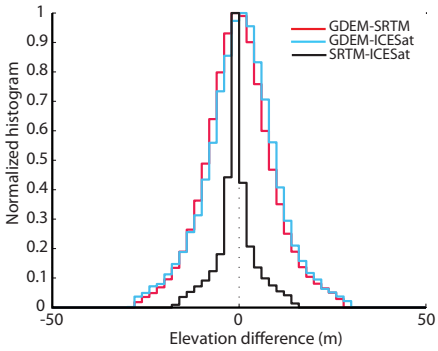

Fig. 4. Histograms of the stable terrain elevation differences after co-registration between the three elevation data global products tested in Case Study 1 (Sect. 5.1): the SRTM, ICESat, and the ASTER GDEM.

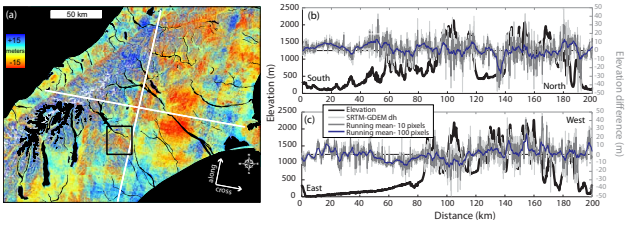

Fig. 5. Vertical differences between SRTM and the ASTER GDEM **(a)**. Elevation changes exemplified for along **(b)** and cross track **(c)** profiles.

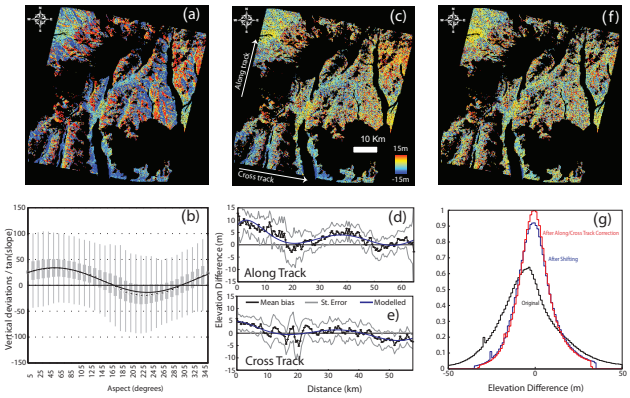

Fig. 6. The processing sequence applied to the 2006 ASTER DEM as compared to the SRTM DEM. **(a)** shows the original elevation differences while **(b)** shows the first iteration relationship to aspect and the cosine-fit solution. **(c)** shows the elevation differences after correcting for the shift and **(d)** and **(e)** shows the residual relationship to the along track and cross track directions, respectively, and the polynomial correction. **(f)** shows the elevation differences after the along and cross track corrections. **(g)** shows the final histograms of the three elevation difference maps of (a), (c) and (e). All glaciers, lakes, ocean and outliers due to clouds are masked out in black.

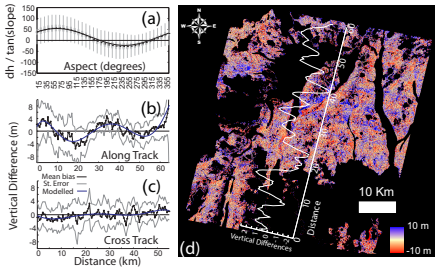

Fig. 7. (a), **(b)** and **(c)** show the first three corrections applied between two ASTER SilcAst DEMs from 2006 and 2002. **(d)** shows the resulting elevation differences with a plot of the mean elevation differences along track. The linear cross-track features that run along track seem to have an amplitude of 1–2 m in the vertical direction. These fluctuations are thought to be induced by unrecorded pitch variations of the satellite, *jitter*.

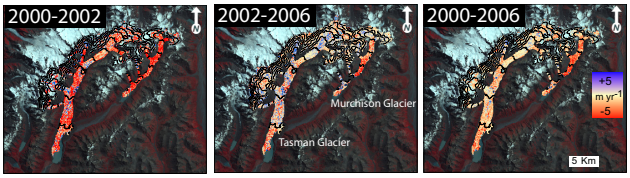

Fig. 8. Elevation changes on the Tasman and Murchison Glaciers from 2000–2002, 2002–2006, 2000–2006. The relative small elevation changes of these glaciers means that the bias induced from both the ASTER scenes and the SRTM will have a large impact on estimates. We therefore do not show elevation change relationships with elevation because it became clear that the high frequency sinusoidal patter of Fig. 7d is superimposed within the change measurements.

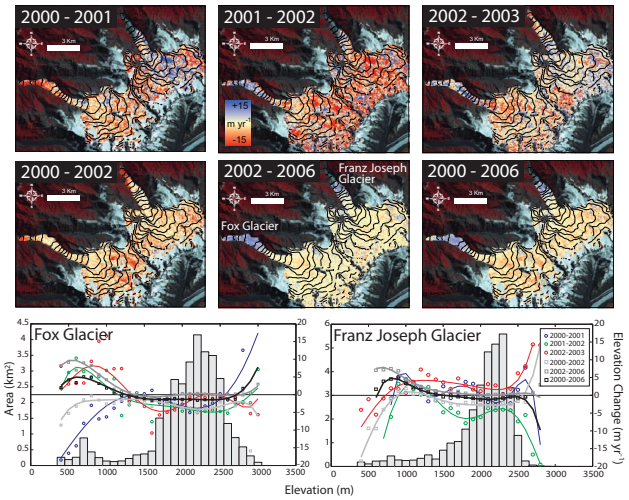

Fig. 9. Elevation changes on the Fox and Franz Joseph Glaciers. The top three images show elevation differences calculated in single years while the middle 3 images are multi-year elevation differences. Clearly apparent is the reduction of noise in the multi-year differences as opposed to the single year differences. Elevation change averages per elevation and associated glacier hypsometry of both glaciers is shown in the lower figures for all the above named differences.

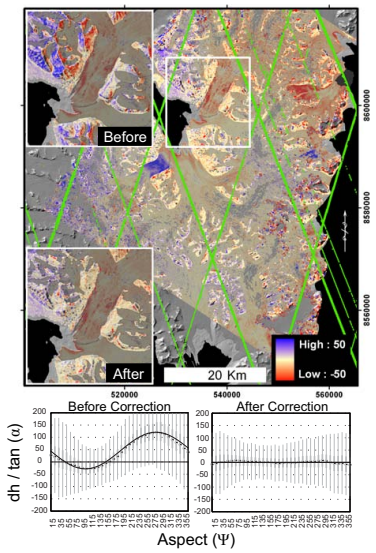

Fig. 10. Top: Elevation differences before and after shifting the ASTER DEM to the SPOT5-HRS DEM. The final shift is ≈ 2.5 ASTER pixels to the west-north-west. The green lines are the ICESat tracks. Bottom: The sinusoidal relationship with aspect before the shift, and the lack of one after shifting.

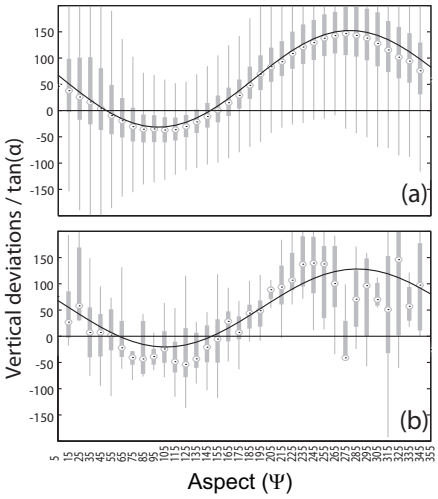

Fig. 11. The first iteration of the co-registration between the ASTER DEM and the aerophotogrammetric DEM **(a)** and the ASTER DEM and ICESat **(b)**.

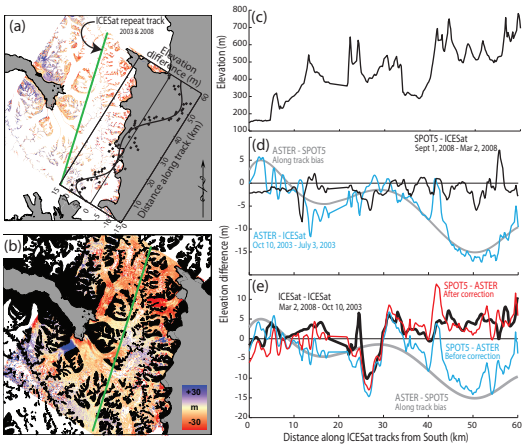

Fig. 12. Elevation differences between the SPOT5-HRS and ASTER DEMs over the non-glaciated regions **(a)** and the glaciated regions **(b)**. The graph inset in (a) shows the along track bias measured from the stable terrain and the 6th order polynomial correction. The green line is an ICESat repeat track from 10 October 2003 and 2 March 2008. The elevation profile from the 2003 ICESat track is shown in **(c)**, The differences between DEMs and the ICESat track closest in time to the DEM acquisition is compared **(d)**. The difference of the ASTER DEM is similar to the bias correction as determined between the two DEMs. The elevation changes between 2008 and 2003 are shown in **(e)** before and after correcting for the along track ASTER bias. ICESat to ICESat differences are made by a simple along track interpolation as the cross track separation was not greater than 15 m, which is well within the footprint size of ICESat.

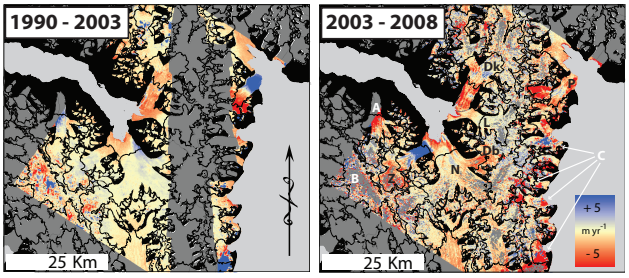

Fig. 13. Elevation changes from 1990–2003 and 2003–2008 after co-registration and adjusting for along/cross track biases. In the 2003–2008 image, we denote data artifacts using white upper case letters in which [**A**] and [**B**] are edge effects and [**C**] are cloud anomalies. Black upper case letters represent individual glacier trends described in the text; [**Z**] Zawadskibreen, [**N**] Nathorstbreen, [**Db**] Dobrowolskibreen, [**L**] Liestølbreen, [**Dk**] Doktorbreen, [**P**] Perseibreen.

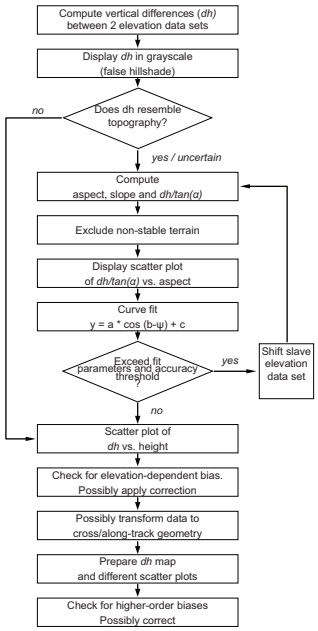

Fig. 14. A suggested methodology for comparing DEMs or elevation products for glacier change detection.

IV

7.4 Article IV:

Nuth C., Schuler T.V., Kohler J., Altena B. and Hagen J.O. (In Prep.). Estimating the long term calving flux of Kronebreen, Svalbard, from geodetic elevation changes and mass balance modelling, ***Journal of Glaciology***

Estimating the long term calving flux of Kronebreen, Svalbard, from geodetic elevation changes and mass balance modelling

Christopher Nuth,[1] Thomas Vikhamar Schuler,[1] Jack Kohler,[2] Bas Altena,[2,3] and Jon Ove Hagen,[1]

[1]*Dept. of Geosciences, University of Oslo, N-0316 Oslo, Norway*
E-mail: christopher.nuth@geo.uio.no
[2]*Norwegian Polar Institute, N-9296 Tromsø, Norway*
[3]*Delft Institute for Earth Observation and Space Systems, Delft University of Technology, 2600 GB Delft,the Netherland*

ABSTRACT. This study independently quantifies geodetic elevation change and models surface mass balance to solve the continuity equation. The approach is tested on two dynamically different glaciers, Kongsvegen and Kronebreen in north-west Svalbard, through two time epochs, 1966-1990/5 (I) and 1990/5-2007 (II). On Kongsvegen, a dynamically inactive glacier, the residual represents an error associated with the method. It is apparent that centerline mass balance estimates are not representative for the entire glacier which we relate to centerline accumulation being larger than the elevation bin average. On Kronebreen, a fast-flowing and actively calving glacier, a significant part of the residual is identified with the long term calving flux. For both glaciers, the cumulative surface mass balance has remained close to zero during the first epoch but has become increasingly negative in the more recent epoch. The long term calving flux of Kronebreen is estimated to be -0.14±0.03 km^3 a^{-1} w. eq. during epoch I and -0.20±0.05 km^3 a^{-1} w. eq. in epoch II. The increase in calving flux corresponds to a decrease in the glacier wide surface mass balance.

INTRODUCTION

Monitoring changes of glaciers, ice-caps and ice sheets is important both in determining the past and present day contribution to sea level fluctuation and to better characterize the present day changes in relation to climatic fluctuations. Area wide glacier mass balance can be defined in terms of the total change in water equivalent volume of a glacier, glacier basin, or glacier region. Defined in this way, the total mass balance has two main components, the surface mass balance (assuming englacial and basal components are negligible) and the calving flux. The surface mass balance can be measured directly using stakes and snow pits on an annual/seasonal basis and can be modelled on a daily basis from meteorological input data. The calving ice loss of marine terminating glaciers, can be determined by multiplying the velocity of ice in the vicinity of the front by the cross sectional area, integrated over time. Continuous velocity variations at the front are difficult to obtain, either because of the high risk for losing GNSS recording instruments, or because remote sensing techniques have not yet been developed to operationally monitor daily, weekly, or monthly velocity averages that can be integrated over a mass balance year. In addition, the cross-sectional area requires the glacier thickness to be known which is not always available. Therefore, the calving flux is difficult to quantify, especially back in time. However, space-borne (Burgess and others, 2005; Kääb and others, 2005), or terrestrial remote sensing (Ahn and Box, 2010) appear to be promising techniques for current and future estimates of velocity.

Estimating the volume change of a glacier through elevation changes is becoming more prevalent with an increasing availability of multi-temporal elevation products. Elevation change is important for determining the contribution of glaciers to sea level change (e.g. Arendt and others, 2002; Abdalati and others, 2004; Zwally and others, 2005; Berthier and others, 2010) and for controlling direct mass balance measurements (e.g. Krimmel, 1999; Elsberg and others, 2001; Zemp and others, 2010). However, interpreting elevation and volume changes is made difficult by the fact that they comprise of both climatic and dynamical components. These components are not independent of each other due to the delayed dynamic response of glaciers to changes in surface mass balance conditions (Jóhannesson and others, 1989).

Comparing geodetic volume changes and the surface mass balance has been commonly limited to land terminating glaciers to control systematic errors that may accumulate in the cumulative estimated mass balance series (Andreassen, 1999; Elsberg and others, 2001; Cox and March, 2004; Thibert and others, 2008). Geodetic volume changes have also been used to constrain mass balance models (Huss and others, 2009). For marine terminating glaciers, the total mass balance includes both the surface mass balance (including basal and englacial balances) and the calving component. Therefore, if the surface mass balance can be properly determined, either through extrapolation of direct point measurements or through modelling, then the residual between geodetic volume change and the surface mass balance represents the calving component, provided no errors.

OBJECTIVES

Previously, the continuity equation has been used to solve for the surface mass balance from remotely sensed elevation changes and horizontal velocities (Gudmundsson and Bauder, 1999; Kääb and Funk, 1999; Kääb, 2000; Hubbard and oth-

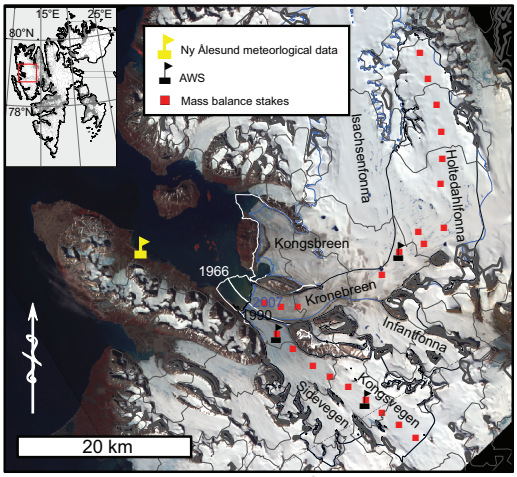

Fig. 1. The location of Kongsvegen and Kronebreen in north-west Svalbard. The location of Ny Ålesund is denoted by the yellow flag at about 15 km from the glacier front. Kongsvegen and Sidevegen are grouped into one system. Kronebreen consists of Holtedahlfonna and Infantfonna that feed the tongue system. To the north of the Kronebreen system lies Kongsbreen/Isachsenfonna. The border between the two systems is sligthly uncertain. Grey lines are 200 m contours.

ers, 2000). The goal of this study is to use mass continuity to compare geodetic elevation change with the surface mass balance of two dynamically different glaciers, one of which is in the quiescent phase of a surge cycle and calving is negligible. The other a persistently fast moving glacier calving into the sea. Mass balance measurements are spatially and temporally limited whereas elevation changes can be measured over the entire glacier through decades. We quantify elevation changes by DEM differencing of three datasets that cover two time epochs over the past 40 years. Direct specific mass balances measurements are collected at only a few points continuously over the past 10-20 years. Therefore, direct mass balance measurements are linked to temperature and precipitation measured since 1969 at a meteorological station in Ny Ålesund using a classical degree day melt model and a multiple linear regression model for precipitation distribution. Similar to Huss and others (2009), we do not consider this approach as a physical reproduction of the mass balance, but rather as a tool for spatial and temporal interpolation/extrapolation, i.e. homogenization of the mass balance time series. Finally, we propose that the difference between the area-integrated elevation change and surface mass balance provides an estimate of the long term calving flux of a marine terminating glacier.

STUDY LOCATION

The two glaciers analyzed in this study, Kongsvegen and Kronebreen, are located in the vicinity of Ny Ålesund in north-west Svalbard (Fig. 1). Kongsvegen is ≈27 km long spanning elevations from 0-800 m.a.s.l. covering a total area of ≈180 km^2. The surface mass balance is measured by the Norwegian Polar Institute (NP) since 1986 using a series of ≈10 stakes along the centerline (Hagen and others, 1999). The glacier is in a quiescent phase since the last surge in 1948 (Melvold and Hagen, 1998) and the elevation changes are approximately equal to the surface mass balance due to negligible glacier flow (Melvold and Hagen, 1998; Hagen and others, 1999, 2005). Therefore, Kongsvegen is an ideal reference case to ensure consistency between the elevation changes and the mass balance model. For our study, we include Sidevegen as a part of Kongsvegen because these two glaciers share the glacier tongue and the valley.

The Kronebreen glacier system is ≈50 km long with an elevation range from 0-1400 m. The ≈390 km^2 area comprises three named ice masses: the fast flowing glacier tongue, Kronebreen; the larger upper catchment, called Holtedahlfonna (previously called Snøfjellfonna by Goto-Azuma and others (1995) and now called Dovrebreen); and the smaller cirque contributory glacier, Infantfonna. The location of the border between neighboring Isakssonfonna is slightly uncertain. The surface mass balance program on Holtedahlfonna began in spring 2003; 10 stakes were installed along the accessible centerline above the crevasse zone (Baumberger, 2007). In 2008, three additional stakes were installed on the lower crevassed area of Kronebreen.

The two glaciers can be considered as dynamically opposite; Kongsvegen averages yearly velocities of ≈2 m a^{-1} at the front with a maximum of 4 m a^{-1} at the equilibrium line (Melvold and Hagen, 1998; Hagen and others, 1999) while Kronebreen exhibits average daily velocities of up to 2-3 m day^{-1} at the front (Kääb and others, 2005). The velocity of Kronebreen is consistent between measurements made in 1964 (Voigt, 1966), in 1986 (Lefauconnier and others, 1994b) and around 2000-2002 (Kääb and others, 2005). It is therefore one of the most persistent fast flowing glaciers in Svalbard.

DATA

Glaciological Data

Surface mass balance measurements (Østrem and Brugman, 1991) are acquired using 6 m stakes drilled into the ice/firn where the length of the exposed stake is measured on an annual/seasonal basis. Additional accumulation measurements are acquired across the glacier by snow depth sounding or radar profiling in April/May. In this study, only measurements at stake locations are used for model calibration because they are consistent through the entire time series. Summer measurements are typically acquired in early September. Due to weather related inaccessibility, not all stakes have been measured at the end of summer every year. Therefore, we use the net change in exposed stake heights between two successive April/May measurements minus the previous winters accumulation to derive the summer balance. Direct specific mass balance data is available from 1987 to 2008 for Kongsvegen and from 2003 to 2010 for Kronebreen. Details of the first years of measurements on each glacier are given by Melvold and Hagen (1998), Hagen and others (1999) and Baumberger (2007). Due to the heavily crevassed glacier tongue of Kronebreen, mass balance measurements were not obtained below 500 m.a.s.l. before 2008. Three stakes in this region have been maintained since 2008, however, potential winter ablation has not been successfully measured due to disappearance of the stakes between autumn and spring.

Meteorological Data

Precipitation and temperature have been measured in Ny Ålesund since 1969 by the Norwegian Meteorological Institute

Table 1. Description of the data used in this study on Kongsvegen (KNG) and Kronebreen (KRB). The measurements include temperature (T), precipitation (P), winter, summer and net specific mass balance ($b_\mathrm{w}, b_\mathrm{s}, b_\mathrm{n}$), sonic sensor depth gauge (S) and elevation (z). On KNG, there are two operational AWS for the period 2007 to 2009. KRB has one AWS operational since 2007, the second since 2009. The data originates from the Norwegian Meteorological Institute (met.no), the Norwegian Polar Institute (NP), the University of Oslo (UiO) and from the SPOT5 satellite (Korona and others, 2009).

Year	Paramater	Type / Origin	Source	Resolution	Glacier
1969 - 2009	T, P	Ny Ålesund Meteorological Station	met.no	Daily	KNG / KRB
1987 - 2008	$b_\mathrm{w}, b_\mathrm{s}, b_\mathrm{n}$	Mass Balance Stake Measurements	NP	Seasonal	KNG
2003 - 2010	$b_\mathrm{w}, b_\mathrm{s}, b_\mathrm{n}$	Mass Balance Stake Measurements	NP / UiO	Seasonal	KRB
2007 - 2009	T, S	Automatic Weather Station (AWS)	NP	Hourly	KNG / KRB
1966	z	DEM + contours	NP	10 m	KNG / KRB
1990	z	Aerial photogrammetric DEM	NP	10 m	KRB
1995	z	Aerial photogrammetric DEM	NP	10 m	KNG
1996	z	GPS profile	UiO	10 sec	KRB
2007	z	Satellite stereoscopic DEM	SPOT5	40 m	KNG / KRB

(met.no). The station in Ny Ålesund was moved in 1974 to about 34 m lower than the original location. Small lapse corrections (0.2^{o}C) have shown to have little significance in correlations with mass balance (Lefauconnier and Hagen, 1990). Synoptic weather observations were carried out (3-4 times daily) until 1994 when an automatic weather station began continuously monitoring at an hourly recording interval (met.no, 2011). The pre-1994 precipitation measurements were collected manually using a rain-gauge whereas after 1994, weight of the collected precipitation in the rain-gauge is measured at an hourly interval (met.no, 2011). We use daily average and maximum temperatures and daily accumulated precipitation to drive the surface mass balance model. In addition, automatic weather stations (AWS) on Kongsvegen and Kronebreen are used to validate distribution of temperature data from Ny Ålesund (Fig. 1).

Elevation Data

The elevation data consist of Digital Elevation Models (DEM) and a GPS profile (Table 1). The 1966 and 1990 DEMs were generated from vertical aerial imagery acquired in summer, made on a digital photogrammetric workstation (Altena, 2008). The data is incomplete in some regions due to low visible contrast, rendering image matching difficult. The 1966 DEM gaps are filled with the 1966 contour data made previously from an analogue photogrammetric workstation using the same images. The 1990 data contains a 10 m resolution though low visible contrast resulted in no data above ≈700 m.a.s.l. on Kronebreen. Therefore, we adjust a 1996 differential GNSS elevation profile measured along the approximate centerline every 10 seconds to represent the missing 1990 elevations. The 1990 DEM only covers the tongue of Kongsvegen, therefore a digitially derived aerophotogrammetric DEM from 1995 vertical images is used. The 2007 DEM is a SPOT5-HRS product (GES07-043-NorthWestSvalbard) obtained through the IPY-SPIRIT project (Korona and others, 2009). The DEM is created from stereo imagery of a forward and backward looking sensor with a base-to-height ratio of 0.8 (Bouillon and others, 2006). In Svalbard, SPOT5-HRS DEMs are reported to have an elevation accuracy of 3 m and a precision of 5 m relative to ICESat (Korona and others, 2009; Nuth and Kääb, 2010).

THEORY

Mass Continuity

Glacier elevation changes, mass balance and flux are related through the equations of mass continuity. A detailed derivation and discussion of glacier mass continuity can be found in Cuffey and Paterson (2010). Here, we simplify the discussion and list the assumptions related to combining elevation changes and the surface mass balance. For any volume element of a given material having density ρ, mass continuity is written:

$$\frac{\partial \rho}{\partial t} + \nabla\left(\rho \vec{u}\right) + \beta = 0 \tag{1}$$

where $\vec{u}$ is a velocity vector and β is a production term. Equation 1 states that any local change in density is balanced by the net flux of material into or out of the considered volume plus any source or sink of mass. Integration from the bed (h_b) to the surface (h_s) provides the continuity equation for a vertical column through a glacier:

$$\frac{\partial}{\partial t}\int_{h_b}^{h_s} \rho \, dz = b - \nabla \vec{q} \tag{2}$$

where

$$b = b_s + b_e + b_b \tag{3}$$

$$\nabla \vec{q} = \int_{h_b}^{h_s} \nabla\left(\rho \, \vec{u}\right) dz \tag{4}$$

The term on the left side of eq. 2 represents the change in mass of the given volume and may be approximated through gravity variations (e.g. Wahr and others, 2004; Luthcke and others, 2008) or elevation changes. On the right, the mass balance (b) is the sum of surface (b_s), englacial (b_e) and basal (b_b) components (eq. 3). Equation 4 defines the horizontal flux divergence ($\nabla \vec{q}$) as the column average velocity multiplied by the density, ρ, which closely approximates the density of ice in cases where firn is a small proportion of the ice thickness (Cuffey and Paterson, 2010).

To relate the mass change (left side of eq. 2) to observed elevation changes ($\frac{\partial h}{\partial t}$), we introduce an effective density (ρ_eff) to express the temporal and vertical changes of the column density:

$$\frac{\partial}{\partial t}\int_{h_b}^{h_s} \rho \, dz \approx \frac{\partial h}{\partial t} \cdot \rho_\mathrm{eff} \tag{5}$$

It is also convenient to continue in water equivalent units because this is the common measuring practice for the glacier

mass balance (b). We now assume that englacial and basal mass balances are negligible ($b_e << b_s$ and $b_b << b_s$) and that the flux divergence ($\nabla\vec{q}$) represents mass change of incompressible ice. The continuity expression can then be reduced to:

$$\frac{\partial h}{\partial t} \cdot \kappa = (b_s + \cdot\nabla\vec{q}) \cdot \rho_w^{-1} \quad (6)$$

where ρ_w is the density of water and κ is a conversion factor from height differences to water equivalent changes:

$$\kappa = \frac{\rho_{\text{eff}}}{\rho_w} \quad (7)$$

If $\frac{\partial h}{\partial t}$ is observed over a significantly long time period, κ can be approximated by the density ratio of ice to water (0.9) below the ELA. This because small changes in the less dense snow have little impact on the column average density and thus all changes will be of incompressible glacier ice. In the firn area, changes in the proportion of firn to the ice column can alter κ due to the compressibility of firn. Often, it is assumed that firn thickness and density are constant through time ("Sorge's Law", Bader, 1954) in which case $\kappa = 0.9$.

Solving mass continuity over the entire glacier system requires integration of eq. 6 over the glacier surface area (A):

$$\int\int_A \frac{\partial h}{\partial t} \cdot \kappa \cdot \; dxdy = \frac{\partial V}{\partial t} = B - \int\int_A \nabla\vec{q}\; dxdy \quad (8)$$

All terms in water equivalent, this relates the volume change ($\frac{\partial V}{\partial t}$) to the flux divergence ($\nabla\vec{q}$) and the glacier-wide mass balance (B). Applying the divergence theorem to the last term in eq. 8 results in the relationship between the glacier-wide integrated flux and the water equivalent flux through a boundary (R):

$$\int\int_A \nabla\vec{q}\; dxdy = \oint_R \left(\vec{q}\,\vec{n}\right) dr \quad (9)$$

and substitution into eq. 8 results in:

$$\frac{\partial V}{\partial t} = B - \oint_R \left(\vec{q}\,\vec{n}\right) dr \quad (10)$$

where $\vec{n}$ is the normal vector to the closed boundary (R). The second term on the right may represent the influx of ice by avalanching or the loss through calving.

Using eq. 10, we consider two solutions: non-calving and calving glaciers. Often for non-calving glaciers, $\oint_R (\vec{q}\,\vec{n})\, dr$ is assumed equal to zero resulting in:

$$\frac{\partial V}{\partial t} = B \quad (11)$$

This has formed the basis of many comparison studies aimed to control systematic errors in the cumulative direct surface mass balance integration by using geodetically measured volume changes (e.g. Krimmel, 1999; Elsberg and others, 2001; Cox and March, 2004; Thibert and others, 2008; Zemp and others, 2010, etc.). For a calving glacier, $\oint_R (\vec{q}\,\vec{n})\, dr$ is equal to the flux (Q) through the boundary (R) of the glacier:

$$\frac{\partial V}{\partial t} = B + Q \quad (12)$$

Practically solving mass continuity of an entire glacier system requires definition of the boundary geometry. For simplicity or due to lack of updated maps, this geometry may be held constant. For example, Elsberg and others (2001) introduce the concepts of a *reference* and *conventional* surface for mass balance integration and suggest a transformation between them. The *reference* surface is a constant map year and considered to be more climatically related as it removes the effects of surface change on the mass balance. The *conventional* mass balance is the actual mass change of the glacier relevant for hydrological and sea-level change studies. Equation 12 can be modified to handle the volume of retreat/advance seperately:

$$\frac{\partial V_{r/a}}{\partial t} = B_{r/a} + Q_{r/a} \quad (13)$$

where

$$Q_{r/a} = Q' - Q \quad (14)$$

Derived in this way, $\frac{\partial V}{\partial t}$ and B of eq. 11 and 12 can be solved using a *reference* surface defined as the smallest glacier area. Q is then the ice flux through the cross sectional area (flux gate) defined by the glacier front at the time of smallest glacier area (i.e. the most recent area in cases of retreat). $\frac{\partial V_{r/a}}{\partial t}$, and $B_{r/a}$ are the volume change and mass balance of the receding (r) or advancing (a) area. $\frac{\partial V_{r/a}}{\partial t}$ is unproblematic to quantify provided knowledge of the basal elevation or depth below sea level in the retreat or advance area. $B_{r/a}$ can be solved by assuming a linear retreat of the front. $Q_{r/a}$ is defined as the retreat/advance flux and is the difference between the net flux into or out of the glacier and the flux out of the gate defined by the front of the smallest area (Q). Hence, $Q_a > 0$ and $Q_r < 0$.

Table 2. Precision and accuracy of the geodetic data sets. The shift vector solutions for the co-registration (dx, dy, & dz) between the elevation products (A=1966; B=1990; C=1995; D=2007) is shown. The standard deviation of stable terrain after co-registration shown represents the stochastic error (precision) associated with an individual elevation change pixel or point. The triangulated residuals in the lower section of the table represent the systematic coherence (accuracy) between the three or four data products. Most important is the residual about the Z-axis which is the systematic vertical bias remaining. All units are in meters.

Vector Notation	dx	dy	dz	σ
$\overrightarrow{AB}$	0.00	0.00	-0.73	8.12
$\overrightarrow{AC}$	0.00	0.00	2.08	5.42
$\overrightarrow{AD}$	27.52	-41.14	-2.40	10.22
$\overrightarrow{BC}$	0.00	0.00	2.50	4.40
$\overrightarrow{BD}$	26.95	-42.50	-3.20	6.33
$\overrightarrow{CD}$	28.76	-41.88	-4.85	7.50
$\overrightarrow{AB} + \overrightarrow{BD} - \overrightarrow{AD}$	-0.56	-1.37	-1.53	-
$\overrightarrow{AC} + \overrightarrow{CD} - \overrightarrow{AD}$	1.24	-0.74	-0.37	-
$\overrightarrow{AB} + \overrightarrow{BC} - \overrightarrow{AC}$	0.00	0.00	-0.31	-
$\overrightarrow{BC} + \overrightarrow{CD} - \overrightarrow{BD}$	1.81	0.63	0.85	-
$\overrightarrow{AB} + \overrightarrow{BC} + \overrightarrow{CD} - \overrightarrow{AD}$	1.24	-0.74	-0.68	-

METHODS

Elevation and volume changes

Elevation changes are calculated for two time epochs using the data listed in Table 1; 1966-1995-2007 for Kongsvegen and 1966-1990-2007 for Kronebreen. The 1966, 1990 and 1995 DEMs are resampled to 40 m (SPOT5-HRS DEM resolution) using a 4x4 window average block filter on the original 10m products. DEM pairs are co-registered using the sinusoidal dependency between the vertical differences over stable terrain with aspect (Nuth and Kääb, 2010). The most distinct

shift between the products occur in the 2007 SPOT5-HRS DEM (≈1.5 pixels) because the 1966 and 1990 data are made using roughly the same ground control points. The triangulation of shift vectors between three DEMs for Kongsvegen and Kronebreen show a horizontal and vertical coherency of less than 2 m (Table 2). This vertical residual represents the accuracy after removal of vertical systematic biases, and becomes noticeable when analyzing the mean glacier elevation change. The stochastic errors (precision) of the datasets are generally better than 10 m (σ in Tab. 2). No elevation dependent biases are detected.

Estimating volume changes from elevation changes can be accomplished using two methods, typically depending on the data available; i.e. center line profiles (Arendt and others, 2002) or full range DEMs (Berthier and others, 2010). The volume change derived from differential DEMs is the summation of the elevation change pixels over the glacier surface multiplied by the pixel area (*grid* method). If only centerline data is available, a *hypsometric* approach can be employed assuming elevation changes across an elevation bin are normally distributed (Berthier and others, 2004). In this method, volume change is derived by summation of the product between elevation change as a function of elevation (average or centerline assumed average) by the glacier hypsometry (area-altitude distribution). Converting volume change to mass change require knowledge of the effective density, typically assuming all changes are of ice ($\kappa = 0.9$).

Surface mass balance (SMB) model

The SMB model is driven at a daily time step using meteorological data from Ny Ålesund. The model is calibrated for each glacier individually using the entire time series of available point mass balances (Table 1) in order to derive model parameters individually for each glacier. This decision is based upon *a prior* knowledge that Kongsvegen receives on average slightly more accumulation at its highest elevation (800 m) in comparison to Kronebreen at 1400 m, and due to the large super-imposed ice zone on Kongsvegen (König and others, 2002; Langley and others, 2007; Brandt and others, 2008), and the possible lack of one on Kronebreen (Baumberger, 2007).

Distributing temperature

Temperature is distributed over the glacier by applying a lapse rate to the (mean and maximum) daily temperatures measured in Ny Ålesund. Lapse rates generally vary depending upon the moisture content of the atmosphere with average values around -0.0066 Km^{-1}, referred to as the environmental lapse rate. Lapse rates are calculated between the Ny Ålesund station and the four Automatic Weather Station (AWS) data that are available for the period 2007-2009. The calculated lapse rates are slightly skewed with an average of $-0.0085\ K\ m^{-1}$ and a standard deviation of 0.004 $K\ m^{-1}$ (Fig. 2). The skewed distribution is a result of the cold drier conditions in winter where lapse rates are closer to -0.01 $K\ m^{-1}$. Removal of all temperatures below -10^oC result in normally distributed lapse rates with a mean equal to the environmental rate of -0.0066 $K\ m^{-1}$, which is used in this study for distributing temperature. For melt modelling, a lapse rate higher than the environmental lapse rate would result in more Type **I** errors than Type **III** (see Fig. 2 and caption for a description of error types) leading to an overestimation of melt.

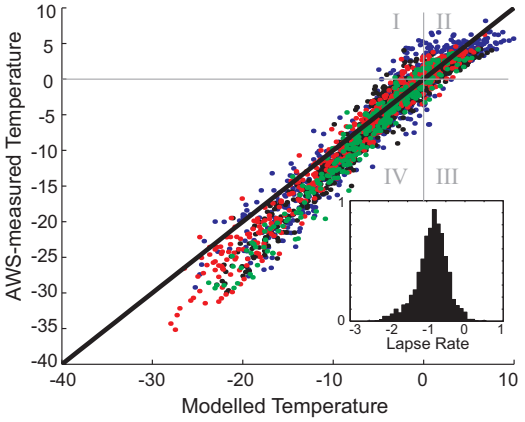

Fig. 2. Measured and modelled temperatures at each AWS from Ny Ålesund using the environmental lapse rate of -6.6 $K\ km^{-1}$. The inset shows the histogram of calculated lapse rates ($K\ km^{-1}$) of all the stations. The AWS's at Kongsvegen stakes 1 and 6 are shown in blue and black, respectively where those on Kronebreen stakes 2 and 4.5 are shown in red and green, respectively. The roman numerals represent the error type quadrants relevant for model melt where the 0^oC threshold distinguishes between melt and no melt. In Type **I** errors, melt is observed but not modelled (underestimation) whereas Type **III** errors result in days that melt is modelled but not observed (overestimation). Type **II** and **IV** errors are when both measured and modelled temperatures are above and below zero, respectively.

Distributing precipitation

Accumulation in the region is highly dependent upon elevation and related to the sum of precipitation from October to May at the Ny Ålesund meteorological station (Lefauconnier and others, 1999). The Ny Ålesund precipitation time series is spatially and temporally distributed over the glaciers using a stepwise multiple regression between the winter balance measurements and elevation (z), sum of precipitation (P_{sum}), mean winter temperature, distance to Ny Ålesund and geographic location. The final regression model containing only significant parameters is:

$$A\,(x, y, a) = c_1 \cdot z\,(x, y) + c_2 \cdot z\,(x, y) \cdot P_{\mathrm{sum}}\,(w) \qquad (15)$$

where $A\,(x, y, a)$ is a rasterized accumulation map [m a^{-1}] (see Taurisano and others, 2007; Schuler and others, 2007) describing the spatial distribution (x and y are UTM coordinates) for each mass balance year based upon the sum of precipitation (P_{sum}) from October to May (w). The regression coefficients, c_1 and c_2, are obtained independently for each glacier through least squares minimization of all available stake measurements and carry the units [-] and [m^{-1}], respectively. The root mean square error (RMSE) between the stake measurements and the model is 0.11 and 0.15 m w. eq. for Kronebreen and Kongsvegen, respectively (Fig. 3). We assume that lateral variability of accumulation at a particular elevation interval is normally distributed around the centerline stake measurements. An independent regression coefficient for P_{sum} became insignificant after inclusion of the interaction term ($z \cdot P_{\mathrm{sum}}$) because a relatively low precipitation year at sea level (e.g. Ny Ålesund) does not necessarily result in low accumulation at higher elevations on the glacier and

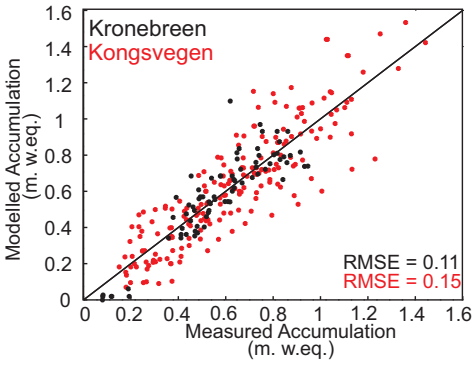

Fig. 3. Measured vs. modelled accumulation at the stake measurments of Kongsvegen and Kronebreen. The specific point error is ≈ 0.15 m. w. eq. (RMSE)

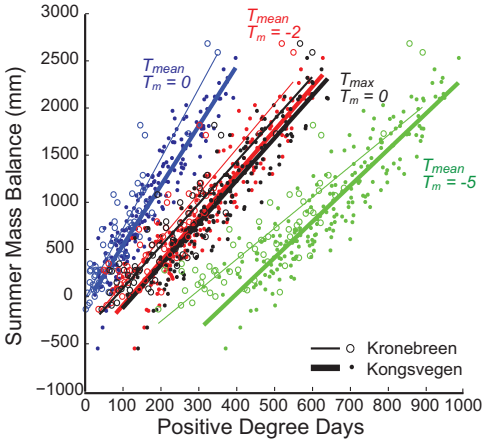

Fig. 4. Sum of positive degree days (PDD) vs. the summer ablation (plotted with melt as positive) for each stake and year for Kongsvegen and Kronebreen. Four scenarios for calculating PDDs are shown; three using the mean diurnal temperature (T_{mean}) with $t_m = 0$, -2 and -5 and one using the maximum diurnal temperature (T_{max}) and $T_m = 0$

thus the inter-annual variability of accumulation at sea-level is larger than that at higher elevations.

Implementation of the regression model is obtained by first determining the annual accumulation map ($A\,(\boldsymbol{x}, \boldsymbol{y}, a)$ in Eq. 15) that contains daily time step, t. This accumulation map is then normalized using the Ny Ålesund record of daily precipitation, $P\,(t)$, divided by the sum of precipitation, $P_{\boldsymbol{sum}}$, in the respective winter (w = Oct-May) or summer (s = Jun-Sept) season:

$$A\,(x, y, t) = A\,(x, y, a) \cdot \frac{P\,(t)}{P_{\mathrm{sum}}\,(w/s)} \qquad (16)$$

$A\,(x, y, t)$ is the daily spatially distributed accumulation field. This approach assumes that the summer precipitation distribution is similar to the previous winter. If the mean temperature at pixel i is below the snow temperature threshold (T_s), then snow is distributed. We choose T_s to be +1.5 ^{o}C as it has been observed that mixed rain/snow occurs up to at least 2^o over the freezing point (CRREL, 1956).

Melt Model

The high correlations between temperature and several of the energy balance components (Braithwaite, 1981; Ohmura, 2001; Sicart and others, 2008) have allowed melt to be successfully modelled using temperature alone (Hock, 2003). We apply a simple melt model, the classical degree day method, as it is only dependent upon temperature of which observations in Ny Ålesund are available. Melt is calculated at each glacier pixel (x, y) for each day (t) that temperature (T) is above the melt threshold (T_m) using separate positive Degree Day Factors (DDF) for snow and ice:

$$Melt(x, y, t) = DDF\,(\mathrm{snow/ice}) \cdot [T\,(x, y, t) - T_m] \qquad (17)$$

DDFs are presumably different for snow and ice covered surfaces due to the varying albedo (Braithwaite, 1995) and thus DDF for ice is assumed higher than that for snow. We determine DDFs by minimizing the RMSE of the residuals between the model and the specific summer net balance stake measurements, independently for each glacier.

The temperature at each grid point (x, y) is estimated by distributing temperature in Ny Ålesund using the environmental lapse rate and the DEM. The diurnal maximum temperature (T_{max}) is used rather than the diurnal average temperature (T_{mean}) because there are many days in early spring and autumn where temperatures above freezing occur (thus melting) but T_{mean} is below freezing due to cold nights. This temporal under-sampling problem induces the DDF for snow to be higher than that for ice in order to compensate for missed melting when $T_{\mathrm{mean}} < 0$ (Van den Broeke and others, 2010). In this study, using T_{mean} also resulted in $DDF_{\mathrm{snow}} > DDF_{\mathrm{ice}}$. Van den Broeke and others (2010) solve this by decreasing T_m. We choose to use T_{max} which is equivalent to setting T_m equal to -2 ^{o}C (Fig. 4).

RESULTS

Geometry Changes

Kongsvegen and Kronebreen have lost about 5% and 1% of their 1966 area, respectively. The majority of area loss occurred in the 1966 - 1990 epoch and the front position has remained relatively stable since 1990. Within the time frame of this study, the medial moraine dividing the two glaciers has migrated reflecting the mass flux variations between the two glaciers (Kääb and others, 2005). In 1966, Kongsvegen occupied ≈50% of the calving front whereas in 2007 the glacier rested on land. The elevation changes for all three epochs are shown in Fig. 5. The retreat of the glacier front is apparent as a linear elevation change rate increasing from the 1966 front to the 1990 front position (in Fig. 5f and g). Retreat from 1990 to 2007 is negligible.

On Kongsvegen, the elevation change rate has remained relatively stable between the two time epochs (Fig. 5f). Above 550 m.a.s.l., the glacier surface elevation increases, greatest along the centerline (up to +1 m a^{-1}) compared to the average of the elevation interval. This is especially true for epoch I, but less so during epoch II which is in agreement with the decreased thickening observed by Hagen and others (2005). Also, elevation increase occur lower (≈ 400 m) on Sidevegen than on Konsvegen (≈ 500 m), visible as the cloud of gray

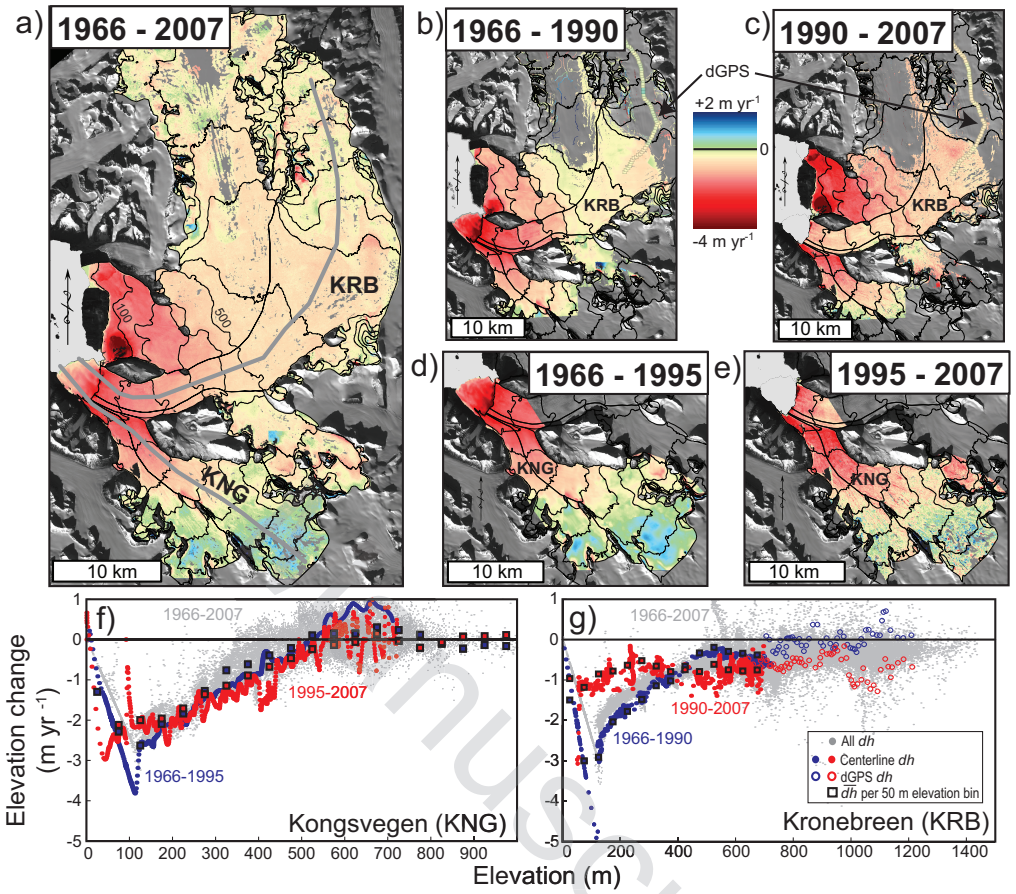

Fig. 5. Elevation change rates on Kongsvegen, Kronebreen and Kongsbreen for [a] the entire time series, 1966-2007, and [b & d] for epoch I (1966-1990/5) and [c & e] epoch II (1990/5-2007). Elevation losses over the marine retreat area do not include ice below sea level. The gray solid lines in [a] represent the centerlines of both glaciers. [f & g] show the elevation change rates as a function of elevation for each glacier. In grey are all $\frac{\partial h}{\partial t}$ pixels from the entire time series (1966-2007) where full spatial distribution is possible. $\frac{\partial h}{\partial t}$ for epoch I and II are shown for the centerline and elevation interval averages.

dots between 300-500 m.a.s.l. in Fig. 5f that deviate from the Kongsvegen centerline.

On Kronebreen, $\frac{\partial h}{\partial t}$ of the glacier tongue for the full period (1966-2007) is similar to Kongsvegen as well as Kongsbreen[1] (Fig. 5a). During epoch I, however, frontal thinning rates were similarly intense at Kongsvegen and Kronebreen, but slightly less pronounced on Kongsbreen (Fig. 5b). Conversely, during epoch II, the largest elevation change rates occur on Kongsvegen and Kongsbreen ($\approx$ -2 to -3 m a^{-1}) while Kronebreen shows a lowering of $\approx$ -1 m a^{-1} over the entire surface (Fig. 5c). Kronebreen's frontal thinning rate has thus been reduced in epoch II by as much as 33-66% the surface lowering rate observed in epoch I. The spatial and temporal $\frac{\partial h}{\partial t}$ variation between the glaciers and epochs suggest dynamic variation.

Due to the lack of data in the upper area of Kronebreen (mainly in the 1990 DEM), the centerline differential GPS profile from 1996 is compared to both the 1966 and 2007 DEMs (Fig. 5b,c and g). Before differencing, the mean difference between the dGPS and overlapping 1990 DEM is estimated and removed from the 1996 heights to provide an estimated 1990 surface. This assumes that the relative geometry has remained constant between 1990 and 1996 and all elevation differences are uniform within this period, which at least seems to be the case for the longer 1966-2007 differences which remain relatively constant from $\approx$ -0.75 to +0.25 m a^{-1} above 700 m.a.s.l. However, from 1966-1990, the elevation change rates above 700 m.a.s.l. was closer to zero while after 1990 they were closer to -1 m a^{-1}. In summary, above 400 m.a.s.l., the elevation change rate is less negative during epoch I, while below 400m the elevation change rate is less negative during epoch II. Contrasting to Kongsvegen, lateral variability of elevation changes at the highest elevation bins seem to be limited, allowing an assumption of center-line values to represent the entire elevation bin.

[1]See Fig. 1 for the location of Kongsbreen in relation to Kongsvegen and Kronebreen

Table 3. Calibrated parameter sets for the precipitation distribution model (the c_1 and c_2 of eqn. 15) and Degree Day Factors (DDF) of the melt model (eqn. 17). Three periods are shown on Kongsvegen because the time series is long enough to analyze different parameter sets for the two epochs. Also shown is the Root Mean Square Error (RMSE) between the specific mass balance measurements and the model for all years.

	Winter			Summer			Net
	c_1 [–]	c_2 [m^{-1}]	RMSE [m a^{-1}]	DDF_{snow} [mm $K^{-1}day^{-1}$]	DDF_{ice} [mm $K^{-1}day^{-1}$]	RMSE [m a^{-1}]	RMSE [m a^{-1}]
Kongsvegen							
1987 - 2008	0.00066	0.00239	0.24	3	3.5	0.26	0.35
1987 - 1995	-	-	0.25	3.3	3.4	0.18	0.31
1995 - 2008	-	-	0.22	2.8	3.6	0.25	0.36
Kronebreen							
2003-2010	0.00045	0.0011	0.18	3.1	4.7	0.29	0.33

Surface Mass Balance (SMB) model

Table 3 shows calibrated DDF values and the root mean square error (RMSE) between measured and modelled SMB from various periods. On Kongsvegen, the 21 year stake record results in DDFs of 3.0 and 3.5 mm $K^{-1}day^{-1}$ for snow and ice, respectively. On Kronebreen, DDFs for snow and ice are 3.1 and 4.7 mm $K^{-1}day^{-1}$, respectively. Using these parameter sets, the model is applied to the time series of meteorological data. Figure 6 shows the mass balance measured at each stake vs. the corresponding modelled value for all years (individual years are shown in Fig. A1). On Konsgvegen, the RMSE of winter, summer and net stake mass balances is 0.24 m, 0.26 m and 0.35 m a^{-1}, respectively (Tab. 3). Similarly on Kronebreen, the RMSE is 0.18, 0.29 and 0.33 m a^{-1} for the winter, summer and net stake mass balances, respectively.

Figure 7 shows the modelled cumulative net mass balance since 1969. In general, SMB of Kongsvegen has remained close to zero until becoming more negative in the late 1990s. Kronebreen was slightly positive during epoch I, but also turned more negative in epoch II. Superimposed on the figure are the geodetic balances estimated for the entire period and in epoch I (1966-1990/5) and II (1990/5-2007). The difference between the entire geodetic time series (1966-2007) and the sum of epoch I and epoch II is the un-removed systematic bias shown in the residual triangulation of Table 2.

On Kongsvegen, the volume change estimated by interpolating the spatially variable $\frac{\partial h}{\partial t}$ is ≈3 m more negative than SMB (Fig. 7). The underestimation of the SMB model is an extrapolation failure due to the predominance of z for distributing T and P, and therefore horizontal variability is not accounted for. Spatial variability is seen in the elevation difference maps (Fig. 5a and f) in which the centerline $\frac{\partial h}{\partial t}$ shows much larger thickening than the average per elevation bin above the ELA. Integrating the centerline $\frac{\partial h}{\partial t}$ using the *hypsometric* approach results in a geodetic balance more similar to the modelled SMB (Fig. 7). Considering velocities are negligible on Kongsvegen (Melvold and Hagen, 1998), the spatial variability of $\frac{\partial h}{\partial t}$ is governed by SMB, most likely to the distribution of snowfall which is slightly positively biased towards the centerline.

Figure 7 also presents the results of the SMB model on Kronebreen from 1969 to present. The cumulative mass balance remained slightly positive until the mid-1990s, where similarly to Kongsvegen, the mass balance became more negative. The geodetic balance of Kronebreen shows a loss of ≈18-20 m w.eq. within the time period. The strikingly large difference between the volume change and SMB is proposed to be caused by calving.

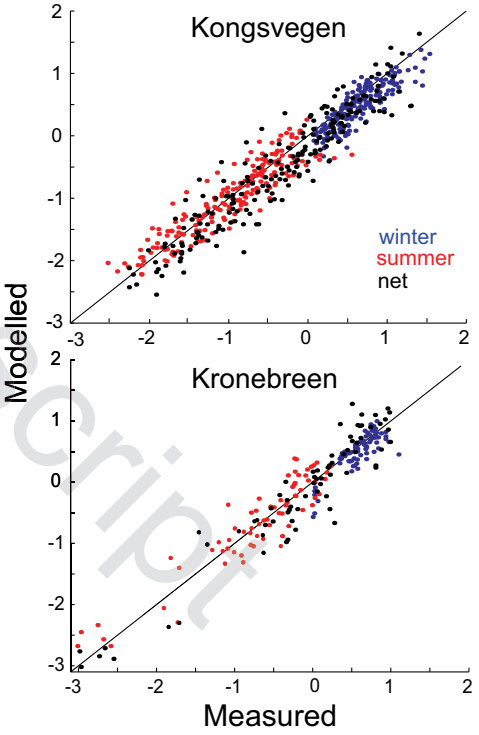

Fig. 6. The measured vs. modelled winter (blue), summer (red) and net (black) stake mass balance on Kongsvegen from 1987-2008 and on Kronebreen from 2003-2010. The RMSE for each season is presented in Tab. 3

Flux Divergence

Figure 7 makes it clear that on Kronebreen the residual between the geodetic balance and SMB is significantly negative. This component reflects the loss of ice due to calving, and is on the order of 10 times the cumulative SMB. To analyze this

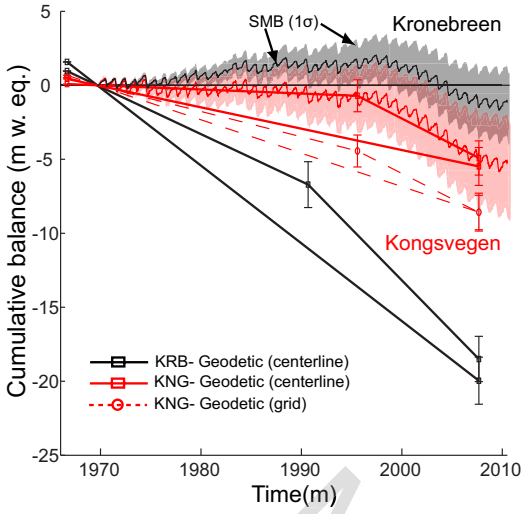

Fig. 7. The cumulative surface mass balance (SMB) model for Kongsvegen (red) and Kronebreen (black). The error zone is one standard deviation (σ) of model runs using DDFs of $\pm$0.5 around the central values provided in Table 3. The cumulative geodetic balance is also shown at squares and circles with connecting lines. The dotted red line shows the geodetic balance estimated using the full range $\frac{\partial h}{\partial t}$ field while the straight lines show those using the centerline. Kronebreen is only shown with the centerline value as there was no visible difference between the centerline and full range $\frac{\partial h}{\partial t}$ field in the 1966-2007 period. All changes are relative to 1969 when the meteorological observations were initiated.

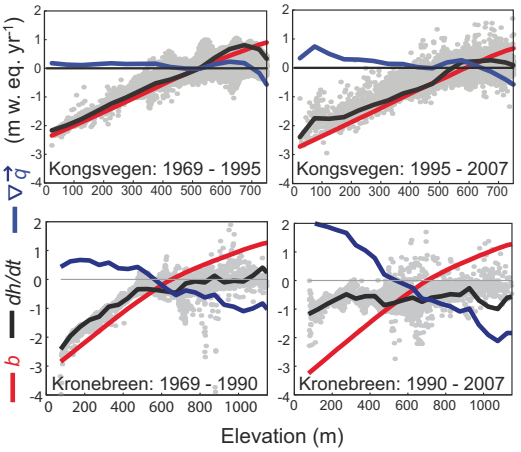

Fig. 8. The annual surface mass balance rates (b), elevation change rates ($\frac{\partial h}{\partial t}$) and the difference between them on Kongsvegen (top) and Kronebreen (bottom). Elevation change rate pixels are shown in gray. On Kongsvegen, $\nabla\vec{q}$ is essentially zero and thus the blue line represents an error term as $\frac{\partial h}{\partial t}$ and b have been shown to be equal (Melvold and Hagen, 1998; Hagen and others, 2005). On Kronebreen, $\nabla\vec{q}$ is positive below the ELA and negative above. The slope of $\nabla\vec{q}$ with elevation increased from epoch I to epoch II.

in more detail, the average annual surface mass balance and elevation change is plotted by elevation (Fig. 8). On Kongsvegen, the difference between these curves is small and represents any systematic error related to $\frac{\partial h}{\partial t}$ and b. This error can be introduced, for example, with a failed prescription of ρ_{eff} in κ (eq. 6 and 7) or to unaccounted internal accumulation. On Kronebreen, the difference between $\frac{\partial h}{\partial t}$ and b is greater. We propose that $\nabla\vec{q}$ is dominated by the emergence velocity below the ELA as errors related to ρ_{eff} are minimal. Above the ELA, this may represent the submergence velocity though greater uncertainty prevails due to the compressible firn area. The slope of $\nabla\vec{q}$ with elevation has increased from epoch I to epoch II. This is interpreted by a larger influx of ice that compensates for ice loss through the SMB, resulting in a relatively flat $\frac{\partial h}{\partial t}$ gradient with elevation. Above the ELA, submergence rates may be on the order of -1 to -2 m a^{-1}, though unaccounted internal accumulation in the SMB or a lower κ in the conversion of $\frac{\partial h}{\partial t}$ to water equivalent will reduce this value.

The use of the smallest glacier area as a *reference* surface for integration of the geometric changes and mass balance components makes a drainage basin balance assessment possible (similar to Bindschadler, 1984). The 2007 front position functions as a flux gate in all calculations. The integration of the SMB over this area in both epochs is the glacier wide balance (B in eq. 13). Integration of the elevation changes over this same area results in the volume change ($\frac{\partial V}{\partial t}$). The difference results in an estimate of the ice flux (Q) through the 2007 flux gate. To account for the retreat, we also estimated the volume of ice loss over the area of retreat ($\frac{\partial V_r}{\partial t}$) using the bathymetry in the retreat areas. SMB of the retreat area (B_r) is estimated by applying the SMB model to the entire area of retreat, and linearly scaling the time series of B_r down to zero. This essentially assumes a linear retreat of the front.

Table 4 provides estimates of the components in eq. 12, 13 and 14 for both glaciers and epochs assuming $\kappa = 0.9$. On Kongsvegen, B is the largest component of $\frac{\partial V}{\partial t}$ and the magnitude of B increased three-fold from the first to second epoch. A slight residual between $\frac{\partial V}{\partial t}$ and B persist on Kongsvegen. Kronebreen exhibits opposite behavior. In the first epoch, B is 2.5% of $\frac{\partial V}{\partial t}$, making the calving flux (Q) 97.5% of ice loss during this epoch. In the second epoch, B doubled, comprising 25% of $\frac{\partial V}{\partial t}$ while Q represents 75% of ice loss. Despite the decrease in the proportional calving to volume change, the effective calving through the 2007 flux gate (Q) nearly doubled in epoch II compared epoch I. The difference is slightly reduced when calculating the net flux (Q') including the retreat flux (Q_r) which is dependent not only on Q but also to the underlying topography of the retreat area.

DISCUSSION

Assumptions and Errors

The significance of errors on estimations is strongly dependent on the magnitude of the observed glacier changes. Many approaches for estimating errors in both direct glaciologic mass balances and geodetic volume change estimates have been applied, commonly using statistical theory of stochastic error propagation. For example, Thibert and others (2008) and Zemp and others (2010) keep very detailed track of systematic uncertainties that are combined with the stochastic error to form the total error. The stochastic errors of the

Table 4. The volume change ($\frac{\partial V}{\partial t}$), surface mass balance B and flux (Q) estimated for both glaciers in epoch I (1969 - 1990/5) and II (1990/5 - 2007). The components of the retreated area ($\frac{\partial V_r}{\partial t}$ and B_r) between 1966 and 1990/5 are also provided. The area of Kongsvegen is 182, 173 and 173 km^2 in 1966, 1995 and 2007, respectively. The area of Kronebreen is 392, 388 and 387 km^2 in 1966, 1990 and 2007, respectively. All mass continuity components are provided in water equivalent units km^3 a^{-1}.

	$\frac{\partial V}{\partial t}$	$\frac{\partial V_r}{\partial t}$	B	B_r	Q	Q'	Q_r
Kongsvegen							
Epoch I	-0.005 (±0.006)	-0.020 (±0.002)	-0.023 (±0.010)	-0.015 (±0.004)	0.018 (±0.012)	0.013 (±0.013)	-0.005 (±0.004)
Epoch II	-0.061 (±0.016)	- -	-0.071 (±0.017)	- -	0.010 (±0.023)	- -	- -
Kronebreen							
Epoch I	-0.125 (±0.025)	-0.023 (±0.003)	0.006 (±0.020)	-0.012 (±0.003)	-0.130 (±0.031)	-0.141 (±0.031)	-0.011 (±0.004)
Epoch II	-0.267 (±0.034)	- -	-0.069 (±0.029)	- -	-0.198 (±0.045)	- -	- -

estimates are relatively easy to handle while the systematic errors are difficult to detect and quantify. In this section, the stochastic and controlled systematic errors of each of the estimated mass continuity components are described first. Following is a discussion of systematic errors related to the assumptions we have applied, including sensitivity tests on these assumptions.

For the geodetic estimates, the stochastic point error is estimated as the standard deviation (σ) of elevation residuals between two DEMs over stable terrain (Tab 2, maximum 10 m). The error about the mean elevation change is then obtained by the standard error equation, assuming an autocorrelation length of 1 km (Nuth and others, 2007). Systematic errors in the DEMs are controlled by first co-registering the data, and the triangulated elevation residual between three DEMs is an estimate of the systematic bias remaining; the lower panel of Tab. 2, specifically 1960-1990-2007 for Kronebreen and 1966-1995-2007 for Kongsvegen. Systematic and stochastic errors are combined through the root sum of squares (RSS) resulting in a final error dominated by the systematic component. The geodetic error is then ≈10-25% of the volume change (Tab. 4), though can be larger than 100% when the change is small (Kongsvegen-Epoch I).

Errors of the direct specific stake measurements of an annual resolution are relatively small compared to the error introduced by spatial extrapolation (i.e. not capturing the horizontal variability). Additionally, we model SMB empirically by relating the specific seasonal winter and summer measurements to temperature and precipitation. The accuracy of this approach is strongly dependent upon the calibrated model parameters. Therefore, error of the cumulative mass balance series is estimated by taking one standard deviation of model outputs by varying DDFs for snow and ice of 0.5 mm ^{o}C^{-1}day^{-1} around the central value provided in Table 3. The error in B is ≈30-200% of the Kongsvegen $\frac{\partial V}{\partial t}$ since changes are not strongly different from zero. On Kronebreen, error in B is on the order of 10-15% of $\frac{\partial V}{\partial t}$ (Tab. 4).

The error for the calving flux is then the combined RSS of the $\frac{\partial V}{\partial t}$ and B errors, and is about 25% of estimated calving flux on Kronebreen (Tab. 4). On Kongsvegen, we do not expect much ice loss through calving and therefore any residual between $\frac{\partial V}{\partial t}$ and B is associated to some un-removed systematic biases. Some ice could be lost through entrainment into Kronebreen at the tongue, though the sign of the calving would be negative rather than positive. Interestingly, the magnitude of the bias is of the same order of magnitude as the estimated decadal average accumulation of superimposed ice (Brandt and others, 2008), an effect that would cause a positive value in the difference between $\frac{\partial V}{\partial t}$ and B.

The weakest part of our application of the mass continuity equation is the potential bias induced by assumptions made in simplifying the mass continuity equations. The density ratio, κ, required to convert elevation changes into water equivalent volume changes is not completely certain and commonly assumes a constant value equal to the density of ice. This assumption is satisfied in the ablation area, but is questionable in the compressible firn pack. In the firn area, the density of ice can be assumed based upon Sorge's Law which states that the density at a given depth does not change with time, provided a constant accumulation rate (Bader, 1954). However, a change in the firn pack thickness and/or density will invalidate Sorge's Law. We also assume that englacial and basal mass balance components are negligible, but these components are probably orders of magnitudes smaller than the surface component (Cuffey and Paterson, 2010). Last, mass balance measurements (b) made in the accumulation area assume that all melt discharges from the glacier although internal accumulation may be occurring. To assess the sensitivity of these assumptions on Q, we apply two scenarios, the first related to $\frac{\partial h}{\partial t}$ in the definition of κ and the second related to b. The scenarios are based upon varying these terms above the average ELA, defined at 500 and 700 m.a.s.l. for Kongsvegen and Kronebreen, respectively.

Scenario 1: Test of firn thickness changes. Use $\kappa = 0.55$ for $\frac{\partial h}{\partial t}$ above the ELA.

Scenario 2: Test of internal accumulation. Assume that 50% of the modelled mass losses (b) above the ELA are maintained in the system.

These scenarios provide upper and lower bounds to the derived flux through a fixed gate (Q) based upon simplified assumptions of systematic bias (Tab. 5). The effect of scenario 1 is opposite on the two glaciers because Kongsvegen is thickening above the ELA whereas Kronebreen is thinning above

Table 5. Sensitivity tests applied on the mass continuity solution of Q where $\Delta Q = Q_{ref} - Q_{scenario}$. The reference assumes $\kappa = 0.9$ over the entire glacier. Scenario 1 assumes $\kappa = 0.55$ above the ELA. Scenario 2 assumes that 50% of melt above the ELA is maintained in the system. The ELA is for these sensitivity tests held constant at 500 and 700 m.a.s.l. for Kongsvegen and Kronebreen, respectively. All units are km^3 a^{-1} water equivalent.

	Kongsvegen				Kronebreen			
	$\frac{\partial V}{\partial t}$	B	Q	ΔQ	$\frac{\partial V}{\partial t}$	B	Q	ΔQ
Period I - Reference	**-0.005**	**-0.023**	**0.018**	**-**	**-0.125**	**0.006**	**-0.131**	**-**
Scenario 1	-0.023	-0.023	0.000	0.018	-0.123	0.006	-0.129	-0.002
Scenario 2	-0.005	0.007	-0.012	0.030	-0.125	0.030	-0.155	0.024
Scenario 1 + 2	-0.023	0.007	-0.030	0.048	-0.123	0.030	-0.153	0.022
Period II - Reference	**-0.061**	**-0.071**	**0.010**	**-**	**-0.267**	**-0.069**	**-0.198**	**-**
Scenario 1	-0.066	-0.071	0.005	0.005	-0.224	-0.069	-0.155	-0.043
Scenario 2	-0.061	-0.031	-0.030	0.040	-0.267	-0.028	-0.239	0.041
Scenario 1 + 2	-0.066	-0.031	-0.035	0.045	-0.224	-0.028	-0.196	-0.002

the ELA. Scenario 2 obviously increases the SMB. Cases of firn compaction would theoretically reduce κ with limits approaching zero if the entire $\frac{\partial h}{\partial t}$ is the result of firn compaction. However, this is rather unlikely mainly because the positive and negative observed $\frac{\partial h}{\partial t}$ above the ELA on Kongsvegen and Kronebreen, respectively, would imply that the firn pack of these two adjacent glaciers is expanding and compressing, respectively, despite the rather similar climatic situations. In addition, changes in the firn thickness of the upper basin of Kronebreen have not been observed between 1992 and 2005 (Uchida and others, 1993; Sjögren and others, 2007; Nuth and others, 2010). In summary, the worst-case scenario of these simplifying assumptions results in a 20% difference in estimates of Q for Kronebreen. On Kongsvegen, the effects are slightly larger due to the smaller magnitude of $\frac{\partial V}{\partial t}$, however, the good coherence between $\frac{\partial V}{\partial t}$ and B through eq. 11 (Fig. 7) infer a proper assumption of κ.

Interpretation

The comparison between SMB and geometric changes is based upon mass continuity. We also utilize concepts derived by Elsberg and others (2001) about the difference between the *conventional* mass balance which is the actual mass change and the *reference* mass balance which is integration over a constant geometry. In their study, the reference surface is held constant at the largest area and positive corrections are applied based upon the geodetic volume changes, since the glacier is thinning and retreating. In this study, the *reference* mass balance is obtained through integration over the newest (i.e. smallest) area and transformation to conventional mass balances is in the negative direction to account for frontal retreat (B_r). The use of the smallest area additionally allows for full balance assessment (as in Bindschadler, 1984) of the glacier basin by using the most recent front position as a flux gate.

Kongsvegen provides control on the SMB model because it is in its quiescent phase of a surge cycle (Melvold and Hagen, 1998; Hagen and others, 2005). However, Figure 5f shows the centerline elevation change rates on Kongsvegen are not perfectly representative for the entire surface of Kongsvegen. Figure 7 shows the cumulative geodetic balances computed by the *grid* approach and by the *hypsometric* approach using the centerline. The cumulative surface mass balance matches closest to the centerline geodetic estimates. The lack of significant ice flow suggests that spatial $\frac{\partial h}{\partial t}$ variability, which is most dominant above the ELA, is governed by SMB variability. This may be due to radiation variability, which can affect melt (Arnold and others, 2006), previously hypothesized to cause geodetic balances to be more negative than either traditionally measured mass balances or centerline extrapolated estimates on a nearby small valley glacier, Midtre Lovénbreen (Rees and Arnold, 2007; Barrand and others, 2010). If this were so, then we could expect that the reduced radiation along the edges of the glacier due to topographic shading (Arnold and others, 2006) would reduce melt and thus a centerline estimate would be more negative than a glacier-wide estimate. The opposite is seen here (as well as in the previous studies mentioned above).

We suggest instead that lateral accumulation variability is responsible for the underestimation of the modelled SMB and centerline geodetic balance (Fig. 7). Centerline $\frac{\partial h}{\partial t}$ above 500 m on Kongsvegen is more positive than the elevation bin average (Fig 5) and slightly larger accumulation is measured along the main centerline than in the two northern basins measured within the past 10 years (Kohler, unpublished). Accumulation affects the timing of albedo decrease within the summer mass balance season and the DDF transition from snow to ice within the model. This results in the model underestimating melt in areas where snow accumulation is overestimated. Therefore, the combined affect of an overestimated accumulation and an underestimated melt result in an underestimated cumulative SMB (and centerline geodetic balance) as compared to the full spatially integrated geodetic balance (Fig. 7).

The SMB of Kongsvegen has decreased drastically in epoch II (Table 4), and especially since the late 1990s - early 2000s (Fig. 7). On Kronebreen, a similar decrease in the SMB is modelled, though this is not as great because of the higher elevation range of the Kronebreen basin. Similar rapid (geodetic) mass balance decreases have been observed on two small land-terminating glaciers in western and central Spitsbergen (Kohler and others, 2007). Since 2007, it seems that the cumulative SMB has become less negative on both glaciers, similar to other measurements of surface mass balance and elevation changes in Svalbard (Moholdt and others, 2010a,b).

On Kronebreen, $\frac{\partial V}{\partial t}$ estimated from the centerline $\frac{\partial h}{\partial t}$ and full spatially integrated $\frac{\partial h}{\partial t}$ are similar within the errors. $\frac{\partial V}{\partial t}$ is much larger than B in magnitude and therefore, the flux of ice through the 2007 flux gate (Q) is the main contributor to $\frac{\partial V}{\partial t}$ over the past four decades. Interestingly, despite the increased proportion of B to $\frac{\partial V}{\partial t}$ from epoch I to epoch II

(2.5% to 25%), Q has nearly doubled (Tab. 4). Including the calving retreat flux (Q_r) to estimate the total calving flux (Q') slightly reduces the difference. However, Q_r and therefore Q' is dependent upon both the influx of ice upstream (Q) as well as the underlying topography. For example, Vieli and others (2001) model a rapid retreat over a basal depression and suggest that the rapid retreat is more dominantly an effect of bed topography rather than changes in climate. Therefore, it may be more feasible in this study to compare values for Q out of a fixed flux gate. It remains unclear how the retreat flux (Q_r) effects Q during the retreat of epoch I.

We only can speculate on reasons for the calving flux increase as direct measurements of velocity covering the entire period are not available. Available measurements do show inter-annual variability (Kääb and others, 2005) although no drastic increases have been detected over the past four decades (Voigt, 1966; Lefauconnier and others, 1994a; Kääb and others, 2005). The flux of ice comprises both deformation and sliding components. Deformation velocity reacts slowly due to dependence upon ice thickness and slope. Conversely, glacier sliding reacts faster in relation to the subglacial drainage conditions (Iken and Bindschadler, 1986; Kamb, 1987). Recently, accelerated glacier motion has been observed to be related to water pulses that exceed the drainage system capacity (Bartholomaus and others, 2008). Schoof (2010) suggests that increased sliding velocities are due to more frequent water pulses rather than due to an increase in the melt volume. Our calving estimates are averages over decades and may be indirectly related to the temporal average decrease in B. Since Kronebreen is losing volume over the entire glacier basin, especially in epoch II, ice deformation is supposedly decreasing. Therefore, it can be suggested that the increase in calving flux is related to the sliding velocity, and possibly an increase in the decadal average frequency and magnitude of water pulses.

CONCLUSIONS

In this study, we apply mass continuity to solve for the calving flux of a marine terminating glacier, Kronebreen, provided the elevation changes and surface mass balance. Elevation changes are derived for two epochs, 1966-1990/5 and 1990/5-2007. The SMB is modelled using a degree day approach for melt and a regression scheme for precipitation, both calibrated against observations. The negligible calving and quiescent phase behavior of neighboring Kongsvegen provides additional control on the SMB model. To practically apply mass continuity, we define our *reference* surface (Elsberg and others, 2001) as the 2007 (smallest) area which declares this front position as a flux gate.

In the case of Kongsvegen over the 1966-2007 period, the geodetic balance calculated using the full spatial coverage of $\frac{\partial h}{\partial t}$ is 3 m more negative that the modelled cumulative SMB and the centerline estimated geodetic balance. We suggest that this is a result of lateral accumulation variability, especially above the ELA which is not accounted for by the centerline stake measurements. Such variability would cause a reduction in the albedo (and DDF) earlier in the summer season, thus producing more melt. This combined with a lower accumulation results in a lower SMB. Using the centerline estimates of volume change, we find small residuals between $\frac{\partial V}{\partial t}$ and B, which are not significantly different from zero, possibly reflecting un-removed systematic bias.

On Kronebreen, lateral variability is minimal as shown by the elevation changes (Fig. 5g). The large and systematic difference between the volume change and the SMB (Fig. 5 and Table 4) represent the loss of ice through calving. When analyzed locally, the difference represents an estimate of the long term average emergence velocities (Fig. 8) given that our definition of the effective density is correct and internal accumulation is negligible. From mass continuity, we estimate the long term average calving flux to be -0.14 ± 0.03 and -0.20 ± 0.05 km^3 a^{-1} for epoch I and II, respectively.

The surface mass balance of both glaciers has remained close to zero until the late 1990s when it became increasingly negative. Since 2007, the mass balance has stabilized. On Kongsvegen, the annual average glacier-wide SMB (centerline) doubled from -0.21 ± 0.08 m a^{-1} in epoch I to -0.41 ± 0.10 m a^{-1} for epoch II. On Kronebreen, the annual average glacier-wide SMB is more drastically negative from -0.02 ± 0.06 m a^{-1} for epoch I to -0.18 ± 0.03 m a^{-1} for epoch II. On Kronebreen, the calving flux represented 95% and 75% of the geodetic volume change in epoch I and II, respectively. Despite the decrease in the proportion of calving loss to volume loss, the average calving flux increased in epoch II. The increase in flux may only be speculated to be a result in a change in basal hydrological conditions, possibly indirectly related to the rapid decrease of the surface mass balance within epoch II which could lead to more frequent and intense melt pulses that would increase velocities and calving rates (Schoof, 2010).

In summary, geodetic elevation changes have been independently compared with a modelled surface mass balance of a land terminating glacier and a marine-terminating glacier. On calving glaciers, the residual may be large enough to allow significant estimation of the long term calving flux, reducing the need for expensive velocity and ice thickness measurements. Nonetheless, comparison of this approach in cases where continuous long term velocity measurements of the calving glacier tongue are available will provide insightful validation. Furthermore, future applications of surface mass balance models run by regional climate models may soon allow larger spatial extrapolation which can be combined with the more readily available geodetic volume change estimates by DEM differencing to better define the proportion of ice loss to calving.

ACKNOWLEDGEMENTS

This work was made possible through the IPY-GLACIODYN project (176076) funded by the Norwegian Research Council (NFR). The final stage was supported by funding to the ice2sea project from the European Union 7th Framework Programme, grant number 226375, ice2sea contribution number 025. Field work from 2007-2010 was partially funded by the Arctic Stipend provided by the Svalbard Science Forum. Many thanks to Geir Moholdt, Markus Engelhardt, and Torbjørn Østby for proofing early versions of the manuscript. Thanks to the Norwegian Polar Institute mapping department for providing the early DEMs. The SPOT5-HRS DEM (ID: SPI08-025-Svalbard) was obtained through the IPY-SPIRIT program (Korona et al., 2009) ©CNES 2008 and SPOT Image 10 2008 all rights reserved.

REFERENCES

Abdalati, W., W. Krabill, E. Frederick, S. Manizade, C. Martin, J. Sonntag, R. Swift, R. Thomas, J. Yungel and R. Koerner, 2004. Elevation changes of ice caps in the Canadian Arctic Archipelago, *Journal of Geophysical Research-Earth Surface*, **109**(F4), 11.

Ahn, Y. and J. E. Box, 2010. Glacier velocities from time-lapse photos: technique development and first results from the Extreme Ice Survey (EIS) in Greenland, *Journal of Glaciology*, **56**(198), 723–734.

Altena, B, 2008. Hypsometric measurements of Holtedahlfonna in 1966 and 1990, Bachelor Intership Report - Hogeschool Utrecht / The Norwegian Polar Institute.

Andreassen, L. M., 1999. Comparing traditional mass balance measurements with long-term volume change extracted from topographical maps: A case study of Storbreen glacier in Jotunheimen, Norway, for the period 1940-1997, *Geografiska Annaler Series A-Physical Geography*, **81A**(4), 467–476.

Arendt, A. A., K. A. Echelmeyer, W. D. Harrison, C. S. Lingle and V. B. Valentine, 2002. Rapid wastage of Alaska glaciers and their contribution to rising sea level, *Science*, **297**(5580), 382–386.

Arnold, N. S., W. G. Rees, A. J. Hodson and J. Kohler, 2006. Topographic controls on the surface energy balance of a high Arctic valley glacier, *Journal of Geophysical Research-Earth Surface*, **111**(F2), 15.

Bader, H, 1954. Sorge's Law of densification of snow on high polar glaciers, *Journal of Glaciology*, **2**(15), 319–323.

Barrand, Nicholas E., Timothy D. James and Tavi Murray, 2010. Spatio-temporal variability in elevation changes of two high-Arctic valley glaciers, *Journal of Glaciology*, **56 (199)**, 771–780.

Bartholomaus, T. C., R. S. Anderson and S. P. Anderson, 2008. Response of glacier basal motion to transient water storage, *Nature Geoscience*, **1**(1), 33–37.

Baumberger, A, 2007. Massebalanse på Kronebreen/Holtedahlfonna, Svalbard - kontrollerende faktorer, Master's thesis, University of Oslo, Norway.

Berthier, E., Y. Arnaud, D. Baratoux, C. Vincent and F. Rémy, 2004. Recent rapid thinning of the "Mer de Glace" glacier derived from satellite optical images, *Geophysical Research Letters*, **31**(17).

Berthier, E., E. Schiefer, G. K. C. Clarke, B. Menounos and F. Remy, 2010. Contribution of Alaskan glaciers to sea-level rise derived from satellite imagery, *Nature Geoscience*, **3**(2), 92–95.

Bindschadler, R.A., 1984. Jakobshavn Glacier Drainage-basin - A Balance Assessment, *Journal of Geophysical Research-Oceans*, **89**(NC2), 2066–2072.

Bouillon, Aurlie, Marc Bernard, Patrick Gigord, Alain Orsoni, Vronique Rudowski and Alain Baudoin, 2006. SPOT 5 HRS geometric performances: Using block adjustment as a key issue to improve quality of DEM generation, *ISPRS Journal of Photogrammetry and Remote Sensing*, **60**(3), 134 – 146.

Braithwaite, R.J., 1995. Positive degree-day factors for ablation on the Greenland ice-sheet studied by energy-balance modeling, *Journal of Glaciology*, **41**(137), 153–160.

Braithwaite, R. J., 1981. On Glacier Energy-balance, Ablation, and Air-temperature, *Journal of Glaciology*, **27**(97), 381–391.

Brandt, O., J. Kohler and M. Luthje, 2008. Spatial mapping of multi-year superimposed ice on the glacier Kongsvegen, Svalbard, *Journal of Glaciology*, **53**(184), 73–80.

Van den Broeke, M., Carlijn Bus, Janneke Ettema and Paul Smeets, 2010. Temperature thresholds for degree-day modelling of Greenland ice sheet melt rates, *Geophysical Research Letters*, **37**(18), L18501–.

Burgess, D. O., M. J. Sharp, D. W. F. Mair, J. A. Dowdeswell and T. J. Benham, 2005. Flow dynamics and iceberg calving rates of Devon Ice Cap, Nunavut, Canada, *Journal of Glaciology*, **51**(173), 219–230.

Cox, L. H. and R. S. March, 2004. Comparison of geodetic and glaciological mass-balance techniques, Gulkana Glacier, Alaska, USA, *Journal of Glaciology*, **50**(170), 363–370.

CRREL, 1956. Summary Report of the Snow Investigations - Snow Hydrology, *Tech. rep.*, North Pacific Division, Corps of Engineers, U.S. Army, Portland, Oregon.

Cuffey, K.M. and W.S.B. Paterson, 2010. The Physics of Glaciers, Elsevier, Inc., fourth ed.

Elsberg, D. H., W. D. Harrison, K. A. Echelmeyer and R. M. Krimmel, 2001. Quantifying the effects of climate and surface change on glacier mass balance, *Journal of Glaciology*, **47**(159), 649–658.

Goto-Azuma, K., S. Kohshima, T. Kameda, S. Takahashi and J.O. Hagen, 1995. An ice-core chemistry record from Snøfjellafonna, northwestern Spitsbergen, *Annals of Glaciology*, **21**, 213–218.

Gudmundsson, G. H. and A. Bauder, 1999. Towards an indirect determination of the mass-balance distribution of glaciers using the kinematic boundary condition, *Geografiska Annaler Series A-Physical Geography*, **81A**(4), 575–583.

Hagen, J. O., T. Eiken, J. Kohler and K. Melvold, 2005. Geometry changes on Svalbard glaciers: mass-balance or dynamic response?, *Annals of Glaciology*, **42**, 255–261.

Hagen, J. O., K. Melvold, T. Eiken, E. Isaksson and B. Lefauconnier, 1999. Mass balance methods on Kongsvegen, Svalbard, *Geografiska Annaler Series A-Physical Geography*, **81A**(4), 593–601.

Hock, R., 2003. Temperature index melt modelling in mountain areas, *Journal of Hydrology*, **282**(1-4), 104–115.

Hubbard, A., I. Willis, M. Sharp, D. Mair, P. Nienow, B. Hubbard and H. Blatter, 2000. Glacier mass-balance determination by remote sensing and high-resolution modelling, *Journal of Glaciology*, **46**(154), 491–498.

Huss, Matthias, Andreas Bauder and Martin Funk, 2009. Homogenization of long-term mass-balance time series, *Annals of Glaciology*, **50**, 198–206.

Iken, A. and R. A. Bindschadler, 1986. Combined Measurements of Subglacial Water-pressure and Surface Velocity of Findelengletscher, Switzerland - Conclusions About Drainage System and Sliding Mechanism, *Journal of Glaciology*, **32**(110), 101–119.

Jóhannesson, T., C. Raymond and E. Waddington, 1989. Timescale for adjustment of glaciers to changes in mass balance, *Journal of Glaciology*, **35**(121), 355–369.

Kääb, A., 2000. Photogrammetric reconstruction of glacier mass balance using a kinematic ice-flow model: a 20 year time series on Grubengletscher, Swiss Alps, *Annals of Glaciology*, **31**, 45–52.

Kääb, A. and M. Funk, 1999. Modelling mass balance using photogrammetric and geophysical data: a pilot study at Griesgletscher, Swiss Alps, *Journal of Glaciology*, **45**(151), 575–583.

Kääb, A., B. Lefauconnier and K. Melvold, 2005. Flow field of Kronebreen, Svalbard, using repeated Landsat 7 and ASTER data, *Annals of Glaciology*, **42**, 7–13.

Kamb, B., 1987. Glacier surge mechanism based on linked cavity configuration of the basal water conduit system, *Journal of Geophysical Research-Solid Earth and Planets*, **92**(B9), 9083–9100.

Kohler, J., T. D. James, T. Murray, C. Nuth, O. Brandt, N. E. Barrand, H. F. Aas and A. Luckman, 2007. Acceleration in thinning rate on western Svalbard glaciers, *Geophysical Research Letters*, **34**(18), 5.

König, M., J. Wadham, J. G. Winther, J. Kohler and A. M. Nuttall, 2002. Detection of superimposed ice on the glaciers Kongsvegen and midre Lovenbreen, Svalbard, using SAR satellite imagery, *Annals of Glaciology*, **34**, 335–342.

Korona, J., E. Berthier, M. Bernard, F. Rémy and E. Thouvenot, 2009. SPIRIT. SPOT 5 stereoscopic survey of Polar Ice: Reference Images and Topographies during the fourth International Polar Year (2007-2009), *ISPRS Journal of Photogrammetry and Remote Sensing*, **64**(2), 204–212.

Krimmel, R. M., 1999. Analysis of difference between direct and geodetic mass balance measurements at South Cascade Glacier, Washington, *Geografiska Annaler Series A-Physical Geography*, **81A**(4), 653–658.

Langley, K., S. E. Hamran, K. A. Høgda, R. Storvold, O. Brandt, J. O. Hagen and J. Kohler, 2007. Use of C-band ground penetrating radar to determine backscatter sources within glaciers, *IEEE Transactions on Geoscience and Remote Sensing*, **45**(5), 1236–1246.

Lefauconnier, B. and Jon Ove Hagen, 1990. Glaciers and climate in Svalbard: statistical analysis and reconstruction of the Brøggerbreen mass balance for the last 77 years, *Annals of Glaciology*, **14**, 148–152.

Lefauconnier, B., J. O. Hagen, J. B. Orbaek, K. Melvold and E. Isaksson, 1999. Glacier balance trends in the Kongsfjorden area, western Spitsbergen, Svalbard, in relation to the climate, *Polar Research*, **18**(2), 307–313.

Lefauconnier, B., J. O. Hagen, J. F. Pinglot and M. Pourchet, 1994a. Mass-balance estimates on the glacier complex Kongsvegen and Sveabreen, Spitsbergen, Svalbard, using radioactive layers, *Journal of Glaciology*, **40**(135), 368–376.

Lefauconnier, B., J. O. Hagen and J. P. Rudant, 1994b. Flow speed and calving rate of Kongsbreen glacier, Svalbard, using SPOT images, *Polar Research*, **13**(1), 59–65.

Luthcke, S. B., A. A. Arendt, D. D. Rowlands, J. J. McCarthy and C. F. Larsen, 2008. Recent glacier mass changes in the Gulf of Alaska region from GRACE mascon solutions, *Journal of Glaciology*, **54**(188), 767–777.

Melvold, K. and J.O. Hagen, 1998. Evolution of a surge-type glacier in its quiescent phase: Kongsvegen, Spitsbergen, 1964-95, *Journal of Glaciology*, **44**(147), 394–404.

met.no, 2011. The Norwegian Meteorological Institute - www.met.no, website, [accessed Jan. 20, 2011].

Moholdt, G., J. O. Hagen, T. Eiken and T. V. Schuler, 2010a. Geometric changes and mass balance of the Austfonna ice cap, Svalbard, *The Cryosphere*, **4**, 1–14.

Moholdt, G., C. Nuth, J.O. Hagen and J. Kohler, 2010b. Recent elevation changes of Svalbard glaciers derived from ICESat laser altimetry, *Remote Sensing of Environment*, **114**(11), 2756–2767.

Nuth, C. and A. Kääb, 2010. What's in an elevation difference? Accuracy and corrections of satellite elevation data sets for quantification of glacier changes, *The Cryosphere Discussions*, **4**, 2013–2077.

Nuth, C., J. Kohler, H. F. Aas, O. Brandt and J. O. Hagen, 2007. Glacier geometry and elevation changes on Svalbard (1936-90): a baseline dataset, *Annals of Glaciology*, **46**, 106–116.

Nuth, C., G. Moholdt, J. Kohler, J. O. Hagen and A. Kääb, 2010. Svalbard glacier elevation changes and contribution to sea level rise, *Journal of Geophysical Research-Earth Surface*, **115**.

Ohmura, A., 2001. Physical basis for the temperature-based melt-index method, *Journal of Applied Meteorology*, **40**(4), 753–761.

Østrem, G. and M. Brugman, 1991. Glacier mass-balance measurements: a manual for field and office work, vol. NHRI Science Report 4, Environment Canada, National Hydrology Research Institute, Saskatoon.

Rees, W. G. and N. S. Arnold, 2007. Mass balance and dynamics of a valley glacier measured by high-resolution LiDAR, *Polar Record*, **43**(227), 311–319.

Schoof, C., 2010. Ice-sheet acceleration driven by melt supply variability, *Nature*, **468**(7325), 803–806.

Schuler, Thomas Vikhamar, Even Loe, Andrea Taurisano, Trond Eiken, Jon Ove Hagen and Jack Kohler, 2007. Calibrating a surface mass-balance model for Austfonna ice cap, Svalbard, *Annals of Glaciology*, **46**, 241–248.

Sicart, J. E., R. Hock and D. Six, 2008. Glacier melt, air temperature, and energy balance in different climates: The Bolivian Tropics, the French Alps, and northern Sweden, *Journal of Geophysical Research-Atmospheres*, **113**.

Sjögren, B., O. Brandt, C. Nuth, E. Isaksson, V. Pohjola, J. Kohler and R. S. W. Van De Wal, 2007. Determination of firn density in ice cores using image analysis, *Journal of Glaciology*, **53**(182), 413–419.

Taurisano, A., T. V. Schuler, J. O. Hagen, T. Eiken, E. Loe, K. Melvold and J. Kohler, 2007. The distribution of snow accumulation across the Austfonna ice cap, Svalbard: direct measurements and modelling, *Polar Research*, **26**(1), 7–13.

Thibert, E., R. Blanc, C. Vincent and N. Eckert, 2008. Glaciological and volumetric mass-balance measurements: error analysis over 51 years for Glacier de Sarennes, French Alps, *Journal of Glaciology*, **54**(186), 522–532.

Uchida, Tsutomu, Kokichi Kamiyama, Yoshiyuki Fujii, Akiyoshi Takahashi, Toshitaka Suzuki, Yoshitaka Yoshimura, Makoto Igarashi and Okitsugu Watanabe, 1993. Ice core analyses and borehole temperature measurements at the drilling site on Asgardfonna, Svalbard, in 1993, *Memoirs of National Institute of Polar Research. (Special issue)*, **51**, 377 – 386.

Vieli, A., M. Funk and H. Blatter, 2001. Flow dynamics of tidewater glaciers: a numerical modelling approach, *Journal of Glaciology*, **47**(159), 595–606.

Voigt, Ulrich, 1966. The Determination of the direction of movement on glacier surfaces by terrestrial photogrammetry, *Journal of Glaciology*, **6 (45)**, 359–367.

Wahr, John, Sean Swenson, Victor Zlotnicki and Isabella Velicogna, 2004. Time-variable gravity from GRACE: First results, *Geophysical Research Letters*, **31**(11), L11501–.

Zemp, M., P. Jansson, P. Holmlund, I. Gärtner-Roer, T. Koblet, P. Thee and W. Haeberli, 2010. Reanalysis of multi-temporal aerial images of Storglaciären, Sweden (1959-1999); Part 2: Comparison of glaciological and volumetric mass balances, *The Cryosphere*, **4**(3), 345–357.

Zwally, H. J., M. B. Giovinetto, J. Li, H. G. Cornejo, M. A. Beckley, A. C. Brenner, J. L. Saba and D. H. Yi, 2005. Mass changes of the Greenland and Antarctic ice sheets and shelves and contributions to sea-level rise: 1992-2002, *Journal of Glaciology*, **51**(175), 509–527.

APPENDIX

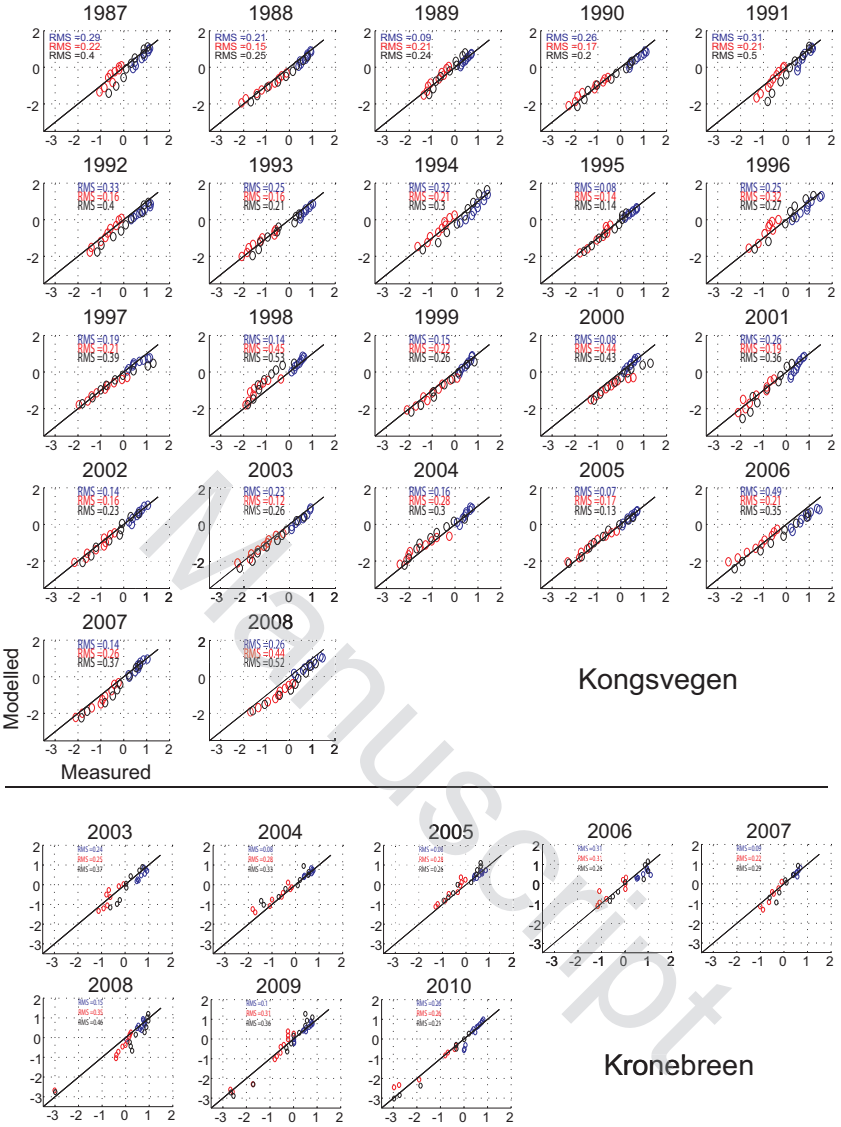

Fig. A1. The measured vs. modelled winter (blue), summer (red) and net (black) surfae mass balance for each year, on each glacier. The colored RMS values are shown with average annual values between 0.1 and 0.5 m w.eq.